Experimental Investigation of Nickel based Cordierite Monolith and Perovskite Oxide Catalysts for Model Biogas Dry Reforming

THESIS

submitted in partial fulfillment
of the requirements to

Birla Institute of Technology and Science, Pilani (BITS Pilani)
For the award of the degree

of

Doctor of Philosophy

by

Ramakrishna Chava

Under the supervision of

Prof. Srinivas Appari

Under the co-supervision of

Prof. Banasri Roy

DEPARTMENT OF CHEMICAL ENGINEERING

BIRLA INSTITUTE OF TECHNOLOGY AND SCIENCE, PILANI-333031

(RAJASTHAN) INDIA

2023

BIRLA INSTITUTE OF TECHNOLOGY AND SCIENCE, PILANI-333031, RAJASTHAN (INDIA)

CERTIFICATE

This is to certify that the thesis entitled **"Experimental Investigation of Nickel based Cordierite Monolith and Perovskite Oxide Catalysts for Model Biogas Dry Reforming"** and submitted by **Mr. Ramakrishna Chava**, ID No. **2017PHXF0424P** for the award of Ph.D. of the Institute embodies original work done by him under my supervision.

(Signature of the Supervisor)

Prof. Srinivas Appari

Department of Chemical Engineering

(Signature of the Co-Supervisor)

Prof. Banasri Roy

Department of Chemical Engineering

BITS Pilani, Pilani Campus

Date:

Dedication

My thesis is dedicated to my father and mother for their unconditional love and support. I Love you dad this is for you and thank you for providing everything

Acknowledgement

I am filled with great pleasure as I express my sincere gratitude to all the individuals who have supported me in achieving this milestone. First and foremost, I would like to express my heartfelt appreciation to my supervisor, Prof. Srinivas Appari, Associate Professor of the Department of Chemical Engineering at BITS-Pilani, for his constant guidance and support throughout my Ph.D. program. I consider myself fortunate to have him as my advisor, who has contributed to a meaningful and productive doctorate experience by providing excellent guidance, encouragement, and support in attending conferences and pushing me towards new ideas and high-quality work. I also extend my gratitude to my co-supervisor, Prof. Banasri Roy, Former HOD, and Professor of the Department of Chemical Engineering at BITS-Pilani, for her valuable suggestions and insights. Her passion and knowledge in analytical techniques and her inspiration towards research have been a source of motivation for me.

I am grateful to Prof. V Ramgopala Rao, Vice-Chancellor of the University, and Prof. Souvik Bhattacharya, former Vice-chancellor, Prof. Sudhirkumar Barai, Director of BITS Pilani, for providing me with the necessary facilities and support to successfully pursue my research. I also acknowledge Prof. M. B. Srinivas, Dean of AGSRD, and Prof. Jitendra Panwar, Former Associate Dean of AGSRD, for creating a supportive environment for my Ph.D. program. My Doctoral Advisory Committee members, Prof. Bhanu Vardhan Reddy Kuncharam, and Prof. Krishna Chaitanya Etika, deserve a special mention for their valuable comments and suggestions that encouraged me to broaden my research perspectives. I would also like to express my appreciation to the Heads of the Department of Chemical Engineering, Prof. Pratik N. Sheth, and Former Head Prof. Banasri Roy.

I would like to extend my thanks to all the faculty members of the Department of Chemical Engineering, including Prof. Hare Krishna Mohanta, Prof. Arvind Kumar Sharma, Prof. Smita Raghuvanshi, Prof. Suresh Gupta, Dr. Priya Sande, Dr. Ajay Kumar Pani, Dr. Amit Jain, Dr.

Somak Chatterjee, Dr. Sarbani Ghosh, Dr. Mohit Garg, and Dr. Jay Pandey, for their support during various phases of my doctoral study. My sincere gratitute to the Dr. Yenumala Sudhakar performing TEM and TPR analysis, I extend my gratitute to Prof. KK Pant head of CRE Lab IIT Delhi for TPD analysis. I am also grateful to all the project students, namely Mr. Prasad, Mr. Devendra, Mr. Harshal, Mr. Surya, Mr. Kartik, and Mr. Anurag, who were a part of this research work. Additionally, I would like to thank all the research scholars of the department. I also extend my thanks to my friends Mr. Anil Kumar Seriyala, Mr. Rajesh Kumar Bheema, Ms. Ip didi, Ms. Soumya Jena, Ms. Shaile, Mr. Ashok, Dr. Adzra, Dr. Raghavendra, Dr. Sudir, and Dr. Pritam. I would like to give a special thanks to Ms. Taniya Kumari Shaw for her love and support. I am also grateful to Mr. Ashok Saini for his assistance in laboratory work and to Mr. Kuldip Kumar for his help with analytical equipment. I would also like to express my gratitude to Mr. Suresh Kumar, Mr. Jeevan Lal Verma, Mr. Jangvir Sheron, and Mr. Sundar for their cooperation during this work.

Lastly, I am grateful to my parents for their unconditional love and sacrifices, which have enabled me to achieve what I have in life. I would also like to thank my beloved sister, Sai Lakshmi, for her encouragement and affection. Finally, I give thanks to the Almighty for giving me the strength and patience to work and for helping me.

Abstract

Biogas is an attractive energy resource that can be utilized in numerous ways, such as producing electricity, biofuel, fertilizers, and hydrogen. The presence of impurities (CO_2, N_2, O_2, and H_2S) has limited the direct utilization of biogas without purification. However, biogas can be converted into synthesis gas ($CO+H_2$) through dry reforming over a catalyst at high temperatures (> 750℃), which eliminates additional and expensive purification for CO_2 removal and improves biogas efficiency. Syngas is an essential intermediate for producing liquid transportation fuels such as methanol and diethyl ether. However, the catalysts used in dry reforming of biogas are prone to severe catalyst deactivation due to sintering and coking, resulting in decreased catalytic activity. Various metals such as Ni, Co, Fe, Pt, Pd, Ru, and Rh are catalysts for the DRBG process. Due to the high activity and availability, Ni is accepted widely as a catalyst. However, Ni catalysts are highly prone to carbon deposition and sintering in DRBG conditions. The Ni-based catalysts' sintering and coking can be overcome by improving metal support interactions, decreasing particle size, or doping Ni in stable structures such as perovskite oxides.

In this study, Ni-based catalysts are developed using alumina coated on cordierite ($2MgO.2Al_2O_3.5SiO_2$) supports. The Ni/Al_2O_3-cordierite catalysts are prepared using sol-gel synthesis followed by the wet impregnation method. Three different types of catalysts are studied by varying calcination times, such as 4 h (C-4), 10 h (C-10), and 20 h (C-20). The strong metal support interaction was achieved by increasing calcination time from 4 h to 20 h. Prolonged calcination led to the formation of (Ni-Mg) Al_2O_4 spinels which are evident from the XRD and TPR analysis.

The reduction of these spinels in the presence of H_2 for 13 h produced smaller Ni nanoparticles on the cordierite support. The average Ni particle size was reduced from 35 nm

to 11 nm by increasing calcination time from 4 h to 20 h. Similarly, H_2 chemisorption shows high dispersion of the C-20 catalyst. In addition, FESEM EDX reveals the diffusion of Mg and Si present in the cordierite to the active layer, and the maximum concentration of these elements is observed for C-20 catalyst. Activity experiments are performed at 800 °C for three different ratios of CH_4/CO_2 = 1.0, 1.5 and 2.0. For the equimolar ratio (CH_4/CO_2), all the catalysts displayed a stable activity for 40 h time on stream, having a conversion of 95% of CH_4 and 86% of CO_2, respectively. For the CH_4/CO_2 of 1.5 and 2.0, the catalysts showed a distinct activity, and among all the catalysts, C-20 showed high stability and activity. Both the C-4 and C-10 catalysts showed high deactivation due to carbon deposition and particle sintering during DRBG. The high activity of C-20 catalysts is attributed to the small Ni particles, strong metal-support interaction, and high dispersion.

Moreover, the CeO_2 modifier decreases the carbon deposition on the Ni/Al_2O_3 cordierite catalysts. The addition of CeO_2 to Alumina coating has decreased the catalytic activity of the catalysts due to the coverage of Ni sites by Ce. It was observed that the graphitic nature of the carbon is considerably reduced with the incorporation of CeO_2. The monolith catalysts showed promising results in the activity study for DRBG.

The Ni's metal-support interaction and anti-sintering are also improved by doping Ni in a stable perovskite oxide (ABO_3) support. Upon reduction under H_2, the Ni nanoparticles are exsolved from the perovskite oxide support. Moreover, carbon deposition can be reduced by creating oxygen vacancies in the structure. Barium (Ba) is selected as another dopant along with Ni, which can create oxygen vacancies and enhance the metal support interaction. Both Ni and Ba are co-doped in an A site deficient $La_{0.9-x}Ba_xNi_{0.15}Al_{0.85}O_3$ (x = 0, 0.02, 0.04, and 0.06) perovskite oxide system prepared using citrate sol-gel synthesis method and calcined at 850 °C for 7 h. The XRD analysis exhibits the host perovskite oxide structure and the exsolved

Ni phase for all prepared catalysts. The partial doping of Ba improves the metal support interaction and oxygen vacancies that enhance catalytic activity and stability, as the TPR and XPS analysis revealed.

HRTEM analysis of reduced catalysts (LB6AN-15) shows highly exsolved Ni nanoparticles on the perovskite support. The stability experiment on $La_{0.9-x}Ba_xNi_{0.15}Al_{0.85}O_3$, for x=0 catalyst, reduced activity due to the catalyst deactivation by sintering, as confirmed by XRD and FE-SEM. The $La_{0.84}Ba_{0.06}Al_{0.85}Ni_{0.15}O_3$ (LB6AN-15) exhibited the highest catalytic stability with having CH_4 and CO_2 conversions of 60% and 93% for 40 h due to the strong metal support interactions, high oxygen vacancies, and anti-sintering of exsolved Ni nanoparticles in DRBG. Among all the studied catalysts C-20 monolith and LB6AN-15 perovskite oxide displayed stable catalytic activity in DRBG experiments.

Keywords: Biogas, Dry reforming, Monolith catalyst, Perovskite oxides, Metal support interaction, Stability, Dispersion, Catalyst deactivation

Table of Contents

List of Figures

List of Tables

List of Abbreviations/Symbols

AD: Anaerobic digestion

ALD: Atomic layer deposition

ATR: Auto thermal reforming

BET: Brunauer-Emmett-Teller

BG: Biogas

CFR: Carbon formation rate

CHP: Combined heat and power plants

CM: Combustion

CNG: Compressed natural gas

CNT: Carbon nanotubes

CP: Co-precipitation

CSG: Citrate sol-gel

DFT: Density functional theory

DR: Dry reforming

DRBG: Dry reforming of biogas

DRM: Dry or co_2 reforming of methane

FE-SEM: Field emission scanning electron microscopy

FSP: Flame spray pyrolysis

FTIR: Fourier transform- infrared spectroscopy

FT: Fischer Tropsch

FWHM: Full width half maximum

GC: Gas chromatography

GHG: Green-house gases

GNC: Glycine nitrate combustion

GW: Gigawatts

HP: Homogenous precipitation

HPWS: High- pressure water scrubbing

HT: Hydrothermal

ICC: Internal combustion engine

IEA: International energy agency

IR: Industrial revolution

JCPDS: Joint committee on powder diffraction standards

ME: Modified oleylamine

MFC: Mass flow controllers

MO: Molten oxide

MTOE: Million tons of oil equivalent

OS: One-step

OSC: Oxygen storage capacity

PEM: Proton exchange membrane

PO: Partial oxidation

PP: Precipitation

RWGS: Reverse water gas shift reaction

SC: Solution combustion

SEM: Scanning electron microscopy

SG: Sol-gel

SMSI: Strong metal-support interaction

SOFC: Solid oxide fuel-cell

SR: Steam reforming

ST: Solvothermal synthesis

TCD: Thermal conductivity detector

TD: Thermal decomposition

TEM: Transmission electron microscopy

TGA/DTA: Thermo-gravimetric analysis/ differential thermal analysis

TOS: Time on stream, h

TPD: Temperature programmed desorption

TPR: Temperature programmed reduction

TWH: Terawatt hour

WGSR: Water gas shift reaction

WHSV: Weight hourly space velocity

WI: Wet impregnation

XPS: X-ray photoelectron spectroscopy

XRD: X-ray diffraction

β_{CH4}: Response factor of CH_4

β: Full width half maximum

λ: Wavelength, nm

T: Temperature, ℃ or Kelvin

1. Introduction

1.1 Brief History of Energy

The first industrial revolution (IR) began in the United Kingdom during the 18th century (1750 to 1840) and established the widespread use of fossil fuels, such as coal, as a source of energy for factories, steam-powered engines, ships, and railways, transforming manufacturing across the globe. Prior to this, global energy relied heavily on natural resources such as wind, water, and biomass burning. Abraham Darby's smelting of iron in Coalbrookdale using coke was a significant turning point in the development of industries that relied on coal as an energy source. The invention of steam engines revolutionized steam-powered sectors and transportation [1]. Additionally, the use of fossil fuels expanded from coal to natural gas and petroleum during the second and third industrial revolutions between 1870 and 2010. Worldwide energy consumption is increasing due to globalization, with fossil fuels such as coal, oil, and natural gas providing the bulk of the required energy. Globalization has improved human lives in terms of economic progress and technological advancement [2]. Figure 1.1 shows the various fuels utilized worldwide from 1800 to late 2020. Until 1950, the usage of coal was predominant compared to fossil fuels such as oil and natural gas. The primary energy transition occurred after the mid-20th century (1940 to present), from coal to utilizing oil and gas resources such as gasoline, natural gas, and other crude oil products. This period saw a rise in the oil industry, surpassing coal as the primary energy source. The primary reasons behind this energy transition were the ease of transportation of fluid forms of oil compared to coal, and the high energy density of oil, which improved economic efficiencies coal and high energy density, which improved economic efficiency [3].

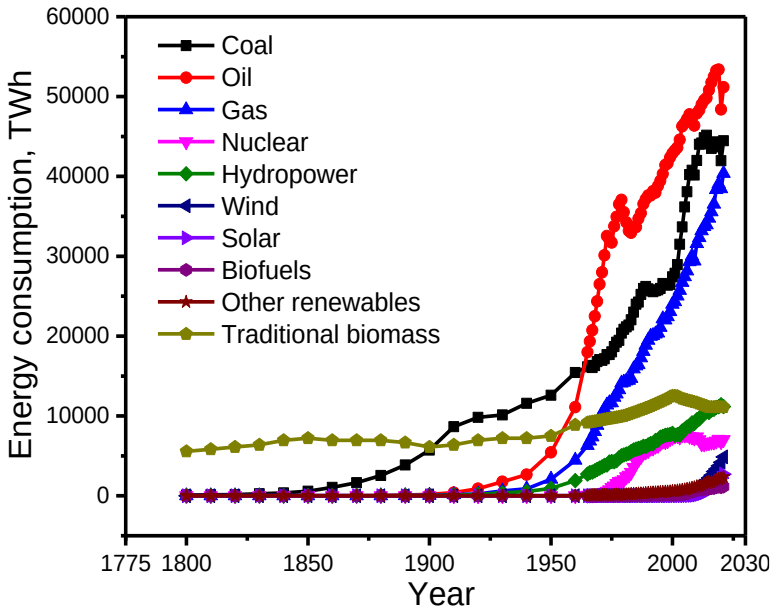

Fig.1. 1 Variation in global energy consumption from 1800 to 2022

Furthermore, the discovery of oil reserves around the world, particularly in the USA and Middle East countries, also contributed to the extensive use of hydrocarbons such as oil and natural gas over coal. The three major fuels that dominated the 20th century were coal, oil, and natural gas. These three fossil fuel reserves are the building blocks of globalization. It is indisputable that the industrial revolution, driven by fossil fuels, made human life more sophisticated by providing convenient access to things like electricity and transportation, improving quality of life. However, our growing reliance on fossil fuels has caused a significant increase in greenhouse gas emissions such as CO_2, CH_4, and NO_x, affecting the environment and human health.

The current global energy demand is estimated to be 165279 TWh and is expected to continue increasing over the next 100 years. India, the world's second-largest populated country, is positioned third 3rd in energy consumption globally [4]. The primary energy consumption in India was found to be 809.2 million tons of oil equivalent (Mtoe) in 2018, projected to reach 1825 Mtoe by the end of the 21st century [4]. Figure 1.2 shows the annual CO_2 emissions from coal, Oil, gas, flaring, cement, and other industries. Fossil fuels such as coal, oil, and gas continue to produce a higher amount of CO_2 emissions since the first IR

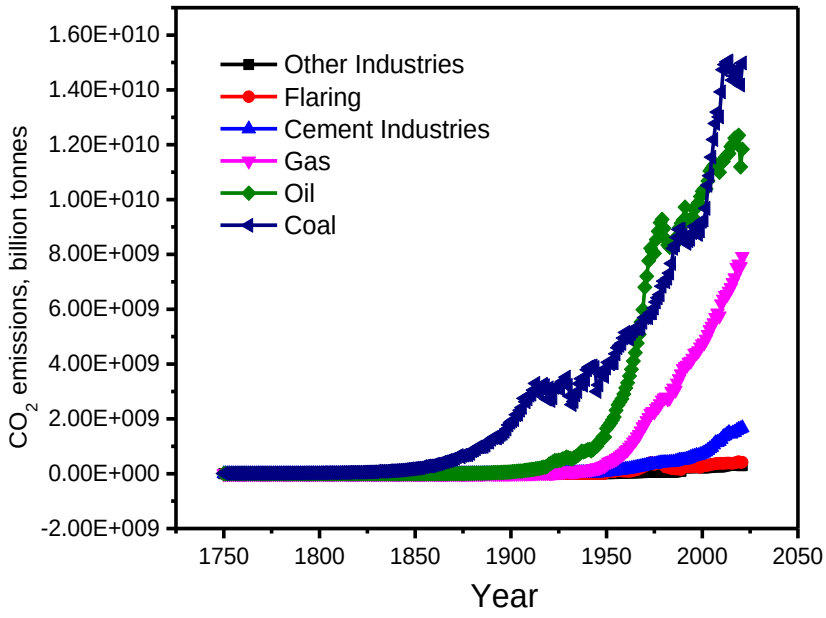

Fig.1. 2 CO_2 emissions from various sources

CO_2, the most significant contributor to greenhouse gas emissions, is responsible for 76% of climate change and global warming. The remaining 24% of emissions are composed of CH_4 (16%), NOx (6%), and fluorinated gases (2%). A report from the Intergovernmental Panel on Climate Change (IPCC) indicates that the pace of CO_2 emissions has nearly doubled over the past decade. The massive increase in CO_2 emissions, from 277 ppm in 1750 to 407 ppm in 2020, results from the excessive use of fossil fuels such as coal, crude oil, and natural gas for energy production [5]. The rise in CO_2 levels in the Earth's atmosphere poses a significant threat to the ecosystem, with negative consequences on sea level rise, ocean acidification, global warming, extinction of species, and human health. Apart from GHG emissions and climate change, the scarcity of fossil fuels will be a massive threat due to their overuse. For instance, the depletion of fuel reserves is predicted to occur in 35, 107, and 37 years for oil, coal, and gas reserves, respectively [6].

Additionally, the confinement of resources like oil is restricted to a few specific regions of the world, such as Organization of the Petroleum Exporting Countries (OPEC), the USA, Canada, and Russia. Because of this, nations that do not have significant petroleum reserves

are forced to deal with economic downturns or difficulties in international trade, primarily because they must import oils. The Russian invasion of Ukraine in 2014 and 2022 worsened the already existing tensions in the energy sector. Russia is the largest exporter of fossil fuels globally and a major supplier to Europe, with 20% of the energy consumed in the European Union coming from Russia in 2021. This dependence on Russia has been recognized as a strategic vulnerability, but efforts to diversify sources of energy imports have not been successful, and Russia continues to supply a large portion of Europe's energy. The above factors indicate an urgent need to shift from fossil fuels to renewable energy sources, such as biomass, wind, solar, and biogas (BG)

To combat climate change, several developing nations are looking into carbon-free, long-term renewable energy sources. Over 10% of the United Kingdom's total energy consumption in 2017 came from renewable sources, a number that has been continuously rising. The European Commission has mandated a deadline of 2050 for achieving zero net emissions of greenhouse gases. The production of energy from biogas (BG) is an alternative to existing energy sources and can help mitigate climate problems. BG has the potential to play a significant role in expanding the market for renewable energy, and it is anticipated that global demand for biogas will more than double over the next few years, rising from 14.5 gigawatts (GW) in 2012 to 29.5 GW in 2022 [7].

1.2 Biogas

Biogas (BG) is produced through the anaerobic digestion (AD) of biomass such as food, plant debris, animal manure, sewage sludge, and biodegradable municipal waste. The AD process involves four stages, as illustrated in Fig. 1.3. These stages include hydrolysis, acidogenesis, acetogenesis, and methanogenesis, and are carried out by a group of bacteria that includes fermentative bacteria (Bacteroidetes, Firmicutes, and Proteobacteria), acidogenic bacteria (Clostridium, Peptococcus Anaerobius, Lactobacillus, and Actinomyces), and

acetogenic bacteria (Syntrophomonus, Methanosarcina, Methanococcus, and Methanobacterium) [8,9].

During hydrolysis, complex organic matter, such as cellulose and hemicellulose, is broken down into soluble monomers, such as amino acids, sugars, and fatty acids. In Acidogenesis, the hydrolysis products are converted into short-chain organic acids (propionic, acetic, and formic), aldehydes, CO_2, and hydrogen. In the acetogenesis process, syntrophic acetogenic bacteria convert volatile fatty acids, alcohol, and aromatic compounds into acetate, H_2, and CO_2. Finally, in methanogenesis, acetic acid is converted into CH_4 and CO_2 in the presence of acetoclastic methanogenesis, while hydrogenotrophic methanogens generate CH_4 from H_2 and CO_2.

The composition of the produced BG depends on the type of biomass used and the operating parameters of AD reactors such as pH, temperature, C/N ratio, organic loading rate, retention time, and substrate-to-inoculum ratio. Depending on the origin of biomass, the produced BG typically contains methane (CH_4: 35 – 70%), carbon dioxide (CO_2: 30 – 50%), and traces of nitrogen (N_2: 0 – 15%), oxygen (O_2: 0 – 1%) and hydrogen sulfide (H_2S : 0 – 3%) [5,10,11].

Of all the parameters, operating temperature is a critical aspect for determining the functioning of AD reactors which directly affects the microbe activity and CH_4 yield [12]. AD reactors typically operate at two different temperature ranges: mesophilic (25 – 40 ℃) and thermophilic (50 – 65 ℃). Thermophilic digesters are favorable for higher CH_4 yield due to enhanced reaction kinetics, and bacterial development in short retention time [12]. In contrast, mesophilic digestors are preferred for their high stability and easy maintenance [13].

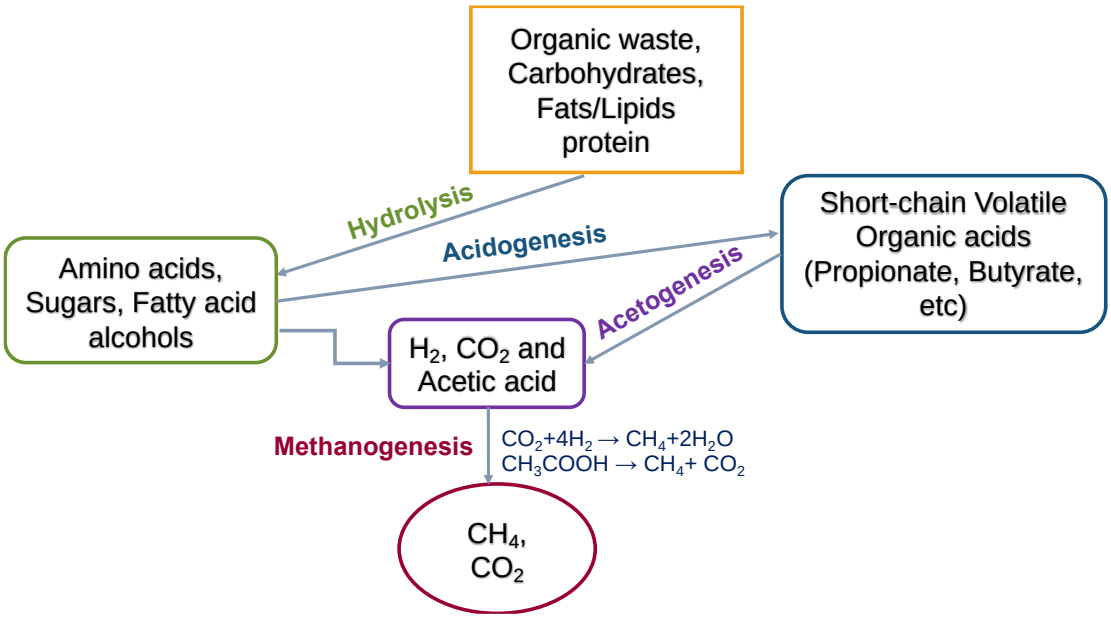

Fig.1. 3 Various stages of Biogas production in AD operation

1.2.1 Status of Biogas Production

According to the International Energy Agency (IEA) report, global biogas production reached 35 Mtoe in 2019, with a total installed capacity of over 19 GW [14]. Europe is currently the largest biogas producer, accounting for 70% of the total global production, followed by Asia, which accounts for approximately 20%. Germany is the leading producer of biogas in Europe, with a production capacity around 15 Mtoe, while China is the largest producer in Asia with a production capacity of around 11.6 Mtoe, and India is also a significant producer, with a production capacity of 1.66 Mtoe [15]. Regarding the types of feedstocks used for biogas production, manure and organic waste are the most widely used, accounting for about 70% of the total feedstock. Other feedstocks used include energy crops, such as maize and grass, and food waste. In conclusion, the global biogas production industry is growing and significantly impacts reducing greenhouse gas emissions and improving waste management practices. The market is anticipated to expand in the coming years due to the rising demand for renewable energy sources and the requirement for sustainable waste management practices.

Table 1. 1. Biogas composition from different sources

Composition	Sewage sludge	Landfills	Wastewater	Agricultural waste	Food waste
CH_4 (%)	60-70	35-65	55-58	55-58	68
CO_2 (%)	34-38	30-45	32-50	37-38	26
H_2O (%)	1-7	1-5	1-5	-	-
H_2S (ppm)	0-4000	0-100	0-4000	2100-7000	36-115
NH_3 (ppm)	50-100	0-5	0-100	-	-
H_2 (%)	Traces	0-5	Traces	-	-
N_2 (%)	0-2	5-15	Traces	1	3-5
O_2 (%)	Traces	0-1	Traces	1	-
Siloxanes	0-0.2	0-0.2	0-0.5	-	-

1.2.2 Biogas Applications

BG is renewable and can be utilized in numerous ways, such as producing heat and electricity using combined heat and power plants (CHP), biofuel (biomethane), biofertilizers, fuel cells and H_2 production via reforming techniques [16–18]. A significant amount of BG is utilized in CHP to generate heat and electricity [19]. The main downside related to the utilization of biogas for CHP is the poor efficiency of turbines. Consequently, the development of microturbine power generators led to an enormous growth in the use of BG in CHP systems for electricity generation. Fuel cells are likely the most innovative application of biogas and are used to produce both electrical and thermal power, making them a unique alternative to CHP systems for energy production. Recent advancements in fuel cells resulting in low emissions (CO_2, NO_x) and high efficiency make them practical for power generation and transportation. Power

is produced using a variety of fuel cells, including proton exchange membrane (PEM), molten oxide (MO), and solid oxide fuel cells (SOFC). The PEM fuel cells employ a polymer membrane as the electrolyte, operate at 80 ℃, and have an electrical efficiency between 40 to 50 percent. As an electrolyte, MO fuel cells use different salts, including sodium, magnesium, and carbonates, and operate at higher temperatures (600 to 700 ℃) with an efficiency of 60 to 80%. Likewise, SOFC operates at high temperatures (800 - 1000 ℃) with a 60% efficiency [20]. BG can also be used as fuel in the form of biomethane for transportation purposes to replace existing gasoline. Currently, a few countries like Germany, Sweden, Denmark, the Netherlands, and South Korea are using biomethane as fuel for vehicles [17].

However, the presence of impurities in BG limits the direct utilization and demands biogas upgrading for the above applications. For instance, CO_2 in BG decreases the calorific value, and the presence of H_2S causes the corrosion of engines. Impurities in biogas, (as shown in Table 1.1) for instance, H_2S, O_2, and siloxanes, have a considerable effect on the reforming of biogas. This raises a need for biogas purification using various techniques such as absorption, adsorption, membrane, cryogenic, and biological methods [21]. Table 1.1 shows the composition of BG and its impact on their utilization.

1.2.3 Biogas purification

The raw biogas requires purification to remove impurities such as CO_2, H_2S, H_2O, and NH_3 before being used directly in CHP, reforming, and fuel cells. Table 1.2. shows the amount of H_2S tolerable by various biogas utilization processes [22]. Several technologies are adopted for biogas upgrading's, such as absorption, adsorption, membrane separation, cryogenic separation, and biological treatments.

The typical absorption methods employed are high-pressure water scrubbing (HPWS) and organic physical scrubbing (OPS), known as physical absorption. In addition, chemical processes such as amine scrubbing, and inorganic solvent scrubbing are also employed to

remove CO_2 and other impurities. Raw biogas scrubbing is traditionally carried with water or organic solvent in packed bed columns, and it works based on the solubility of the various constituents in water/organic solvents.

Using HPWS, CO_2 and H_2S can be removed and contain 95% of CH_4 in BG. The consumption of H_2O needed for HPWS depends on the operating conditions and size of the packed bed column. Organic scrubbing is similar to water scrubbing and involves solvents such as polyethylene glycol and selexol. The amount of solvent required is less than in water since the solubility of CO_2 is higher in polyols than in water. In the case of chemical absorption, a reaction occurs between absorbate and absorbing gas components. For instance, Amine is used for chemical absorption, which reacts with CO_2 or H_2S and forms Diethanolamine, Monoethanolamine, or a combination of both. This method gives high purity of CH_4 (99%) owing to the high selectivity of CO_2 with the solvent. However, the regeneration of solvents is an energy-intensive process. Non-organic solvents having high alkaline nature are also used for CO_2 capture, similar to amine scrubbing.

Inorganic solvents NaOH, KOH, $Ca(OH)_2$, NaOH, KOH, and $Ca(OH)_2$ are used to remove the CO_2 from BG. When CO_2 reacts with one of these solvents, it is converted into carbonate forms such as sodium, potassium, and calcium. In the last decade, the focus on BG separation shifted towards membrane technology due to its economic feasibility and ease of operation. Membrane separation works based on the difference in concentration, pressure, temperature, CH_4, and other gas impurities in the BG mixture [23]. The standard membranes used in BG purification are composed of cellulose acetate, polysulfone, polyetherimide, and polyvinylidene fluoride [24]. Multistage operations are used to obtain high purity with 99% CH_4 recovery, which is higher than normal single-stage operations.

Table 1. 2. H_2S limits for various biogas technology processes

H_2S, ppm	**Biogas technology**
< 1000	Stirling engines and Boilers
< 10	Household cooking
< 500 < 50 (varies based on engines)	Internal combustion engines (ICC)
< 10, 000	Turbines
< 70, 000	Micro-turbines
< 4	Natural gas
< 1	Protan-exchange membrane fuel cells
< 20	Phosphoric acid fuel cells
< 10	Molten carbonate fuel cells
< 1	Solid oxide fuel cells

In the case of cryogenic separation, BG purification is carried out based on its boiling point differences. Compressed biogas is cooled and condensed in this operation for CO_2 separation, and the gas phase is maintained as CH_4. These operating conditions are typically at 80 atm and -170 ℃. Depending on the purity of BG, it can be employed in two ways, such as combined heat and power (CHP engines), also known as the first-generation usage, and the second is the production of syngas ($CO + H_2$) through reforming technologies [21]. To generate power in CHP engines, BG should have less than 250 ppm of H_2S and require purification. The variable

quantity of CH_4 and the presence of CO_2 in BG limit CHP systems usage [10,25]. For reforming operations, it is generally suggested that the H_2S content in biogas should be less than 0.5 ppm to avoid catalyst poisoning [26].

1.3 Reforming technologies

Catalytic reforming is ideal for converting BG into synthesis gas, formerly known as syngas (H_2+CO), which eliminates the need for additional and expensive purification processes for CO_2 removal and improves BG efficiency [5]. Syngas is an important raw material for producing liquid transportation fuels and other chemical products via the well-known process called Fischer-Tropsch (FT) synthesis [27,28]. The FT process converts syngas into hydrocarbons over catalysts such as Fe, Fe-K/SiO_2, ZSM-5, and Zn/Fe [28–30]. The products from the FT synthesis depend on the H_2/CO ratio, temperature, and catalyst composition. Increasing H_2/CO (1.0 to 3.0) changes the product composition from liquid fuels to long-chain paraffin [28,31]. Syngas can be produced from BG by using various reforming techniques such as dry reforming (DR), steam reforming (SR), and auto thermal reforming (ATR) [32,33].

1.3.1 Steam reforming

Steam reforming of biogas **(**SRBG) is a reaction that occurs above 700℃ between steam and CH_4 to produce H_2 and CO. Syngas produced from SRBG contains H_2/CO > 1.0, which enhances the formation of undesirable light hydrocarbons in the FT process. Moreover, SRBG requires a high H_2O/CH_4 ratio to produce hydrogen, and excess steam increases CO_2 formation via water-gas-shift reaction (WGSR). These make SRBG economically and environmentally unfavourable [34]. The main reactions involved in this process are.

$$CH_4+H_2O \leftrightarrow CO + 3H_2,\ \Delta H^0_{298} = +206\ kj/mol \qquad (1.1)$$

$$CO+ H_2O \leftrightarrow CO_2 + H_2,\ \Delta H^0_{298} = -\ 41\ kj/mol \qquad (1.2)$$

$CH_4+CO_2 \leftrightarrow 2CO + 2H_2$, ΔH^0_{298} = +247 kj/mol (1.3)

1.3.2 Dry reforming

Principally, dry reforming of biogas (DRBG) converts the two major global warming gases (CH4 and CO2) into valuable products over the catalysts. DRBG is a reaction between CH_4 and CO_2 over a catalyst into syngas (H_2/CO) with a ratio of 1.0. DRBG occurs at a temperature above 700 ^oC and 1.0 atm pressure. The feasible reactions are as follows.

$CH_4 + CO_2 \leftrightarrow 2CO + 2H_2$, ΔH^0_{298} = +247 kJ/mol (1.4)

$CO_2 + H_2 \leftrightarrow CO + H_2O$, ΔH^0_{298} = +41 kJ /mol (1.5)

$2CO \leftrightarrow C + CO_2$, ΔH^0_{298} = - 172.4 kJ /mol (1.6)

$C + CO_2 \leftrightarrow 2CO$ ΔH^0_{298} = + 171 kJ /mol (1.7)

$CH_4 \leftrightarrow C + 2H_2$, ΔH^0_{298} = +74.9 kJ /mol (1.8)

1.3.3 Autothermal reforming

"Auto thermal" refers to a reaction that does not require any external heat source. This is an efficient method for creating H_2 because it meets the heat demand of endothermic processes by releasing heat as a byproduct of exothermic reactions. However, a significant challenge is the high cost of oxygen separation, and maintaining a constant temperature is also difficult due to the exothermic reaction.

Among all the reforming processes, DRBG is a potential reforming process that converts GHG emissions (CH_4 and CO_2) into valuable syngas (H_2/CO) ratio of 1.0. Despite its advantages, the industrial implementation of DRBG is still limited due to challenges, such as catalyst deactivation, which plays a crucial role in facilitating the reaction between CH_4 and CO_2 can be affected by other factors such as carbon deposition, sintering, and H_2S poisoning.

1.4 Characteristics of dry reforming of biogas

Dry reforming of biogas (DRBG) is an extended application of dry or CO_2 reforming of methane (DRM), and it was first studied by Fischer and Tropsch (1928) as a potential alternative to the existing steam reforming of methane for syngas production [35]. The primary difference between DRM and DRBG is the molar ratio of CH_4 to CO_2 in the feed gas. DRM uses equimolar amounts of CH_4 and CO_2 as feed, whereas in DRBG CH_4 to CO_2, the ratio varies from 1.0 to 2.0. The CH_4/CO_2 ratio depends on the type of biomass and operating conditions in the biomass digester [21,34,36].

Apart from the desired DRBG, a few side reactions are significant at the reforming conditions, which may dictate the carbon deposition and the product compositions (H_2 and CO). The side reactions are reverse-water gas-shift reaction (RWGS: reaction 1.5), CO_2 or carbon gasification (Eq. 1.7), boudouard reaction (Eq. 1.6), and methane cracking (Eq. 1.4) [10,37,38]. The boudouard and CH_4 cracking reactions contribute to carbon formation. The boudouard reaction can be avoided by operating dry reforming at above 700 ℃, whereas CH_4 cracking is inevitable due to higher temperatures and higher ratios of CH_4/CO_2, which ultimately forms carbon deposition on the catalyst surface, leading to the catalyst deactivation [10,39]. The RWGS occurs along with the DRM compared to DRBG, indirectly contributing to carbon gasification, and enhancing CO_2 conversions. The occurrence of RWGS depends on the reaction temperature and CH_4/CO_2 [34,40,41]. An increase in temperature and CH_4/CO_2 ratio leads to a decrease in RWGS reaction due to the high favorability of reforming reaction since CO_2 is the limiting reactant [37–39,41].

Clearly, in the case of DRBG, CH_4 decomposition is significantly higher due to the high content of CH_4 in the feed mixture. Also, the occurrence of RWGS is also less likely, making the operating conditions tend towards carbon deposition than normal CO_2 reforming.

1.4.1 Thermodynamic analysis

Thermodynamic equilibrium calculations for DRBG are essential in identifying multiple reactions and feasible operating conditions. The GASEQ equilibrium calculations, based on Gibb's free energy minimization method, are used to understand the effect of temperature and CH_4/CO_2 ratios in DRBG. Gaseous products such as CH_4, CO_2, H_2, CO, H_2O, C_2H_4, C_2H_6, CH_3OH, and CH_3OCH_3, as well as solid carbon (graphite), are considered for DRBG based on the literature [42]. The equilibrium calculations are performed at 1 atm pressure, in the temperature range of 400 – 1000 ^oC, with CH_4/ CO_2 varying from 1.0 to 2.0.

The conversions of CH_4 increase with temperature due to the endothermic nature of DRBG. At a lower feed ratio, The CH_4 conversions are increased with increasing temperature for all the CH_4 /CO_2 ratios, as shown in Fig. 1.4. At a lower feed ratio (CH_4/CO_2 = 1.0), the CH_4 conversions are significantly higher compared to high CH_4/CO_2 ratios, particularly for lower temperatures (< 700 °C). The high conversions at CH_4/CO_2 = 1 are due to the formation of undesired CH_4 via exothermic methanation reaction, mainly when the temperature is below 450 °C. However, at higher temperatures, the conversions are similar for all the CH_4/CO_2 ratios due to significant CH_4 decomposition and DRBG. Nikoo et al.[41] also reported similar observations in their thermodynamic analysis based on Gibbs free energy minimization using Aspen plus modeling.

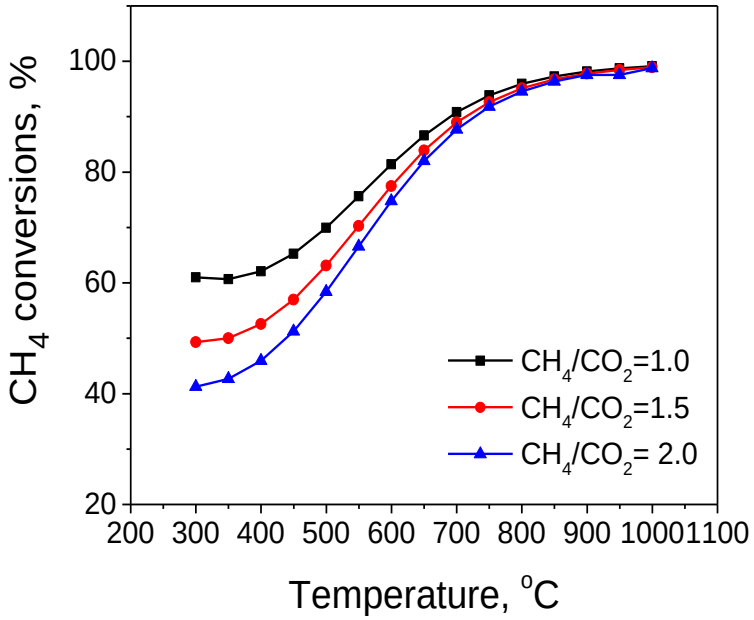

Fig.1. 4 CH_4 equilibrium conversion as a function of temperature and CH_4/CO_2 ratio at 1 atm.

Figure 1.5 shows the effect of temperature on CO_2 equilibrium conversions at various CH_4/CO_2 ratios. The equilibrium CO_2 conversions initially decreased from 300 ℃ to 550 ℃ and then gradually increased with increasing temperature, reaching a maximum CO_2 conversion for all the feed ratios above 900 ℃.

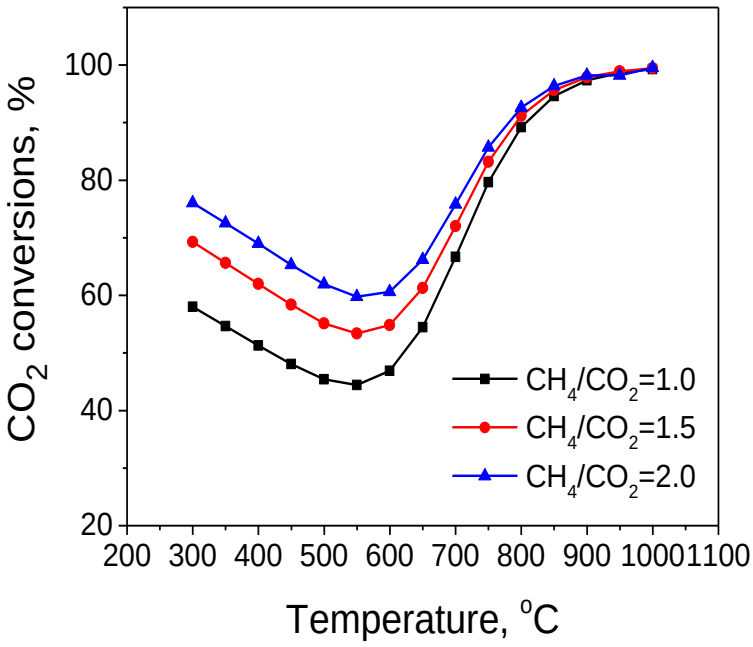

Fig.1. 5 CO_2 equilibrium conversion as a function of temperature and CH_4/CO_2 ratio at 1 atm.

The initial decrease in CO_2 conversions is attributed to the formation of water and solid carbon from an exothermic reduction of CO_2 [41,43]. For temperatures between 600 – 900°C, CO_2 conversions rely solely on CH_4/CO_2 ratios and are found to be at a maximum for higher CH_4/CO_2 ratios since CO_2 becomes a limiting reactant in the DRBG. The equilibrium conversions of CH_4 and CO_2 obtained in this study are similar to the recent results by Li et al. [43]. Figure 1.6 illustrates the effect of temperature on equilibrium moles of H_2 at various CH_4/CO_2 ratios. An increase in temperature and equilibrium moles of H_2 at various CH_4/CO_2 ratios is attributed to the formation of H_2 from enhanced DRBG and CH4 cracking. The CO moles increase with increasing temperature for all the CH_4/CO_2 ratios, as shown in Figure. 1.7. The higher CO moles at higher temperatures are due to the CO formation being an endothermic reaction. The CO moles are higher for $CH_4/CO_2 = 1$ than $CH_4/CO_2 > 1$ due to CO_2 acting as a limiting reactant for CH_4/CO_2 ratios > 1.0. The ratio (H_2/CO) determines the further utilization of syngas through FT synthesis to produce higher alcohols [44,45].

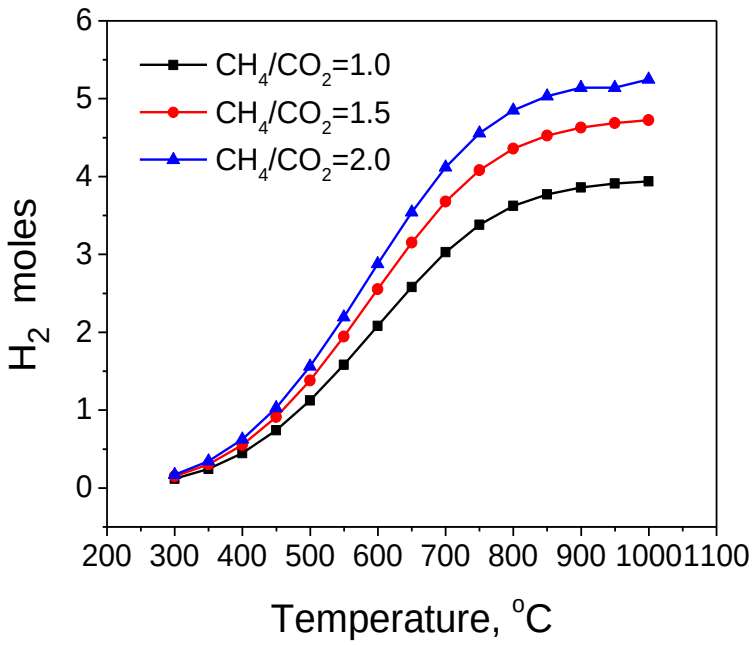

Fig.1. 6 Equilibrium moles of H_2 as a function of temperature and CH_4/CO_2 ratio at 1 atm.

As shown in Figure.1.8, the higher values of H_2/CO in the temperature range of 300 – 550°C are due to the decomposition of methane. The DRBG should operate above 700 °C to

achieve the optimum H_2/CO ratio of ~1.0, as shown in insert Fig.1.8. Additionally, an increase in CH_4/CO_2 leads to H2/CO ratio arising, which is substantial at lower temperatures below 500°C. However, the H_2/CO ratio decreases at higher temperatures due to the thermodynamic shift toward a dry reforming reaction.

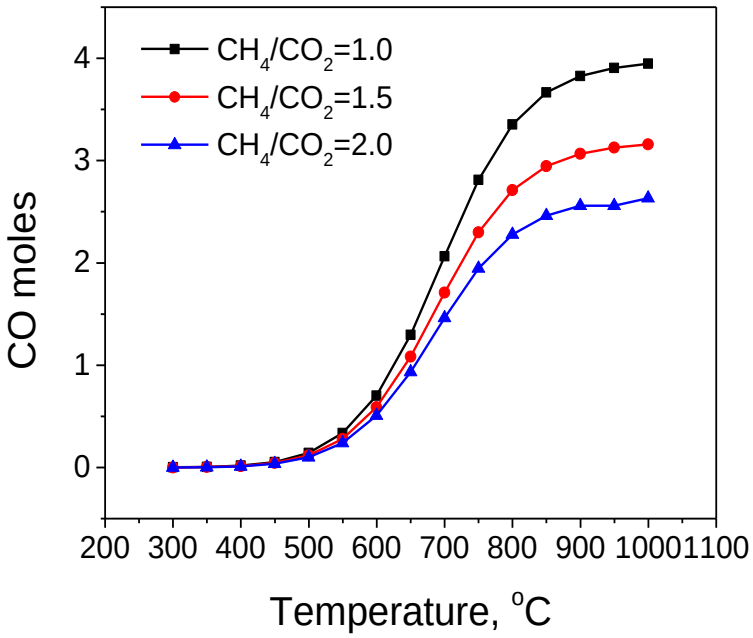

Fig.1. 7. Equilibrium moles of CO as a function of temperature and CH_4/CO_2 ratio at 1 atm.

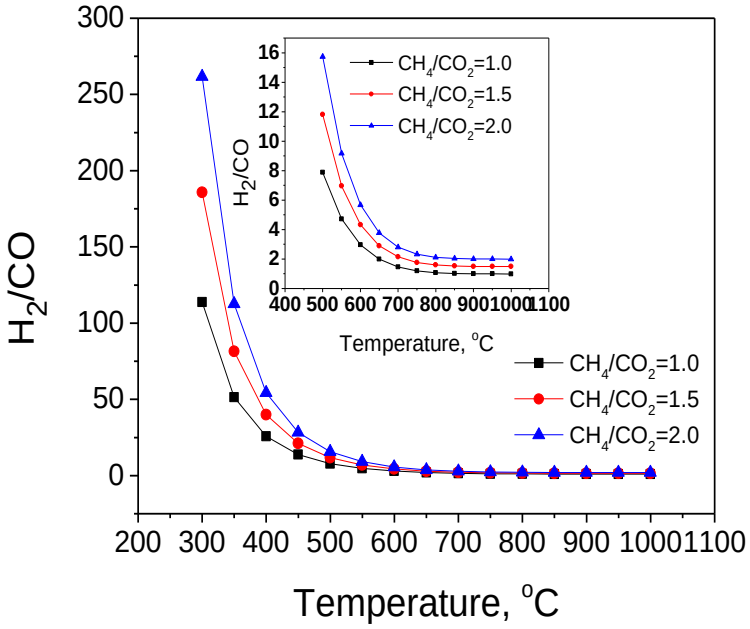

Fig.1. 8. Equilibrium molar H_2/CO as a function of temperature and CH_4/CO_2 ratio at 1 atm.

1.5 Catalyst deactivation

The deactivation of catalysts is a significant challenge that industries must overcome to avoid the high expense of replacing catalysts, which can cost billions of dollars. Catalyst deactivation can occur either physically or chemically. Physical deactivation involves pore clogging due to the active surface area reduction caused by sintering (agglomeration of particles). The chemical pathway includes poisoning of active sites with contaminants present in the reaction mixture, coking, and pore obstruction due to coking. The deactivation mechanisms can be categorized as thermal deterioration or sintering, coking or fouling and poisoning.

1.5.1 Sintering

Sintering is a process that occurs in metal catalysts, both supported and unsupported, where the metal particles on the surface grow due to thermal activation. This growth leads to a reduction in the active surface area and activity of the catalyst. This can occur due to two primary mechanisms shown in figure 1.9: atomic migration and particle migration [46]. Atomic migration occurs when metal atoms diffuse from one particle to another and accumulate on the surface of other particles. This process can lead to the formation of metal bridges between particles, causing them to agglomerate and form larger particles. In contrast, particle migration occurs when catalyst particles move and collide with each other, leading to coalescence and the formation of larger particles.

The temperature and the catalyst properties, such as particle size, dispersion, metal support interaction and porosity, primarily influence the sintering of catalysts in dry reforming. Among all the factors, the sintering of catalysts commonly relies on the reforming temperature. For instance, higher temperatures, typically above 500 ℃, increase the sintering rate [46].

This is because sintering occurs beyond the Tamman temperature (half the temperature of the melting point), above which metal atoms begin to exhibit mobility. The noble metals exhibit greater sintering resistance due to their higher Tamman temperatures (Ru, 1089 °C; Rh, 856 °C; Pt, 741 °C; Pd, 662 °C). Ni is the most studied metal for DRBG due to its lower cost; however, its Tamman temperature (590 °C) leads to inevitable sintering under typical reforming conditions (> 600 °C) [47]. To mitigate sintering, several approaches can be employed. One common strategy is to use catalysts with high dispersion, which allows for more active sites and reduces the likelihood of particle agglomeration. Another approach is to modify the catalyst surface with additives or promoters to stabilize the metal particles and prevent sintering.

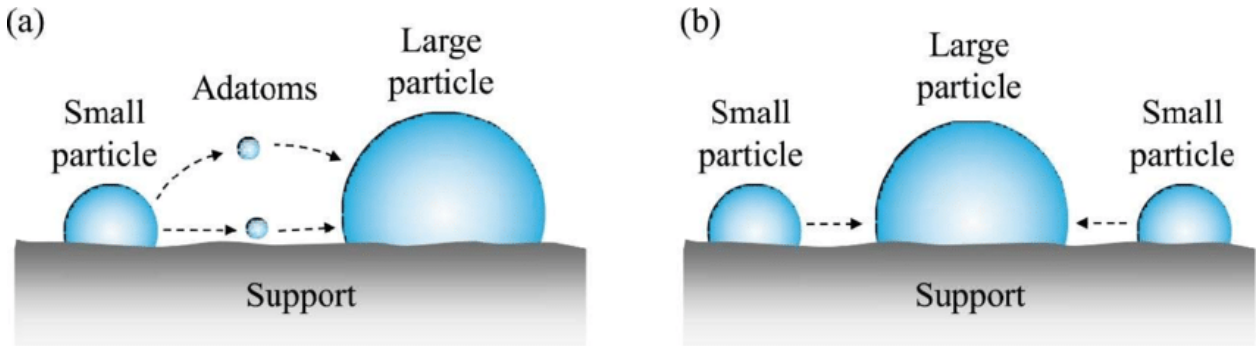

Fig.1. 9 metal sintering mechanisms: a) atomic migration, b) particle migration [47]

1.5.2 Coking

Catalyst deactivation caused by the formation of coke or carbon deposition on the catalyst surface is a significant issue in developing catalysts for DRBG. Coke refers to the unwanted buildup of carbon-containing compounds on the catalyst surface, which results in a loss of catalytic activity due to the blockage of active sites and/or pores. Carbon deposition can lead to the direct covering of active sites, the formation of filamentous carbon, blockage of pores, which restricts the access of reactants to active sites, and degradation of the catalyst structure,

as shown in figure 1.10 These effects can significantly reduce the catalyst's activity and eventually leads to its deactivation [48].

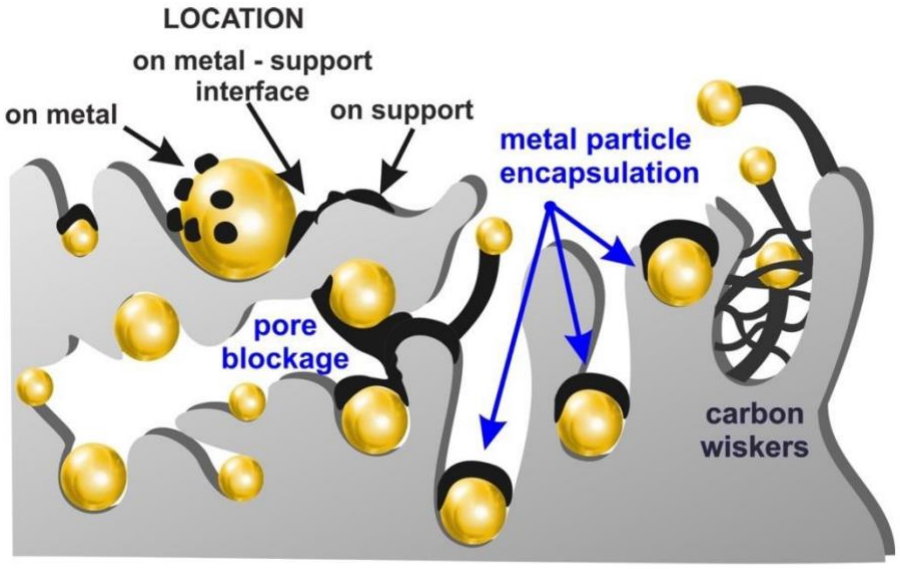

Fig.1. 10 Formation of coke deposition on the catalyst surface [48]

Depending on the type of catalysts and DRBG operating conditions, several carbon deposits, such as amorphous, filamentous and graphitic carbon, are formed on the catalyst surface.

i) Amorphous carbon is a disordered form of carbon that lacks a well-defined crystal structure. It is typically formed by the accumulation of carbonaceous species on the catalyst surface, which can lead to the formation of a carbon layer that covers the active sites of the catalyst. This layer can block reactant molecules from reaching the active sites, decreasing catalytic activity. However, amorphous carbon can be easily gasified in DRBG in the oxidative environment, such as CO_2 or through oxygen generated from the catalyst supports [49].

ii) Filamentous type of carbon deposition occurs at high temperatures, usually above 450°C, and is characterized by the formation of carbon nanotubes (CNTs) and/or carbon nanofibers (CNFs), which have a filament-like structure. The formation of

these structures is caused by the adsorption of coke precursors such as CH_4 and CO_2 on metal sites, which then dissociate to give atomic carbon. The carbon atoms then diffuse through the bulk or surface of the metal particle, nucleating and precipitating from the surface where it is supported, lifting it as the carbon filament grows, with the metal particle on its top. This type of mechanism is known as tip-grown carbon, as shown in figure 1.11 a. It is generally observed for larger particles (> 5 nm) with weak metal-support interaction; in contrast, base-grown CNT forms for smaller particles (< 5 nm) due to strong metal-support interaction. The carbon filament grows from the base of the metal particle. Additionally, base-grown carbon does not disrupts the catalytic activity because of gasification by oxygen atoms released in reforming. Filamentous carbon is relatively difficult to remove from the catalyst surface compared to amorphous carbon.

iii) Graphitic carbon is a highly ordered carbon form with a well-defined crystal structure. It is the most stable form of carbon and is typically formed at high temperatures. Graphitic carbon deposition on the catalyst surface can result in a loss of catalytic activity because it can form a thick layer that covers the active sites and reduces the surface area of the catalyst.

In DRBG, the carbon formation mainly results from the CH_4 cracking and the Boudouard reaction [50–53]. Thermodynamically, carbon deposition decreases with increasing temperature, CO_2/CH_4 ratio, and decreasing pressure [40]. DRBG is preferred in the temperature range from 750 to 800 ℃ to minimize the catalyst sintering and energy consumption [38]. However, carbon deposition is significant via CH_4 cracking in DRBG above 750 ℃. The carbon originating from CH_4 cracking is highly reactive compared to the carbon from the Boudouard reaction [52,54]. High operating temperatures are favorable for dry reforming of CH_4 or biogas, and the deposited carbon is easily gasified by both CO_2

gasification and RWGS reaction. However, the catalysts employed in dry reforming, particularly Ni-based catalysts, are prone to sintering at high temperatures (> 750 ℃), making it difficult for long-term catalyst stability. The high amount of CH_4 in the biogas limits the carbon gasification routes (CO_2 and RWGS), makes the catalyst vulnerable to carbon deposition, and ultimately leads to the catalyst deactivation by carbon.

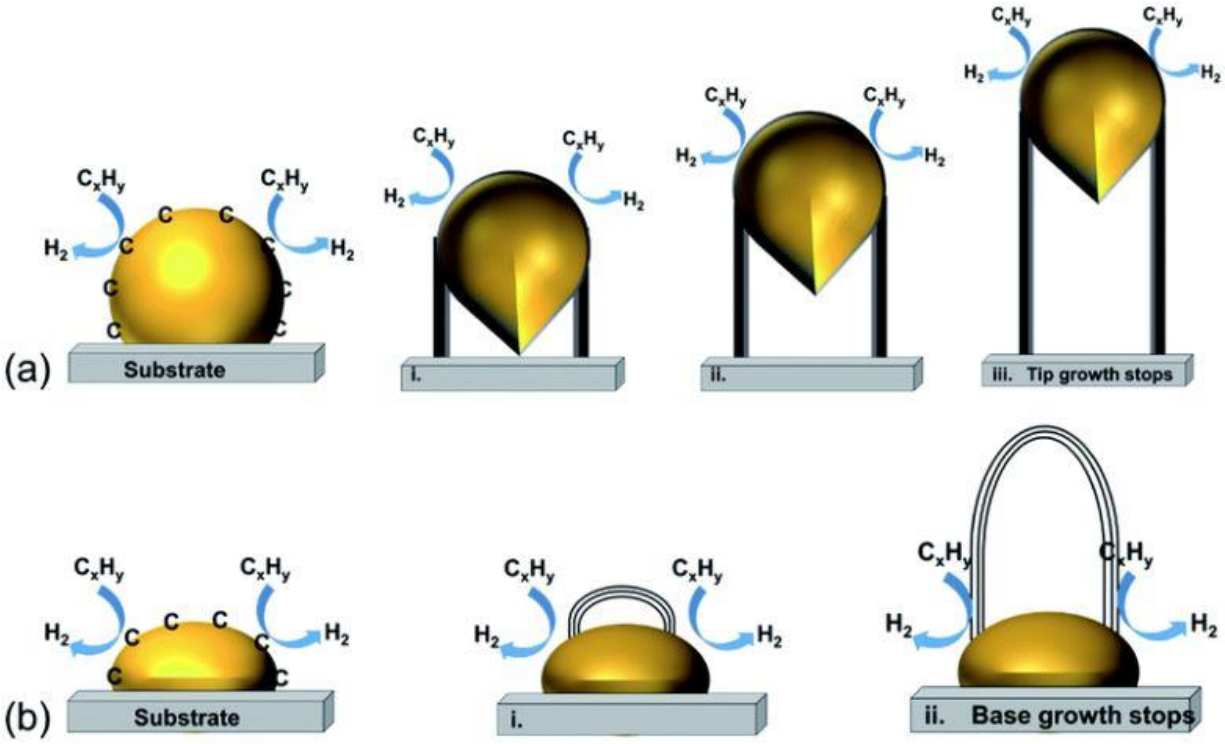

Fig.1. 11 Carbon growth mechanisms on catalyst surface a) Tip growth, b) Base growth [55]

1.5.3 Impact of H_2S

In addition to carbon deposition and sintering in DRBG, the trace amounts of H_2S have been proven to negatively impact the valorization of BG through various utilization methods, such as CHP engines, CNG, and syngas production. In particular, in the case of DRBG, H_2S disrupt the catalyst functioning by adsorbing on active sites and causing irreversible severe catalyst deactivation [36,56,57]. The deactivation of Ni catalysts due to H_2S poisoning (as shown in

figure. 1.12) mainly depends on the amount of H_2S in BG and the operating temperature. The mechanism in DRBG in the presence of H_2S is postulated as [36,56,58].

$$H_2S^{*} + \Leftrightarrow H_2S_{(g)} + * \quad (1.9)$$

$$H_2S_{(g)} + Ni \Leftrightarrow Ni\text{-}S + H_{2\,(g)} \quad (1.10)$$

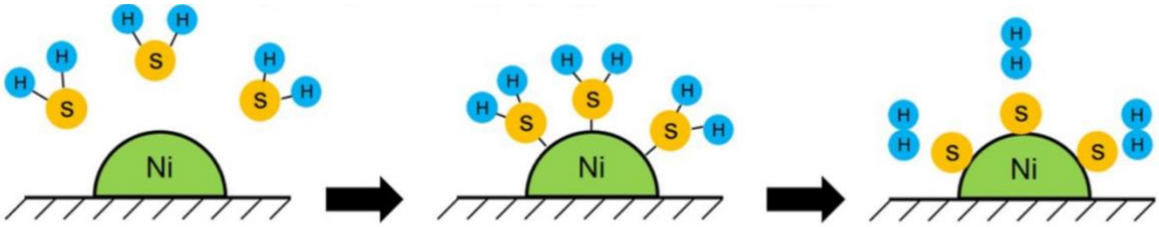

Fig.1. 12 H_2S poisoning on Ni catalyst surface in reforming of methane [59]

Where * represents the Ni active site. H_2S dissociates on active sites and forms Ni-S, reducing the active sites for the reactants and ultimately leading to catalyst deactivation. To protect catalysts from deactivation. It is essential to avoid catalyst poisoning. This can be achieved by purifying the BG before DRBG and improving catalyst compositions with sulfur-tolerant materials. Various strategies have been explored to develop sulfur-resistant catalysts, including bimetallic catalysts, rare earth metal oxides (CeO_2), and perovskite oxide-based catalysts [60–62].

1.6 Summary

Syngas is an essential intermediate product that produces an extensive range of liquid fuels. It is a mixture of carbon monoxide (CO) and hydrogen (H_2), and the ratio of CO to H_2 determines its use. A popular approach to produce syngas with a ratio of 1.0 is using the DRBG process. Biogas is reformed with CO_2 to produce syngas with a 1:1 ratio of CO to H_2. One of the significant challenges in the DRBG process is catalyst deactivation due to carbon deposition. Catalysts play a critical role in determining the catalyst activity and stability.

However, high temperatures in the DRBG process can cause various problems that can lead to catalyst deactivation.

These problems include sintering, which occurs when the metal particles on the catalyst surface become agglomerated and lose their catalytic activity, carbon deposition, where carbon accumulates on the catalyst surface; and H_2S poisoning, where sulfur impurities in the feedstock poison the catalyst and deactivates the catalyst.

Chapter-2

2 Literature Review

2.1 Introduction

Designing a stable catalyst for the DRBG is decisive in preventing catalyst deactivation due to carbon deposition and poisoning [56,63,64]. Various types of non-precious (Ni, Co, Cu, and Fe) and precious (Pt, Pd, Ir, and Rh) metals have been studied as catalysts for DRM and DRBG [65–67]. For instance, Fonseca et al.[68] investigated the activity of 1 wt% Pt deposited over various supports, such as Al_2O_3, CeO_2-Pr/Al_2O_3, CeO_2-Nb, and CeO_2-ZrO_2 using the wet impregnation (WI) method. Results showed that the Pt/CeO_2-Pr-Al_2O_3 catalyst displayed high activity and low carbon deposition, leading to a CH_4 conversion of 65% and a CO_2 conversion of 70% in a TOS of 24 hours. However, Pd catalysts have been found to be unstable in DRM due to heavy carbon deposition [69]. The Rh and Ir-based catalysts are known for their high activity. For instance, Moreira et al. [70] prepared highly stable 0.1 wt% Rh/Al_2O_3 catalysts using the WI method and observed no signs of deactivation for 184 hours in DRM. Maina et al. [71] developed coke-tolerant 1.0 wt% Ir/Al_2O_3 catalysts using the WI method. These catalysts displayed high stability for 60 hours, with CH_4 and CO_2 conversions of 80% and 90% at 750°C. Additionally, the Ir particles were highly tolerant to sintering and showed no significant change in particle size.

Even though noble metals are highly coke tolerant, the main disadvantage of using noble metal catalysts in dry reforming is their high cost. These metals are precious and rare, which makes them expensive and inaccessible for many industrial applications. Furthermore, the preparation of these catalysts often requires complex and multi-step synthesis methods, which can further increase their cost. After noble metals, Ni-derived catalysts gained the utmost importance because of their high activity and cheap abundance [72]. However, Ni particles are

prone to sinter at higher temperatures (> 600 °C), making them vulnerable to coke deposition in the DRM process [63,73]. Different metal oxide supports such as Al_2O_3, La_2O_3, CeO_2, MgO, and ZrO_2 have been explored to overcome catalyst deactivation [50,74,75].

Studies on Ni/γ-Al_2O_3 showed severe catalyst deactivation due to Lewis's acid sites on an alumina support. These sites improve the C-H bond scission more than carbon gasification [35,76]. To reduce the rapid deactivation of Ni/γ-Al_2O_3 catalysts, La_2O_3 has been used in a few studies as an additional modifier to balance the Lewis acid sites and improve the thermal stability of the catalysts. Many research groups have explored La_2O_3 as support, enhancing thermal stability and forming reactive lanthanum oxy-carbonate ($La_2O_2CO_3$) [77,78]. Like La_2O_3 support, CeO_2 is also explored as an active support for Ni catalysts due to its oxygen storage capacity (OSC), improved metal-support interaction, and activation of C-H bonds [79–82]. Studies also used cordierite monoliths ($2MgO.2Al_2O_3.5SiO_2$) as structural support due to their negligible mass transfer resistances, high surface area per unit volume of the catalyst, less pressure drops and can easily scale-up [83–85]. Additionally, anti-sintering and coke tolerance of Ni catalysts can be obtained by controlling particle size and mobility during DRBG. This can be achieved by using Ni in distinct structures like perovskite oxide materials. Perovskite oxide catalysts gain more popularity in catalysis applications due to their structural-thermal stability and OSC. The structural flexibility of perovskite oxides is ideal for many applications, especially for DRBG due to the carbon tolerance [86–92].

In this chapter, an exhaustive review is conducted for Ni catalysts supported by a variety of metal oxides, such as Al_2O_3, CeO_2, monoliths and perovskite oxide catalysts respectively. The section begins with conventional Ni/-γAl_2O_3 catalysts, including preparation techniques and deactivation caused by carbon deposition. The roles of Ni-CeO_2 catalysts in DRM are discussed thoroughly in sec 2.3, and Ni supported on monolith catalysts is discussed in sec 2.4. Sections 2.5, 2.6 and 2.7 are devoted to the perovskite oxide catalysts. A detailed discussion is

made of Ni and non-Ni-based perovskite oxide systems. A separate section is dedicated to the deactivation of the catalyst due to H_2S in the biogas feed mixture. Furthermore, a literature summary is provided at the end of the chapter 2 to help identify research gaps and develop research objectives.

Most of the existing literature is focused on a methane dry reforming with a CH_4/ CO_2 ratio of 1.0. However, since biogas consists of a CH_4/ CO_2 ratio of > 1.0, studies on dry reforming of biogas are limited. Therefore, following sections mainly cover the dry reforming of methane (DRM) with a CH_4/CO_2 ratio of 1.0.

2.2 Ni/γ-Al_2O_3 catalysts

Table 2.1 displays the Ni/γ-Al_2O_3 catalysts that have been extensively studied to reform hydrocarbons by various techniques, owing to their high thermal stability and surface area. Most studies focused on varying the Ni metal loading from 5wt% to 35wt%, and the catalysts were synthesized using wet impregnation (WI), low-temperature plasma, and hydrothermal synthesis methods [93–97]. Although WI is a commonly used method that allows for simply adding an active metal layer to the catalyst support, it leads to the non-uniform distribution of metal over oxide supports (Al_2O_3), which is not ideal for hydrocarbon reforming. To improve the dispersion of Ni, researchers have employed new synthesis strategies such as plasma discharge to produce small particles and in-situ derived Ni nanoparticles from the layered hydroxide structures (LDH). For instance, Zhu et al. [93] investigated DRM over 5 wt% Ni/Al_2O_3 catalysts prepared using two approaches: with and without plasma treatment. Plasma treatment resulted in small Ni particles compared to WI. Plasma discharge was carried out in a quartz tube at room temperature, maintaining a pressure of 100-200 Pa, and at a voltage of 900 V using argon glow. Activity experiments were carried out at 750 ℃ for CH_4/CO2 of 1.0, and

it was observed that low-temperature plasma-treated catalysts displayed high activity and less carbon deposition than WI catalysts.

Similarly, Xu et al. [98] prepared Ni/Al_2O_3 catalysts derived from layered double hydroxides (LDH) to improve Ni dispersion. The catalysts were prepared using the precipitation method with urea as a precipitant. The prepared catalysts displayed high activity and coke tolerance than WI catalysts due to the strong metal support interaction (SMSI) between Ni and Al_2O_3. SMSI interactions play a critical role in Ni dispersion and sintering resistance during DRM. Catalysts with SMSI are less susceptible to sintering than those with poor metal-support interaction. In WI catalysts, most of the Ni is reduced from the bulk NiO, which has poor interaction with the support, leading to the agglomeration of Ni nanoparticles during the reduction and DRM.

In addition to catalyst preparation technique, calcination temperature plays a significant role in physicochemical properties such as particle size, surface area, and activity of catalysts. As a thumb rule, a very high-calcination temperature leads to particle agglomeration and resulting catalyst deactivation [99]. However, a few studies reported the positive influence of high-temperature calcination, particularly for Ni/Al_2O_3 catalysts [95,100]. At high temperatures (> 700 °C), the Ni^{2+} cations are highly mobilized and readily react with Al_2O_3 to form a complex nickel aluminate structure ($NiAl_2O_4$). In this, Ni^{2+} ions reside tetrahedrally, and Al^{3+} ions occupy octahedral positions [101,102]. However, the arrangement of cations in tetra and octahedral sites mainly depends on the temperature and concentration of cations. Cations (Ni^{2+} and Al^{3+}) are generally randomized based on the inversion factor (x). The actual distribution of every spinel is characterized by an inversion parameter x, defined as the proportion of B-type cations in the tetrahedral site. Consequently, x equals 0 for a completely normal spinel, 1 for a perfectly inverted spinel, and 0.67 for a random spinel. The particles generated from the in-situ reduction of such spinels have strong metal support interaction

(SMSI) with the support, which further prevents the catalyst from sintering and carbon deposition. However, $NiAl_2O_4$ is inactive, and high reduction time and temperature are required to reduce the Ni-Al spinel.

Calcinating Ni/Al_2O_3 catalysts create the SMSI at higher temperatures (> 700 ℃) [95,100]. Calcination temperatures ranging from 450 to 900℃ were used during the calcination synthesis to create SMSI. For instance, Zhou et al. [100] studied the role of calcination temperature on catalytic activity and carbon tolerance in DRM. The Ni/Al_2O_3 catalyst calcined at temperatures such as 700, 800 and 900℃ for 5 h. High-temperature calcined catalysts (900℃) displayed more stable catalytic activity than the low-temperature calcined catalysts (350 and 700℃). Depending on the calcination temperature, Ni and Al oxides are formed. For the catalysts calcined at 350 and 700 ℃, NiO, Al_2O_3 and $NiAl_2O_4$ are reveled in XRD patterns. In the case of high temperature (900℃) calcination, only $NiAl_2O_4$ phase is observed. Furthermore, the reduction of $NiAl_2O_4$ resulted in small Ni^0 particles (19 nm) firmly anchored with the support. Whereas Ni reduced from NiO is prone to sinter, resulted in high carbon formation. The SMSI generated during high-temperature calcination results in enhanced catalytic activity and decreased carbon formation on the surface of the catalysts. For instance, He et al. [95] reported a similar observation for Ni/Al_2O_3 catalysts prepared using WI and calcined at 750 ℃. The catalysts were calcined at various temperatures, such as 450, 550, 650, and 750℃. The catalyst calcined at 750℃ displayed high activity and stability for 200 h TOS in DRM. The high temperature calcination led to the formation of $NiAl_2O_4$ formation, which ultimately produced small Ni nanoparticles (9 nm) during the reduction. Despite a decrease in surface area and Ni reduction degree with increasing calcination temperature, effective dispersion, and Ni particle size decrease. The dispersion improved from 4.7 (450℃) to 7.3 for 750℃ calcined catalysts.

Although Ni/Al_2O_3 catalysts exhibit high activity in DRM, they have been found to be deactivated for model DRBG studies [96,103]. For instance, Pawar et al. [103] studied the DRBG over Ni/Al_2O_3 catalysts prepared using WI and calcined at 800 ℃ for 6 h. Activity studies showed that the conversion of CH_4 decreased from 99 to 54 with an increase in CH_4/CO_2 ratio from 1.0 to 2.0. The decrease in conversions is attributed to the severe carbon deposition (7% to 50%) due to the excess CH_4 cracking. CO_2 conversions were unaffected because it was the feed's limiting reactant. DRBG being an endothermic reaction, increasing the reaction temperature from 600 - 800ºC resulted in enhanced CH_4 conversions. Additionally, the spent catalyst Raman analysis revealed graphitic carbon on the catalyst surface, which is detrimental to the catalytic activity. Similarly, a heavy carbon deposition of 35% was reported by a recent study on DRBG over Ni/Al_2O_3 catalysts at 800℃ for CH_4/CO_2 = 2.0 [96].

Table 2. 1. Overview of Ni-γAl_2O_3 catalysts used in DRM

Catalyst	**Catalyst preparation**					**Reforming conditions**			**Conversions ,(%)**		**Carbon (%)**	**TOS (h)**	**Reference**
	Method	**Calcination conditions**		**Reduction conditions**		**CH_4/CO_2**	**GHSV (h^{-1}) or WHSV[1] ($m^3h^{-1}kg^{-1}$)**	**Temperature (℃)**	**CH_4**	**CO_2**			
		Temperature (℃)	**Time, (h)**	**Temperature (℃)**	**Time, (h)**								
5Ni/Al_2O_3 plasma treated	W.I	600	4	700	2	1	48000	750	82	86	0.0829	50	[93]
5Ni/Al_2O_3without-plasma treated	W.I	600	4	700	2	1	48000	750	74	80	0.413	10	[93]
16Ni/Al_2O_3	W.I	300	5	800	1	1	480[1]	700	-	-	36.9	100	[100]
		700									16.3		
		900									7.9		
Ni/Al_2O_3	W.I	800	6	-	-	1	12[1]	600	77	70	40	12	[103]
						1.5		600	60	73	-		
						1.75		600	58	76			
						2.0		600	50	75	55		
						1		700	89	87	-		
						1.5		700	65	84			
						1.75		700	59	85			
						2		700	43	82			
						1		800	99	95	7		
						1.5		800	63	93			
						1.75		800	60	94			

						2.0		800	54	96	50		
15Ni/Al_2O_3	W.I	800	4	600	10	1	15[1]	600	4	50		4	[97]
				650				650	25	54			
				700				700	55	84			
30Ni/Al_2O_3	W.I	800	4	600				600	5	47			
				650				650	25	65	-		
				700				700	36	70			
15Ni/ Al_2O_3	USACP	700	4	600	2	1	12000	700	45	74		5	[104]
20Ni/ Al_2O_3									52	75			
25Ni/ Al_2O_3									70	80			
25Ni/ Al_2O_3									77	70			
10Ni/ Al_2O_3	WI	800	-	900	2	2	-	700	50	70	35	40	[96]
								800	60	75	-		
12 Ni/Al_2O_3	WI	550	4	750	2	1	-	800	60	70	27	50	[98]
12NiAl-LDH	PP								69	74	7		
10Ni/Al_2O_3	WI	450	3	750	1.5	1	24000	700	73	80	-	50	[95]
		550							77	83			
		650							81	86			
		750							83	88			
		750							82	88	10	200	
10Ni/Al_2O_3	WI	600	3	800	2	1	36[1]	700	73	87	7.96	6	[94]

2.3 Ni-CeO_2 catalysts

In addition to improving MSI and modifying the surface properties (basicity) of support, selecting oxygen storage carrier materials like CeO_2 is an effective strategy for developing a stable Ni-based catalyst for DRM. The variable oxidation states of Ce (+3 and +4) in CeO_2 make it an attractive choice as a support for the Ni catalysts. Typically, CeO_2 releases oxygen and generates an oxygen vacancy (O_V) that migrates to the surface to oxidize deposited carbon in a reduction atmosphere. Additionally, O_V created in an oxidative environment can promote the activation of CO_2. The oxidation-reduction cycle of Ce ($Ce^{4+} \Leftrightarrow Ce^{3+}$) increases the activity and stability of Ni/CeO_2 catalysts [105–107].

Existing studies have majorly concentrated on modifying preparation methods, adding modifiers (Al_2O_3, La_2O_3, and ZnO) and varying amounts of Ni for developing stable catalysts for DRM [106,108–112]. For example, Ni et al. [109] prepared a highly coke-tolerant Ni/CeO_2 catalyst for DRM using HT synthesis. The authors also prepared a similar catalyst with the precipitation method and observed fewer conversions than the HT process. The lower activity of the catalysts is attributed to poor MSI that resulted in the larger Ni crystallites (30 nm) in fresh reduced catalysts. The high activity of the HT catalysts is related to their SMSI, presence of high oxygen vacancies and small Ni particles (10 nm) generated from the synthesis.

Similarly, Pizzolato et al. [106] studied the role of different preparation methods (WI, CP, and CM) on the stability and activity of Ni/CeO_2 catalysts. The catalysts prepared by the CP method showed high CH_4 and CO_2 conversions in DRM at 700 °C due to high BET surface area of Ni/CeO_2 (30 m^2/g) than WI (8 m^2/g) and CM (18 m^2/g) catalysts.

Few researchers have improved the activity of WI catalysts by modifying with SG, US (ultra-sonication), and HT synthesis in DRM [108,111,113]. For instance, Pham et al.[108] used the modified WI method by combining it with the CP during catalyst synthesis. In a

particular synthesis, supports are prepared by CP and Ni is loaded by the WI method. Activity results showed high conversions of CH_4 and CO_2 to the individual methods alone. Similarly, Gao et al. [111] prepared Ni/CeO_2 catalysts by varying the support morphologies, such as dumbbell, bouquet, and shuttle-shapes with the help of HT synthesis. The dumbbell form of CeO_2 support showed more SMSI than the rest, and XPS revealed a high O_V concentration, resulting in increased conversions of CH_4 and CO_2 in DRM.

Few studies have also varied the amount of Ni from 2.5 wt.% (the lowest), and 80 wt.% (the highest) on CeO_2 supports [105,110]. For instance, Kim et al. [105] prepared Ni/CeO_2 catalysts by varying the Ni from 2.5 wt.% to 20 wt.% using a one-pot synthesis method. An increase in the Ni beyond 12.5 wt.% led to particle agglomeration due to poor MSI. Activity results showed that 12.5 Ni/CeO_2 catalysts displayed high activity and stability for more than 50 h in TOS. Rashid et al. [110] observed a similar decrease in conversions of CH_4 and CO_2 with an increase in Ni from 20 to 80 wt%. Catalysts were prepared using the reverse microemulsion method and calcined at 450 ℃ for 2 h. TEM analysis showed the particle agglomeration with an increase in Ni amount, and the optimum amount of Ni loading was found to be 40 wt.% which displayed higher conversions of CH_4 and CO_2.

Researchers have also studied the effect on catalytic activity by adding various basic and inert supports such as MgO, La_2O_3, and SiO_2 to the Ni/ CeO_2 catalysts [107,114,115]. The addition of MgO and La_2O_3 notably improved the adsorption of oxygen species on CeO_2 and enhanced MSI due to the formation of spinel-type structures such as $MgNiO_2$. La_2O_3. The activity results revealed a positive influence on both CH_4 and CO_2 conversions than Ni/CeO_2 catalysts. The inclusion of SiO_2 improved the dispersion of Ni compared to Ni/CeO_2 catalysts and decreased carbon deposition in DRM.

Overall, Ni/CeO_2 catalysts, in combination with various additional supports such as La_2O_3, MgO, and SiO_2 showed high activity in DRM. additionally, one must carefully choose the selection of calcination and reduction conditions due to the loss of O_V and BET surface area of CeO_2 at higher temperatures (>700 ^oC). The optimum amount of Ni loading helps avoid Ni nanoparticles' sintering, and based on the literature, it should be between 2.5 - 12.5wt%

2.4 Monolith-based Ni catalysts

Utilizing various modifiers such as MgO and SiO_2 is not ideal for upscaling DRM due to their added cost and dominated by external resistances (mass and heat) offered by pellets. Recent studies have focused on developing Ni-supported ceramic cordierite monolith catalysts to overcome the above problems [116–119]. The monolith support provides less mass and heat transfer resistance compared to pellets. The typical monolith (cordierite:Mg_2 $Si_5Al_4O_{18}$) consists of oxides of Al_2O_3, MgO, and SiO_2 and indirectly improves the activity of the catalysts [120]. However, one of the significant challenges in developing monolith reactors is the deposition of adequate catalytic layers that can endure critical reaction conditions (high temperature > 700°C) and, in certain circumstances, mechanical vibrations to provide good stability.

In general, the bare monolith has a low surface area (< 10 m^2/g), and wash-coating techniques are used to enhance the surface area. Wash coating is carried out using three different methods: colloidal, slurry and sol-gel coating. The Colloidal coating is a process that involves the application of a thin layer of colloidal suspensions or suspensions of solid particles in a liquid medium onto a bare monolith. The liquid medium can be either water or an organic solvent. The colloidal suspension is prepared by mixing a support solution with a stabilizing agent, such as polyvinyl alcohol (PVA) or polyvinyl acetate (PVAc).

Table 2. 2 Overview of Ni-γAl_2O_3 catalysts used in DRM

Catalyst	**Catalyst preparation**					**Reforming conditions**			**Conversions, (%)**		**Carbon (%)**	**TOS (h)**	**Reference**
	Method	**Calcination conditions**		**Reduction conditions**		**CH_4/CO_2**	**GHSV (h^{-1}) or WHSV[1] ($m^3h^{-1}kg^{-1}$)**	**Temperature (℃)**	**CH_4**	**CO_2**			
		Temperature (℃)	**Time, (h)**	**Temperature (℃)**	**Time, (h)**								
10Ni/CeO_2	CI	600	4	500	1	1	-	700	60	70	20.3	10	[107]
Ni/La_2O_3-CeO_2									72	84	15.3		
Ni/MgO-CeO_2									83	88	10.3		
Ni/CaO-CeO_2									70	79	8.7		
Ni/ZnO-CeO_2									70	79	2.7		
Ni/CeO_2-Al_2O_3	SG	600	4	550	2	1	-	500	12	20	-	50	[121]
2.5Ni/CeO_2	OP	400	4	800	1.5	1	24000	700	40	56	0	50	[105]
								800	80	92	0	50	
7.5Ni/CeO_2								700	55	65	0	50	
								800	90	93	0	50	
12.5Ni/CeO_2								700	60	69	12.5	50	
								800	95	95	0	50	
20Ni/CeO_2								800	93	93	25	10	
14 Ni/CeO_2	WI	700	6	500	1	1	12000	700	5	10	9.6	20	[106]
	CP								40	69	2.3	30	
	CM								20	40	2	30	
10Ni/CeO_2-Al_2O_3	WI	600	3	750	2	1	36[1]	700	65	77	5.2	6	[108]
	CP								27	47	-	6	
	WI+CP								70	81	5.2	6	
Ni/CeO_2	HT	700	5	700	1	1	-	700	39	50	0.7	8.3	[109]

	PT								4	7	0	4	
Ni/CeO_2	WI								4	7	0	4	
$20Ni/CeO_2$	ME	450	2	550	2	1	120000	800	24	32	0.1[1]	2	[110]
$40Ni/CeO_2$									55	64	1.0[1]		
$80Ni/CeO_2$									50	60	1.4[1]		
$40Ni_{0.75}Ce_{0.25}/Al_2O_3$	CSG	700	3	400	1	1	-	700	82	92	45	16	[122]
$10Ni/CeO_2$	SG followed WI	600	2	600	1	1	-	650	30	43	24	-	[115]
$10Ni/CeO_2$-Al_2O_3	WI	800	8	800	1	1	60000	700	20	60	-	100	[123]
								600	30	70	-	20	
								800	50	75	-	20	
10Ni/5Al-1Ce	ABS	500	4	600	-	1	-	700	90	96	-	8	[124]
10Ni/1Al-1Ce						1			60	80			
10Ni/5Al-1Ce						1	-	550	30	40			
						0.5			55	30			
						0.33			65	27			
$10Ni/CeO_2$	US assisted WI	800	6	700	1	1	21600	800	50	59	42	6	[111]
$10Ni/CeO_2$ (Shuttle shape)	HT followed by WI	500	5	700	1	1	21600	800	72	75	34		
$10Ni/CeO_2$ (Bouquet shape)									82	83	38.6		
$10Ni/CeO_2$ (Dumbbell shape)									92	90	32.2		
Ni/CeO_2-Al_2O_3	ALD	-	-	700	1	1	90000	700	63	68.2	-	-	[125]
				800	1	1	90000	800	83	86	-	-	
$4Ni/CeO_2$	Autoclave	450	4	450	3	1	300000	700	30	40	-	-	[126]
$4Ni/CeZrO_2$									50	65			
$10Ni/CeO_2$-Al_2O_3	CP	600	5	800	1	1	900000	800	75	85	-	5	[112]
	WI								50	65			
	SG								60	73			

	CA								70	80			
5Ni/3CeO_2-SiO_2	WI						15000	800	95	93		10	[114]
5Ni/9CeO_2-SiO_2									96	96			
5Ni/18CeO_2-SiO_2									97	97			
5Ni/30CeO_2-SiO_2									93	90			
5Ni/CeO_2									90	85			
5Ni/28CeO_2-ZrO_2	CP followed by WI	600 and 400	2	600	1	1	30000	700	38	52		24	[113]
5Ni/44CeO_2-ZrO_2									30	45			
5Ni/75CeO_2-ZrO_2									34	48			
5Ni/CeO_2									20	35			

The colloidal suspension is applied onto the support layer, usually by spin-coating or dip-coating. The support layer is dried, causing the colloidal particles to adhere to the surface, forming a thin, uniform layer. The sol-gel method is a process that involves the formation of a gel-like material from a solution. The sol-gel process is based on the chemical reaction between a metal alkoxide and a polymerizing agent. The metal alkoxide solution is prepared by mixing a metal salt solution with alcohol, such as ethanol or methanol. A Polymerizing agent is added, causing the metal alkoxide solution to gel. The gel is then applied onto the support layer, usually by dip-coating or spin-coating. The support layer is then dried, causing the gel to transform into a solid material, forming a thin, uniform layer.

The most prevalent deposition technique is the wash coating of slurry containing the active catalyst on ceramic monoliths using SG synthesis. Several factors and slurry qualities must be regulated for a consistent, repeatable, and mechanically stable wash coat, including pH, particle size, viscosity, slurry concentration, and binders. For example, Agrafiotis et al. [127] studied the role of viscosity and slurry concentration on the reproducibility of γ-Al_2O_3 wash coat over cordierite monoliths. It was observed that the optimum amount of wash coat (15 wt.%) was obtained for the slurry having a viscosity of 50 – 150 mPa.s with a slurry concentration of 40 wt.% solids.

Pawar et al. [116] studied the DRBG over Ni/γ-Al_2O_3-Monolith catalysts prepared using the wash coat method, which involves dip-coating of bare monoliths in a solution containing boehmite (AlOOH), and Ni loading was carried out by WI method. Activity analysis was carried out at 800 ℃ with a feed ratio (CH_4/CO_2) = 2.0. The activity experiments revealed that the conversions of CH_4 and CO_2 are 42% and 88%, respectively, for 6 h TOS. The monolith catalysts displayed high conversions and stability than the Ni/γ-Al_2O_3 pellets [128]. The presence of Si and Mg in the monolith improved the MSI and Ni dispersion compared to pellets.

Similarly, the high activity of Ni/Al_2O_3-monolith catalysts was reported by Soloviev et al. [119] for DRM. Researchers also studied the influence of promoters (K_2O, Na_2O, and Li_2O) on the activity of the catalysts. K_2O displayed high activity, and Lithium (Li) showed low activity. Adding these promoters in small quantities (0.6K_2O and 0.9Na_2O) improved the MSI between Ni and Al_2O_3. In the case of catalysts having Li_2O, the MSI was poor due to the corrosion effect of Li at high temperatures. For example. Agueniou et al. [118] emphasized the role of the (4.5Ni-Ce-Zr/monolith) structure by comparing the activity performance with pellet-shaped catalysts in DRM. The catalysts were prepared using the wash coating method and calcined at 450 ℃ for 5 h. The monolith catalysts showed stable activity for 50 h TOS compared to pellets.

Furthermore, researchers also studied bi-metallic catalysts supported by monolith catalysts, for example. Leba et al. [129] carried out DRM on 8Ni-2Co/MgO-monolith catalysts at 750 ℃ and observed stable activity for 24 h TOS. The catalysts were prepared using a MgO wash coat followed by WI of Ni and Co precursor solutions. Activity results revealed that monolith catalysts are stable up to 48 h TOS with CH_4 and CO_2 conversions of 85% and 89%, respectively. Similarly, Luisetto et al. [130] compared the activity of Ni and Ni-Ru supported on monolith catalysts and observed that 2 wt% Ru improved the stability of the catalysts. The Ni-Ru monolith catalysts' high stability pertained to the Ni's high reducibility and less carbon deposition on the catalyst surface compared to mono Ni supported on Monolith.

Even though monolith catalysts are a possible alternative to current pellets for scaling up processes, the thickness of the support layer and active layer deposition plays a significant role in catalyst activity and stability and needs to be explored. For biogas reforming, a crucial challenge is the deposition and optimization of catalytic layers on substrates with complicated geometries. Since some active layers are restricted to a small portion of the monolith, the wash coat process poses challenges for uniform layer distribution. Although considerable work has

been spent on this subject, comprehensive and satisfactory control of the wash coat qualities has not yet been established.

Table 2. 3 Overview of Ni cordierite monolith catalysts

Catalyst	**Catalyst preparation**					**Reforming conditions**			**Conversions,(%)**		**Carbon (%)**	**TOS (h)**	**Reference,**
	Method	**Calcination conditions**		**Reduction conditions**		**CH_4/CO_2**	**GHSV (h^{-1}) or WHSV[1] ($m^3h^{-1}kg^{-1}$)**	**Temperature (°C)**	**CH_4**	**CO_2**			
		Temperature (°C)	**Time, (h)**	**Temperature (°C)**	**Time, (h)**								
Ni/Al_2O_3-Monolith	WI	800	4	800	3	2	33[1]	800	42	88	-	5	[116]
8Ni-2Co/MgO-Monolith	WI	500	5	800	1	1	84000	750	85	89	-	48	[129]
4.5Ni-Ce-Zr/monolith	WC-Slurry	450	1	600	2	1	115	750	82	90	33	50	[118]
$10Ni/Al_2O_3$-Monolith	WI	600	5	800	1	1	134328	800	30	36	86	60	[130]
10Ni-2Ru/ Al_2O_3-Monolith							169811		60	70		60	
Ni/Al_2O_3-Monolith	WI	750	3	700	2	0.78	-	700	96	-	-	-	[119]

2.5 Perovskite oxides for DRM

Recently, perovskite oxide catalysts have gained interest due to their unique structural characteristics and articulating properties that favor DRBG for carbon-free operation. The structure has the formula ABO_3, known as perovskite oxide materials. The generalization of these materials originated from the discovery of $CaTiO_3$ by Gustav Rose in 1839 and is named after Russian researcher Count Lev Alekseevich Perovskite. In the perovskite oxide (ABO_3), atoms of A are bigger than B. Typically, rare earth or alkaline earth elements occupy the A site, and transition metal elements reside in the B site. The ABO_3 perovskite oxide has a cubic structure in which each A site atom has a coordination number of 12, and the B site has 6-fold coordination. However, perovskites can exhibit hexagonal or orthorhombic structures due to different cation sizes [131]. The structural stability of the perovskite oxide material is determined using the Goldschmidt factor, T.

$$T = \frac{(r_A + r_O)}{1.414(r_B + r_O)} \qquad (2.1)$$

Where

r_A , r_B = Radius of cations A, B (nm)

r_O = Radius of anion O (nm).

For an ideal perovskite material, the factor is between 0.8 to 1.0 [132]. With the help of doping in either A site/ B site or in both A and B sites, one can obtain various new materials using perovskite. The ABO_3 offers great catalytic features such as structural stability, with A-site doping cations like Ce^{+4}, Sr^{+2}, Ca^{+2}, $Ba^{+2,}$ and Sm^{+2}, and B-site doping cations like Mg^{+2}, Co^{+2}, $Fe^{+2,+3}$, Cr^{+3}, Zn^{2+}, and Ti^{+3}, which are beneficial for the CRM [133,134,143,135–142]. Various researchers have studied the basic perovskite $LaNiO_3$ as a catalyst in CR, which displays carbon tolerance for a feed ratio of CH_4/CO_2=1.0. However, these catalysts undergo structural

breakage during reduction, a main concern for catalyst deactivation. The reduction behavior of ABO_3 (A: La or Sr; B: Co, Mn, Fe, Ni, or Cu) structures is shown in Fig. 2.1. When the ABO_3 catalyst is exposed to an H_2 environment, the structure breaks into A_2O_3 and B [88]. The reduction of ABO_3 occurs in a two-step way with the formation of ($A_{n+1}B_nO_{3n+1}$) Ruddlesden-popper phase and metal oxide (BO). For instance, $LaNiO_3$ catalysts are reduced into La_2O_3 and Ni^0 [88,144,145]. Overall, during the in situ reduction process, the $LaNiO_3$ structure breaks into Ni/La_2O_3, decreasing metal-support interaction that leads to the sintering of Ni particles [146]. To avoid that, several studies have focused on doping active metals (Ni, Co, Pt, Ru, Ir & Rh) in stable perovskite oxides such as $LaCrO_3$, $SrTiO_3$, and $LaMnO_3$ to produce highly dispersed metallic nanoparticles after reduction [147–150].

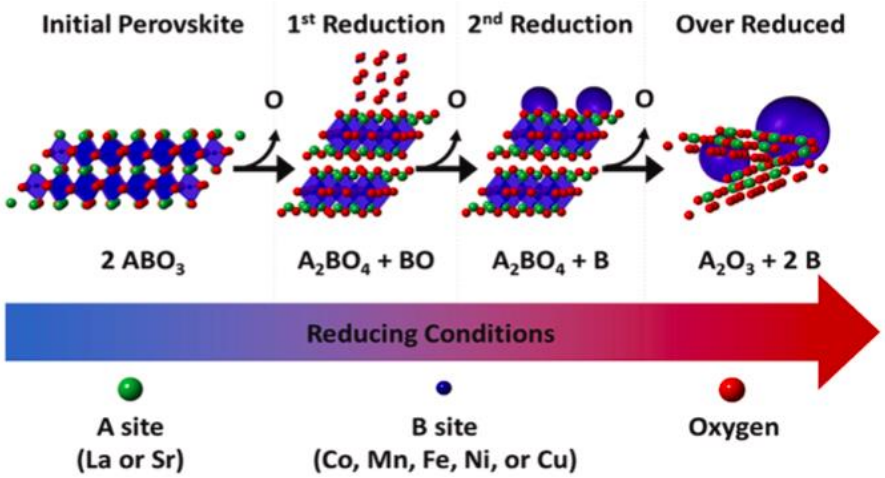

Fig.2. 1. Illustration of $LaNiO_3$ perovskite structure stepwise reduction into La_2O_3 and Ni^0 [88]

$LaNiO_3$ catalysts have been extensively studied in the literature, as mentioned in Table 2.7. The formation of the perovskite structure and its impurities depend on the catalyst's preparation method. As shown in Fig. 2.2, the $LaNiO_3$ catalysts are synthesized using different techniques such as combustion (CM), sol-gel (SG), co-precipitation (CP), and one-step (OS), and hydrothermal (HT) synthesis [151–154]. The HT method results in a small Ni particle size (19

nm), which is desired for minimizing carbon deposition and leading to higher CH_4 conversion than other preparation methods [151]. Additionally, the HT method eliminates admixed phases such as NiO and La_2NiO_4 during $LaNiO_3$ synthesis. Similarly, the $LaNiO_3$ catalyst prepared by the CM shows improved activity and coke tolerance in CRBG compared to that synthesized by the CP method due to the dispersion of small Ni (22 nm) particles over La_2O_3 support and less acidic sites present on the catalyst [154].

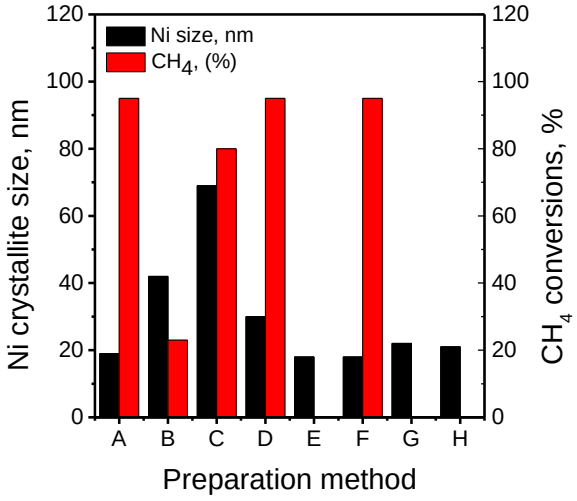

A:Hydrothermal, B:Auto combustion, C:Spray pyrolysis,
D:Spray pyrolysis+ Combustion, E:Co-precipitation,
F:One step synthesis, G:Citrate sol-gel, H:Modified Hydrothermal

Fig.2. 2. Effect of Preparation method on Ni crystallite size and CH_4 conversion for $LaNiO_3$ perovskite oxide catalyst [151–154].

Additionally, reduction conditions also play an essential role in the activity of the catalyst. In many investigations (as mentioned in Table.2.4), catalyst activation/reduction is carried out at 600°C – 800°C. However, a study by Dupeyrat et al. [155] reported a higher activity of $LaNiO_3$ catalysts without any pre-reduction. The authors claim that in-situ reduction of $LaNiO_3$ has occurred during the heating of the catalyst in the presence of CH_4 and CO_2. The catalyst activated under experimental conditions is stable for 100 h TOS without carbon deposition. The high activity and conversions resulted from small Ni nanoparticles (19 nm) on

the La_2O_3. It is also observed that the formation of $La_2O_2CO_3$ plays a significant role in gasifying carbon deposits in CR. The activity of the $LaNiO_3$ catalysts is also enhanced by using different shapes, such as spheres, cubes, and rods prepared using facial CP and HT methods. Due to the strong interaction between Ni and La_2O_3, the rods and spheres exhibited coke tolerance for DRM in 100 h TOS. The excessive carbon (70%) formation on cube morphology is caused by weak metal-support interaction, which is attributed to the NiO on the catalysts support. However, cube $LaNiO_3$ particles show a high conversion of 70% CH_4 due to Ni nanoparticle activity on the tip of multi-walled carbon nanotubes [153].

It is evident from the preceding information that perovskite structures are often created at high temperatures (> 700 °C) and have a low surface area, approximately 10 m^2/g, which restricts their use in catalysis. The surface area can be enhanced by adding oxides like SiO_2, SBA-15, and MCM-41 to the perovskite catalysts. The improvement in the catalytic activity of supported $LaNiO_3$ is observed on SBA-15 and MCM-41 [156,157]. The CH_4 and CO_2 conversions are enhanced by 20% on modified supported catalysts due to the smaller Ni particles (9 nm) compared to the $LaNiO_3$ bulk catalysts (19 nm) [157].

Based on existing investigations, $LaNiO_3$ catalysts are resistant to coke deposition for a feed ratio of 1:1 (CH_4:CO_2) and exhibit stable catalytic activity. However, biogas often contains high CH_4/CO_2 ratios with trace amounts of H_2S, leading to gradual catalyst deactivation. For instance, sulfur deactivation was observed for $LaNiO_3$ catalysts by Gallego et al. [158]. The deposition of coke and the activity of the catalysts depend on the metal-support interaction. Based on the results of DRM, it is evident that $La_2O_2CO_3$ played a crucial role in carbon gasification [159]. However, one major drawback of the $LaNiO_3$ catalyst is that their structural failure in both reduction and DR conditions makes them vulnerable to carbon deposition and catalyst poisoning in DRBG [154,158]. The structural stability, activity, and

coke tolerance of $LaNiO_3$ are improved by doping metal cations in La and Ni sites, which are discussed in detail in the following sections 2.5.1 & 2.5.2

2.5.1 Effect of partial substitution in $LaNiO_3$

Partial metal substitution in $LaNiO_3$ provides a wide variety of catalytic features such as high dispersion, availability of oxygen vacancies, and metal-support interaction. Various kinds of partial substitution are possible in $LaNiO_3$ catalyst systems. The first category comes under substituting La with rare earth or alkaline earth metals to improve oxygen storage capacity and enhance the basic nature of the site. Secondly, Ni is partially substituted with other transitional metals to improve activity and coke tolerance.

2.5.1.1 Partial substitution of La

Substitution of La with rare earth or alkaline earth elements such as Ce, Sr, Ba, Sm, and Ca is expected to improve oxygen carrier capacity, Lewis basicity, and metal-support interaction [134,136–138,160]. The La site substitution for various catalysts is shown in Table 2.5

Cerium (Ce^{4+}) is known for its promoter ability in DRM due to OSC and variable redox behaviour ($Ce^{3+}$and Ce^{4+}). La doping in Ce improves catalytic activity and carbon tolerance [133,146,161,162]. In addition, the partial substitution of Ce exceeding 10 mol% in $La_{1-x}Ce_xNiO_3$ catalysts results in structural modifications, like the formation of admixed phases (NiO, La_2NiO_4, and CeO_2) [160,161]. These phases decrease metal-support interaction, BET surface area, and catalytic activity. Ce doping of 5 and 10 mol% shows high CH_4 and CO_2 conversions [160,161]. The excess Ce doping (10- 40 mol%) results in low conversions; however, it helps carbon gasification [162]. Similarly, in the case of $La_{1-x}Ce_xNi_{0.5}Fe_{0.5}O_3$ (x = 0.4, 0.6, 0.8, & 1.0) perovskite oxide catalysts display high activity and carbon resistance for Ce doping of 40 and 60 mol%. Catalysts high activity and stability are attributed to the

formation of (LaCe)(NiFe)O_3 perovskite phase and oxygen vacancies during the reaction. [146].

The studies suggest that adding optimum amounts of Ce can enhance the coke tolerance and catalyst stability. Despite this, the quantity of Ce doping remains a source of thought. The majority of investigations recommended that up to Ce = 0.1 ($La_{1-x}Ce_xNiO_3$; x =0.1) creates oxygen vacancies and is resistant to coke deposition [160,161].

The promotional effect of Sr^{2+} is reported in many DRM studies for improving Ni dispersion, stability, and coke tolerance [163,164]. The doping of Sr in $La_{1-x}Sr_xNiO_3$ increases the content of oxygen vacancies, thus enhancing the catalyst stability. Moreover, a high quantity of Sr reduces the catalytic activity due to the formation of undesired phases (NiO, La_2NiO_4, SrO, and $Sr_{0.5}La_{1.5}NiO_4$) caused by the limited solubility of Sr^{2+} in the La^{3+} site [139,165]. Interestingly these phases influence the catalytic activity in an ambivalent way. For instance, SrO enhances CO_2 adsorption and forms an active intermediate $SrCO_3$, which removes the carbon on the catalyst surface, resulting in $La_2O_2CO_3$. However, higher loadings of Sr cover Ni active sites, resulting in a loss of catalytic activity [134,139,165]. From the studies, 10 to 40 mol% is sufficient to maintain the high catalytic activity [134,139,165].

Calcium (Ca) is often used to improve thermal and catalytic stability in many reforming studies reported in the literature [166,167]. Doping with Ca minimizes the Ni particle sintering by forming a mixed oxide La-Ca-O support. For instance, Yang et al. [168] reported a 20% enhancement in CH4 and CO2 conversions on $La_{0.9}Ca_{0.1}Ni_{0.5}Fe_{0.5}O_3$ catalysts doped with 10 mol% Ca compared to undoped catalysts.

Table 2. 4 $LaNiO_3$ catalysts DRM

Catalyst	**Catalyst preparation**					**Reforming conditions**			**Conversions, (%)**		**Carbon (%)**	**TOS (h)**	**Reference**
	Method	**Calcination conditions**		**Reduction conditions**		**CH_4/CO_2**	**GHSV (h^{-1}) or WHSV[1] ($m^3h^{-1}kg^{-1}$)**	**Temperature (°C)**	**CH_4**	**CO_2**			
		Temperature (°C)	**Time, (h)**	**Temperature (°C)**	**Time, (h)**								
$LaNiO_3$	A.I	700	6	780	2	1	120[1]	700	90	90	0	100	[155]
$LaNiO_3$	A.C	700	10	700	1		300[1]	700	80	85	-	9	[158]
$LaNiO_3$	HT	600	4	800	1	1	-	800	95	-	-	20	[151]
$LaNiO_3$	CM	600	4	800	1	1	-	800	23	-	-	20	[151]
$LaNiO_3$	SP	600	4	800	1	1	-	800	80	-	-	20	[151]
$LaNiO_3$	SPCM	600	4	800	1	1	-	800	95	-	-	20	[151]
$LaNiO_3$ (cubes)	CP	650	2	800	1	1	125000	650	70	80	70	90	[153]
$LaNiO_3$ (spheres)	CP	650	2	800	1	1	125000	650	40	60	0	90	[153]
$LaNiO_3$ (rods)	MHT	800	2	800	1	1	1250000	650	50	70	0	90	[153]
$LaNiO_3$	CGC	650	5	750	3	1.5	15000	850	94	98	25	50	[154]
$LaNiO_3$	CP	650	5	750	3	1.5	15000	850	90	95	30	10	[154]
$LaNiO_3$	CC	900	5	700	1	1	60[1]	800	95	90	16.8	7	[152]
$LaNiO_3$/SBA-15	NC-SG	700	6	700	2	1	210000	700	80	76	0	50	[156]
$LaNiO_3$/MCM-41	HT	700	6	700	1	1	36000	700	77	66	4.8	50	[157]
$LaNiO_3/SiO_2$	CSG	700	6	700	1	1	36000	700	53	52	5.6	50	[157]
$LaNiO_3$/SBA-15	HT	700	6	700	1	1	36000	700	75	67	4.5	50	[157]

The high activity of catalysts may be related to the stability of Ni particles, which reduces surface carbon deposition. Another study by Lima et al. [136] reported that $La_{0.2}Ca_{0.8}NiO_3$ doped with 80 mol% Ca displayed less carbon deposition with low catalytic activity. It is evident that Ca doping enhances carbon tolerance at low (10 mol%) and high (80 mol%) doping. However, Ca doping exceeding 10 mol%, results in low Ni dispersion due to the formation of unreactive phases of La_2NiO_4, NiO, and CaO [136]. Therefore, optimizing the amount of Ca is crucial in maintaining the stability of the structure and activity of catalysts.

In addition, Ba^{2+} is also used to create OSC and enhance the metal support interaction in $LaNiO_3$ catalysts [137]. However, the presence of NiO, $BaCO_3$, and La_2O_3 in $La_{1-x}Ba_xNiO_3$ (x= 0.05, 0.1, and 0.2) catalyst resulted in less catalytic activity. The addition of Ba impacts coke tolerance, i.e., $La_{0.8}Ba_{0.2}NiO_3$ shows negligible carbon deposition for 20 h TOS in CRM owing to the presence of $BaCO_3$ [137].

Similar coke tolerance is observed for Sm^{3+} $La_{1-x}Sm_xNiO_3$ (x = 0.1, 0.3, 0.5, 0.7, 0.9 & 1.0) catalysts in reforming of CH_4 with CO_2 and O_2. Doping of Sm improves the dispersion of Ni over La-Sm-O mixed oxide, stabilizing the Ni particles in reforming. The lowest Sm doped (x = 0.1) and highest Sm doped (x = 0.9 & 1.0) perovskite oxides exhibit high activity due to the high Ni dispersion on La_2O_3-Sm_2O_3 and flexible redox chemistry of Sm_2O_3 [138].

Table 2. 5La site substitution in $LaNiO_3$

Catalyst	Catalyst preparation					Reforming conditions			Conversions, (%)		Carbon, (%)	TOS (h)	Reference
	Method	Calcination conditions		Reduction conditions		CH_4/CO_2	GHSV (h^{-1}) or WHSV[1] ($m^3h^{-1}kg^{-1}$)	Temperature, (°C)	CH_4	CO_2			
		Temperature ,(°C)	Time, (h)	Temperature , (°C)	Time, (h)								
$La_{0.9}Ce_{0.1}NiO_3$	PC	700	2	850	2	1	10000	800	90	85	-	22	[133]
$La_{0.95}Ce_{0.05}NiO_3$	ACD	800	10	700	5	1	-	750	50	60	-	-	[161]
$La_{0.6}Ce_{0.4}Ni_{0.5}Fe_{0.5}O_3$	SGC	950	4	700	2	1	12000	750	63	73	-	25	[146]
$La_{0.9}Ce_{0.1}\ NiO_{3-\delta}$	CM	700	6	700	5	1	600000	700	41	41	16	5	[162]
$La_{0.9}Sr0.1NiO_3$	OM	1000	10	500	5	1	24[1]	700	-	38	0	7	[139]
$La_{0.6}Sr_{0.4}NiO_3$	AC	900	2	700	2	1	-	700	85	71	-	-	[165]
$La_{0.9}Sr_{0.1}NiO_3$	EDTA C	800	5	900	1	1	70[1]	650	25	20	0	20	[134]
$La_{0.95}Ca_{0.05}NiO_3$	CM	900	10	700	5	1	72[1]	750	77	83	0.03^{CFR}	10	[136]
$La_{0.9}Sr_{0.1}Ni_{0.5}Fe_{0.5}O_3$	EDTA C	550	5	700	1	1	3000	700	60	64	0	20	[168]
$La_{0.9}Ca_{0.1}Ni_{0.5}Fe_{0.5}O_3$	EDTA C	550	5	700	1	1	3000	700	56	60	1	20	[168]
$La_{0.1}Sm_{0.9}NiO_{3-\delta}$	SGC	800	4	800	1	1	15[1]	800	98	61	0	120	[138]
$La_{0.9}Ba_{0.1}NiO_3$	SGC	800	4	800	1	1	200000	700	40	55	0.16^{CFR}	20	[137]

CFR – Carbon formation rate, $g_{carbon}.g_{catalyst}^{-1}.h^{-1}$

2.5.1.2 Partial substitution of Ni

To improve the stability and activity of Ni for CRM, various studies explored Ni partial doping with alkaline earth metal Mg and transitional metals such as Fe, Co, Mn, Cr, and Zn. These catalysts are prepared mainly by sol-gel and combustion methods [135,140,141,169,170] as shown in Table 2.6. Modifying Ni using Mg as a promoter over different supports such as Al_2O_3, SiO_2, and ZrO_2 is a well-established strategy to increase metal-support interaction and coke tolerance [171–173]. The introduction of Mg in $LaNi_{1-x}Mg_xO_{3-\delta}$ (x = 0.02, 0.06, 0.1, & 0.2) catalysts decreased the amount of carbon deposition and enhanced CH_4 conversions. However, at higher Mg doping, catalytic activity decreases due to the formation of admixed phases such as NiO, La_2NiO_4, and MgO in the catalyst [140]. Due to smaller Ni active sites, the 10 mol % Mg doping shows high activity and less carbon deposition than $LaNiO_3$ catalysts [140].

The substitution of Co in Ni results in the formation of Ni-Co alloy during the reduction of $LaNi_{1-x}Co_xO_3$ catalysts, which improves the metal-support interaction and enhances carbon tolerance. The incorporation of Co^{3+} in Ni^{3+} is confirmed with the positive shift in XRD patterns which is due to the lattice contraction (replacing bigger cations with smaller cations: Ni^{3+} = 0.56Å, Co^{3+} = 0.52Å) [141]. Due to the proximity of ionic radii (Ni^{3+} = 0.56 Å, Co^{3+} = 0.52 Å), the Co cations can readily displace Ni cations up to 50 mol%; above this, the $LaNiO_3$ phase is starting to fade out and replaced by $LaCoO_3$. The doping of Co (<60 mol%) improves the activity of the catalysts and inhibits carbon deposition due to the synergetic effect of Ni-Co alloy on $La_2O_2CO_3$ support. At higher loadings (> 60 mol%), carbon deposition decreases, and the activity of the catalysts is reduced due to the less reactivity of Co atoms and partial blockage of Ni sites by Co atoms [140,141,174]. For instance, Gallego et al. [140] prepared a carbon-free catalyst by doping 100 mol% Co in place of Ni on $LaNiO_3$; nevertheless, the conversions are low (10% CH_4 and 24% CO_2 at 700°C) after 15 h TOS. It is evident from the studies that

the presence of undesired phases led to the downfall of the catalysts. The use of solvents in perovskite catalyst synthesis plays an essential role in controlling particle size [175]. A study by Mousavi et al. [175] prepared $LaNi_{0.5}Co_{0.5}O_3$ catalysts using two different solvents, such as magnetized (treated) and non-magnetized (nontreated) water. The catalysts prepared using magnetized water show high CH_4 conversion due to the small Ni particles (21 nm). Also, the purity of the perovskite phase is improved due to an increase in viscosity and a decrease in surface tension of the $LaNi_{0.5}Co_{0.5}O_3$ catalyst prepared using magnetized water. Overall, coke deposition is minimized by doping Co in the Ni site. However, the conversions are decreased due to the partial covering of active Ni sites with Co [141,174].

According to DRM studies alloying Fe with Ni as a bi-metallic catalyst stabilizes Ni nanoparticles against sintering and improves coke tolerance [176–178]. The substitution of Fe with Ni in $LaNiO_3$ facilitates the formation of highly dispersed Ni and Ni-Fe nanoparticles over La_2O_3 support, which improves the coking resistance of $LaNi_{1-x}Fe_xO_3$. As reported by earlier studies, the XRD peak shift towards lower angles indicates the inclusion of Fe in Ni [142,179]. The amount of doped Fe results in the structural change of $LaNiO_3$ (rhombohedral) to $LaFeO_3$ (orthorhombic). Even though catalysts are tolerant to carbon deposition, the activity is reduced due to the formation of inactive $NiFe_2O_4$. The 60 mol% of Fe in Ni, $LaNi_{0.4}Fe_{0.6}O_3$, exhibits high conversions of CH_4 and CO_2 [142,179].

A recent study on DRM over $LaNi_{0.8}Fe_{0.2}O_3$ catalyst shows coke tolerance compared to undoped $LaNiO_3$ catalyst. Fe doping prevented Ni nanoparticle sintering by forming Ni-Fe alloy during the reduction process [169]. A similar effect of Fe substitution in Ni is reported by Song et al. [180]. The prepared $LaNi_{0.5}Fe_{0.5}O_3$ catalyst displays less coke deposition and higher structural stability than undoped $LaNiO_3$ perovskite catalysts. The Fe doping in $LaNiO_3$considerably enhances carbon tolerance. However, the structure of perovskite oxide is not retained without being further subjected to an oxygen environment.

Due to high Ni reducibility and other cation dopants, the perovskite structure is unstable in an H_2 environment. To improve the structural stability in reduction conditions, researchers have doped non-reducible cation Cr^{+3} in Ni sites [143,170]. For instance, Nakamura et al. [181] studied the stability of the $LaCrO_3$ in reducing conditions and found that the structure remained stable up to an oxygen partial pressure of 10^{-21} atm. The addition of Cr in $LaNi_{1-x}Cr_xO_3$ (x = 0 – 1.0) significantly improves the stability of the perovskite for the doping of 40 mol% and above. However, the conversions of CH_4 were considerably low (30%, and 5% CH_4 for x = 0.6, and 0.8, respectively) compared to 80% CH_4 conversion in 20 mol% doped catalysts. The activity of the catalysts decreases with an increase in Cr amount and becomes 0% for 100 mol% doping [143]. Similar findings of Cr doping in the $LaNiO_3$ system were observed by Odedairo et al. [170] under microwave irradiation. The partial doping of Cr in $LaNiO_3$ changes the structure from orthorhombic ($LaCr_{0.9}Ni_{0.1}O_3$) to rhombohedral ($LaCr_{0.3}Ni_{0.7}O_3$) due to difference in cation ion sizes. Among all the prepared catalysts, $LaCr_{0.6}Ni_{0.4}O_3$ shows high activity and stability in CRM due to its oxygen mobility and Ni dispersion in the perovskite matrix. Overall, the ratio of Cr^{3+} to Ni^{3+} influences oxygen releasing capacity and the dispersion of Ni.

Doping of Zn (20 mol%), i.e., $LaNi_{0.8}Zn_{0.2}O_3$ improves the strength of mixed oxide support (Zn-O-La), leading to improved activity and coke tolerance. However, higher doping of Zn (>20 mol%) result in catalyst deactivation due to the admixed phases La_2NiO_4 and ZnO [135]. Similar activity was observed in 20 mol% of Ru in $LaNi_{1-x}Ru_xO_3$ [182]. In another study, adding Ti to Ni in $LaNiO_3$ improves the carbon tolerance and activity due to the stabilization of Ni nanoparticles. It was observed that optimum doping of 40 mol% to 60 mol% in $LaNi_{1-x}Ti_xO_3$ (x = 0 – 1.0) resulted in high activity [183].

Clearly, at higher amounts of doping, the conversions decrease due to the formation of admixed phases. Optimum doping is recommended for better catalytic activity and stability.

All B site substitutions have improved thermal stability and coke deposition. However, perovskite oxide stability poses many challenges, particularly in reducing environments and during reforming reactions, which could play a vital role in enhancing metal dispersion and limiting carbon deposition in harsh reforming conditions.

2.6 Exsolution in perovskite oxide systems

The structural failure of $LaNiO_3$ catalysts in a reduction environment is a severe obstacle for Ni-derived perovskites in DRM. The structural instability of these catalysts enhances Ni particle sintering, eventually leading to severe catalyst deactivation. Non-Ni-based perovskite oxide systems ($LaCrO_3$, $SrTiO_3$, $LaMnO_3$, and $LaScO_3$) are used as a host material to dope the active metal that exsolves from the parent structure upon reduction [148,149,184–186]. Exsolution or solid phase crystallization (SPC) is a novel technique for developing stable catalysts. In SPC, metal cations (M^{n+}) (M: preferably transition metals) are doped into the structure and subjected to H_2 reduction for the exsolution of active metals (M^0). The detailed mechanism of exsolution and their driving force for particle generation have been reported in various studies [187–189]. For example, Gao et al. [186] proposed the mechanism of exsolution, which involves four steps: diffusion, reduction, nucleation, and growth, as shown in Fig 2.3. Ni^{2+} diffuses from bulk to the oxide surface ($La_{0.4}Sr_{0.4}Sc_{0.9}Ni_{0.1}O_{3-\delta}$) and is further reduced to Ni^0 in the presence of H_2. Afterward, metallic particles undergo nucleation and subsequent growth on the surface. According to Gao et al. [186] nucleation and growth depend on operating parameters such as reduction time, temperature and structural defects (A site, oxygen vacancies, and dislocations), mechanical stress, and strain. Additionally, kinetic models have been developed based on three constraints: strain, reactant, and diffusion, to predict the catalyst particle size. Based on the experimental results (exsolved particle size), both strain and reactant models can depict the actual mechanism of the exsolution. Hence it is

essential to create defects in the structure that favors exsolution compared to non-defective structures.

Table 2. 6 Ni site substitution in $LaNiO_3$

Catalyst	Catalyst preparation					Reforming conditions			Conversions, (%)		Carbon, (%)	TOS ,(h)	Reference
	Method	Calcination conditions		Reduction conditions		CH_4/CO_2	GHSV (h^{-1}) or WHSV[1] ($m^3h^{-1}kg^{-1}$)	Temperature, (°C)	CH_4	CO_2			
		Temperature (°C)	Time, (h)	Temperature ,(°C)	Time, (h)								
$LaNi_{0.98}Mg_{0.02}O_{3-s}$	AC	700	6	700	-	1	600000	700	56	67	27	15	[140]
$LaNi_{0.9}Co0.1_yO_{3-\delta}$	AC	700	6	700	-	1	600000	700	44	62	2	15	[140]
$LaNi_{0.7}Co_{0.3}O_3$	RSG	750	4	-	-	1	15[1]	800	99	99	0.3	-	[141]
$LaNi_{0.5}Co_{0.5}O_3$	MWPM	800	5	800	1	1	12000	800	82	92	-	14	[174]
$LaNi_{0.34}Co_{0.33}Mn_{0.33}O_3$	MWPM	800	5	800	1	1	12000	800	93	92	-	14	[174]
$LaNi_{0.5}Co_{0.5}O_3$	CP	850	10	800	12	1	18[1]	800	55	65	15.2[CFR]	25	[190]
$LaNi_{0.6}Fe_{0.4}O_3$	SGC	800	4	700	2	1	15[1]	800	85	49	0	15	[142]
$LaNi_{0.8}Fe_{0.2}O_3$	DP	800	5	800	4	1	15000	650	33	33	0	12	[191]
$LaNi_{0.8}Fe_{0.2}O_3$	DP	900	10	800	4	1	15000	650	28	28	0	12	[191]
$LaNi_{0.5}Fe_{0.5}O_3$	WI	800	4	700	2	1	12000	750	63	65	2	8	[180]
$LaNi_{0.75}Fe_{0.25}O_3$	SG	700	7	-	-	1	-	700	71	81	-	-	[192]
$LaNi_{0.8}Fe_{0.2}O_3$	CP	850	2	800	2	1	13700	800	60	86	20	34	[169]
$LaNi_{0.8}Mn_{0.2}O_3$	CP	750	2	800	2	1	13700	800	85	92	60	34	[169]
$LaNi_{0.6}Cr_{0.4}O_3$	MA	900	2	800	2	1	72[1]	800	53	65	0.04[CR]	50	[143]
$LaCr_{0.6}Ni_{0.4}O_3$	CP	850	5	-	-	1	-	-	70	85	-	30	[170]
$LaNi_{0.8}Zn_{0.2}O_3$	SG	750	3	-	-	1	-	750	86	92	0.3	85	[135]

CFR Carbon rate, $g_{carbon}.g_{catalyst}^{-1}.h^{-1}$

Additionally, particle size relies on temperature and soaking time in the H_2 environment. Due to strong metal support contact and high dispersion, exsolved perovskite catalysts are more active than wet-impregnated catalysts.

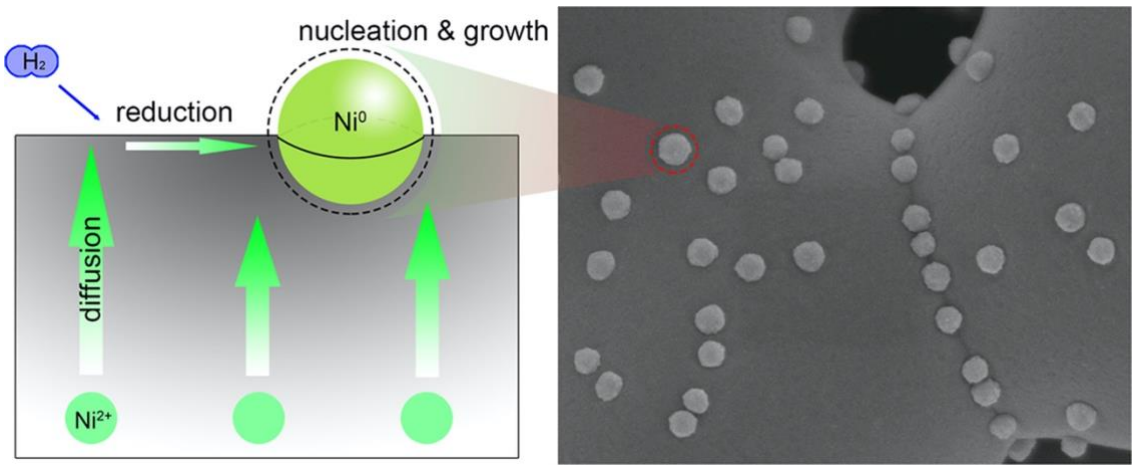

Fig.2. 3 Schematic representation of Exsolution of Ni from $La_{0.4}Sr_{0.4}Sc_{0.9}Ni_{0.1}O_{3-\delta}$ perovskite and its corresponding SEM [186]

As shown in figure 2.4, impregnated catalysts have reduced metal-support contact, resulting in particle agglomeration during CO_2 reforming. In the case of exsolution, catalyst particles are firmly connected to the oxide support, inhibiting particle growth [193].

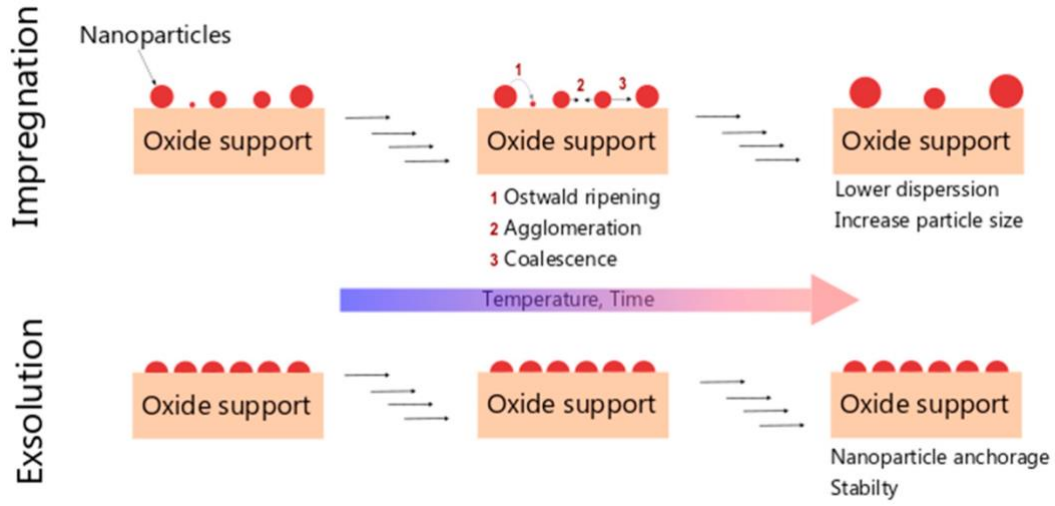

Fig.2. 4 Dispersion of nanoparticles on oxide supports prepared by conventional impregnation and exsolution methods [193]

The resulting exsolved particles are firmly connected with the support metal oxide and offer coke tolerance with the evolution of the base growth of carbon. These properties make exsolved nano-particles on perovskite oxides highly desirable for reforming studies [194,195]. Such catalyst systems improve the dispersion of active metals by resisting the sintering of nanoparticles.

2.6.1 Ni-doped exsolution

In Ni-doped exsolution, Ni is substituted in numerous perovskite oxide systems such as $SrTiO_3$, $LaMnO_3$, $LaFeO_3$, and $La_{0.8}CrO_3$. These catalysts are synthesized in different methods such as citrate sol-gel and combustion, as mentioned in Table 2.7. The exsolution of active catalysts takes place under the reduction environment. The exsolved catalyst systems display high activity and resistance to carbon formation during the DRM due to their strong interaction with the host perovskite oxide, improved dispersion, and small particle size. The exsolution phenomenon facilitates the high activity of catalysts with low doping. For example, 5 mol% on Ni in $Sr_{0.92}Y_{0.08}Ti_{0.95}Ni_{0.05}O_3$ catalyst demonstrates stable catalytic activity for more than

100 h TOS. The catalysts activated under N_2 show higher activity (72% CH_4) than that of the catalysts reduced under the H_2-N_2 mixture (67% CH_4). The formation of Ni hydrates in H_2 reduction environment results in the loss of active Ni sites, which causes a decrease in the activity of catalysts [147].

The $La_{0.46}Sr_{0.34}Ti_{0.9}Ni_{0.1}O_3$ perovskite catalysts display similar activity of Ni doping for CRM. The catalyst is stable up to 100 h TOS with negligible carbon formation compared to the conventional wet impregnation (WI) (3 wt% Ni/$La_{0.46}Sr_{0.34}TiO_3$) catalyst. The high activity and carbon tolerance are attributed to the finely dispersed Ni nanoparticles (4 to 11 nm) over the host perovskite oxide ($SrTiO_3$) [184]. The superior dispersion and the structural stability of the exsolved catalyst systems are proven to replace conventional catalysts. For instance, Wei et al. [185] prepared Ni exsolved from $La_{0.9}Mn_{0.8}Ni_{0.2}O_3$ and Ni impregnated on $LaMnO_3$. Activity results of exsolved catalysts are stable and show higher conversions of more than 80% (CH_4 & CO_2) than WI catalysts, which display poor stability within 2 h TOS. The high activity and coke tolerance of exsolved catalysts are attributed to the small Ni particles (20 nm), strong metal-support interaction, and OSC in the catalyst system. Another study by Wei et al.[148] illustrated the importance of controlled doping of Ni nanoparticles in A-site deficient $La_{0.8}CrO_3$ catalysts by co-doping Sr and Ni cations. The $La_{0.6}Sr_{0.2}Cr_{0.85}Ni_{0.15}$ shows high activity and less coke deposition due to high oxygen vacancies and basicity. A similar effect of A-site deficient $La_{0.8-x}Sr_xCr_{0.85}Ni_{0.15}O_{3-s}$ (x = 0.2) material is observed in the SOFC study [196].

Exsolution studies on bimetallic catalysts such as Ni-Fe, Ni-Fe-Co, and Ni-Re are also explored [49,197,198]. A recent study by Shah et al.[49] elucidated the role of La to Fe ratio in the exsolution of Ni-Fe alloy in $LaFeO_3$ structure. La:Fe ratio of 1:0.9 displays high CH_4 conversion (63%) due to an excellent dispersion of Ni-Fe (3%) with a mean particle size of 34 nm. The doping of Ni in Fe does not change the orthorhombic structure of $LaFeO_3$. However,

in the case of reduced catalysts, the Ni-Fe phase appears along with the admixed phases of La_2O_3, $La_2(OH)_3$, and Fe_2O_3.

In the above studies, A-site deficient catalysts result in the small exsolved Ni nanoparticles (20 nm) [185]. However, the study by Shah et al. [49] showed relatively larger nanoparticles (100 to 300 nm) for A-site deficient catalysts due to Ni-Fe on the catalyst surface. In addition, Shah et al.[197] reported a comparison of catalysts prepared by exsolution of Ni-Fe-Co alloy and wet impregnated catalysts for DRM. The 5 mol% Ni and Co-doped A site deficient catalyst ($La_{0.9}FeNi_{0.05}Co_{0.05}O_3$) shows high activity (85% and 94% CH_4 and CO_2 conversions, respectively) compared to 8 mol% Ni and 2 mol% Co-doped catalysts. The high activity and stability due to A-site deficiency led to the Ni-Fe-Co alloy's higher exsolved Ni content (6.6%).

Similar alloy exsolution was studied by Zubenko et al. [198] over Ni and Ru doped $LaFeO_3$. The prepared catalysts ($LaRe_xFe_{0.8}O_{3+\delta}$-$La_3ReO_8$, and $LaNi_{0.2}Re_xFe_{0.6}O_{3+\delta}$-$La_3ReO_8$; $x<0.2$) display stable conversions of 94% (CH_4 & CO_2) for 70 h TOS without any carbon deposition. The high-temperature TPR peak shift confirmed the introduction of Re and Ni improved metal-support interaction. Even though the perovskite structure is not retained, the exsolved Ni and Re are highly anchored with the La_2O_3 support after reduction, as observed in the TEM analysis of reduced catalysts. The Re and Ni co-doped catalysts show high activity and stability among all the catalysts due to the strongly exsolved Ni and Re particles with the support.

2.6.2 Non-Ni-doped perovskite oxide systems

A few studies have reported exsolution of Co, Pt, Pd, Rh, Ir, and Ru based perovskite oxides prepared using modified pechini method [149,199]. For instance, Hyeng oh et al. [149] studied the doping of Co, Rh, and Ir in $LaCrO_3$ catalysts for reforming and observe high activity

with Ir doped ($LaCr_{0.95}Ir_{0.05}O_{3-\delta}$) catalysts. Fig 2.5 shows the exsolution of Co, Rh, and Ir and their energy change before and after exsolution. The exsolution energy is computed using DFT calculations on $LaCrO_3$ in the (001) plane with Co, Rh, and Ir doping in the Cr atom. Compared to Rh (-0.8 eV) and Co (-0.37 eV), Ir has the highest exothermic energy (-1.01 eV) of all the elements. The enhanced activity and stability of the Ir-doped catalyst may be ascribed to the increased surface exsolution of Ir^0 (4 nm) particles.

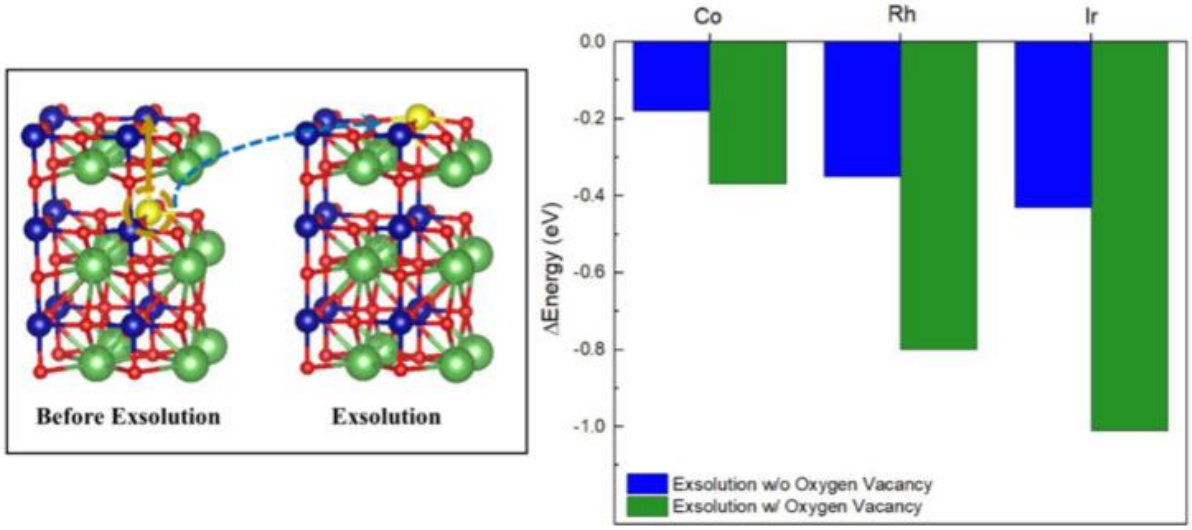

Fig.2. 5 Schematic representation of exsolution of Ir, Co, and Rh from $LaCr_{0.95}M_{0.05}O_3$ (M:Ir, Co, or Rh) and exsolution energy with and without oxygen vacancy [149]

Similar activity is displayed in in $Sr_{0.92}Y_{0.08}Ti_{1.95}Rh_{0.05}O_{3-\delta}$ catalysts doped with 5 mol% Rh. Activity results show that catalyst reduced at high temperature (1000 ^oC) perform better due to high Rh metal concentration (Rh metal: Rh Oxide = 1: 1.12) on the catalyst surface. Moreover, carbon formation on the spent catalysts follows the base growth mechanism to prevent the active Rh particles from sintering, and thus displaying stable activity for 25 h [199]. Even though catalysts reduced at 800 ^oC have a particle size of 2 nm, they still exhibit significant deactivation due to incomplete catalyst reduction on the catalyst support. Additionally, Rh catalysts having a particle size of less than 2 nm tend to decrease the density

of step-edge sites responsible for the C-O recombination reaction, which gasifies deposited carbon [199,200]. The Ru (5 to 10 mol%) doped $Sr_{0.92}Y_{0.08}Ti_{1-x}Ru_xO_3$ catalysts show coke stability for 100 h after being activated at 900℃ in H_2 for 24 h. The high activity and coke tolerance are attributed to the small Ru (10 nm) exsolved particles on the perovskite support [201].

Introducing active metals such as Ni, Co, Pt, Ir, Rh, and Ru in perovskite oxide systems is an effective way to control the particle size and maintain the oxide structure intact in CR. A site deficiency, reduction temperature, and soaking time are vital factors in determing the amount and rate of exsolution in the catalyst activation process. In exsolved perovskite oxide systems, the exsolved particle size often plays an essential role in catalyst activation. Particle size mainly depends on the reduction temperature of the catalyst, and the effect of reduction temperature on particle size differs for various perovskite oxide systems, as shown in Figure 2.6. No significant change was observed in the particle size in the monometallic exsolution. For instance, $La_{0.46}Sr_{0.34}Ti_{0.9}Ni_{0.1}$ activated at two different temperatures, such as 800 ℃ and 950℃, display a Ni particle size of 11 and 14 nm, respectively. A similar observation is reported in the case of $Sr_{0.92}Y_{0.08}Ti_{1.95}Rh_{0.05}O_3$ catalysts reduced at 800 ℃ and 1000 ℃. In addition, the catalysts reduced at higher temperatures display activity as same as those at lower temperatures due to controlled exsolution of the catalyst systems [184,199]. However, in the case of bi-metallic or alloy exsolution, reduction temperature played a vital role in maintaining the particle size. The catalysts $LaFe_{0.9}Ni_{0.05}Co_{0.05}O_3$ activated at two different temperatures, such as 800℃ and 950℃, exhibit particle sizes of 23 nm and 66 nm, respectively. The increment in particle size of exsolved (Ni-Fe-Co) particles at 950℃ is due to the large exsolution of the active cations in the B site and leads to poor catalytic activity in catalysts activated at 950℃ [197]. A similar particle size increment is shown in $La_{0.9}FeNi_{0.05}Co_{0.05}O_3$ perovskite catalyst from 25 nm to 95 nm, resulting in low catalytic activity [197].

Table 2. 7 Exsolution perovskite oxide systems in CO_2 reforming

Catalyst	Catalyst preparation					Reforming conditions			Conversions, (%)		Carbon, (%)	TOS, (h)	Reference
	Method	Calcination conditions		Reduction conditions		CH_4/CO_2	GHSV (h^{-1}) or WHSV[1] ($m^3h^{-1}kg^{-1}$)	Temperature (°C)	CH_4	CO_2			
		Temperature ,(°C)	Time, (h)	Temperature (°C)	Time, (h)								
$Sr_{0.92}Y_{0.08}TiO_3$	PM	650	5	750	4	1.0	18000	800	70	-	-	100	[147]
$Sr_{0.92}Y_{0.08}TiO_3$	PM	650	5	750	4	2.0	18000	800	50	-	-	10	[147]
$La_{0.46}Sr_{0.34}Ti_{0.9}Ni_{0.1}O_3$	CM	800	4	950	2	0.83	26400	700	38	38	0	100	[184]
$Ni/LaSrTiO_3$	WI	800	4	950	2	0.83	26400	700	40	40	2.1	100	[184]
$La_{0.46}Sr_{0.34}Ti_{0.9}Ni_{0.1}O_3$	CM	800	4	950	2	2	26400	700	18	40	3	20	[184]
$La_{0.46}Sr_{0.34}Ti_{0.9}Ni_{0.1}O_3$	CM	800	4	700	2	2	26400	700	20	60	4.8	100	[184]
$La_{0.9}Mn_{0.8}Ni_{0.2}O_3$	MSG	800	-	800	3	1	12000	700	81	82	0.6	24	[185]
$Ni/LaMnO_3$	WI	800	-	800	3	1	12000	700	40	40	20	24	[185]
$La_{0.6}Sr_{0.2}Cr_{0.85}Ni_{0.15}O_3$	SC	1300	3	800	6	1	12000	800	90	90	0	24	[148]
$La_{0.9}FeNi_{0.1}O_{3-\delta}$	SGP	700	4	700	2	1	-	700	80	83	-	24	[49]
$LaFe_{0.9}Ni_{0.1}O_{3-\delta}$	SGP	700	4	700	2	1	-	700	78	83	-	24	[49]
$LaFeNi_{0.1}O_{3-\delta}$	SGP	700	4	700	2	1	-	700	40	60	-	24	[49]
$La_{0.9}FeNi_{0.05}Co_{0.05}O_3$	SGC	700	4	800	2	1	-	900	90	93	-	24	[197]
$La_{0.9}FeNi_{0.05}Co_{0.05}O_3$	SGC	700	4	950	2	1	-	900	90	92	-	24	[197]
$LaFe_{0.9}Ni_{0.05}Co_{0.05}O_3$	SGC	700	4	800	2	1	-	800	77	85	-	24	[197]
$LaFe_{0.9}Ni_{0.05}Co_{0.05}O_3$	SGC	700	4	950	2	1	-	900	77	85	-	24	[197]
$LaFe_{0.9}Ni_{0.02}Co_{0.08}O_3$	SGC	700	4	950	2	1		900	73	84	-	24	[197]
$LaFe_{0.9}Ni_{0.08}Co_{0.02}O_3$	SGC	700	4	950	2	1		900	56	79	-	24	[197]
$La_{0.75}Sr_{0.25}Cr_{0.5}Fe_{0.35}Ni_{0.15}O_3$;	MCM	1300	4	900	20	0.5	-	-	65	80	-	20	[202]
$LaNi_{0.2}Fe_{0.8}O_3$	PM	700	6	860	1	1	34285	800	30	50	-	5	[198]
$LaRe_xFe_{0.8}O_{3+\delta} - La_3ReO_8$	PM	700	6	860	1	1	34285	800	16	40	-	5	[198]

$LaNi_{0.2}$ $Re_xFe_{0.6}O_{3+\delta}$ – La_3ReO_8	PM	700	6	860	1	1	34285	800	75	80	-	5	[198]
$Sr_2Fe_{0.65}Ni_{0.35}MoO_{6-\delta}$,	MPM	1000	10	900	2	1	24[1]	850	52	72	-	10	[193]
$Sr_2Fe_{0.5}Ni_{0.5}MoO_{6-\delta}$	MPM	1000	10	900	2	1	24[1]	850	45	70	-	10	[193]
$Sr_2Fe_{0.35}Ni_{0.65}MoO_{6-\delta}$	MPM	1000	10	900	2	1	24[1]	850	40	62	-	10	[193]
$LaCr_{0.95}Co_{0.05}O_{3-\delta}$	PM	800	10	800	12	1	4000	750	0	-		-	[149]
$LaCr_{0.95}Rh_{0.05}O_{3-\delta}$	PM	800	10	800	12	1	4000	750	75	-	-	-	[149]
$LaCr_{0.95}Ir_{0.05}O_{3-\delta}$	PM	800	10	800	12	1	4000	750	81	-	0	60	[149]
$Sr_{0.92}Y_{0.08}Ti_{1.95}Rh_{0.05}O_{3-\delta}$	PM	650	10	800	24	1	12000	900	91	94	-	-	[199]
$Sr_{0.92}Y_{0.08}Ti_{1.95}Rh_{0.05}O_{3-\delta}$	PM	650	10	900	24	1	12000	900	98	99	-	-	[199]
$Sr_{0.92}Y_{0.08}Ti_{1.95}Rh_{0.05}O_{3-\delta}$	PM	650	10	1000	24	1	12000	900	98	99	-	-	[199]
$Sr_{0.92}Y_{0.08}Ti_{0.9}Ru_{0.1}O_{3-\delta}$	PM	650	10	900	24	1	12000	750	80	85	-	100	[201]
$Ru/Sr_{0.92}Y_{0.08}TiO_{3-\delta}$	PM	650	10	900	24	1	12000	750	70	75	-	100	[201]
$Sr_{0.92}Y_{0.08}Ti_{0.98}Ru_{0.02}O_{3+/-\delta}$	PM	1000	5	900	2	1	12[1]	800	99	99	0	40	[92]
$PrBaMn_{1.7}Ni_{0.3}O_{5+\delta}$	PM	600	4	900	0.5	1	-	800	-	30	-	100	[203]

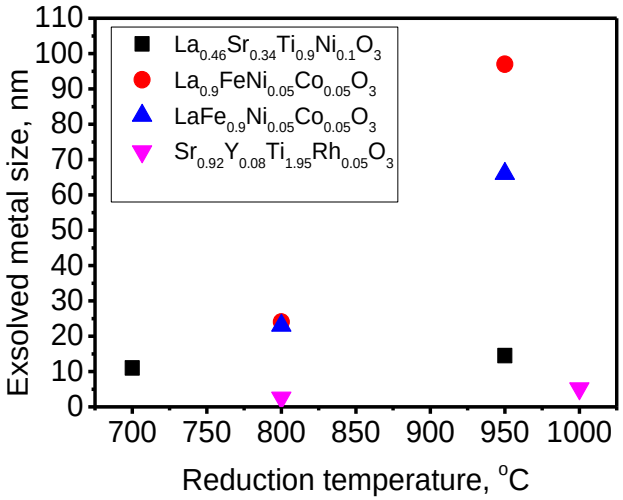

Fig.2. 6 Effect of reduction temperature on exsolved metal particle size for three different catalysts [184,197,199]

The exsolution of the B site is more pronounced in perovskites with an A/B ratio of less than 1 compared to conventional ABO_3, owing to the high equilibrium response of exsolution [195]. Many studies have recommended a high temperature (> 800°C) activation and the use of defective A-site materials for the solid- phase exsolution. Exsolution is an alternative method for conventional wet impregnated (WI) catalysts, which usually require high metal loading. Exsolved catalysts outplayed WI catalysts even with the low metal loading (0.05 to 5 wt%) in perovskite oxide.

Figure 2.7 illustrates the CH_4 and CO_2 conversions, as well as the carbon deposition on doped $LaNiO_3$ and exsolved catalysts. The carbon deposition is substantial in doped $LaNiO_3$ and negligible in exsolved catalysts. The introduction of alkaline earth metals such as Sr and Ca led to decreased carbon deposition, which is attributed to the improved interaction between Ni and perovskite support and OSC. However, the conversions of CH_4 are reduced due to the partial coverage of active Ni with alkaline earth metals [168]. In the case of exsolved catalysts such as $La_{0.6}Sr_{0.2}Cr_{0.85}Ni_{0.15}O_3$ and $Sr_{0.92}Y_{0.08}Ti_{0.98}Ru_{0.02}O_3$, the perovskite structure is retained, resulting in enhanced conversions and low carbon deposition [92,148].

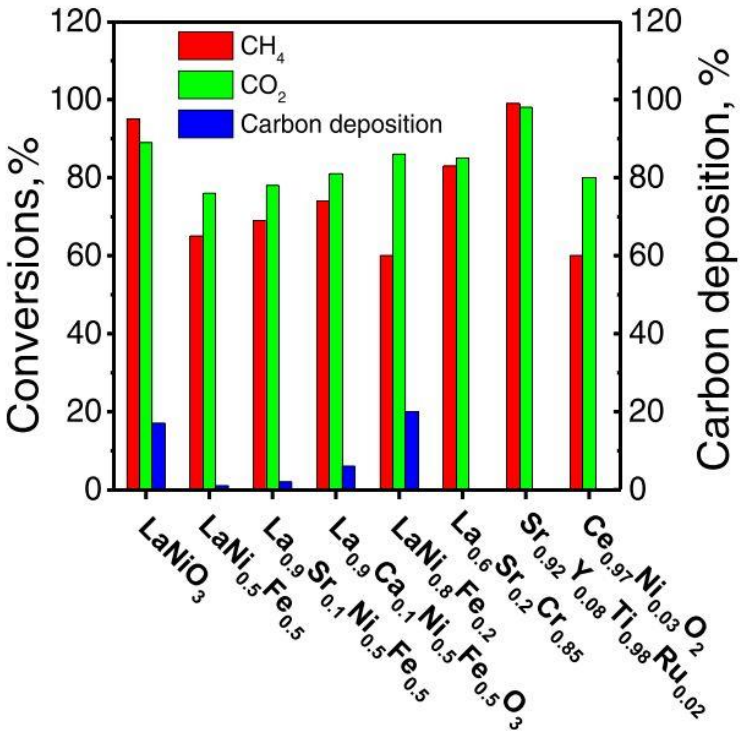

Fig.2. 7 Comparison of CH_4, CO_2 conversions & carbon deposition over various catalysts in CRM at 800°C for CH_4/CO_2=1.0 [92,148,152,168,169,204]

2.6.3 Exsolution in other oxide supports

Exsolution in pyrochlores ($A_2B_2O_7$), spinels (AB_2O_4), and mixed oxide materials has also explored [204–212]. Exsolution in these catalysts minimizes the prolonged calcination and charge balancing difficulties encountered in traditional exsolution systems. Pyrochlores are also studied due to their excellent thermal stability and high oxygen mobility, which primarily impact the activity and coking resistance in DRM. For instance, 6 wt% Ni-doped $La_{1.95}Sr_{0.05}Zr_{1.44}Ni_{0.56}O_{7-\delta}$ catalysts display coke tolerance for more than 45 h. The high activity and conversions of catalysts are attributed to the strong interaction between Ni and pyrochlore support, which predominantly reduce the Ni sintering, while the structure is also retained after the reduction [206]. Interestingly Ni is not detected in XRD patterns of reduced catalysts, which may be due to the incorporation of Ni in the pyrochlore structure. However, the presence of exsolved Ni is detected in SEM. Similar activity is observed over 10 wt% Ni over $La_2Zr_2O_{7-\delta}$

catalysts in the bi-reforming of methane [207]. In another study, doping of 20 mol%, Ru in $Sm_2Ce_2O_7$ catalysts display unusual activity and stability for more than 4 days due to small 2 nm nanoparticles and a high dispersion (65%) over pyrochlore support. Also, Also, Ru exsolution is more effective for CO_2 reforming than the wet impregnated Ru on $Sm_2Ce_2O_7$ catalysts. The introduction of Ru in Ce leads to more oxygen vacancies due to the charge difference of the host cation [208]. Despite the excellent stability of pyrochlore catalysts, the immediate breakdown of CH_4 into C and H_2 renders them unsuitable for CRBG. For instance, Kumar et al. [213] reported a reaction mechanism for DRM on Ni-doped $La_2Zr_2O_7$ catalysts. According to this study, as shown in Figure 2.8, there are two possible pathways for the reforming reaction to occur. In the first scenario, CO_2 dissociates into carbon and oxygen at the metal-support interface. Concurrently, CH_4 decomposes into C and H_2 on the metallic sites. The oxygen atom eventually recombines with the carbon on the Ni surface to generate two CO molecules, as shown in Figure 2.8 a. In the second process, both CO and CO_2 are formed, as shown in Figure 2.8 b. which results from the interaction between carbon and oxygen atoms on the surface of CO_2 molecules. Based on this process, the catalyst deactivation is caused by carbon from CH_4 cracking.

In addition, the impregnation of Ni on defective spinel such as $Mg_{0.388}Al_{2.408}O_4$ support shows high catalyst stability due to the optimum Mg/Al ratio and the ratio of acidic to basic sites [210]. The doping of 3 mol% Ni in CeO_2 ($Ce_{0.97}Ni_{0.03}O_2$) [204] displayed catalyst stability for 80 h due to the formation of NiO-CeO_2 solid solution that enhances the Ni dispersion. Similarly, Ni exsolution in phyllosilicate (Ni-Mg/SiO_2) shows excellent stability due to the 10 nm Ni particle [172].

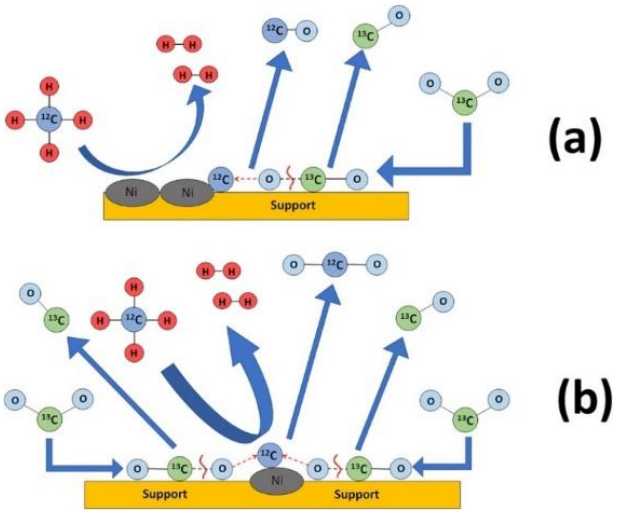

Fig.2. 8 Possible CRM mechanism over Ni doped $La_2Zr_2O_7$ catalysts a) formation of CO, b) formation of CO and CO_2. [213]

Although exsolution has many advantages, such as high dispersion, anchored nano-particles with support, and structural stability in reduced conditions, it has certain limitations for practical applications. The significant constraints are the limited solubility and low exsolution from the host cation lattice. A significant part of cation stays within the bulk of host cation due to the slow diffusion rates of cations in the perovskite oxide. Additionally, the low solubility of dopant metal in host cations decreases the exsolution during the reduction process [214–216]. To overcome these challenges, few researchers propose the topotactic exsolution method. In this method, additional cations are added to the existing B site cations, which promotes the exsolution of B site cations without breaking the perovskite structure [216,217]. For instance, Joo et al. [216] studied the reforming of methane over Ni-Fe nanoparticles on A-site deficient perovskite oxide ($La_{0.6}Sr_{0.2}TiO_{3-\delta}$) catalysts. Initially, $La_{0.6}Sr_{0.2}Ti_{0.85}Ni_{0.15}O_{2.95}$ catalysts are prepared using pechini sol-gel method, followed by Fe_2O_3 deposition using the atomic layer method, and catalysts are reduced at 850 ^oC for 30 min.

Table 2. 8 Exsolution in mixed oxide systems

Catalyst	Catalyst preparation					Reforming conditions			Conversions, (%)		Carbon, (%)	TOS, (h)	Reference
	Method	Calcination conditions		Reduction conditions		CH_4/CO_2	GHSV (h^{-1}) or WHSV[1] ($m^3h^{-1}kg^{-1}$)	Temperature, (℃)	CH_4	CO_2			
		Temperature (℃)	Time, (h)	Temperature (℃)	Time, (h)								
Ni/YSZ	BM	1600	-	-	-	1	-	800	94	97	1.3	300	[205]
$La_{1.95}Sr_{0.05}Zr_{1.904}Ni_{0.096}0_{7-\delta}$	MPM	1000	8	800	2	1	-	900	54	74	-	45	[206]
$La_{1.95}Sr_{0.05}Zr_{1.44}Ni_{0.56}0_{7-\delta}$	MPM	1000	8	800	2	1	-	900	98	97	-	45	[206]
Ni/ $La_2Zr_2O_7$	MCM	500	4	650	1	1	30[1]	700	86	90	0.01[CFR]	360	[207]
$Sm_2Ru_{0.2}Ce_{1.8}O_7$	SGCM	800	3	700	1	1	-	700	70	-	-	50	[208]
Ni/Mg_x Al_yO_4 (x/y = 0.9)	SG	800	4	800	2	1	24200	700	70	76	0.0	30	[210]
Ni/Mg_x Al_yO_4 (x/y = 0.24)	SG	800	4	800	2	1	24200	700	80	85	0.0	30	[210]
$Ce_{0.97}Ni_{0.03}O_{2-\delta}$	SG	400	24	800	1	1	5000	800	60	80	0	80	[204]
Ni-Mg/SiO_2	HT	-	-	700	5	1	18000	700	90	91	21	50	[172]
$Ni_{0.05}Mn_{0.95}O$	CP	750	4	500	1	1	-	800	83	-	-	-	[211]
$Ni_{0.4}Mg_{0.6}O$	CP	800	5	800	5	1		750	99	-	0	1000	[212]

CFR Carbon rate, $g_{carbon}.g_{catalyst}^{-1}.h^{-1}$

2.6.4 Other perovskite oxide systems

As shown in Table 2.9, in addition to $LaNiO_3$, different perovskite systems such as $BaZrO_3$, $SrZrO_3$, $CaZrO_3$, $GdFeO_3$, $NdCoO_3$, $CeNiO_3$, and $LaAlO_3$ have been employed for CO_2 reforming [150,218–221] as shown in Table 7. For instance, Dama et al. [218] studied CRM over three different perovskite catalysts $CaZr_{0.8}Ni_{0.2}O_3$, $SrZr_{0.8}Ni_{0.2}O_3$, & $BaZr_{0.8}Ni_{0.2}O_3$ and observe that $CaZr_{0.8}Ni_{0.2}O_3$ catalysts show high activity and conversions for 500 h TOS. Doping of Ni in $CaZrO_3$ enhances the dispersion of Ni (13%) compared to $SrZrO_3$ (4.0%) and $BaZrO_3$ (3.9%), which results in less carbon formation. Similarly, Ni-doped in $SrZrO_3$ catalyst shows remarkable stability for 240 h with negligible carbon deposition in CRBG at 800℃ for CH_4/CO_2 = 2.0. The excellent stability and coke tolerance are attributed to the high promotional effect of 4 mol% Ni doped in $SrZrO_3$ [222]. Similar coke tolerance is reported on Ni-Fe doped in $SrZrO_3$ catalysts for CRBG with CH_4/CO_2=2.0 at 700-900℃. These catalysts have high oxygen mobility and structural stability resulting in stable activity for 20 h TOS [223].

Apart from Ni catalysts, noble metals such as Pt, Rh, & Ru doped perovskite catalysts in $BaZr_{1-x}M_xO_3$ (x = 0.1351; M = Pt, Rh, & Ru) are also tolerant to carbon deposition. The Rh-doped perovskite shows high activity due to the high reducibility of $BaZr_{0.8649}Rh_{0.1351}O_3$ compared to Pt and Ru catalysts [219]. Similar activity is observed in A- site modified $Azr_{1-x}Ru_xO_3$ (x = 0.08, 0.13, & 0.11; A=Ca, Ba, &Sr) catalysts for CRM. Among all the catalysts, $SrZrRuO_3$ displays low coke deposition and high conversions due to strong interaction between Ru and the perovskite matrix $SrZrO_3$ [220]. The doping of 2 mol% noble metals Pt, Pd, & Ru on $LaAlO_3$ perovskite oxide has developed effective coke tolerance for 50 h TOS. Among all the doped catalysts, $LaAl_{0.98}Ru_{0.02}O_3$ displays high activity due to pronounced thermal stability between Al and Ru, which prevents the catalysts from sintering and coke deposition [150].

A recent study by Alenazey et al. [221] developed a new perovskite catalyst, $CeCo_xNi_{1-x}O_{3+\delta}$ (x = 0 to 0.8), and investigate the role of Co in CRM. The $CeNiO_3$ displays high activity

and stability for 24 h TOS. It is observed that Co affects the catalytic activity due to the CH_4 activation is not favorable on Co [221]. However, Yafarova et al. [224] reported an effect of Co in $GdFeO_3$ catalysts. The doping of Co enhances the catalytic activity and reduces carbon deposition in DRM. After reduction, the high activity is attributed to forming active sites such as Co/CoO-Gd_2O_3 on the catalyst surface. Similarly, $NdCoO_3$ perovskite catalysts exhibited coke tolerance in DRM. The high activity and superior coke tolerance are attributed to the strong interaction between Co and the Nd_2O_3 support [225].

Table 2. 9 Various perovskite oxide systems in DRM

Catalyst	Catalyst preparation					Reforming conditions			Conversions, (%)		Carbon, (%)	TOS, (h)	Reference
	Method	Calcination conditions		Reduction conditions		CH_4/CO_2	GHSV (h^{-1}) or WHSV[1] ($m^3h^{-1}kg^{-1}$)	Temperature ,(°C)	CH_4	CO_2			
		Temperature (°C)	Time, (h)	Temperature, (°C)	Time, (h)								
$CaZr_{0.8}Ni_{0.2}O_3$	SGC	800	6	600	6	1	28000	800	95	95	0	500	[218]
$SrZr_{0.8}Ni_{0.2}O_3$	SGC	800	6	600	6	1	28000	800	85	85	0.0024^{CFR}	12	[218]
$BaZr_{0.8}Ni_{0.2}O_3$	SGC	800	6	600	6	1	28000	800	30	30	0.0072^{CFR}	12	[218]
$BaZr_{0.8649}Rh_{0.1351}O_3$	SGC	850	5	-	-	1	-	750	76	-	0.0019^{CFR}	65	[219]
$BaZr_{0.8649}Ru_{0.1351}O_3$	SGC	850	5	-	-	1	-	750	60	-	0.0027^{CFR}	65	[219]
$BaZr_{0.9272}Pt_{0.0728}O_3$	SGC	850	5	-	-	1	-	750	35	-	0.0094^{CFR}	65	[219]
$BaZr_{0.8649}Ru_{0.1351}O_3$	MCM	900	6	-	-	1	-	650	70	73	0.0049^{CFR}	75	[220]
$CaZr_{0.91087}Ru_{0.08913}O_3$	ACM	900	6	-	-	1	-	650	40	44	0.028^{CFR}	75	[220]
$SrZr_{0.88729}Ru_{0.11271}O_3$	ACM	900	6	-	-	1	-	650	75	80	0.0097^{CFR}	75	[220]
$LaAl_{0.98}Pd_{0.02}O_3$	SCM	700	3	400	1	1	48000	800	60	70	-	-	[150]
$LaAl_{0.98}Pt_{0.02}O_3$	SCM	700	3	400	1	1	48000	800	58	96	-	-	[150]
$LaAl_{0.98}Ru_{0.02}O_3$	SCM	700	3	400	1	1	48000	800	80	97	-	24	[150]
$SrZr_{0.96}Ni_{0.04}O_3$	HT	-	-	850	-	2.0	-	900	55	99	2.5	240	[222]
Ni-Fe/ $SrZrO_3$	HT	-	-	900	2	2	-	900	50	99	0	20	[223]

CFR Carbon formation rate, $g_{carbon}.g_{catalyst}^{-1}.h^{-1}$

2.7 Summary of Literature review

Dry reforming of biogas is a sustainable process for converting the two global warming gases, such as CH_4 and CO_2, into syngas. However, this process faces obstacles in the form of catalyst poisoning due to the presence of H_2S and heavy carbon deposition during the dry reforming. Thermodynamically, DRBG is favorable above 800 ℃ and at 1 atm pressure to minimize carbon deposition, but high temperature leads catalyst sintering. Ni catalysts are extensively studied due to their high activity and cheap abundance. However, Ni catalysts are prone to deactivate due to the carbon formation and sintering in CRBG. Numerous catalysts supports, such as Al_2O_3, La_2O_3, CeO_2 and MgO, are employed to improve the catalyst dispersion, metal-support interaction, basicity, and oxygen vacancies to enhance the catalyst stability.

The Ni/Al_2O_3 catalysts suffer from deactivation due to carbon deposition. The introduction of basic supports such as La_2O_3 and MgO enhanced the catalyst stability through carbon gasification and SMSI. The neutral supports like SiO_2 helped increase the catalysts' surface area and minimized the Ni particle sintering by restricting the particle movement. However, the activity and stability of these catalysts highly rely on the preparation method and regular arrangement of mesopores. Due to their chemical composition and uniform arrangement of channels, cordierite as catalyst support is preferred. The application of these decreases the pressure drop, which is dominant in powder/pellet type catalyst; moreover, monolith catalysts have higher surface area per volume and offer negligible heat and mass transfer resistances than the pellets. Bare monolith has low surface area that needs to be improved by wash coating with the high surface area supports. However, wash coating method and the non-uniform adherence of the wash coat restricted their use.

Recently, structural catalysts such as perovskite oxides (ABO_3) have gained popularity due to their strong metal interaction, facilitating oxygen vacancies and improving thermal stability. The $LaNiO_3$ perovskite oxide catalysts have shown high activity and stability in reforming applications. The reaction kinetics on $LaNiO_3$ reveal that CO_2 reforming follows a dual site mechanism with Ni and La_2O_3 as active sites. Typically, CH_4 activates on the metal surface, and CO_2 reacts with La_2O_3 to form reactive intermediate $La_2O_2CO_3$, which plays a significant role in carbon gasification. In these systems, catalyst preparation plays a significant role in avoiding undesirable phases such as NiO and La_2NiO_4. Irrespective of the preparation method, high temperature (> 700 ℃) and prolonged calcination are required to form the pure $LaNiO_3$ phase. The low surface area of perovskite oxides can be improved with addition of SBA-15 and MCM-41, which exhibited better activity than bare $LaNiO_3$ catalysts. However, the deposition of coke and the activity of the catalysts depend on the metal-support interaction. The lanthanum oxy-carbonate ($La_2O_2CO_3$) formation in CO_2 reforming played a vital role in gasifying carbon on the catalyst surface. Even though $LaNiO_3$ perovskite oxide catalyst display high stability and activity, the structural failure of the catalysts in reduction and reaction environments makes them vulnerable to catalyst deactivation in the long run.

To counteract this, the doping of La is doped with various rare/alkaline earth cations such as Ce^{4+}, Sr^{2+}, Ba^{2+}, $Ca^{2+,}$ and $Sm^{3+,}$ to create oxygen vacancies and improve the thermal stability of the perovskite catalyst. The substitution of Ce up to 5 mol% affects catalytic activity, but at higher loadings, it harms metal-support interaction, considerably decreasing the catalytic activity. A similar analogy applies to Sr doping in CR. Studies suggest that Sr doping of 10 mol% leads to a fall in catalytic activity due to un-reactive phases such as $Sr_{0.5}La_{1.5}NiO_4$.

The Ca doping enhances the basic nature of $LaNiO_3$ and results in coke tolerance in dry reforming. A similar coke tolerance effect is observed for Ba doped catalysts. The presence of Ba increase in oxygen vacancies and strengthens the basic sites of the catalysts, enhancing coke gasification. However, coke tolerance is attained for La site doping, the catalyst activity is considerably reduced, and needs to be investigated to improve the catalytic activity.

The Ni substitution with various alkaline earth/ transitional metals such as Mg^{2+}, Co^{2+}, Fe^{3+}, Cr^{3+}, & Cu^{2+} has improved metal-support interaction, catalytic activity, and carbon tolerance. The Co-doped catalysts effectively prevent carbon deposition by covering a few active Ni sites. Also, they improve the interaction between Ni-Co and La_2O_3, thus preventing catalysts from sintering at higher temperatures. The amount of Co doping has increased catalytic activity, but at higher doping levels Co (typically > 60 mol%), the activity is reduced. In Fe^{3+} substituted catalysts, the synergetic effect of Ni-Fe alloy is beneficial for decreasing carbon deposition on the catalysts. Mg^{2+}, Co^{2+}, and Fe^{3+} improved Ni's thermal stability and coke tolerance in $LaNi_{1-x}M_xO_3$ (M = Mg^{2+}, Co^{2+}, and Fe^{3+}) catalyst system. However, the catalyst's structure is broken during the reduction and reforming conditions. Being a less reducible cation, the doping of Cr^{3+} improves the structural stability of the perovskite. An increase in Cr^{3+} doping leads to a decrease in catalytic activity due to the static nature of Cr under reaction conditions. Overall, the formation of $La_2O_2CO_3$ is observed on the spent catalysts, which played a vital role in gasifying carbon deposition during the reforming reaction.

Although $LaNiO_3$, $La_{1-x}M_xNiO_3$ (M: Ce, Sr, Ca, & Ba), and $LaNi_{1-x}M_xO_3$ (M: Co, Mg, Fe, Zn, & Cr) perovskite systems have shown coke tolerance in reforming, they still have some problems particularly in retaining perovskite structure, sintering of catalyst, and finding optimum doping of cations that can balance the carbon deposition and catalytic activity. These challenges

are overcome using exsolved perovskite catalysts, involving doping Ni or other active metal in a stable perovskite system. During the reduction, active metal is exsolved from the perovskite oxide, intact within the structure. The exsolution in perovskites brought significant changes in terms of catalyst preparation and catalyst activation. The exsolved nanoparticles generated from perovskite materials exhibit a robust metal-support interaction, owing to the capacity of structural stability before and after the reaction, preventing catalyst sintering and ultimately reducing carbon deposition. The exsolved catalysts are more effective than the conventional impregnation catalysts. In the exsolution, active metals are anchored within the host structure, making it hard for carbon deposition on the catalyst surface. In such systems, the formation of carbon follows the base-growth mechanism, which does not impact catalytic activity. A similar exsolution behavior is observed in pyrochlores and mixed-oxide support structures. However, these research areas need to be explored for better understanding of exsolved catalysts during the reduction.

2.7.1 Research gaps

1. Most of the studies described above focused on developing catalysts for DRM (CH_4/CO_2= 1.0) and there are very few studies that exist for DRBG.
2. In catalyst preparation, calcination temperature and time play a pivotal role in creating SMSI, which helps determine the catalyst's anti-sintering and anti-coking abilities. There were no concrete studies on the effect of calcination time of the catalyst; instead, existing studies have centered on altering calcination temperature.
3. A significant number of catalysts studied for DRBG are in pellet form, which is limited for practical application in scale up. Only a few studies discuss cordierite catalysts.
4. Also, the perovskite oxide catalysts studied so far are primarily of the $LaNiO_3$ type, and the structure of these catalysts is highly unstable in reduction and reforming conditions.

There were no studies available based on DRBG over perovskite oxide catalysts in terms of structural stability and activity.

5. A-site deficient perovskite oxides play a crucial role in the exsolution of B-site active metals, yet most studies only concentrate on defect-free perovskite oxide catalysts. This narrow focus fails to fully explore the potential of the A-site deficient perovskite oxides in DRBG.

2.7.2 Research Objectives

1. To prepare Ni-loaded alumina washcoated monoliths with varying calcination times and investigate their catalytic activity for model biogas reforming.
2. To prepare Ni-loaded alumina-ceria washcoated monoliths and assess their catalytic performance for model biogas reforming.
3. To prepare and examine the catalytic activity of Ba-loaded Ni exsolved perovskite catalysts for model biogas dry reforming.

Chapter-3

3 Research Methodology

3.1 Introduction

This chapter discusses the research methodology adopted in this study. It entails the preparation of Ni-based monolith and powdered catalysts using sol-gel and wet-impregnation methods. The prepared catalysts are characterized using various techniques to understand the structural properties, metal-support interaction, surface chemistry and morphology, and the nature of carbon deposition. These techniques include X-ray diffraction (XRD), Fourier transform infrared (FTIR), temperature programmed reduction (TPR), pulse-chemisorption, X-ray photoelectron spectroscopy (XPS), field emission scanning electron microscopy (FESEM), transmission electron microscopy (TEM), Raman analysis, and thermogravimetric analysis-differential thermal analysis (TGA-DTA). Additionally, the methodology used for the catalytic activity studies includes calibration of the mass flow controllers (MFC) and gas chromatography (GC).

3.1.1 Cordierite catalyst

Cordierite monolith structures ($2MgO.2Al_2O_3.5SiO_2$) are commonly used in catalytic applications due to their high mechanical strength, ability to withstand high temperatures and temperature shocks, and low thermal expansion and provide high catalytic surface area per unit volume. However, cordierite has a major drawback in terms of its low BET surface area, which is an important factor in determining the catalytic activity of a material. The BET surface area of cordierite is around 0.7 m^2/g [226], which is relatively low compared to other materials used as catalytic supports. To improve the surface area, boehmite ($Al_2O_3.H_2O$) was chosen as a support material to wash-coat the cordierite monoliths. It has a high BET surface area of around 448 m^2/g

and good metal-support interaction, making it an ideal choice for catalytic applications. The wash-coating process involves applying a thin layer of boehmite onto the surface of the cordierite monoliths, thereby increasing the surface area and improving the metal-support interaction. The process starts with preparing a boehmite suspension, which is achieved by mixing the boehmite powder with a liquid medium, such as water or an organic solvent. The mixture is then sonicated for a homogeneous mixture. The resulting suspension is then applied onto the surface of the cordierite monoliths, usually by dip-coating or spin-coating. The mechanism for the formation of a uniform layer is based on the adsorption of boehmite particles onto the surface. The adhesion is due to the interaction between the boehmite particles and the cordierite surface, which can be physical, chemical, or a combination of both. The drying process is crucial in forming the thin, uniform layer, as it causes the boehmite particles to adhere to the cordierite surface. Various methods exist in the literature, such as colloidal, slurry coating and sol-gel methods for wash-coating on bare monoliths.

3.1.2 Sol-gel

The sol-gel method synthesizes solid materials from a liquid precursor, commonly known as sol. The sol is a nanoparticle suspension that can be converted into a gel by chemical or physical reactions. The resulting gel can then be dried and subjected to additional processing, such as heat treatment, to create a solid material with a clearly defined microstructure. In the sol-gel process, the precursor solution often comprises metal or metal oxide precursors and chemicals that can be used to adjust the particle size and form. Following the development of the sol, the gel is dried and heated, causing the precursor particles to undergo a structural transformation and create a solid catalyst. In addition to activating the catalytic activity of the metal or metal oxide, heat treatment can also enhance its catalytic properties. The mechanism involved in the manufacture of catalysts

using the sol-gel method controls the size, shape, and distribution of the metal or metal oxide particles, as well as the chemical composition. By selecting precursors, reagents, and processing conditions, it is possible to adjust the catalytic activity and selectivity of the end product [227]. Overall, the sol-gel process provides a versatile and cost-effective way to create catalysts with well-defined structures and features that can be tuned to specific applications. It is one of the most well-established methods for preparing nano catalysts.

3.1.3 Alumina Wash-Coating

The colloidal coating process involves applying a thin layer of colloidal suspensions or suspensions of solid particles in a liquid medium onto a support layer. The liquid medium can be either water or an organic solvent. To prepare the colloidal suspension, a metal salt solution with a stabilizing agent, such as polyvinyl alcohol (PVA) or polyvinyl acetate (PVAc), and then sonicated to break down the metal salt into smaller particles. These particles are then stabilized by the stabilizing agent before being applied to the support layer, usually by spin-coating or dip-coating. The support layer is dried, the colloidal particles adhere to the surface, forming a thin and uniform layer.

The slurry coating method involves applying a mixture of powders and a liquid medium onto a support layer. The slurry mixture is prepared by mixing desired metal or metal oxide with a liquid medium, such as water or an organic solvent. The slurry is then applied onto the support layer, usually by dip-coating or spin-coating. The support layer is then dried, causing the powder particles to adhere to the surface, forming a thin and uniform layer.

The sol-gel method is a process that involves the formation of a gel-like material from a solution. The sol-gel process is based on the chemical reaction between a metal alkoxide and a

polymerizing agent. The metal alkoxide solution is prepared by mixing a metal salt solution with alcohol, such as ethanol or methanol. The polymerizing agent is then added, causing the metal alkoxide solution to gel. The gel is then applied onto the support layer, usually by dip-coating or spin-coating. The support layer is then dried, causing the gel to transform into a solid material, forming a thin and uniform layer.

3.1.4 Al_2O_3-CeO_2 Wash-Coating

In a typical synthesis, monolith blocks are cut down into a size of (2 cm* 2 cm), washed with distilled water, and kept in a muffle furnace at 500℃ to eliminate impurities present in the bare monoliths. As discussed above, using the sol-gel method, these samples are wash coated with a 10% CeO_2 + 90% AlOOH solution. To make the support solution, boehmite (PURALOX SBa 200, Sasol, Germany), urea (99.5, Merck, India), nitric acid (71 vol%, SDFCL, India) are mixed in a ratio of 2:1:5 M, and cerium (III) nitrate hexahydrate is added with continuous stirring for 5 h at room temperature. The bare monoliths are then washcoated with the support solution. Finally, the catalysts are calcined at 800℃ for 4 h in a muffle furnace, maintaining a heating rate of 2℃/min

3.1.5 Wet Impregnation

The wet impregnation method (WI) is commonly used for load nickel (Ni) onto cordierite monolith catalysts. In the WI method, a solution containing Ni ions is prepared, and the cordierite washcoated monolith immersed in it. The Ni ions are then adsorbed onto the surface of the cordierite, filling its pores. The monolith is then dried to remove the solvent, and the Ni ions are stabilized on the surface. After drying, the monolith is calcined at high temperatures to activate the Ni ions and convert them into NiO. The calcination process also removes any remaining solvent, water, or other impurities.

Wet impregnation has the benefit of being an easy and inexpensive process. It also allows for precise control over the amount of Ni loaded onto the cordierite monolith. This is important because the activity of the catalyst are highly dependent on the amount of Ni that is loaded. Another advantage of the wet impregnation method is that it allows for the preparation of homogeneous Ni distribution on the cordierite monolith. This is important because a homogeneous Ni distribution ensures that the cordierite's entire surface is active and contributes to the catalytic reaction.

However, there are some challenges associated with the wet impregnation method, however. One of the challenges is that the Ni ions may not fully penetrate the pores of the cordierite monolith, resulting in uneven Ni loading. This can lead to Ni particle sintering and low dispersion, resulting reduced catalytic activity Another challenge is that the Ni ions may not be properly stabilized on the cordierite surface. This can result in Ni loss or sintering during the calcination process, which will reduce the overall activity of the catalyst. To overcome these challenges, it is important to carefully control the conditions of the wet impregnation process, such as the concentration of Ni ions in the solution and the duration of immersion. Additionally, optimizing the calcination conditions, such as the temperature and calcination soaking time, is also important to ensure that the Ni ions are properly activated and stabilized on the cordierite surface.

3.1.6 Ni loading

An aqueous solution of $Ni(NO_3)_2.6H_2O$ (Merck, 99%, Germany) was prepared for performing impregnation. This solution was made by dissolving 29.1 grams of $Ni(NO_3)_2.6H_2O$ in 100 mL of deionized (DI) water, resulting in a 1 M solution. The process for loading the metal was similar to the wash coating procedure explained above. The calcined monoliths were then dipped in the solution for 10 seconds before being removed, and any excess liquid was shaken off. The monoliths were then placed placed horizontally in a microwave oven and dried at 110°C for one

hour, the dipping and drying procedure was repeated four times before the final calcination. After the final calcination (800 ^{o}C, ramp rate of 1 ^{o}C/min), the weight gain of the monoliths was observed to be around 14%.

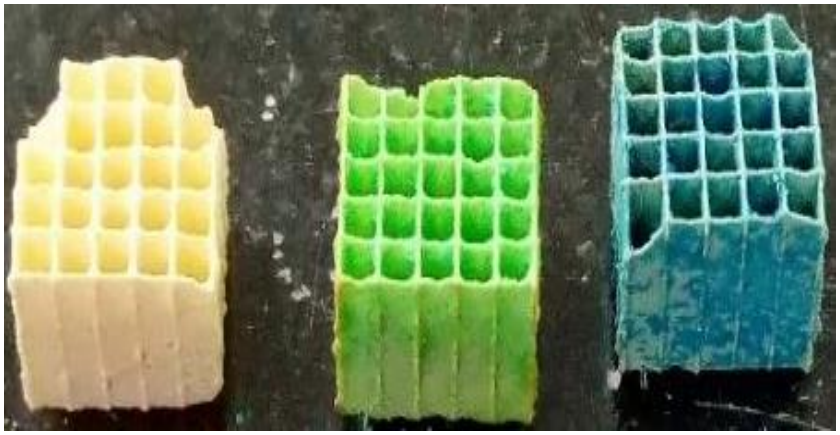

Fig.3. 1 Cordierite monolith images A) Wash coat, B) After Ni loading, and C) Calcined catalyst at 800 ℃

3.2 Powder catalyst

3.2.1 Citrate sol-gel

The citrate sol-gel method is a variation of the conventional sol-gel method, in which citric acid is used as a chelating agent to promote the formation of the gel-like structure. In the sol-gel method, the precursors are mixed with a solvating agent, such as water, to form a homogeneous solution. The solvating agent is then removed through evaporation, forming a gel-like structure. The citrate sol-gel method offers several advantages over the traditional sol-gel method. Firstly, citric acid is a strong chelating agent, which promotes the formation of a stable gel-like structure. Secondly, the polyesterification reaction between ethylene glycol and citric acid leads to the formation of a

continuous polymer network that enhances the mechanical stability of the gel. Finally, the citrate sol-gel method is more cost-effective and environmentally friendly than other conventional methods.

3.2.2 Perovskite catalysts

Perovskite powders (ABO_3: A = La and Ba, B = Al and Ni) are prepared using citrate sol-gel synthesis, as shown in Fig 3.2 [228,229]. To synthesize of A-site deficient perovskite oxide catalysts, $La_{0.9-x}Ba_xAl_{0.85}Ni_{0.15}O_3$, the citrate sol-gel method. In this process, precursors such as lanthanum nitrate hexahydrate, aluminium nitrate nonahydrate, barium nitrate, and nickel nitrate hexahydrate are dissolved in deionized water and mixed with citric acid monohydrate and ethylene glycol in a 1:2 ratio of metal nitrates to citric acid and ethylene glycol. The combination of metal nitrates, citrate, and the chelating agent ethylene glycol is vigorously stirred at 55°C until it forms a gel-like consistency. This gel is then dried at 110 °C overnight and heated at 300°C for 1 hour. The heating process initiates the polyesterification reaction between ethylene glycol and citric acid, which forms a continuous polymer network. The resulting xerogel is then pressed into powder form and calcined at 850°C for 7 hours using a programmable muffle furnace. The heating rate during the calcination process is set at 2°C per minute [230–232].

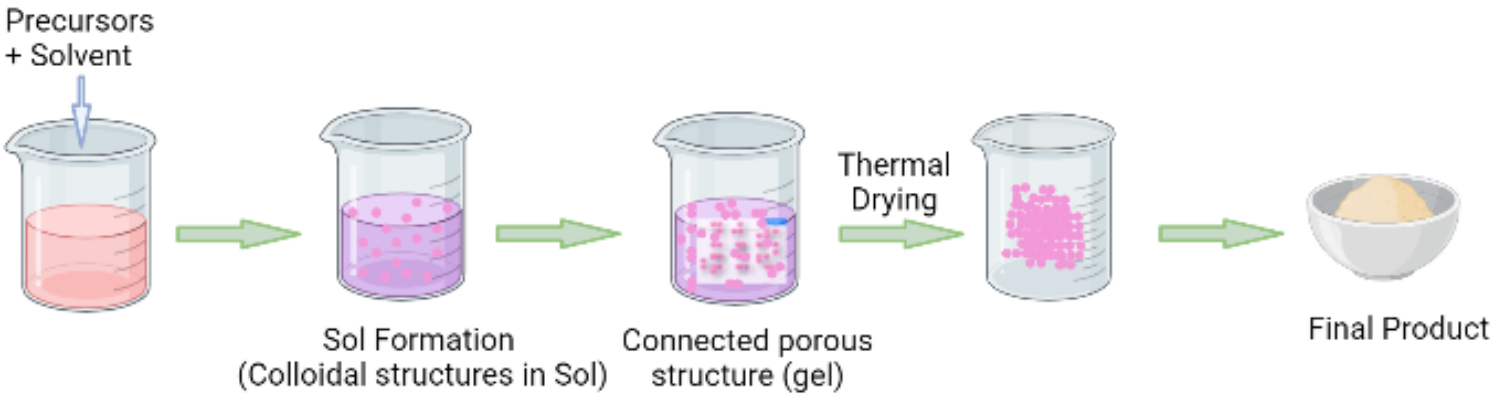

Fig.3. 2 Schematic representation of different stages of citrate sol-gel process [233,234]

3.3 Physicochemical characterization

3.3.1 FTIR

FTIR is a versatile technique that can be applied to various samples, including solids, liquids, and gases. This technique exposes the sample to an infrared beam and measures the resulting absorption or emission spectrum, providing valuable insights into the vibrational modes of the sample's molecules. When combined with other analytical techniques, FTIR spectra can help a gain comprehensive understanding of the properties and behaviour of materials.

The functional groups present in the prepared samples are identified by Fourier-transform infrared spectroscopy spectra (Perkin Elmer Frontier ^{TM}) of calcined samples with KBr and recorded from 400 cm^{-1} to 4000 cm^{-1}. To prepare the samples for analysis, it is mixed with KBr (potassium bromide) and then ground into a fine powder to form a homogenous mixture. The resulting mixture is then pressed into a pellet, which is transparent to infrared radiation, and placed in the FTIR spectrometer for analysis. KBr is used as the matrix material in FTIR analysis because

it is a good IR transparent material and does not interfere with the infrared spectra of the sample. Additionally, KBr is chemically stable, readily available, and relatively inexpensive, making it a convenient choice for FTIR analysis.

3.3.2 XRD

The crystal phase and structure of the prepared catalysts are identified using X-ray diffraction (Rigaku miniflex II, CuKα, λ = 0.154 nm, 30 Kv, and 15 mA) from 20 to 80 degrees at a scan speed of 2 degree/min. X-ray powder diffraction (XRD) is a non-destructive analytical technique that determines the crystalline structure of a material by measuring the diffraction patterns produced by X-rays when they interact with the sample. XRD is widely used in material science, particularly for identifying and characterizing the phase of powder samples. In the context of catalysts, XRD is used to determine the catalytic material's phase purity and particle size, which are crucial factors in determining its catalytic activity and stability. In XRD, a collimated beam of X-rays is directed to a powdered sample, which is typically mounted on a sample holder. As the X-rays pass through the sample, they interact with the atoms in the crystal lattice, producing diffracted X-rays. These diffracted X-rays form a unique pattern to the crystal structure of the material and its lattice parameters, such as the unit cell dimensions. This pattern can be captured by a detector, typically a scintillation counter or an imaging plate, and the resulting data can be analyzed to determine the crystalline structure of the sample.

The XRD pattern produced by the sample provides information on the crystal structure of the material and it can be compared to reference patterns in a database, such as the Joint Committee on Powder Diffraction Standards (JCPDS), to identify the phases present in the sample. This information is crucial in determining the composition and purity of the catalytic material and in understanding how the material will behave under different conditions. In addition to phase

identification, XRD can also be used to estimate the particle size of a powder sample. The particle size can be estimated from the width of the diffraction peaks in the XRD pattern, which results from the interference of X-rays diffracted by different regions of the crystal lattice. The broader the peaks, the larger the particle size, and vice versa. The Scherrer formula is commonly used to estimate the particle size. This formula relates the width of the diffraction peak, the crystallite size, and the X-ray wavelength. The formula is given as:

$D = K\lambda / \beta \cos \theta$……(3.1)

where

D is the crystallite size, K is a constant (0.9 to 1.0), λ is the X-ray wavelength, β is the full width at half maximum of the diffraction peak, and θ is the diffraction angle.

3.3.3 BET surface area

Brunauer-Emmett-Teller (BET) analysis is used to calculate the total surface area of the catalysts. BET analysis (Micrometrics ASAP 2020 analyzer) measures the specific surface area, which is the material's total surface area per unit mass. Another important factor that affects the surface area determined using BET analysis is the size and distribution of the pores in the material. Materials with large, well-defined pores will have a higher surface area than materials with small, randomly distributed pores. Therefore, the surface area determined using BET analysis will depend on the material's physical properties and the method used to prepare the sample. BET analysis is based on the physical adsorption of gas molecules on a solid surface and the relationship between the amount of adsorbed gas and the pressure of the adsorbing gas. The total surface area of a material can be determined by analyzing the amount of nitrogen adsorbed onto the surface at different pressures.

First, the sample is degassed to remove any trapped gas, and then a known volume of nitrogen gas is introduced into the sample chamber at low pressure. The pressure in the chamber is gradually increased, and the amount of nitrogen adsorbed onto the surface is measured. The resulting data is plotted as the amount of nitrogen adsorbed versus pressure, and the BET equation is used to fit the data and calculate the specific surface area.

3.3.4 Temperature Programmed Reduction

Temperature-programmed reduction (TPR) is used to determine the reduction temperature of catalyst samples. TPR provides valuable information regarding the interaction between the active metal and the support material, in addition to any significant findings regarding the interaction of the metal with other metals and the support. Higher reduction temperatures indicate more robust interactions between the metal and its support. The AutoChem II 2920 Micrometrics system is utilised for the TPR studies. The catalyst is placed in a quartz tube supported by quartz fibre. At a rate of 10 Celsius per minute, the catalyst is elevated to 200 °C. This temperature is maintained for one hour in an argon stream circulating at 30 ml/min to remove any absorbed moisture. The catalyst is cooled to 50 ℃ as the final step. After preparation, the catalyst is heated to 900 ℃ at a rise rate of 10 ℃/min in a mixture of 10% hydrogen and argon. A thermal conductivity detector is used to keep track of the amount of hydrogen that is consumed (TCD). TPR curves allow for the extraction of the following types of information:

1. The temperature at which the reduction peaks indicates the degree of interaction between the active metal and the support, as well as the ease of the metal reduction. The increased difficulty in reduction at higher reduction temperatures can can be attributed to the greater degree of interaction between the active metal and support.

2. Multiple peaks indicate the presence of the element metal on the support in a various forms,

each with a unique level of interaction with the support.

3.3.5 Temeprature Programmed Desorption

In the presence of acidic molecules such as CO_2, temperature-programmed desorption (TPD, Micromeritics AutoChem II, 2920) is typically used to measure the intensity of basic sites on the catalyst. Based on the desorption peak temperature in TPD, basic sites are classified as weak (200°C), medium (200–400°C), strong (400–600°C), and very strong (> 650°C). This classification is based on the intensity of the interaction between CO_2 molecules and the catalyst, with more basic sites favouring CO formation. The 100 mg samples were degassed at 300°C for 60 minutes in 40 ml min1 of He flow. The sample was then chilled to 50°C in He and the gas was replaced with 30 ml/min of 10%CO_2 in He for 30 minutes. The sample was then purged with He for 30 minutes by escalating the temperature to 100 °C at a rate of 1.3 °C per minute to remove the physisorbed CO_2. The sample was then heated at 10°C/min to 1000°C under He flow (40 ml/min) while the TCD signal for desorbed CO_2 was monitored [235–237].

3.3.6 Surface morphology

The surface morphology of the catalysts is studied using field emission scanning electron microscopy (FEM, Nova Nano FE-SEM 450, Oxford Instruments, UK) and Transmission electron microscopy (HR-TEM, Tecnai G2 20 S- Twin, FEI Netherlands. SEM scans the surface of a sample with a focused stream of electrons, producing signals that can be used to build high-resolution pictures and provide information on the sample's surface structure and composition. In contrast, transmission electron microscopy (TEM) involves sending an electron beam through a thin piece of the sample, allowing the observer to view the interior structure of the material. TEM images provide high-resolution images of the sample's internal structure and composition, allowing for assessment of particle size and shape. TEMs can magnify objects up to 2 million

times with enhanced resolution of 0.0001 μm, which is about one to two orders higher than the SEM. For SEM analysis, the powder sample is coated with a thin layer of conductive material, such as gold, to prevent charging during the analysis. This is typically done by sputtering the metal onto the sample in a vacuum chamber. In the case of TEM, analysis of powder samples is done by using copper grids which involves depositing a small amount of the powder sample onto a copper TEM grid. The copper grid provides support for the sample and acts as a conductor for the electron beam used for imaging.

3.3.7 Pulse chemisorption

Hydrogen pulse chemisorption (Micromeritics AutoChem II 2910) is performed to analyze the dispersion and particle size of active Ni on the fresh catalysts. The H_2 dose volume is maintained at 50 cm^3. This technique is used to determine the dispersion of active metal species in catalysts by measuring the adsorption of a probe molecule, such as CO or H_2, on the catalyst surface. The amount of adsorption is related to the dispersion of the active metal species in the catalyst. A highly dispersed catalyst will have a greater surface area for adsorption, resulting in a larger amount of adsorption. Conversely, a poorly dispersed catalyst will have a smaller surface area for adsorption, resulting in a smaller amount of adsorption. Pulse chemisorption is a valuable tool for characterizing catalysts because it provides information about the dispersion and surface area of the active species in the catalyst, which are important factors for catalytic performance. Additionally, pulse chemisorption can be used to study the reaction kinetics of the adsorption process, which can provide insight into the mechanism of catalytic reactions.

3.3.8 XPS

The X-ray photoelectron spectrometer (XPS, Thermo fisher scientific Pvt Ltd, UK) with a monochromatic Al Ka source operated at 200 W/12 KV, having a pass energy of 200 eV for the

high energy spectra was used to identify the elements, surface oxygen carriers, and valance states. The adventitious C (1s) at 284.5 eV was used as a reference for the charge correction of the spectra. XPS is a surface analysis technique that analyzes the binding energy of electrons in the outermost atomic layer of a material. XPS involves bombarding a material with X-rays, which causes electrons to be expelled from their atomic orbitals. The binding energy and atomic type of these expelled electrons are then determined by analysing them. XPS is frequently utilised in the surface characterization of catalysts because it offers information about the surface's composition, electrical structure, and chemical bonds. This knowledge is crucial for understanding catalysis's mechanisms, including surface species' function in catalytic reactions and the influence of surface composition on catalytic activity. XPS can also be used to identify chemical bonding status of surface species and investigate the oxidation and reduction processes that occur on the surface of catalysts.

3.3.9 TGA-DTA

Thermogravimetric and differential thermal analysis (SDTG, DTG-60 H, Shimadzu) in the presence of air (20 ml/min, 10 °C/min) are employed to determine the nature and quantity of carbon deposition on spent catalysts. TGA is a technique for measuring weight change as a function of temperature and is used to determine the quantity of carbon deposited on the surface of a catalyst. The sample is heated in a controlled environment, and the change in weight is recorded. Calculate the weight change caused by carbon deposition by subtracting the weight change caused by other factors, such as metal oxidation or support deformation. As a function of temperature, DTA determines the temperature difference between a sample and a reference. The DTA signal is recorded during the TGA measurement in TGA-DTA. The DTA signal can determine the temperature at which endothermic or exothermic reactions take place, such as the

thermal decomposition of carbon deposited on the surface of the catalyst. TGA-DTA analysis provides information regarding the quantity and thermal stability of carbon deposits on the surface of a catalyst.

3.3.10 Raman analysis

To determine the nature of carbon deposited on the exhausted catalyst surface, Raman spectra (Horiba LabRam HR spectrometer, Model 171) are collected in the range of 1000 to 2900 cm^{-1} using a 532 nm and 680 nm argon laser. Raman analysis is a spectroscopic method for determining the nature of carbon deposits on the surface of a spent catalyst. Raman analysis is based on the interaction of light with molecular bonds in a sample that is vibrating. When laser-generated light interacts with a sample, a portion of the light dissipates, producing a Raman spectrum. The Raman spectrum contains information regarding the sample's vibrational modes, which can be used to identify the chemical species present in the sample. Raman analysis can identify the type of carbon deposited on the catalyst surface in DRBG, including graphitic and amorphous carbon. This information is essential for comprehending the behaviour of the catalyst during the reaction and the effect of carbon deposition on the performance of the catalyst.

3.4 Activity Experiments

3.4.1 Monolith catalysts

The experimental setup for the DRBG for monolith catalysts is shown in Fig. 3.3. The DRBG is carried out using a tubular reactor made of Inconel, a high-temperature-resistant material, which is fitted inside a two-zone furnace with a maximum temperature of 1200°C and is controlled by temperature controllers. The furnace has a preheater and a temperature-maintaining zone to prevent condensation. The catalytic bed is monitored by four K-type thermocouples placed at the top and bottom of the reactor and in the furnace zone. A condenser and gas-liquid separator are

also present at the bottom of the reactor to separate any water produced during the reaction. The Ni-loaded monolith is fixed between two bare monoliths and placed in the reactor's middle portion. Before starting the experiment, gas leak tests are conducted, and the reactor is heated to 800°C over three hours with a flow of N_2 at a rate of 20 ml/min. The Ni-loaded catalyst is then reduced in pure H_2 for 13 hours at 800°C with a flow rate of 40 ml/min. After reduction, the flow of H_2 is stopped, and a mixture of pure CH_4 and CO_2 in different ratios with 50% N_2 dilution is fed to the reactor. The gas mixture is heated to 200°C in the preheater before entering the reactor.

3.4.2 Powdered catalysts

The catalyst activity methodology for perovskite catalysts is similar to that for monolith catalysts, with the exception of reactor used. a quartz tube with 66 cm in length and has an internal diameter of 8 mm is used as a reactor instead of inconel tube and operates at atmospheric pressure. The catalyst particles, weighing 300 mg, are mixed with quartz beads of diameter 1 mm to 2 mm in a ratio of 1:2 (powder to quartz beads). The mixture is loaded into the center of the reactor, creating a catalyst bed 50 mm in length, which is supported at the both ends by quartz wool. The flow rate of the gases, which consists of a mixture of CH_4+CO_2/N_2 in a 1:2 ratio, is kept constant at 120 ml/min. The Weight Hourly Space Velocity (WHSV), is maintained at 24 m^3/(h. kg catalyst) throughout the experiments.

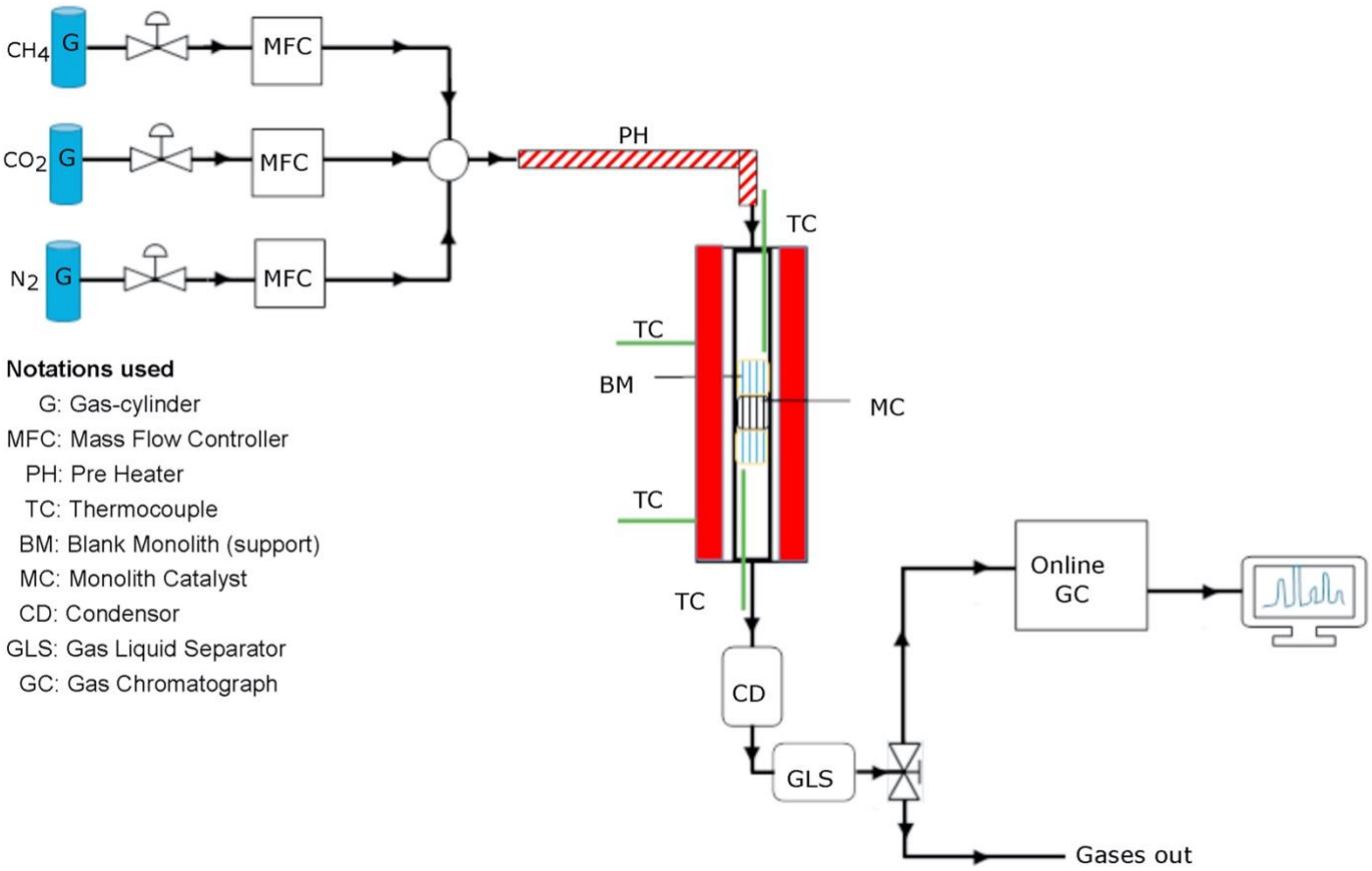

Fig.3. 3 Schematic representation of experimental setup for dry reforming of biogas.

3.4.3 Mass flow controllers

Mass flow controllers (MFCs) are used in a reactor system to control the flow of gases into the reactor. This system has five MFCs, with three from Bronkhorst High Tech and the other by Aalborg. The gases are introduced into the reactor through 1/8-inch lines, with a non-return valve installed on each line to prevent backflow due to pressure build-up within the reactor. Pressure gauges are also installed on each gas line to monitor the pressure levels.

Before starting any reactions, the MFCs must be calibrated to ensure accurate flow control of the respective gases. The flow rate value of each MFC ranges from 0-200 ml/min. It is important to

have accurate control over the flow of gases into the reactor to ensure proper and safe reactions. MFCs in this system allow for precise control of gas flow, ensuring that the desired amounts of gases are introduced into the reactor at the appropriate times. The non-return valves and pressure gauges provide additional safety measures, helping to prevent any potential issues from arising due to pressure build-up within the reactor.

3.4.4 MFC calibration

Calibrating mass flow controllers involves determining the desired flow rate range for a specific reaction. A digital gas meter is used to measure the gas flow rate. By measuring the actual flow rates at the outlet of the MFCs with digital meter, a calibration curve is generated for each gas and MFC. This curve establishes a correlation to ensure the reaction's accurate and consistent flow of gases. The calibration process is crucial to ensuring that the MFCs function within the required range and provide the correct flow of gases for the desired reaction. The MFC calibration of N_2, CH_4, CO_2 , H_2 and CO is calculated based on following equation

$y = mx+C$…….(3.2)

Where

Y = actual MFC value

X= set point

M and C are constants varies depends on the gas

Table.3. 1The constants used for the calibration of MFC

Gas	M value	C value
N_2	1.1676	-3.7905
CH_4	1.27	1.6
CO_2	0.68	-5.87
H_2	1.04	-18.36
CO	0.855	-3.2

3.4.5 GC calibration

Gas chromatography (GC) calibrations are essential to ensuring accurate and reliable results in activity results. Various concentrations of specific gases and nitrogen mixtures are utilized to perform the calibrations. A constant flow rate of 100 ml/min is maintained throughout the process to ensure consistency. The calibration process involves generating response factors for all the gases being analyzed. Response factors are calculated from the chromatographs obtained from the GC analysis. In the example of CH_4, the areas of different compositions of CH_4 and N_2 mixtures are measured from the chromatographs. The response factor is then calculated based on the relationship between the measured areas and the concentrations of CH_4 and N_2. The importance of GC calibrations lies in the accuracy of the results obtained from the analysis. Calibrations ensure that the GC instrument is functioning correctly and the instrument's response to specific gases and mixtures is known. This knowledge is then used to accurately interpret the results of the analysis. The GC calibrations are performed regularly to maintain the instrument's accuracy and ensure reliable results. Any changes in the instrument's performance can be detected and corrected, leading to improved accuracy and precision of the results.

The response factor of each gas denoted as beta is calculated as follows

$$\beta_{CH_4} = \frac{molefraction\ of\ CH_4/molefraction\ of\ N_2}{Peak\ Area\ of CH_4/Peak\ of N_2} \ldots(3.3)$$

$$\beta_{CO_2} = \frac{molefraction\ of\ CO_2/molefraction\ of\ N_2}{Peak\ Area\ of CO_2/Peak\ of N_2} \ldots(3.4)$$

$$\beta_{H_2} = \frac{molefraction\ of\ H_2/molefraction\ of\ N_2}{Peak\ Area\ of H_2/Peak\ of N_2} \ldots(3.5)$$

$$\beta_{CO} = \frac{molefraction\ of\ CO/molefraction\ of\ N_2}{Peak\ Area\ of CO/Peak\ of N_2} \ldots(3.6)$$

Table.3. 2 The response factor value of Individual gases

Gas species	Response factor
CH_4	0.3269
CO_2	1.2166
H_2	0.098
CO	0.9259

The outlet moles of the gas is calculated using the formula

$$n_{CH_4} = \beta_{CH_4} * \left(Peak\ area\ of \frac{CH_4}{Peak} area\ of N_2\right) * inlet\ moles\ of\ N_2 \ldots(3.7)$$

The conversions of CH_4, CO_2, molefractions of H_2 and CO, and H_2/CO ratio are calculated using the formulas as follows

$$CH_4 \text{conversion}, (\%) = \frac{\text{Inlet moles of } CH_4 - \text{Outlet moles of } CH_4}{\text{Inlet moles of } CH_4} * 100 \ldots (3.8)$$

$$CO_2 \text{conversion}, (\%) = \frac{\text{Inlet moles of } CO_2 - \text{Outlet moles of } CO_2}{\text{Inlet moles of } CO_2} * 100 \ldots (3.9)$$

$$H_2 \text{ molefraction} = \frac{\text{out let moles of} H_2}{\text{Total moles}} \ldots . (3.10)$$

$$CO \text{ molefraction} = \frac{\text{out let moles of} CO}{\text{Total moles}} \ldots . (3.11)$$

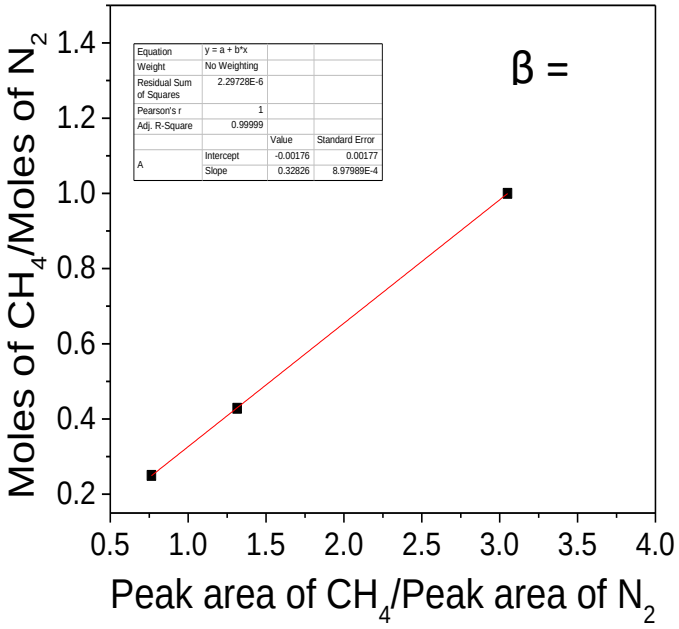

Fig.3. 4 Linear relation between peak area of CH_4/peak area of N_2 versus moles of CH_4/moles of N_2

3.4.6 GC analysis

The reactor exhaust is a mixture of hydrogen and carbon monoxide (product gases), unreacted methane and carbon dioxide, and nitrogen (inert gas). This gas mixture is analyzed using an online GC-2014 (Shimadzu) system, equipped with a thermal conductivity detector (TCD) and a gas sampling valve (MGS-5). The GC system has three sample volume options: 1 ml, 2 ml, and 5 ml. In the current study, a 1 ml sample loop was used throughout. The gas sample is manually injected into the system through the MGS-5. To separate the different components of the gas mixture, a ShinCarbon ST packed column is used. Argon is used as the carrier gas in the GC system. The temperature of the injector port, column, and TCD are maintained at 100°C, 70°C, and 150°C, respectively. The TCD operates with a current of 60 mA. The outlet gas sample is analysed for every 20 minutes, with a GC runtime of 18 minutes. The typical gas peaks appear in the GC chromatgram are displayed in the figure 3.5

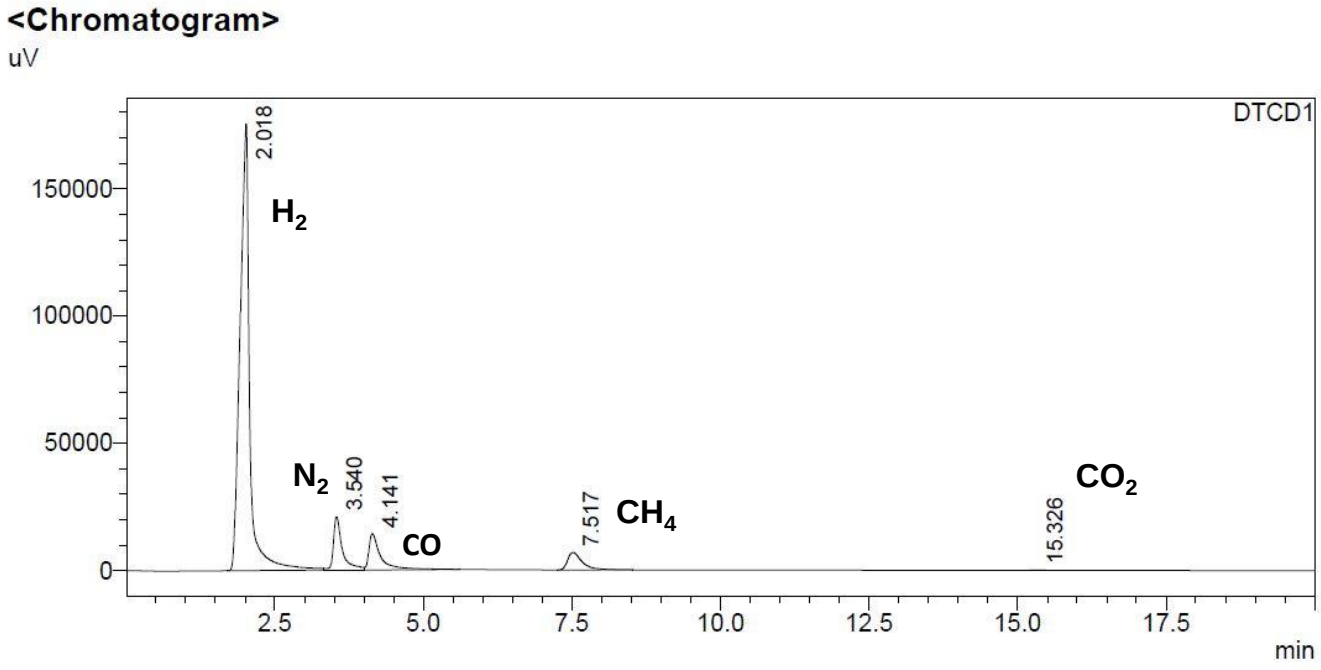

Fig.3. 5 Chromatogram for DRBG analysis

3.5 Summary

The study aims to prepare catalysts for the dry reforming of biogas using sol-gel and wet impregnation methods. Ni-based cordierite catalysts are prepared using the sol-gel method followed by wet impregnation. The citrate sol-gel method is used to prepare perovskite oxide catalysts. These catalysts are characterized to determine their structural and chemical properties before and after the stability experiments of dry reforming of biogas. Techniques such as X-ray diffraction (XRD), Scanning Electron Microscopy (SEM), and BET surface area analysis are used to characterize the monoliths and perovskite catalysts. These techniques help determine the catalysts' crystal structure, surface morphology, and pore structure. Additionally, the chemical composition and distribution of the active catalyst species are also analyzed using techniques such as Energy Dispersive X-ray Spectroscopy (EDS) and X-ray Photoelectron Spectroscopy (XPS). In conclusion, the catalysts are prepared and characterized to understand their properties and suitability for dry reforming of biogas. The results obtained from the characterization techniques provide valuable insights into the structure and composition of the catalysts, which are crucial for understanding their performance in the dry reforming of biogas. The entire thesis is dedicated to the preparation, characterization, and evaluation of these catalysts for the dry reforming of biogas.

Chapter-4

4 Catalytic Activity of Ni/γAl_2O_3 Cordierite Monolith for Dry Reforming of Biogas

4.1 Introduction

This chapter discusses the catalytic activity of Ni/γAl_2O_3 cordierite catalysts calcined at 800℃ for 4 h, 10 h and 20 h. Also, the variation in catalyst morphology due to high-temperature calcination and diffusion of elements such as Si, Al, and Mg from the cordierite surface to the alumina coating was extensively investigated. Various characterization techniques were performed to understand the activity results, including XRD, TPR, Pulse chem, FESEM, TEM, TGA-DTA and Raman analysis are used to comprehend the phase composition, particle size, catalysts-support interaction, microstructure, porosity, particle size and dispersion of the active metal, carbon deposition, and elemental composition of the fresh, reduced and spent catalysts. Activity experiments were performed for CH_4/CO_2 feed ratios; 1.0, 1.5 and 2.0 at 800 ℃.

4.2 Experimental details

4.2.1 Catalyst preparation

The preparation of Ni-loaded monoliths was carried out by a two-step process [238], including the dip coating and calcination of the bare monoliths, followed by the wet impregnation of Ni metal, as discussed in chapter 3. The coated monoliths were then calcined at 800°C for 4, 10, and 20 hours, respectively. The final samples were named C-4, C-10, and C-20, representing the calcination time of 4, 10, and 20 hours, respectively.

4.2.2 Physicochemical characterisation of catalysts

Powder samples were collected by mechanically scraping the surface of the calcined, reduced, and spent monolith catalysts. X-ray diffraction was performed to identify the crystallinity and phase composition of the samples, while the temperature-programmed reduction was performed to study the metal-support interaction. Raman spectra were acquired to understand the nature of carbon deposited on the catalyst after 1 hour of reforming reaction. Thermogravimetric and differential thermal analysis were performed to determine the nature and amount of carbon accumulated on the spent catalysts. Hydrogen pulse chemisorption was performed to analyse the dispersion and particle size of active Ni on the fresh catalysts. The samples' morphology, size, and elemental distribution were studied through field emission scanning electron microscopy and high-resolution transmission electron microscopy. Particle size distribution was calculated through ImageJ analysis software.

4.2.3 Catalytic activity experiments

The monolith catalyst, wrapped with glass cotton, was put between two blank monoliths, and inserted in the middle of the reactor. Before the catalytic activity study, the catalysts are reduced by flowing (15 ml/min) hydrogen at 800℃ for 13 h. A dry reforming reaction is carried out at 800℃ under atmospheric pressure with various CH_4/CO_2 feed ratios; 1.0, 1.5 and 2.0. A condenser is used to cool the effluent gas from the reactor, and the composition of the effluent gas is analysed by using online gas chromatography (GC 2014, Shimadzu) equipped with a TCD detector every 20 min.

4.3 Results and discussion

4.3.1 XRD analysis

XRD patterns indicate the presence of multi-phase oxides in the calcined samples C-4, C-10 and C-20 (Fig 4.1(a)). The strongest peaks, mostly at 2θ 15-35°, are detected from cordierite $Al_4Mg_2O_{18}Si_5$ (PDF -9006272). The peaks at 37.3 and 43.4°could are indexed as NiO (PDF-1010095). The peaks at 37°, 45°, 59.6° and 65.5° indicate the presence of $NiAl_2O_4$ (PDF -9001432) and the intensities of these peaks are observed to be maximum for the C-20 sample, implying the increase of $NiAl_2O_4$ phase amount with calcination time. The peaks at 41.6 and 62.1° correspond to the MgO (PDF-1000053) phase. The broad peaks at 37°, 38.7°, 44°, 46.5°, 54° and 67.4° may correspond to the polycrystalline $MgAl_2O_4$ (PDF-1533155) powder. Although the 100% peak of γ-Al_2O_3 (43.4°; PDF-1000059) overlapped with a NiO peak, the next strongest one (90%, at 57.6°) is visible for all calcined catalysts. Some $NiAl_2O_4$ (two most intense peaks at 37° and 65.5°) and $MgAl_2O_4$ (peaks at 37°, 44°, 46.5°, 54° and 67.4°) phases are observed in the reduced samples (Fig 4.1 (b)). Little Mg might be present (100% peak at ~ 37.1°), but this peak overlaps with the 100% $NiAl_2O_4$ and $MgAl_2O_4$ peaks. γ-Al_2O_3 phase is present (peaks at 43.4, 57.6 and 66.6°). Two peaks at 44.1 and 51.4° depict the presence of metallic nickel. These two peaks, full-width half maxima (FWHM), are broadest for the C-20 sample and sequentially narrowed down in the C-10 and C-4 samples, respectively. The average Ni crystal size calculated by the Scherer equation is found to be 31, 27 and 21 nm for the reduced C-4, C-10, and C-20 samples, respectively, shown in Table 4.1.

The γ-Al_2O_3 peaks are relatively stronger in the XRD profile (Fig 4.1 (c)) of the spent catalysts (peaks at 43.4°, 57.6° and 66.6°) after 1 h of catalytic activity study for the CH_4/CO_2=1.5.

Additionally, $NiAl_2O_4$ and $MgAl_2O_4$ phases also reveal. The metallic Ni peaks remain. The graphitic carbon peak (PDF-751621) could be present at 26.4° (0 0 2); however, that would overlap with the cordierite peak (0 2 4) as reported by other researchers [239–242]. In the literature, overlapping of Al_2O_3 with $NiAl_2O_4$ and NiO with MgO for Ni/γ-Al_2O_3, Ni-Ru/γ-Al_2O_3 and Ni-Co/MgO on cordierite monolith catalysts are reported [129,130,240]. Goyal et al. prepared Ni (12 wt%)/Al_2O_3 cordierite monolith catalysts using solution coating and wet impregnation method, followed by calcination at 500°C in synthetic air (both after Al_2O_3 and Ni loading) for 5 h and reduction at 600 C for 1 h. Both cordierite (between 20 and 35°) and Al-Mg spinel (relatively weak, at 37°, 46.5°, 54°, and 67.4°) peaks are detected for the blank monolith. Leftover NiO with metallic Ni is observed for the reduced catalysts, while metallic Ni is also perceived in the spent catalysts [243]. Wang et al. report the presence of NiO-MgO solid solution and Ni with the cordierite phase for a fresh NiO (8.7 wt%) - MgO (4.3 wt%)/γ-Al_2O_3 cordierite monolith catalyst. The catalysts are prepared by solution coating and wet impregnation method and calcined at 750°C for 10 h (for support) followed by calcination at 750°C after the metal loading [85].

4.3.2 BET analysis

The BET surface area (Table 4.1) of calcined catalysts is 16, 28, and 33 m^2/g for C-4, C-10, and C-20, respectively. For reduced samples, the BET surface area is 13, 16, and 17 m^2/g for R-4, R-10, and R-20, respectively. The results trend is in the same line as the surface area values calculated from the average particle size obtained from FESEM images. However, it is essential to mention that the catalyst powders scrapped from the monolith contain some cordierite phase. Due to that, the absolute values of surface area and other BET results cannot possibly present the real feature of the Ni/γ-Al_2O_3 catalysts and are hence inconclusive.

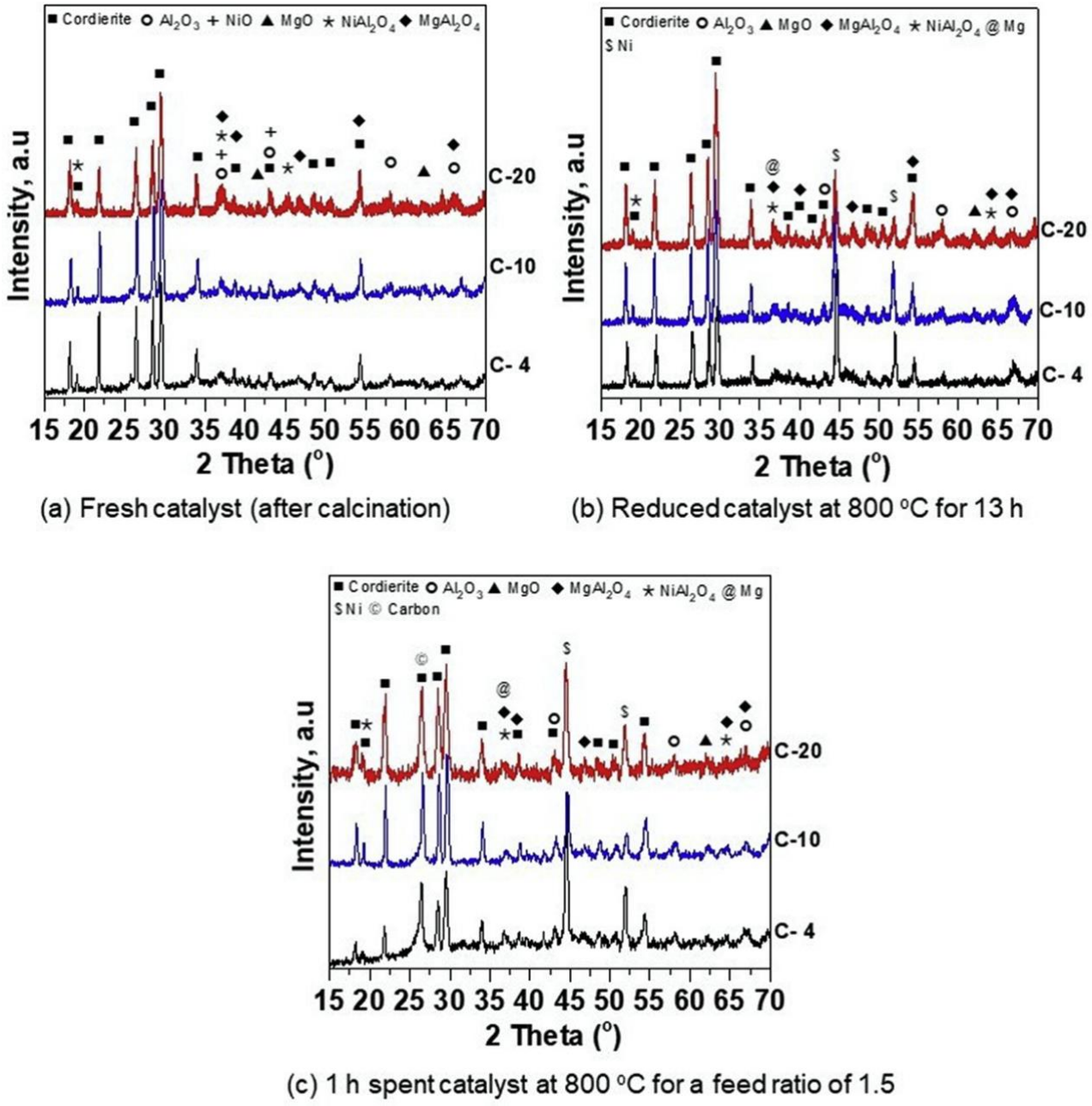

Fig.4. 1 XRD Profiles of the Ni/γ-Al_2O_3 based cordierite monolith catalysts C-4, C-10, and C-20 at different stages.

Table 4. 1 BET & FESEM surface area of calcined and reduced catalyst samples

Catalyst sample	BET surface area (m^2/g)	Surface area from SEM analysis , m^2	Pore volume (cm^3/g)	Avg. pore size (nm)
C-4	16.0	22	0.04	11
C-10	28.0	28	0.055	8
C-20	33.0	70	0.06	7
R-4	13.0	19	0.045	13
R-10	16.0	26	0.05	13
R-20	17.0	52	0.055	14

4.3.3 TPR analysis

Figure 4.2 shows the TPR profiles of the samples. In the case of C-4 and C-10 samples, the three reduction peaks at around 190, 215 and 405^{o}C correspond to easily reducible loosely bonded NiO with the alumina support [244]. The TPR peaks observed at 190, and 220℃ can be attributed to the reduction of free NiO or Ni_2O_3 species, and similar low-temperature peaks were reported by Usman et al. [241] for (80%) Ni/MgO catalyst. For the C-20 sample, two relatively smaller reduction peaks detected at around 350 and 430 ℃ could be related to the loosely bound NiO particles located on the support, whereas a large reduction peak at 785 ℃, resembles a strong interaction of small NiO particles with the support due to formation of (Ni-Mg)Al_xO_4 complex structure [245]. Luisetto et al. report a single TPR peak at 750℃ for a Ni (10 wt %)/Al_2O_3 cordierite monolith catalyst prepared by using a solution coating method for alumina loading followed by calcination at 600 ℃ for 5 h in air and then a wet impregnation method for Ni loading

followed by calcination at 450 ℃ for 2 h in the air [130]. Brussino et al. observe both lower (334 ℃) and higher (770 ℃) temperature TPR peaks for a Ni (20 wt%)/Al_2O_3 cordierite monolith catalyst prepared by using solution coating and wet impregnation methods for Al_2O_3 and Ni loading, respectively. The monolith is calcined at 550 ℃ for 2 h after each loading step [246]. Ciambelli et al. reveal two peaks at around 470 and 900 ℃ for a Ni (9 wt%)/CeO_2-Al_2O_3 cordierite monolith catalyst prepared using solution coating and wet impregnation methods for Al_2O_3 and Ni loading, respectively. The monolith is calcined at 1000 ℃ for 1 h after each loading step [240]. Goyal et al. detects two TPR peaks at around 350 and 630 ℃ for the Ni (12 wt%)/Al_2O_3 cordierite monolith catalyst [243].

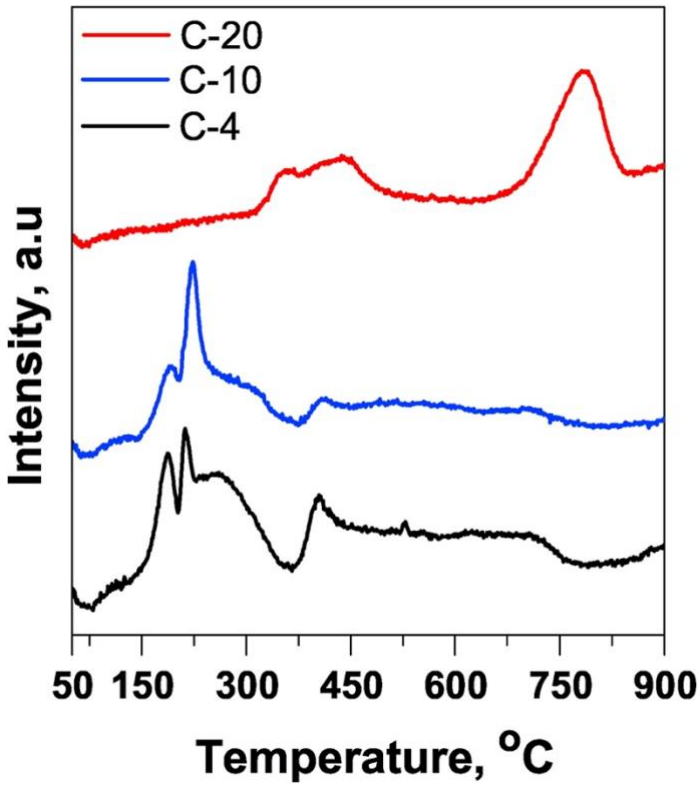

Fig.4. 2 TPR profiles of the Ni/γ-Al_2O_3 based cordierite monolith catalyst.

4.3.4 FESEM and TEM analysis

The calcination time influences the particle morphology & size distribution, and elemental distribution of the catalysts significantly as obtained from the plan view FESEM images of the coatings (Fig.4.3). While all catalysts consist of equiaxed particles, the fresh C-20 powder shows a homogeneous, narrow and monomodal distribution of the particles with average size 19 nm. However, for the fresh C-4 and C-10 samples, relatively heterogeneous and border range particle size distribution (average at 60 and 48 nm, respectively) is clear from Table 4. 2.

Interestingly, the amount of Mg and Si on the coating surface is higher in the C-20 sample compared to C-4 and C-10. The opposite trend is observed for Ni, higher in the C-4 and C-10 samples than in the C-20 samples (Fig 4.3.a). Although the morphology of the particles did not change after reduction, the average particle size increased for the catalysts due to agglomeration (Fig. 4.3.b). The elemental distribution follows the same trend as the calcined catalyst; however, the amount of Mg and Si is relatively higher. Zhou et al. [100] reported a Ni particle size of 21 nm for Ni/ Al_2O_3 catalyst calcined at 900 ℃ for 5 h and reduced at 1100 ℃ for 1 h. In this study, the average particle size of the catalysts does not change much even after 40 h reforming on the stream, irrespective of the feed ratio.

Table 4. 2Physiochemical properties of both calcined and reduced Ni-based monolith catalysts.

Catalyst sample	Dispersion (%)[a]	Metallic surface-area (m^2/g.metal)[a]	Nickel particle dia (nm)[a]	Avg.Ni particle size (nm)[b]	Ni particle size (nm)[c]	Avg.particle size (nm)[d]
C-4	-	-	-	-	-	61
C-10	-	-	-	-	-	48
C-20	-	-	-	-	-	19
R-4	1.5	10	60	35	31	68
R-10	2.0	13.4	45	33	27	51
R-20	13	86.2	7	11	21	25

[a] Calculated from H_2 pulse chemisorption.

[b] Calculated from TEM analysis.

[c] Calculated by Scherrer equation from XRD

[d] Calculated from SEM analysis.

Fig. 4.3.c shows the formation of carbon nanotubes on the spent catalysts after 1 h reaction time with CH_4/CO_2 = 1.5. The spent catalyst C-4 and C-10 follows a tip-growth mechanism, whereas C-20 follows a base-growth mechanism because of the strong metal support interaction. For the C-20 sample amount of C-deposition is less than that of the C-4 and C-10 catalysts. Elemental mapping shows the presence of Ni and Mg on the surface of the C- nanotubes for the C-20 catalyst. However, interestingly Maximum Ni is on the C-20 sample. A similar base-growth carbon mechanism was reported by various researchers [247]. For instance, Luisetto et al. observed a base-growth mechanism in the case of strong metal-support interaction and observed a tip-growth mechanism for metal-support interactions on Mono Ni and Ni/γ -Al_2O_3 monolith catalyst used in dry reforming of methane at 800°C (CH_4/CO_2 = 1.0) [130]. Table 4.3.summarises the elemental distribution on the coating surface of the calcined, reduced and spent samples analysed by EDX.

The diffusion of Mg or Si in the active wash coat has not been reported or discussed for the Ni/γ-Al_2O_3 cordierite monolith catalyst systems.

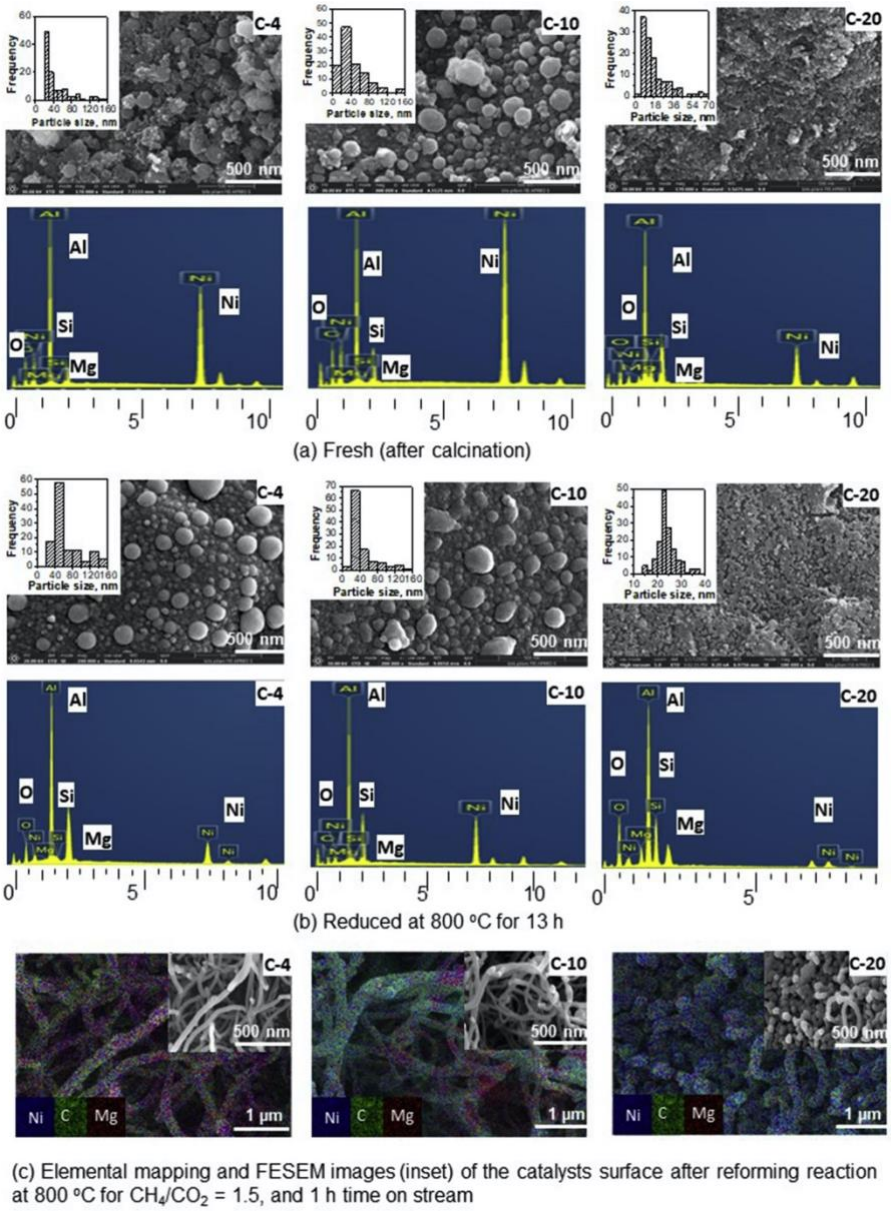

Fig.4. 3FESEM images with particle size distribution (inset images) and EDX spectrums of the surface of the Ni/γ-Al_2O_3 based cordierite monolith catalyst coatings C-4, C-10, and C-20 at different stages.

The cross-sectional FESEM images (Fig 4.4) reveal the average thickness of the fresh active wash coat layers, approximately to be 28 to 30 mm, which is comparable with the coating thickness reported earlier for the fresh Ni (10 wt%)/γ-Al_2O_3 monolith catalyst and could be considered as standard [130]. The EDX spectrum acquired at four different spots along the thickness of the coating (as shown in Fig 4.4) indicates the exponential decrease of Mg and Si concentration from the monolith wall towards the surface. Whereas the concentration of Ni shows the opposite trend, decreasing from the coating surface towards the monolith wall. The maximum near-surface concentrations of Mg and Si elements, 1.33 and 6.36 wt%, respectively, are observed for the C-20 sample. The minimum near-surface concentration of Si is measured to be 0.44 wt% for the fresh C-4 catalyst, but no Mg could be detected.

Table 4. 3 Elemental distribution on the coating surfaces of the calcined, reduced and spent samples analysed by EDX

Element (wt%)	Fresh catalysts			Reduced catalysts			Spent catalysts (1 h CH_4/CO_2 = 1.5)		
	C-4	C-10	C-20	C-4	C-10	C-20	C-4	C-10	C-20
O	22.3	28.8	43.9	17.31	22.34	28.7	-	-	6.47
Mg	0.02	0.3	1.1	0.11	0.8	3.25	0.14	1.04	3.78
Al	41	39.3	34.3	50.3	52.3	49.4	-	-	10.3
Si	0.4	2.13	6.1	0.76	3.02	8.2	0.93	3.76	8.94
Ni	36.3	29.5	14.6	31.5	21.54	10.42	2.93	4.2	9.5
C	-	-	-	-	-	-	96	91	61

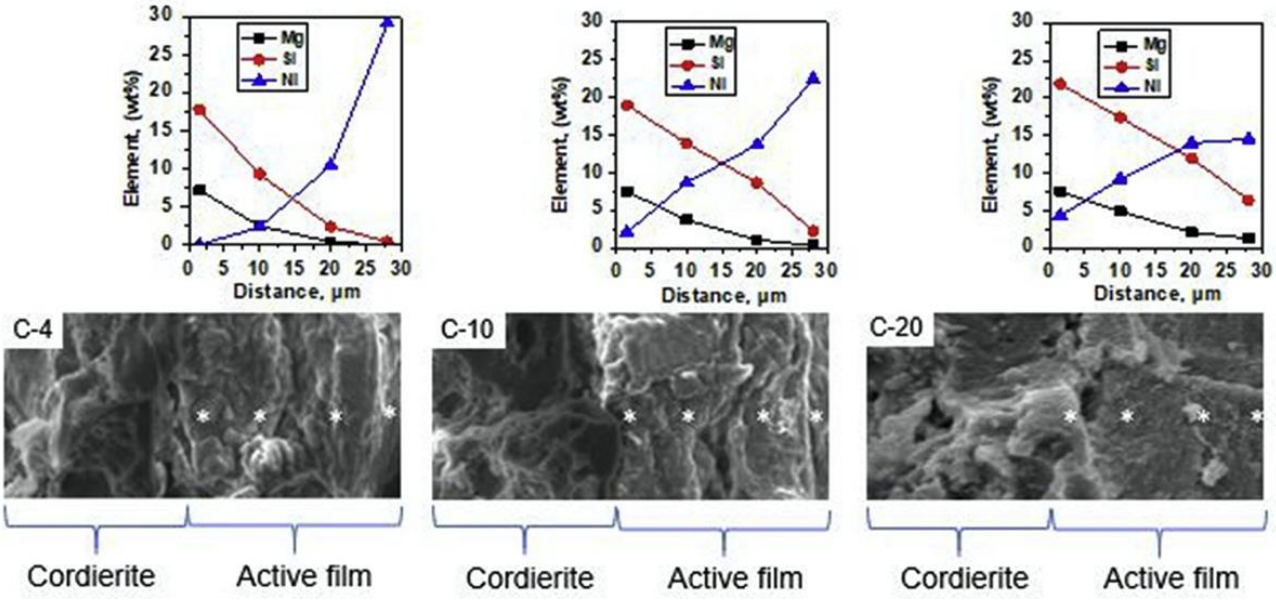

Fig.4. 4 Cross-sectional FESEM images showing the variation of concentration of Mg, Si and Ni from the cordierite (monolith) wall to the Ni-loaded wash coat for the calcined catalysts. The tentative analysis positions are shown by '⋆'.

The bright-field TEM images of the powders (Fig 4.5) depict the average Ni particle size of the reduced catalysts to be 35, 33 and 11 nm, respectively, for the C-4, C-10, and C-20 catalyst powders. This follows the same trend of Ni crystallite sizes calculated from the XRD data (Table 4.2). Villegas et al. report the Ni particle size of around 20 nm for the reduced Ni (5 wt %)/Al_2O_3 cordierite monolith catalyst prepared by using solution coating (for the Al_2O_3 wash coat) and wet impregnation (after Ni loading) methods. The catalyst is calcined at 800°C for 4 h after alumina wash coat loading, calcined at 550°C for 4 h after Ni loading, and finally reduced at 650°C for 1 h in the presence of H_2 [248].

4.3.5 Pulse chemisorption

Pulse chemisorption was performed to determine the reduced catalysts' dispersion and active surface area. The metallic dispersion and the corresponding active metal particle size are calculated to be 1.5, 2.0 & 13%, and 60, 45, &7 nm for the C-4, C-10 and C-20 catalysts, respectively, from the pulse chemisorption data. The amount of metallic Ni per gm of reduced catalyst is calculated to be 0.0008, 0.001, and 0.007 g for C-4, C-10, and C-20 catalysts, respectively. Accordingly, the active metal surface area is 10, 13.4 and 86.2 m^2/g for the C-4, C-10 and C-20 catalysts, respectively (Table 4.2).

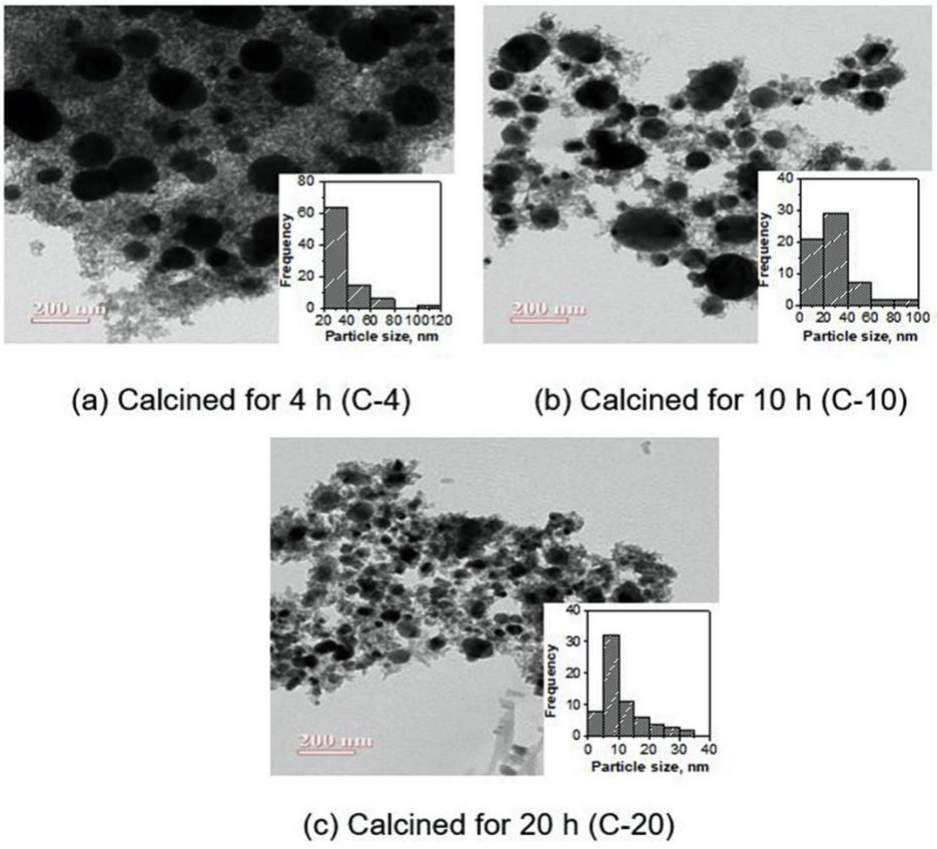

Fig.4. 5 Bright field TEM images and particle size distribution (inset images) of the Ni/γ-Al_2O_3 based cordierite monolith catalysts reduced at 800℃ for 13 h.

4.3.6 Raman analysis

Raman spectra of the spent catalysts for CH_4/CO_2 = 1.5 ratio (Fig. 4.6) show three peaks. The first one at 1350 cm^{-1} corresponds to Band D (represents structural defects or im- perfections in graphitic carbon), and the other one at 1570 cm^{-1} resembles Band G (planar vibrations in graphitic materials), while the G0-band at 2600 cm^{-1} specifies the presence of carbon nanotubes [249,250]. The ratio of the intensity of D and G bands, I_D/I_G, signifies the nature of graphitic carbon formed on the catalyst surface. In the case of the spent C-20 catalyst I_D/I_G ratio (0.95) is calculated to be higher compared to that of the C-4 (0.83) and C-10 (0.88) spent catalysts, which implies that the carbon formed on the surface of C-20 catalyst is less graphitic [251]. Rodrigues et al. reported a similar D band and G band over Ni (6 wt%)/γ-Al_2O_3 monolith spent catalyst for partial oxidation of ethanol to hydrogen production [252].

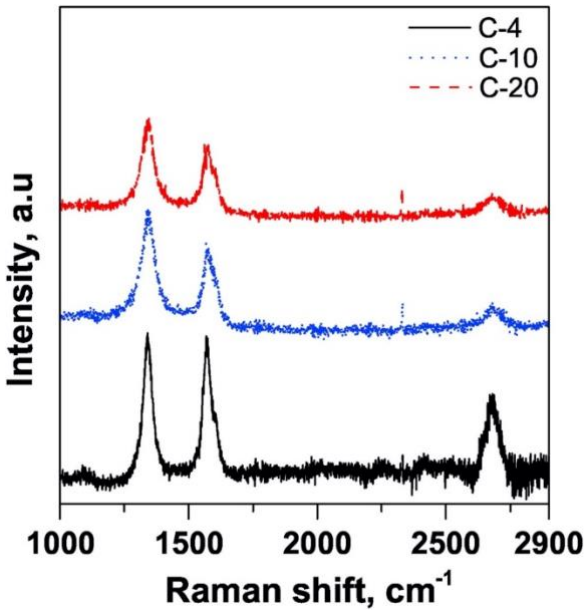

Fig.4. 6 Raman spectra of C-4, C-10, and C-20 after reforming reaction at 800°C for CH_4/CO_2 feed ratio 1.5, and 1 h time on stream

4.3.7 TGA-DTA analysis

The simultaneous TGA-DTA study (Fig. 4.7) is performed on a 1 h spent catalyst to measure the amount and nature of coke deposited on spent catalysts. In the case of CH_4/CO_2 ratio of 1.0, no carbon deposition is found on any catalyst. However, a small weight gain of around 450 to 650℃ is observed due to the oxidation of Ni to NiO. For the feed ratio 1.5, the weight losses for the spent C-4, C-10 and C-20 catalysts are found to be 6.7, 6.3 and 3.5%, respectively. As expected for feed ratio 2.0, weight loss was observed to be the highest; 10.4, 9.4 and 9.4% for C-4, C-10 and C-20, respectively (Fig. 4.7.c). Generally, the DTA exothermic peaks below 400 ℃ can be attributed to the formation of amorphous or highly reactive carbon, and peaks appear at 500 to 650 ℃ associated to filamentous carbon and peaks obtained above 650℃ related to the graphitic carbon [253]. For the feed ratio 1.5 (Fig. 4.7.b) and 2.0 (Fig. 4.7.c), two exothermic peaks, at around 510 and 640℃, for the catalysts are pertaining to the gasification of filamentous carbon to COx, and it is in line with both Raman and SEM analysis of 1 h spent catalyst [254–256]. Rodrigues et al. observed a similar DTA peak around 550 ℃ over Ni (6 wt%)/Al_2O_3 monolith spent catalyst for partial oxidation of ethanol to hydrogen production [252]. From TGA-DTA analysis, the C-20 catalyst exhibited less carbon deposition than C-4 and C-10 catalysts due to higher dispersion and smaller particle size of the active nickel phase.

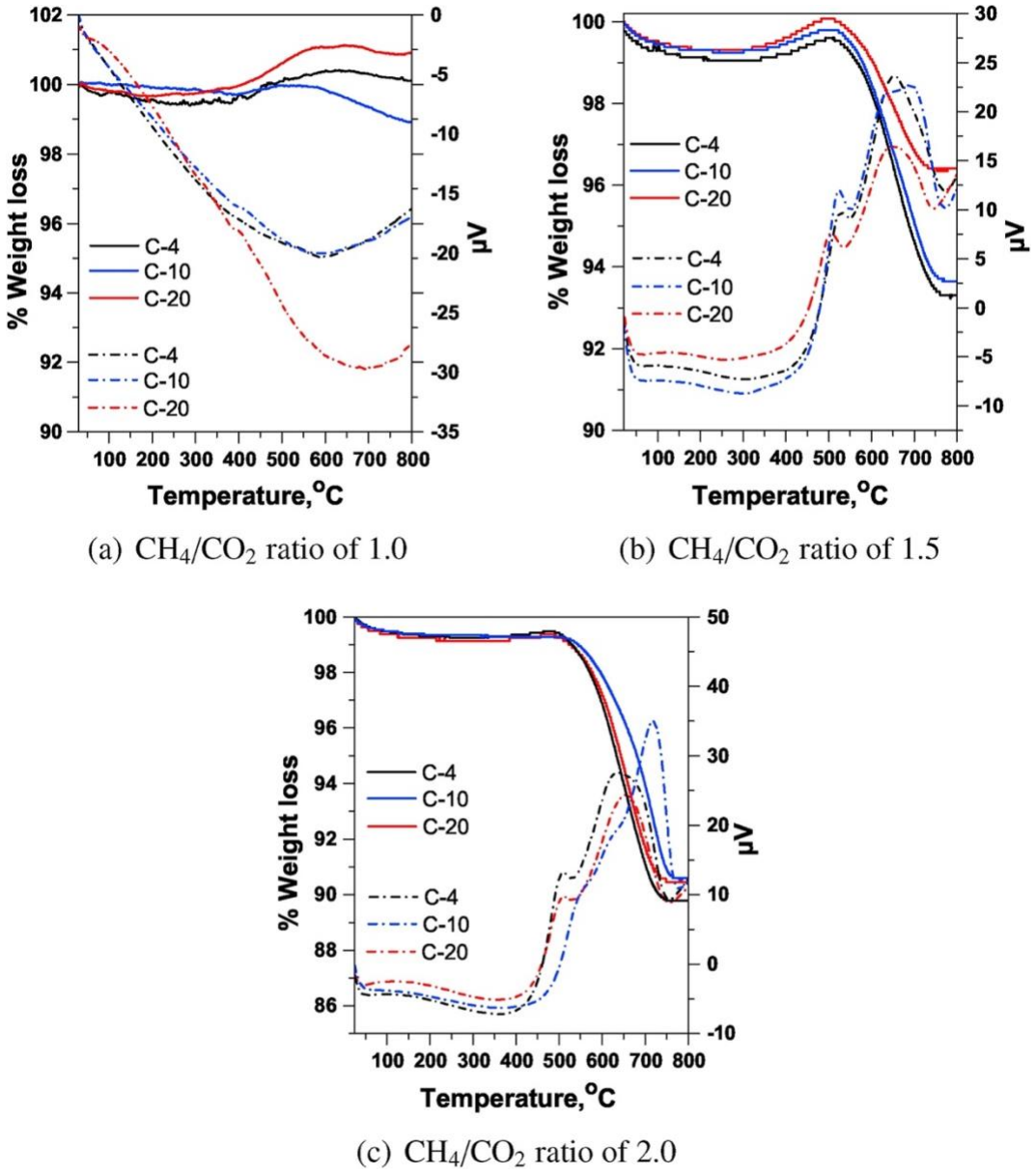

(a) CH_4/CO_2 ratio of 1.0

(b) CH_4/CO_2 ratio of 1.5

(c) CH_4/CO_2 ratio of 2.0

Fig.4. 7 Simultaneous TGA-DTA spectrum of C-4, C-10, and C-20, after reforming reaction at 800 ℃ and 1 h time on stream for different feed ratios of model biogas.

4.4 Activity experiments

Activity experiments were carried out for three different ratios of model biogas (CH_4/CO_2 =1.0, 1.5, & 2.0) to test the activity of C-4, C-10, and C-20 Ni/γ-Al_2O_3 cordierite monolith catalysts. The conversions of CH_4 and CO_2, mole fractions of H_2, CO, and H_2/CO ratio in time on stream (TOS) are shown in Fig. 4.8 for a CH_4/CO_2 ratio of 1.0. All catalysts show stable conversion of 95% in 40 h TOS (Fig. 4.8. a), and the deactivation rate is expressed in terms of a drop in CH_4 conversion is found to be 5%, 4% and 2% after the first 3 h TOS for C-4, C-10, and C- 20, respectively. The initial conversions of CO_2 are around 98% and showed a stable conversion of 86% achieved in 40 h TOS for the catalysts C-4, C-10, and C-20 catalysts (Fig. 4.8.b). The conversion of CH_4 is higher than CO_2 at a CH_4/CO_2 ratio of 1.0. Similar behaviour was also reported by Pawar et al. [103] over Ni/Al_2O_3 catalyst pellets with a weight hourly space velocity (WHSV) of 12000 ml. $(g.cat\ h)^{-1}$. The C-4, C-10, and C- 20 catalysts exhibit similar responses. However, the C-20 catalyst showed a little deactivation rate in both CH_4, and CO_2 conversions compared to the C-4 and C-10 catalysts. The activity results showed that calcination time plays a minor role in catalyst stability for a CH_4/CO_2 ratio of 1.0.

Moreover, the TGA-DTA results for a CH_4/CO_2 ratio of 1.0 showed no carbon deposition on the surface of C-4, C-10, and C-20 spent catalysts. The prepared C-4, C-10, and C-20 monolith catalysts showed better performance than the existing reports on Ni-based monolith catalysts. For instance, Luisetto et al. [130] studied the methane dry reforming with CH_4/CO_2 ratio of 1.0 over Ni (10 wt%)/g-Al_2O_3 monolith catalyst with a GHSV of 134328 ml. $(g.cat\ h)^{-1}$ at 800 °C and reported CH_4 and CO_2 conversions were 60% and 72%, respectively. A recent study by Leba et al. [129] carried out the dry reforming with CH_4/CO_2 ratio of 1.0 on Ni (8 wt%) to Co (2 wt%)/MgO

coated on ceramic monoliths with a GHSV of 84,000 ml. (g.cat h)$^{-1}$ at 800 °C and reported conversions of CH_4 and CO_2 were 86% and 90%, respectively.

The mole fraction of H_2 is almost constant, around 0.3 for all catalysts, as shown in Fig. 4.8.c, and it follows a similar trend of CH_4 conversions. Fig. 4.8.d shows the exit mole fractions of CO and follow the same patterns of CO_2 conversions and varied from 0.36 to 0.32 in 40 h TOS. The H_2/CO ratios are found to be 0.92, 0.94, and 0.95 for C-4, C-10, and C-20, respectively, are shown in Fig. 4.8.e. The H_2/CO ratio remains less than one in 40 h TOS, which may be due to the occurrence of RWGS reaction. Several research groups reported the possibility of RWGS at more than 700°C [41,103,257,258]. However, no moisture was detected in our experiments as we incorporated the gas-liquid separator at the reactor exit before analyzing the sample in online GC. Fig. 4.9 shows the conversions of CH_4 and CO_2, mole fractions of H_2, CO, and H_2/CO ratio for C-4, C-10, and C-20 catalysts at a CH_4/CO_2 ratio of 1.5. The initial conversion of CH_4 is observed to be similar, around 95% for all three catalysts shown in Fig. 4.9.a. A significant drop in CH_4 conversions is observed in the first 3 h of dry reforming due to the blockage of active sites by carbon deposition. However, during the 40 h TOS, the CH4 conversions are almost stable and found to be 54%, 57%, and 67% for C-4, C-10, and C-20 catalysts, respectively. The deactivation rate in terms of a drop in CH_4 conversion is 2% for C-20 catalysts and 20% and 16% for C-4, and C-10 catalysts, respectively. Fig. 4.9.b shows the CO2 conversions 76%, 79%, and 91% were observed for C-4, C-10, and C-20 catalysts after 40 h TOS. The CO_2 conversions are higher than the CH_4 conversions due to the CO_2 as the limiting reactant, the presence of Mg species, and the occurrence of RWGS.

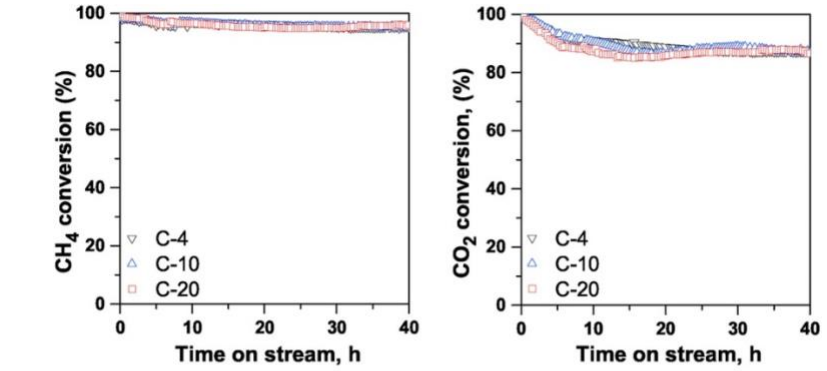

(a) Time on stream conversion of CH_4 (b) Time on stream conversion of CO_2

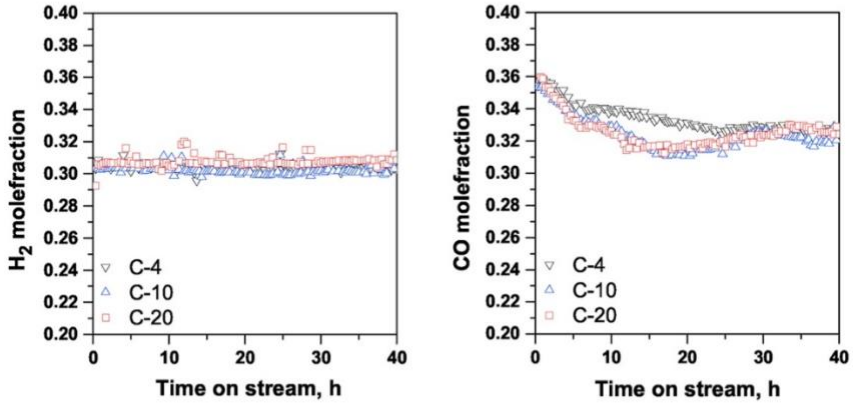

(c) Time on stream mole fraction of H_2 (d) Time on stream mole fraction of CO

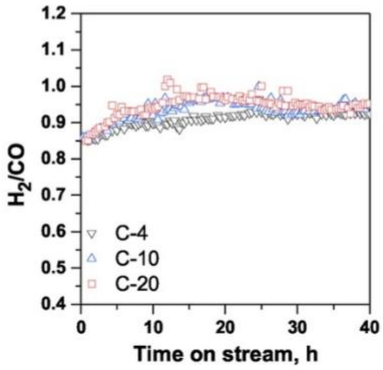

(e) Time on stream of H_2/CO ratio

Fig.4. 8 Profiles of the Ni/γ-Al_2O_3 based cordierite monolith catalysts C-4, C-10, and C-20 for a CH_4/CO_2 ratio of 1.0

The RWGS helps to convert more CO_2 and produce H_2O, which in turn promotes carbon gasification. The C-20 catalyst showed a higher conversion of both CH_4 and CO_2 than the reported

conversions on Ni-based catalysts. For instance, Pawar et al. [103] prepared Ni/Al_2O_3 pellets, calcined them at 800℃ for 4 h and reported that CH_4 and CO_2 conversions were 60% and 90%, respectively, during 12 h TOS for a CH_4/CO_2 ratio of 1.5. Another study by Goula et al. reported CH_4 and CO_2 conversion of 53% and 83% for Ni (8 wt%)/LaZr, Ni (8 wt%)/CeZr catalysts with a GHSV of 120,000 ml. $(g.cat\ h)^{-1}$, respectively, these catalysts are also calcined at 800℃ for 4 h [259]. The lower CH_4 and CO_2 conversions in C-4 and C-10 catalysts might be due to the absence of strong metal-support interaction and the formation of more graphitic carbon on the catalyst surface. The presence of graphitic carbon was confirmed with TGA-DTA and in Raman analysis of 1 h spent catalyst. These results show higher carbon deposition over C-4 and C- 10 catalysts than C-20 catalysts.

The mole fractions of H_2 in 40 h TOS are 0.24, 0.24, and 0.25 for C-4, C-10, and C-20 catalysts, respectively, shown in Fig. 4.9.c, which follows a similar trend of CH_4 conversions. It is observed that the mole fractions of H_2 are similar for C-4, C-10 and C-20 catalysts. This is because both dry reforming and methane cracking are favourable at high temperatures. Fig. 10(d) shows that the mole fraction of CO was found to be 0.22, 0.23, and 0.28 for C-4, C-10, and C-20 catalysts, respectively. The high CO mole fraction indicates that C- 20 catalyst favours the RWGS and reduces the CO disproportionation reaction. The H_2/CO ratios were observed to be 1.0, 0.97, and 0.89 for C-4, C-10, and C-20 catalysts, respectively, are shown in Fig. 4.9.e.

Fig. 4.10 illustrates the conversions of CH_4, CO_2, and mole fractions of H_2, CO, and H_2/CO ratio for CH_4/CO_2 ratio of 2.0. It is evident from Fig.4.10. a that the initial conversions of CH_4 were high; however, a sharp decrease was observed for all three catalysts, which was similar to the trends of the CH_4/CO_2 ratio of 1.5. The precipitous drop in initial conversions might be due to the

blockage of active sites with carbon, which is mainly formed in earlier stages of reforming [25]. These results are also in line with TGA-DTA. The constant and stable conversions of CH_4 in 40 h TOS are found to be 38%, 38%, and 44% for C- 4, C-10, and C-20 catalysts, respectively. The deactivation rates in CH_4 conversions after the first 3 h TOS were found to be 6%, 13% and 4% for C-4, C-10, and C-20, respectively. Higher CO_2 conversions were observed as compared to CH_4 conversions due to the occurrence of RWGS in all three C-4, C-10, and C-20 catalysts. Fig. 4.10.b shows the conversions of CO_2 in 40 h TOS and observed to be 76%, 82%, and 84% for C-4, C-10, and C- 20 catalysts, respectively. As pointed out above, the CO_2 conversions are higher than CH_4 conversions due to the CO_2 as a limiting reactant, and the occurrence of RWGS. It is evident from the results that the C-20 catalysts showed higher conversions in terms of both CH_4 and CO_2 than C-4 and C-10 and stable performance in 40 h TOS. The C-20 catalysts showed better performance in CH_4 and CO_2 conversions than reported elsewhere. For instance, Evans et al. [222] prepared hydrothermally Ni-doped $SrZrO_3$ perovskite and used it for reforming of CH_4/CO_2 ratio of 2.0. The reported conversions of CH_4 and CO_2 after 3 h TOS were 45% and 85%, respectively. The mole fraction of H_2 in 40 h TOS was found to be 0.2, 0.21, and 0.21 for C-4, C-10 and C-20 catalysts, respectively, shown in Fig. 4.10.c.

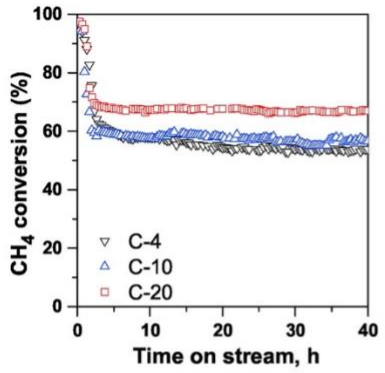

(a) Time on stream conversion of CH_4

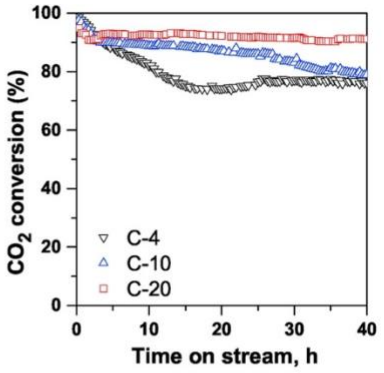

(b) Time on stream conversion of CO_2

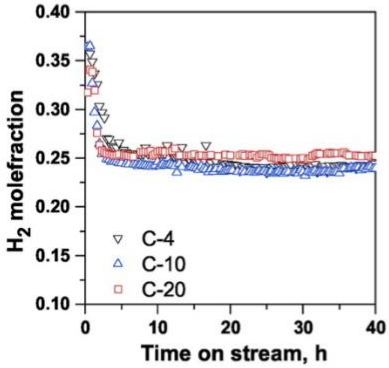

(c) Time on stream mole fraction of H_2

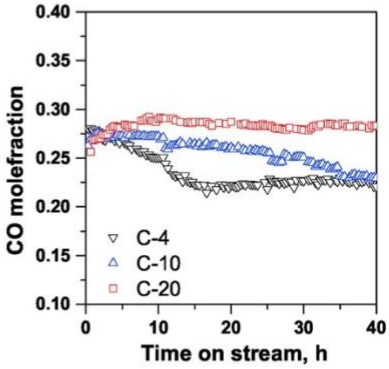

(d) Time on stream mole fraction of CO

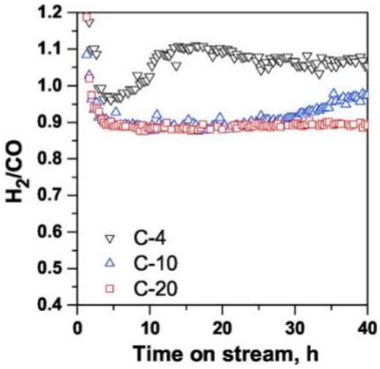

(e) Time on stream of H_2/CO ratio

Fig.4. 9 Profiles of the Ni/γ-Al_2O_3 based cordierite monolith catalysts of C-4, C-10, and C-20 for a CH_4/CO_2 ratio of 1.5.

The mole fraction of CO was found to be 0.19, 0.21, and 0.23 over C-4, C-10, and C-20 catalysts, respectively, are shown in Fig. 11(d). Both H_2 and compositions are observed to follow trends like CH_4 and CO_2 conversions in 40 h TOS of model biogas reforming. The value of H_2/ CO after 40 h was found to be 1.05, 1.0, and 0.95 for C-4, C-10, and C-20 catalysts, respectively, shown in Fig. 4.10.e. Based on the above activity studies, it can be stated that the C-20 catalyst exhibited better activity under harsh dry reforming conditions (CH_4/CO_2 = 1.5 & 2.0) in 40 h TOS.

Analysis of the catalytic activity results shows that the final calcination time of the Ni/γ-Al_2O_3 cordierite monolith-based catalyst systems influence the activity of the catalysis substantially. The catalyst calcined for 20 h reveals higher efficiency in terms of the conversions of CH_4 and CO_2, and catalytic stability. The physicochemical properties of the catalysts disclose a few interesting aspects; the C-20 sample shows the smallest Ni particle size, strongest metal-support interaction, and the least amount of carbon deposition during the reforming reaction. The metal particle size and metal-support interaction are the two critical aspects of the catalysts, depending on the calcination temperature and calcination time. The effect of calcination temperature on the catalytic activity as well as on the physicochemical properties of the catalysts, is well studied. Calcining the cordierite monolith wash coated with Ni salt/γ-Al_2O_3 slurry at high temperature during catalyst preparation is a common practice, and most of the research articles on the Ni/γ-Al_2O_3 cordierite monolith catalyst systems report high temperature (> 600°C) calcination for a relatively short time (10 h) [130]. High temperature enhances the Ni diffusion in the γ-Al_2O_3 structure, and spinel latticed $NiAl_2O_4$ complex oxide is formed. This complex structure could be reduced to metallic Ni/γ-Al2O3 at high temperatures, leading to stable and active Ni/γ-Al2O3 catalyst systems with small metallic particle size distribution. This increases the dispersion and surface area of the active Ni metallic particles on the support matrix. For Ni loading less than 10 wt%, Ni could be consumed

entirely in the spinel structure. At higher loading, the NiO phase could be formed with the spinel. In depositing metal on the wash-coated monolith, Ni precursor mostly accommodates on the surface of the coating and then diffuses slowly in the wash-coat structure with time through high-temperature calcination. The EDX analysis of the C-4 and C-10 shows high amount Ni (30 wt%) on the coating surfaces, which results in the agglomerated NiO particles with some $NiAl_2O_4$ is seen in C-20 but not in C-4 and C-10 from XRD and TPR. Longer calcination time allows the diffusion of Ni in the coating. Additionally, the EDX results show that the alkaline Mg and Si diffuse out from the cordierite monolith in the coating with the increase of calcination time concentration of these elements enhanced in the coating. The fresh C-4 sample amount of Mg and Si are measured to be 0.02 and 0.4 wt%, respectively, while for the sample after 20 h of calcination, these values increase to 1.1 and 6.1 wt%, respectively.

A simple estimation for the diffusion of Mg and Si (Fig. 4.11) calculated using Fick's second law supports the elemental distribution obtained by EDX. The unsteady state diffusion of Mg and Si is calculated using Fick's second law. Diffusion couples assumed in the calculations are $MgO\text{-}Al_2O_3$ and $SiO_2\text{-}Al_2O_3$. The diffusion coefficients are taken from existing literature .i.e in the case of $MgO\text{-}Al_2O_3$ system, the diffusion coefficient is taken from Zhang et al. [260] (D = 3.12E-15) and for $SiO_2\text{-}Al_2O_3$ system diffusion coefficient is obtained from Robert et al. [261] (D= 6.24E-15). The calculated concentration of Si and Mg are shown in (Fig. 4.11) revealing the possibility of diffusion in diffusion couple systems when subjected to the higher temperature. The surface concentration of both MgO and SiO_2 is assumed to be the weight (wt%) of MgO and SiO_2 present in cordierite.

The sample calculation is shown below:

Fick's second law of unsteady state is

$$\frac{C_x - C_0}{C_s - C_0} = 1 - erf\left[\frac{x}{2 * \sqrt{Dt}}\right]$$

Where,

C_x = concentration at length x (0-50 µm) after time t, wt%

D = Interdiffusion coefficient, m^2/sec

C_s = Surface concentration, 13.78 wt% for MgO and 51.31 wt% SiO_2

C_0 = 0, t=0.

Diffusion of the higher amount of Mg, an alkaline earth promoter, from the monolith in the coating leads to the formation of a larger quantity of the $MgAl_2O_4$ phases in the calcined C-20 catalyst, which introduces more basic properties in the support. Additionally, the counter diffusion of Ni and Mg/Si in the coating could be responsible for forming mixed $MgAl_2O_4$/$NiAl_2O_4$ phases. This process practically restructures the wash coat matrix to create an apparently counterintuitive coating morphology with smaller particle size distribution for the longer calcination time, as observed by the electron microscopy results. The increased amount of this mixed oxide phase is also accountable for the stronger active metal-support interaction in the C-20 sample. The smaller active metal enhances the activity of the catalyst, while the basic nature of the catalysts improves the CO_2 adsorption on the catalyst surface, and therefore, less amount of coke deposition occurs on the C-20 compared to the other two samples for all feed ratios [54].

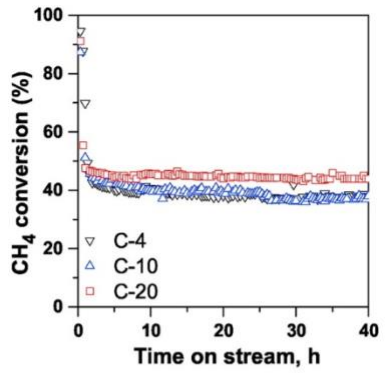

(a) Time on stream conversion of CH_4

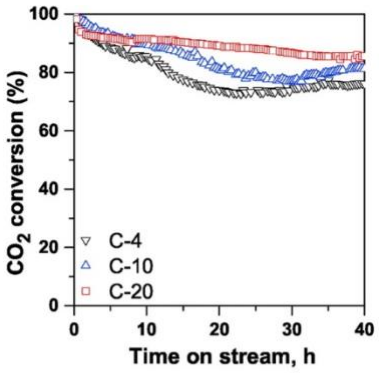

(b) Time on stream of convresion CO_2

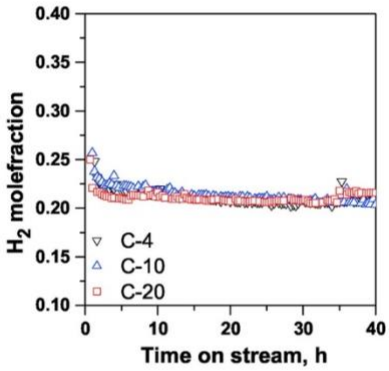

(c) Time on stream mole fraction of H_2

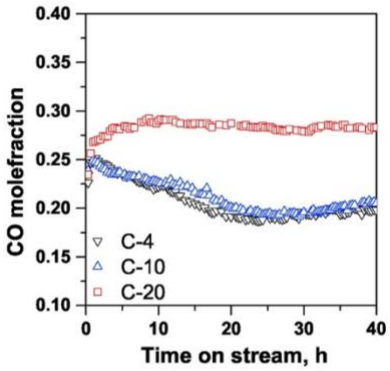

(d) Time on stream mole fraction of CO

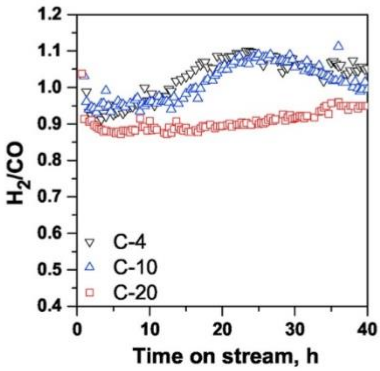

(e) Time on stream of H_2/CO ratio

Fig.4. 10 Profiles of the Ni/γ-Al_2O_3 based cordierite monolith catalysts of C-4, C-10, and C-20 for a CH_4/CO_2 ratio of 2.0

Obviously, the amount of carbon deposition increases with the amount of CH_4 in the feed, but the DTA-TGA and Raman spectroscopy results show the deposited C (especially on the C-20) to be more defective/amorphous filamentous type with less amount of graphitic carbon. This filamentous C is reportedly almost non-functional in deactivating Ni catalyst, although it could be a reason for pore plugging and collapsing the catalyst structure, as observed after 40 h of the reforming study. This nature of C might be responsible for the initial deactivation of the catalysts, but after that, C did not affect the activity. The diffusion of Ni on the carbon filaments helps continue the activity.

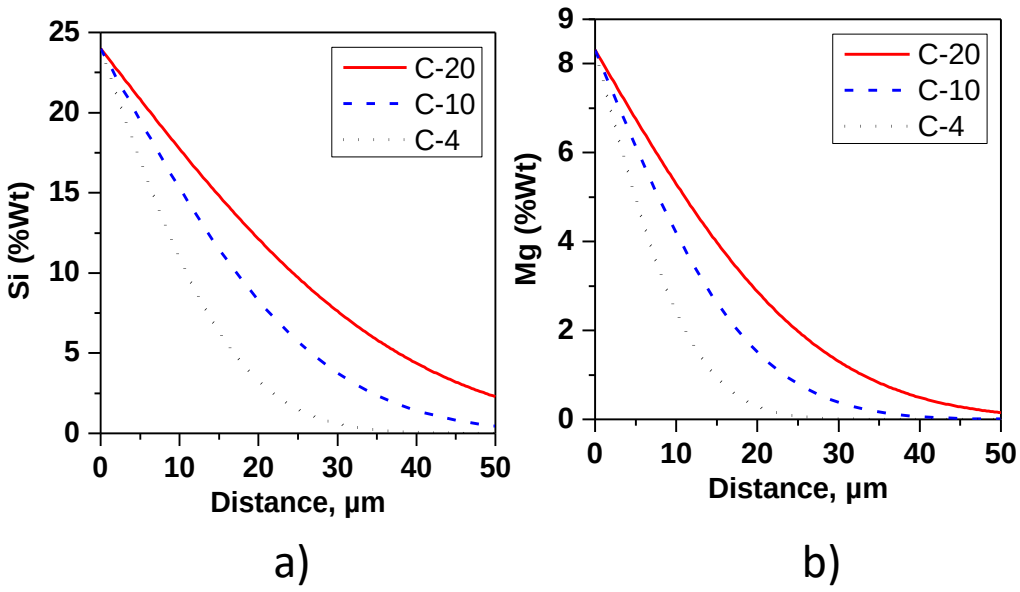

Fig.4. 11Variation in theoretical a) Si and b) Mg concentration in SiO_2 - Al_2O_3 and MgO-Al_2O_3 diffusion couple systems at 1576 ℃ (SiO_2 -Al_2O_3)1326 ℃ (MgO- Al_2O_3) and 1 atm.

4.5 Conclusions

Ni/γ-Al_2O_3 wash-coated monolith catalysts are calcined at 800 °C for 4 h, 10 h and 20 h. The experiments are performed at 800 °C with three different CH_4/CO_2 ratios of 1.0, 1.5 and 2.0. The fresh and used catalysts are characterised using XRD, BET, pulse chemisorption, SEM, TEM, TGA- DTA, and Raman to analyse the phase content, microstructure, and surface chemistry of catalysts. Spinels such as $NiAl_2O_4$ and $MgAl_2O_4$ are detected in XRD with maximum intensity for C-20 catalysts. The TPR results supported the XRD and showed the reduction of (Ni–Mg)Al_xO_4 complex structure at 780 °C, and this high-temperature peak is absent in the catalysts calcined at 4 h and 10 h.

The spinel formation leads to improved Ni dispersion and small Ni particle size during the reduction in H_2 environment. FESEM images of fresh, reduced and spent catalysts clearly showed the influence of calcination time on particle morphology & size distribution and elemental distribution of the catalysts. Moreover, it is also interesting to note that the amount of Mg and Si on the coating surface is higher in C-20 sample compared to C-4 and C-10, and the opposite trend is observed for the amount of Ni, which is higher in C-4 and C-10 samples compare to that in the C-20 catalyst. Elemental mapping shows the presence of Ni and Mg on the surface of the C-nanotubes for all the catalysts. However, the maximum Ni is on the C-20 catalyst. TGA-DTA results showed increased carbon formation with an increase CH_4/CO_2 ratio for all catalysts. However, C-20 catalyst showed less amount of carbon compared to the C-4 and C-10 catalysts. TGA-DTA results were further supported with Raman analysis and confirmed the defective/amorphous filamentous type with less graphitic carbon for the C-20 catalyst. Raman analysis also confirms the formation of carbon nanotubes in all spent catalysts; however, it did not

affect the catalytic activity in 40 h TOS due to the presence of surface Ni on carbon nanotubes in all the catalysts. Catalytic activity results show the positive impact of the calcination time of the Ni-based cordierite monolith catalysts. The catalyst calcined for 20 h reveals stable catalytic activity in 40 h TOS with higher CH_4 and CO_2 conversions than C-4 and C-10 monoliths. The smaller Ni particles and the presence of Mg could be the reasons for the higher catalytic activity of the C-20 catalyst. The Mg provides the basic nature of the support and helps in more CO_2 adsorption on the catalyst surface, and therefore, less coke deposition occurs on the C-20 catalyst for all tested CH_4/CO_2 ratios.

Chapter-5

5 Reforming of Model Biogas using Ni/CeO_2/γ-Al_2O_3 Monolith Catalyst

5.1 Introduction

The CeO_2 has been introduced as a promoter in the Ni/γ-Al_2O_3 cordierite catalyst system. CeO_2 is well-known for its oxygen storage capacity, which promotes the gasification of carbon. By incorporating CeO_2 into the Ni/γ-Al_2O_3 cordierite catalyst, the carbon gasification can be enhanced, reducing the amount of carbon deposition. The use of CeO_2 as a promoter has been widely studied, and its ability to enhance the performance of various catalysts has been well-documented [126,262,263]. In this work, 5 wt% Ni/10 wt% CeO_2/ γ-Al_2O_3 cordierite monolith catalysts are prepared in a two-step method: support is loaded by sol-gel, and active Ni is deposited using the conventional wet impregnation method. Activity studies are conducted for 40 h time on stream at 800℃ by varying the ratio of CH_4 to CO_2 (1.0, 1.5, & 2.0). The physicochemical properties of calcined, reduced and spent catalysts are studied with the help of various characterization techniques such as X-ray diffraction (XRD), scanning electron microscopy (SEM), and Raman spectroscopy.

5.2 Results and Discussion

5.2.1 X-ray diffraction (XRD)

The XRD analysis of Ni/CeO_2/γ-Al_2O_3 monolith catalysts displays the various oxide phases (as shown in Fig 5.1) identified using the crystallography open database (COD). From XRD of calcined catalysts, peaks appeared between 2 theta angles of 15 to 35^o is pertained to cordierite

phase (PDF:9006272), γ-Al_2O_3 (PDF:1000059) is observed at 43.2° and 69.6°. Further, NiO is present at 43.5° (PDF:1010095), and at 37.4° (PDF:9001432), $NiAl_2O_4$ is present due to the interaction between γ-Al_2O_3 and NiO during calcination [65,264]. The presence of CeO_2 (PDF:1562989) at an angle of 28.5° and 47.5° indicates the successful loading of CeO_2 on the cordierite surface. In reduced samples, Ni (111) and (200) phases are appeared 44.3° and 51.8° (PDF:2100640) as displayed in figure 5.1 with the retention of cordierite and γ-Al_2O_3 phases. Moreover, NiO is not detected in reduced samples, maybe due to the reduction of NiO. Using the Scherrer formula, $d = (0.9\ \lambda / \beta\ Cos\theta)$, the crystallite size of Ni is calculated to be 29 nm in the reduced catalyst and the spent catalyst, which is observed to be 35 nm. After the reaction, the Ni phase is observed, having a size of 35 nm along with the carbon peak at 26°. The presence of γ-Al_2O_3 and CeO_2 phase (69.6° and 47.5°) in the spent catalyst indicates the stability of the support even in harsh reforming conditions. In the literature, several researchers observed similar XRD behavior for dry reforming of methane (DRM) over Ni/ γ-Al_2O_3 monolith catalyst calcined at 800°C. Authors have reported cordierite peaks between 15 to 35°, γ-Al_2O_3 at 43.4°, $NiAl_2O_4$ at 37°, 45°, and Ni is reported at 44.1°, 51.4° for reduced and spent catalysts [65,265].

5.2.2 Scanning Electron Microscopy (SEM)

SEM analysis is performed to study the reduced and spent catalysts' particle size and surface morphology, as shown in Fig 5.3 The particle size of the SEM images is calculated using Image J analysis. Fig 5.2 displays monolith channels (passages) after coating with Al_2O_3-CeO_2 having a thickness of ca.100 μm (including channel or shell thickness) provides sufficient area to deposit Ni particles by impregnation [65,266]. In the case of reduced catalysts, particles are uniformly distributed over monolith support.

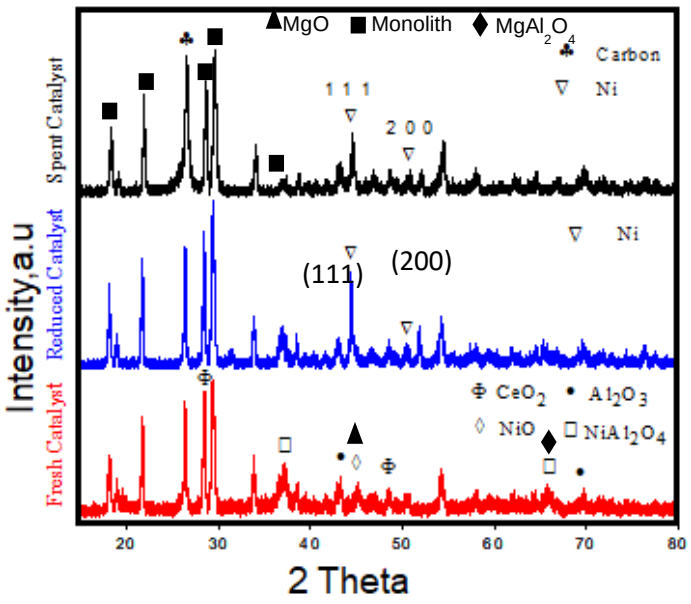

Fig.5. 1XRD patterns of Ni/CeO_2/γ-Al_2O_3 monolith catalysts at different stages: calcined at 800℃ for 20 h, reduced (800℃ for 13 h), and spent catalyst (CH_4/CO_2=1.5 for 1 h).

The particle size of Ni in reduced catalysts ranged between 15 nm to 70 nm, and the average is calculated to be 36 nm. In spent catalysts, the particle size increases due to the formation of carbon over Ni nanoparticles, and the particle size is found to be 41 nm. The particle size calculated in SEM agrees with the XRD results mentioned earlier. Although carbon is formed on the catalyst surface throughout DRBG, it has no effect on the catalyst activity. This is due to the filamentous nature of deposited carbon. The carbon grows on the Ni catalyst surface and uplifts the Ni particle during reforming. The presence of Ni on the top of carbon nanotubes, as shown in Fig.5.c is responsible for the stability of the catalyst irrespective of carbon deposition. A similar

phenomenon of filamentous carbon is well known and reported by several researchers in the literature [65,266].

5.2.3 Raman analysis

The nature of the deposited carbon on the catalyst surface dictates the activity and stability of the catalysts in DRM [65,267,268]. In general, two different types of carbon formed on the catalyst surface such as graphitic carbon and amorphous carbon. Graphitic carbon consists of hexagonal sp^2 carbon stacks bonded with strong covalent bonds, whereas amorphous carbon related to structurally disordered carbon [269–271]. In terms of catalyst deactivation, graphitic carbon is mainly responsible due to its inert nature. The spent catalysts are analysed using Raman spectroscopy, revealing two peaks at 1320 cm^{-1} and 1580 cm^{-1} pertained to the D and G bands shown in Fig 5.4. From the literature D band is related to the disordered carbon, or in other words, the unstable carbon, and the G band refers to the graphitic carbon (relatively inert carbon) [65,272]. Also, the ratio of I_D/I_G determines the degree of carbon's graphitic nature, i.e., high I_D/I_G ratios signify disordered carbon and low values indicate graphitic carbon on the catalyst surface. The I_D/I_G ratio of the spent catalysts (1.8, 1.6, and 1.5) decreased for CH_4/CO_2 = 1.0, 1.5 and 2.0, respectively. From Raman analysis, the graphitic nature of the carbon increased with an increase in the CH_4/CO_2 ratio and thus led to the poor activity of the catalysts. Moreover, it is observed that the addition of CeO_2 increased the I_D/I_G ratio compared to the Ni/Al_2O_3 cordierite catalysts. The I_D/I_G ratio of the spent catalyst for Ni/Al_2O_3 and Ni/CeO_2-Al_2O_3 cordierite catalysts is found to be 0.98 and 1.6 for a reactants feed ratio of 1.5. The introduction of CeO_2 decreased the nature of graphitic carbon on the catalyst surface by enhancing carbon gasification during DRBG.

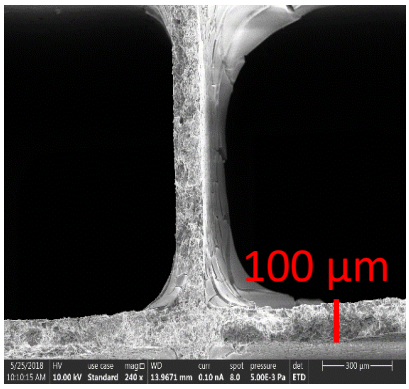

Fig.5. 2 Surface morphology of monolith channels (red line indicates the coating thickness including channel)

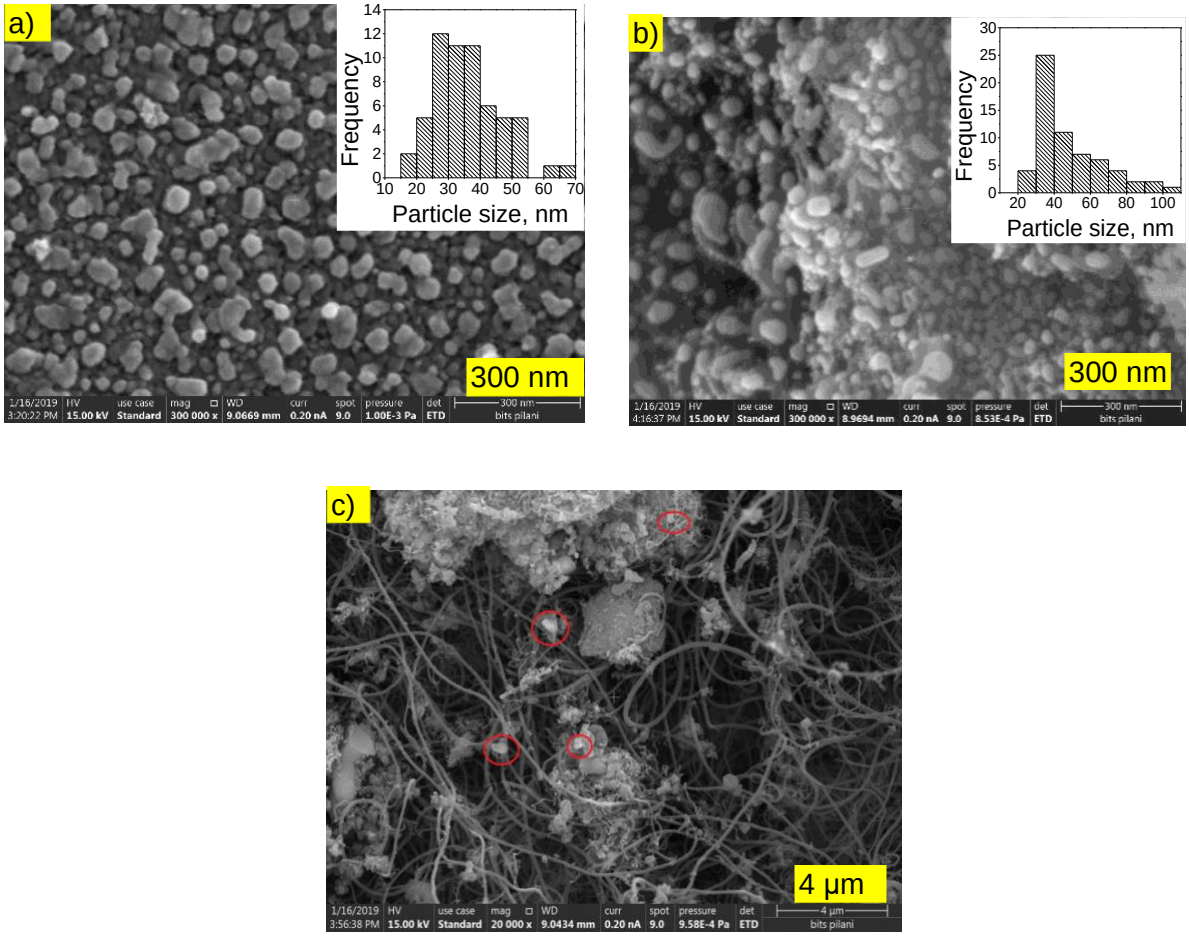

Fig.5. 3 FESEM analysis of Ni-Ce/Al_2O_3 monolith catalysts, a) reduced, b) spent catalyst c) carbon nanotubes (inside red circles indicates Ni particles)

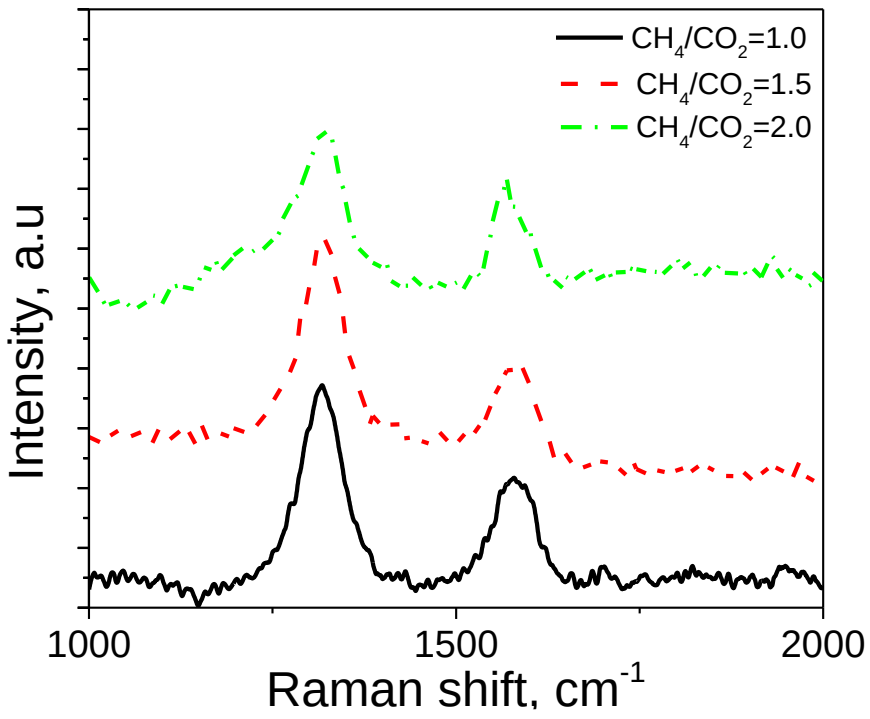

Fig.5. 4 Raman analysis of Ni-Ce monolith catalysts after DRBG for CH_4/CO_2 = 1.0, 1.5, and 2.0 at 800℃ for 40 h

5.3 Catalytic Activity

DRBG studies are conducted on Ni-Ce monolith catalysts for different ratios of CH_4/CO_2 (1.0, 1.5, and 2.0) at 800℃. The conversions of CH_4, CO, yields of H_2, CO, and H_2/CO ratio are calculated and plotted against time on stream (TOS) as shown in Fig 5.5. In the case of CH_4/CO_2 = 1.0, the methane conversions are stable after an initial drop of 10%. The steady-state conversions of CH_4 and CO_2 are found to be 91% and 69% for 40 h TOS. As discussed in the Raman analysis, CH_4 conversions are decreased with increased CH_4/CO_2 ratio, which may be due to the presence of graphitic carbon on the catalyst surface, and low conversions of CH_4 can be attributed to the limited availability of CO_2 to react with the excess CH_4 present in the feed mixture at higher ratios

of CH_4/CO_2. The steady-state conversions of CH_4 is found to be 60%, and 50% for CH_4/CO_2 = 1.5, and 2.0, respectively. Similar catalytic activity is observed by Gonzalez et al.[273] over Ni-Ce supported on nano-fibred alumina for CH_4/CO_2=1.5. The authors reported a CH_4 conversion of 60% at 800 ^oC. The CO_2 conversions rise with an increase in feed ratio, which is obvious due to CO_2 being the limiting reactant in the feed. The carbon formation is observed in SEM and Raman analysis of spent catalysts. The steady-state conversions of CO_2 are found to be 60%, 80%, and 81% after 40 h TOS for CH_4/CO_2 = 1.0, 1.5, and 2.0 respectively. The obtained conversions are higher than the conversions reported over Ni-Ce pellet catalysts in the existing studies [80,112,264,274,275]. For instance, Qin et al.[275] observed a CH_4, CO_2 conversions of 20%, 60% in DRM for CH_4/CO_2 =1.0 at 800 ^oC over 8Ni/20Ce-Al_2O_3 catalysts. Similarly, Luisetto et al.[112] reported a CH_4 and CO_2 conversions of 55% on Ni/CeO_2-Al_2O_3 catalysts. Bereketidou et al.[80] studied DRBG over Ni-Ce/Al_2O_3 catalysts and reported conversions of 35% CH_4 and 58% CO_2 for a CH_4/CO_2 = 1.5 at a temperature of 800 ^oC. The H_2/CO ratio is close to 1.0, which shows the absence of reverse water gas shift reaction during DRBG. For all the feed ratios, the yield of H_2 is in good agreement with the CH_4 conversions, as displayed in Fig 5.5.d The increase in the feed ratio led to the fall of H_2 and CO yields. Similar behaviour of H_2 and CO yield was reported by Goula et al. [258] over Ni/Al_2O_3 catalysts prepared using the wet impregnation method. Overall Ni-Ce monolith catalysts exhibited high stable activity for 40 h TOS for DRBG.

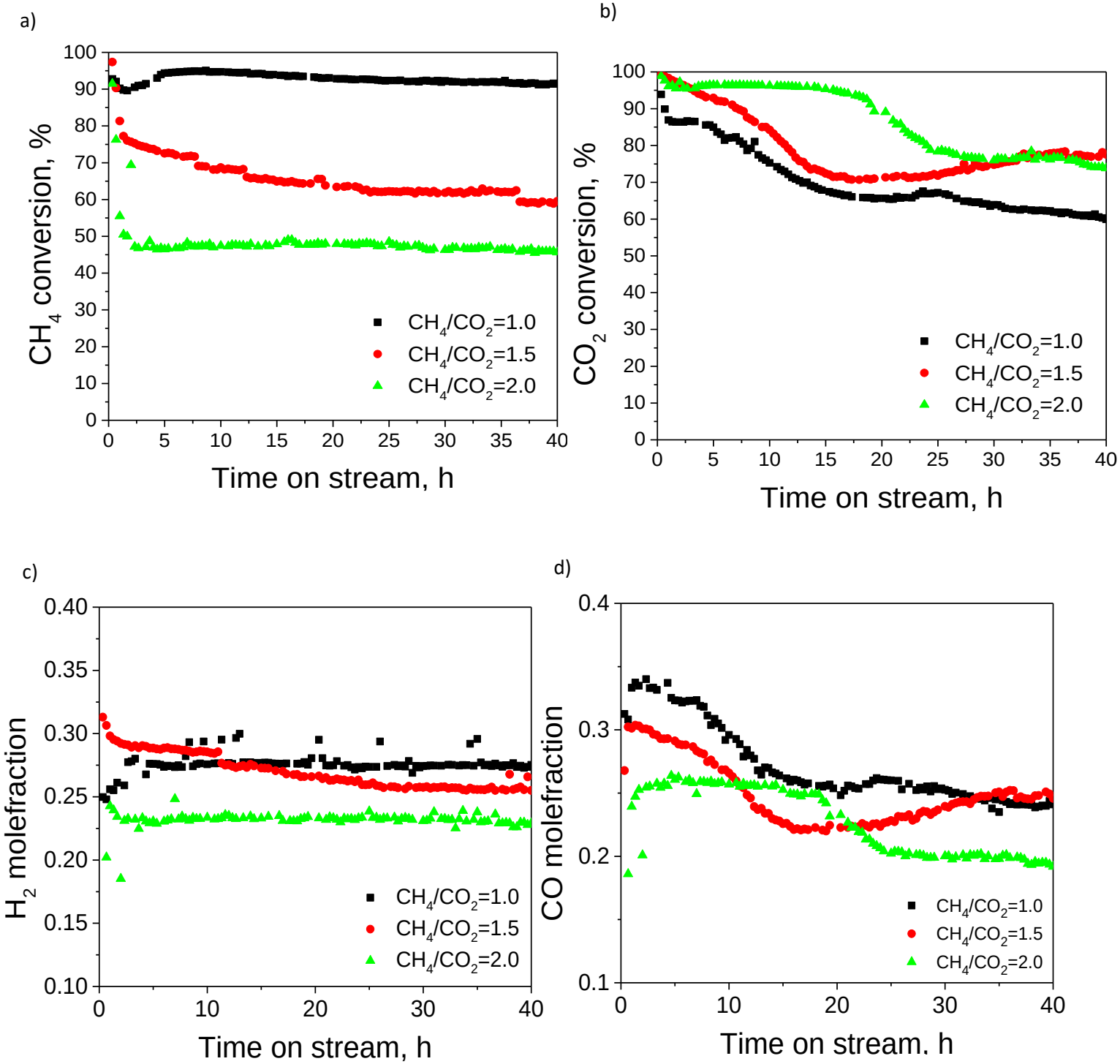
a)
CH4 conversion, %
Time on stream, h
CH4/CO2=1.0
CH4/CO2=1.5
CH4/CO2=2.0
b)
CO2 conversion, %
Time on stream, h
CH4/CO2=1.0
CH4/CO2=1.5
CH4/CO2=2.0
c)
H2 molefraction
Time on stream, h
CH4/CO2=1.0
CH4/CO2=1.5
CH4/CO2=2.0
d)
CO molefraction
Time on stream. h
CH4/CO2=1.0
CH4/CO2=1.5
CH4/CO2=2.0

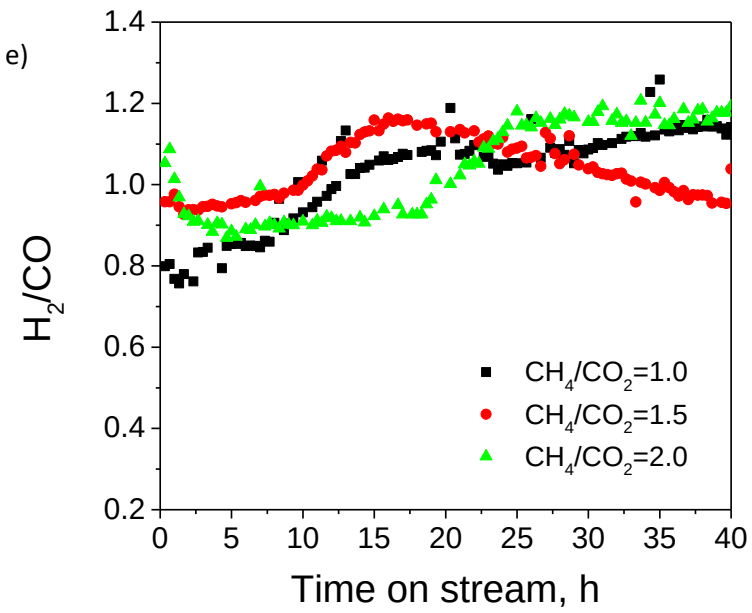

Fig.5. 5DRBG over Ni-Ce monolith catalyst for various ratios of CH_4/CO_2 (1.0, 1.5, and 2.0) ratios at 800℃ a) CH_4 conversion, b) CO_2 conversion, c) H_2 molefraction, d) CO molefraction, and e) H_2/CO

5.4 Conclusions

The prepared Ni-Ce cordierite monolith catalysts displayed excellent stable activity for DRBG experiments studied at 800℃. XRD analysis shows the existence of the Ni phase in the used catalyst, which played a vital role in maintaining stable activity even with the carbon deposition, and the same is reflected in our SEM analysis of spent catalysts. Thus the formation of carbon on the catalyst surface did not deactivate the stability for lower feed ratios. However, higher feed ratios are detrimental to the catalyst activity due to graphitic carbon in the spent catalyst observed using Raman analysis. The best possible conversions of CH_4 are found to be 91% for CH_4/CO_2 = 1.0 at 800℃. The H_2/CO ratio is obtained to be 1.0 for all the ratios studied, which is ideal for FT synthesis.

Chapter-6

6 Investigation of Ba doping in A-site deficient Perovskite Ni-exsolved Catalysts for Biogas Dry Reforming

6.1 Introduction

This chapter investigates the development of an A-site deficient $La_{0.9-x}Ba_xAl_{0.85}Ni_{0.15}O_3$ (x = 0, 0.02, 0.04, and 0.06) perovskite oxide catalyst for dry reforming of model biogas. The fresh and spent catalysts are analyzed using XRD, FTIR, XPS, FESEM, TPR, TGA-DTA, and Raman analysis. The role of Ba in improving metal support interaction and oxygen storage capacity is studied.

One of the key advantages of perovskite oxides is their high anti-sintering properties, which prevent the Ni particles from aggregating and losing their active surface area even under harsh conditions, such as high temperatures and exposure to coke deposition. This makes them highly attractive as catalysts for DRBG [198,276]. In this study, aliovalent cations such as Ba and Ni are co-doped into a novel A-site deficient $LaAlO_3$ perovskite oxide prepared using the citrate sol-gel method. To prevent undesired phases such as $BaAl_2O_4$ and $Ba_4Al_2O_7$ due to Ba doping, the amount of Ba doping was limited up to 6 mol% [277]. Four different catalysts were prepared, denoted as $La_{0.9}Al_{0.85}Ni_{0.85}O_3$ (LAN-15), $La_{0.88}Ba_{0.02}Al_{0.85}Ni_{0.15}O_3$ (LB2AN-15), $La_{0.86}Ba_{0.04}Al_{0.85}Ni_{0.15}O_3$ (LB4AN-15), and $La_{0.84}Ba_{0.06}Al_{0.85}Ni_{0.15}O_3$ (LB6AN-15) catalysts respectively. DRBG experiments are carried out at three different CH_4/CO_2 ratios of 1.0, 1.5 and 2.0 and 800 ^oC. The effect of Ba doping on catalytic activity and carbon deposition was studied by performing short-term (12 h) and long-term (40 h) experiments. Additionally, the impact of Ba on surface

morphology, oxygen vacancies, and metal support interaction was investigated using XRD, TPR, XPS, TGA- DTA, Raman, FE-SEM and TEM.

6.2 Results and discussion

6.2.1 XRD analysis

Figure 6.1. shows the XRD patterns of calcined, reduced and spent catalysts for Ni and Ba co-doped $La_{0.9}AlO_3$. The diffraction patterns of the calcined catalysts are attributed to the $LaAlO_3$ perovskite phase (PDF:5910090) having a cubic structure with Pm-3m space group and a tiny NiO (PDF-1010095) peak at 43.5 - 44^0 (as shown in Fig.6.1. A inset). Similar XRD patterns of $LaAlO_3$ were observed by Aguero et al.[278] for $LaAl_{0.95}Ni_{0.05}O_3$ and $LaAl_{0.8}Ni_{0.2}O_3$ catalysts. Additionally, the maximum intensity XRD peak (33.5^0) of the $LaAlO_3$ phase was shifted slightly towards lower angles for LB2AN-15, LB4AN-15, and LB6AN-15 catalysts (as shown in Fig.6.1.) due to the lattice's expansion caused by the doping of larger Ba^{+2} (0.135 nm) in the smaller La^{+3} (0.106 nm) site. Many studies have reported similar lattice expansion and XRD peak shifts in the perovskite structure catalysts [279–281]. For instance, Bhavani et al. [282] observed the XRD peak shift to lower angles with an increase in Ba substitution for $La_{1-x}Ba_xMnO_3$ (x = 0 to 0.5) catalysts. The peak shift was attributed to the enlargement of the lattice due to the Ba doping. Similarly, Wei et al. [283] observed an XRD peak shift due to the lattice expansion for $LaCrO_3$ catalysts co-doped with Sr and Ni.

In the XRD of reduced catalysts (as shown in Fig 6.1.B), a small exsolved Ni^0 phase is observed (inset image) at ca.44.5^0 (PDF: 2102260), along with the main $LaAlO_3$ phase. The NiO phase was completely reduced into $Ni^{0,}$ confirmed by the absence of a NiO peak in the reduced catalyst. Additionally, the full width half maximum (FWHM) of the Ni^0 peak was found to be

higher for LB6AN-15 catalysts than LB4AN-15, LB2AN-15, and LAN-15 catalysts, which may be due to the occurrence of lattice strain. The Ni crystallite size was calculated using Scherer's equation and found to be 22 nm, 16 nm, 8 nm, and 7.5 nm for LAN-15, LB2AN-15, LB4AN-15, and LB6AN-15 catalysts, respectively.

The diffractograms of spent catalysts (Fig 6.1. C) show the $LaAlO_3$ phase and metallic Ni phase at 44.5 (as shown in inset Fig 6.1. C). The carbon peak was not observed in the spent catalyst, maybe due to the amorphous nature of carbon present in the catalyst [284]. Based on the XRD patterns of reduced and spent catalysts, the perovskite structure was stable without any undesired peaks.

A)

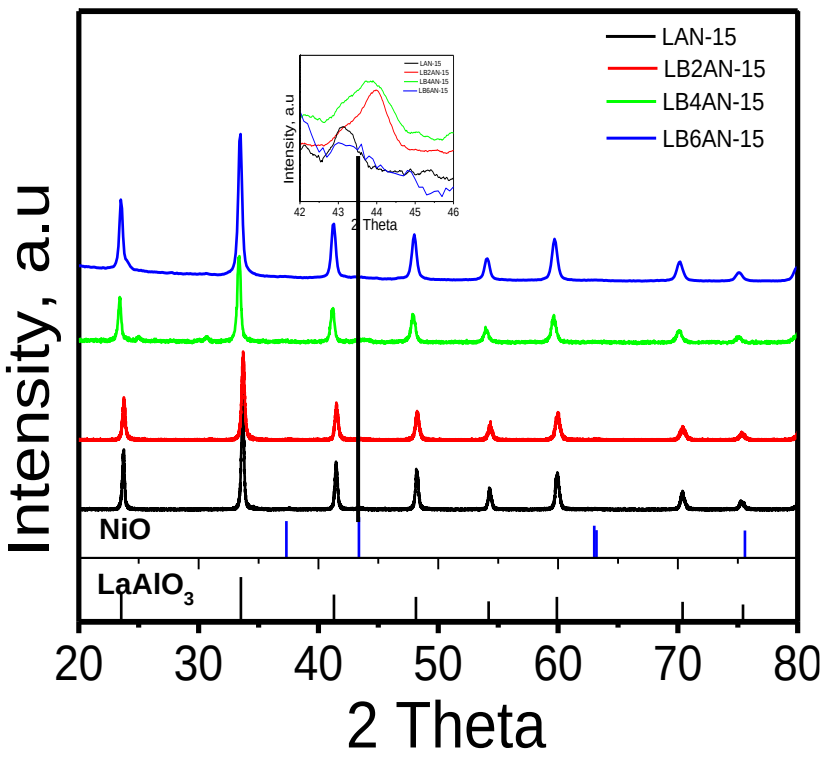

B)

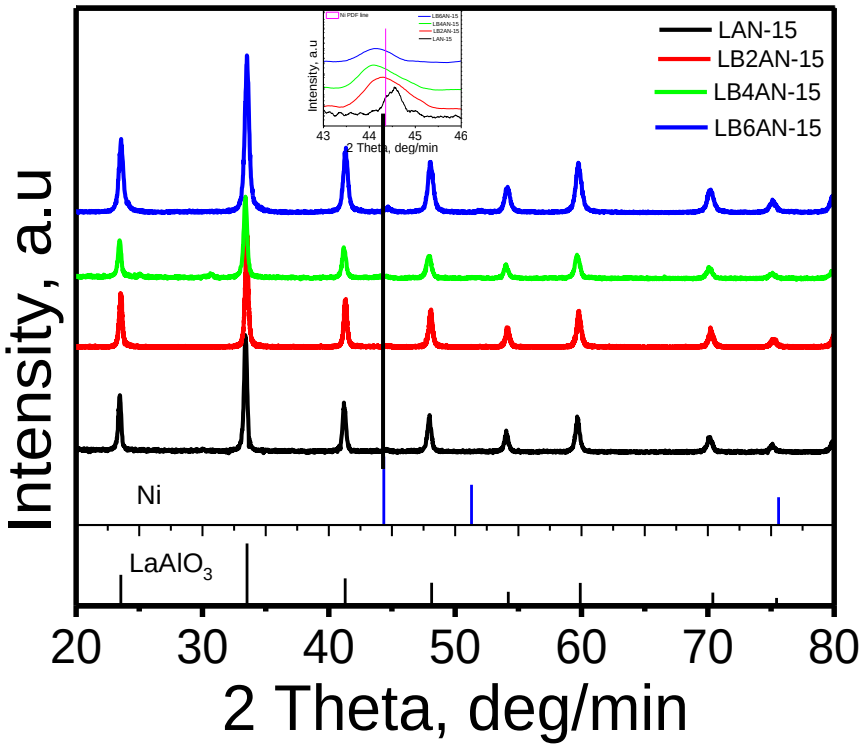

C)

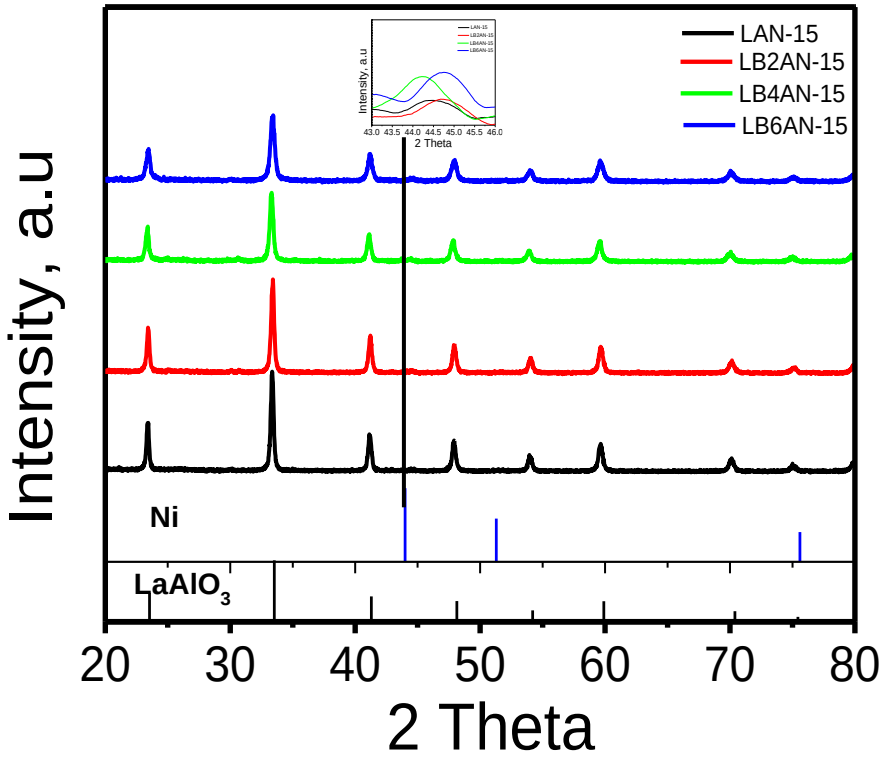

Fig.6. 1XRD analysis of A) after calcination B) after reduction (inside image of Ni peak) C) spent catalyst for 12 h DRBG at 800°C (inside image of Ni peak).

6.2.2 FTIR analysis

Fig. 6.2 shows the FTIR spectra of Ni-doped (LAN-15) and Ni-Ba co-doped (LB2AN-15, LB4AN-15, and LB6AN-15) perovskite catalysts. The Fourier peak at 3430 – 3460 cm^{-1} is related to the stretching vibration of a hydroxyl group (OH^-) due to moisture content in the catalysts [285]. The peak at 663 cm^{-1} is related to the Al-O vibration modes in the $LaAlO_3$ structure. Similar peaks of Al-O functional groups were reported by Silva et al. [286] for $LaAlO_3$ doped with Mn and Sr prepared using the sol-gel method and calcined at 900 ºC for 6 h in air. The doping of Ba is confirmed with the Ba-O stretching peak at 858 and 824 cm^{-1} [287,288]. Also, the peak at 1635 cm^{-1} can be attributed to the barium carbonate [289]. Based on the Al-O vibrations observed in FTIR and the presence of the $LaAlO_3$ phase from XRD results, it is concluded that all prepared catalysts form the $LaAlO_3$ perovskite structure.

6.2.3 TPR analysis

Figure6.3 displays reduction profiles for the LAN15, LB2AN-15, LB4AN-15, and LB6AN15 calcined catalysts. In the LAN-15 catalyst, two peaks are observed at 264℃ and 344℃, which are related to the Ni^0 from the isolated and moderately bonded NiO with the perovskite structure [290–292]. Similar low-temperature TPR profiles were reported in the literature [290,291]. For instance, Figueredo et al. [291] reported TPR peaks at 88 ℃, 233 ℃, and 320 ℃ for 10 wt% $Ni/LaAlO_3$ catalysts, which were related to the reduction of NiO having weak interaction with the $LaAlO_3$ support. Similarly, Bai et al.[87] observed a broad low-temperature peak at 320 ℃ for $Ni/LaAlO_3$ catalyst, which was related to the reduction of weakly bonded NiO with $LaAlO_3$ structure.

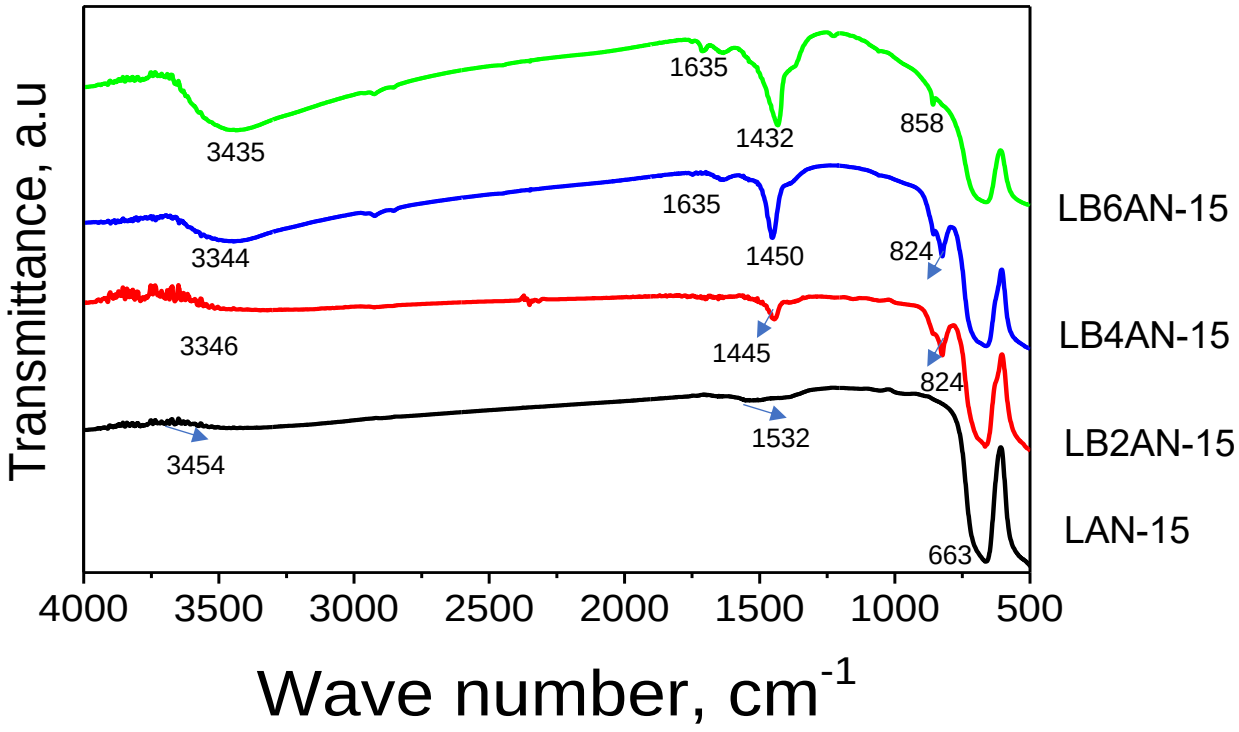

Fig.6. 2 FTIR analysis of calcined catalysts at 850℃ for 7 h

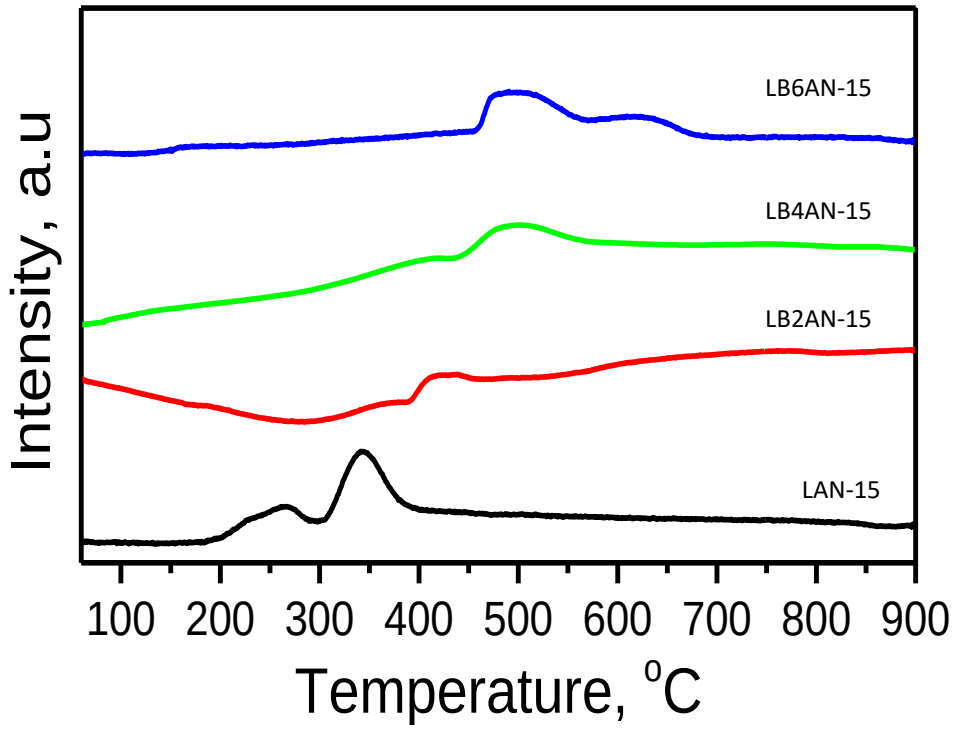

Fig.6. 3 TPR analysis of calcined catalysts at 850℃ for 7 h

In the case of Ni and Ba co-doped (LB2AN-15, LB4AN-15, and LB6AN-15) catalysts, the peaks are shifted to a high temperature, as shown in Fig.6.3. The substitution of Ba in the La site improved the metal-support interaction between the NiO and the $LaAlO_3$ perovskite, which is confirmed with the absence of low-temperature TPR peak for all Ba doped catalysts. In the case of the LB2AN-15 catalyst, two peaks were observed at 380°C and 437°C. These peaks are associated with NiO reduction, which interacts moderately with the $LaAlO_3$ structure. Furthermore, increasing Ba doping from 2 mol% to 6 mol% shifted the TPR peaks to a much higher temperature than LB2AN-15 and LAN-15 catalysts. The LB4AN-15 catalysts show peaks at 416℃ and 500℃ attributed to the Ni^0 from NiO, having moderate and strong interactions with the perovskite matrix [290]. For LB6AN-15 catalysts, two peaks are observed at 490℃ and 620℃ related to the reduction of Ni^0 from the perovskite structure. A similar TPR peak shift was observed in $La_{1-x}Ba_xNiO_3$ (x=0.05, 0.1, and 0.2) catalyst with an increase in Ba amount from 5 mol% to 20 mol% prepared using the citrate method for DRM [137]. Similarly Wei et al. [293] observed two different reduction peaks at 250 ℃ and 600 ℃ for $La_{0.5}Sr_{0.3}Cr_{0.85}Ni_{0.15}O_3$ perovskite oxide catalysts in DRM. The peak observed at 250 ℃ and 600 ℃ are attributed to the reduction of Ni from NiO and the perovskite oxide structure.

6.2.4 TPD

Figure 6.4 shows three desorption peaks for LAN-15 at 189°C, 476°C, and 645°C, associated with weak, medium, and strong basic sites. On the other hand, LB6AN-15 displays peaks at 183°C, 489°C, 540°C, 700°C, and 860°C, corresponding to weak, medium, strong, and very strong basic sites. Moreover, the amount of CO_2 adsorption on the catalyst surface is 145 umol/g and 170 umol/g for LAN-15 and LB6AN-15 catalysts, respectively. The doping of Ba in the La site improved the strength of basic sites. Furthermore, the intensity of low- and high-temperature peaks

increases with the addition of Ba to the perovskite structure. A similar observation was reported by Bhavani et al. [282], who found an increase in the strength of basic sites upon doping Ba in $LaMnO_3$ catalysts for the DRM. Additionally, Al-Fatesh et al. [294] reported an enhancement in the strength of basic sites of 5Ni-4Ba/YZr catalysts, and observed an improvement in catalytic activity due to the increased basic sites.

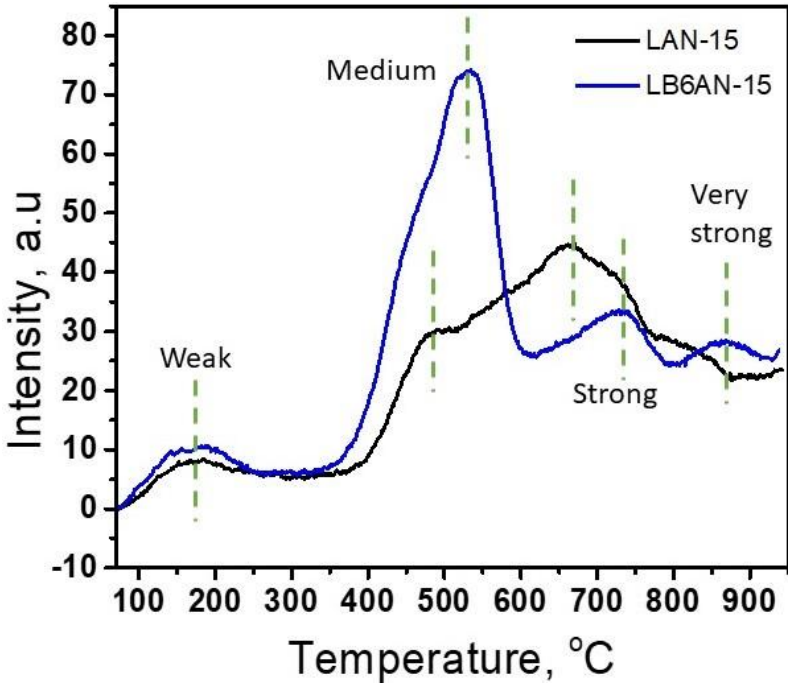

Fig.6. 4 CO_2-TPD analysis of calcined catalysts at 850 ℃ for 7 h

6.2.5 XPS analysis

The XPS analysis of the Ni 3p profile for calcined samples revealed the presence of Ni^{2+}, Ni^{3+} and Al^{3+} at 68.5, 70.5, and 73.7 eV for LAN-15, LB2AN-15, LB4AN-15 and LB6AN-15 catalysts, respectively, as shown in the figure 6.5 The presence of Ni^{2+} is attributed to the presence of NiO on the perovskite oxide structure, which was confirmed by the XRD analysis of the calcined catalysts. Moreover, Ni^{3+} originated from the perovskite oxide structure due to the partial replacement of Al^{3+} ions by Ni^{3+} ions during the catalyst preparation. A similar Ni^{3+} XPS peak

was reported for $LaNiO_3$ by Ning et al.[295] at 70.5 eV. Based on the XPS, it is understood that Ni is present in both the NiO and the perovskite structure. Also, the amount of $Ni^{2+}/Ni^{3+}+Ni^{2+}$ is higher for LAN-15 catalysts (58%) than the Ba-doped catalysts (42%). The higher amount of Ni^{2+} in LAN-15 catalysts could be attributed to weak metal support interaction, resulting in a high amount of NiO on the catalyst surface, as indicated by the low-temperature (264 ^oC and 344 ^oC) TPR peaks resulting from the reduction of NiO to Ni. The amount of Ni^{2+} decreased with Ba doping, likely due to the incorporation of Ni in the perovskite structure, which is reveled in high temperature reduction peaks in TPR. Furthermore, it was observed that the amount of Ni^{3+}/Ni^{2+} + Ni^{3+} increased for the Ba-doped catalysts, with the amount of Ni^{3+} ions presents being 42%, 55%, 57%, and 58% for LAN-15, LB2AN-15, LB4AN-15, and LB6AN-15 catalysts, respectively.

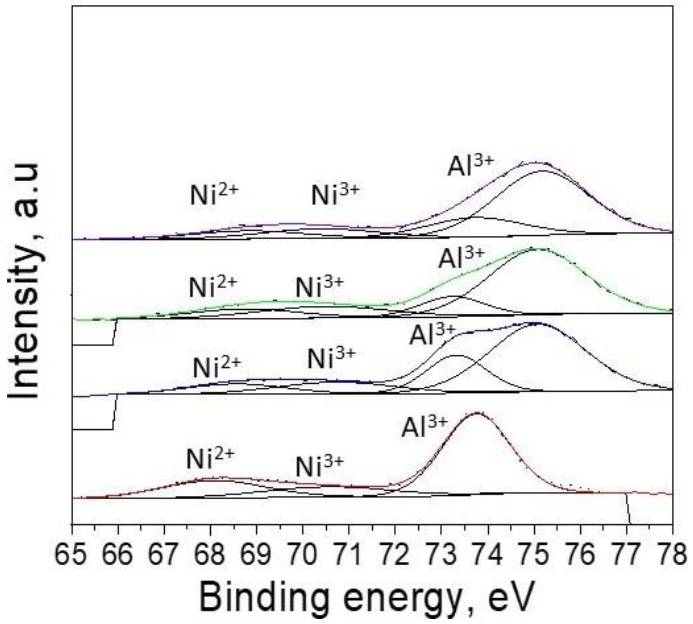

Fig.6. 5 High-resolution XPS analysis of Ni 3p profile for the calcined catalysts

The high resolution spectra of the La 3d core profiles are displayed to understand the variation in the oxidation state of lanthanum after reduction. Four major peaks appear in the LAN-15 catalysts at 833.4, 838.3 and, 848.8, 850.4 eV, which are attributed to the La $3d_{5/2}$ and La $3d_{3/2}$ spectra

corresponding to the La^{+3} on the catalyst surface. Similar peaks appeared for LB2AN-15, LB4AN-15, and LB6AN-15 catalysts, as shown in Fig.6.6 A. Thus, the doping of Ba^{2+} cations unchanged the oxidation state of La and showed +3 in all the Ba-doped catalysts. However, La $3d_{3/2}$ peaks are shifted by 0.6 eV, which may be due to the doping of Ba^{2+} cations [296]. A similar peak shift was observed for $La_{0.8}Ca_{0.2}AlO_3$ perovskite due to the Ca doping in La [297]. The Ba 3d profile displayed two distinct regions: Ba $3d_{3/2}$ (790 to 795 eV) and Ba $3d_{5/2}$ (775 to 780 eV), as shown in Fig.6.6. B. Further, the deconvolution of the 3d spectra resulted in four peaks at 777, 780, 792, and 795 eV related to the presence of BaO or $BaAl_2O_4$ [298,299]. The finding of BaO by XPS analysis agrees with the FTIR interpretation of the Ba-O functional group observed at 824 cm^{-1}.

Fig.6.6 C the O_{1s} profile of the reduced catalysts mainly shows three peaks for Ni-doped catalysts (LAN-15) and four for Ni and Ba co-doped catalysts. The peaks at 527.5 and 529.3 eV are related to the lattice oxygen (O_L) of La-O and Ni-O bonds, respectively. Additionally, peak 531.8 eV is attributed to the oxygen vacancies (O_V), respectively [286,300–302]. Similar peaks were obtained in the recent studies on $LaNiO_{3-\delta}$ perovskite oxide [301] prepared using the pechini sol-gel method. The XPS analysis O 1s profile shows peaks at 527, and 528 eV, which are attributed to the lattice oxygen species of La-O and Ni-O. Che et al. [303] also observed that O 1s XPS peaks at 527.6 and 528.5 eV are related to the La-O and Ni-O bonds. Similar peaks are observed for Ni-Ba doped catalysts. Apart from that, one additional peak was observed at 528.5 eV of the oxygen bonded with the barium cation [299]. Also, the peak positions of Ba-O are shifted towards the right with an increase in Ba from 2 mol% to 6 mol%. The shift indicates the strength of Ba-O increased for an increase in the amount of Ba doping and requires higher energy to eject an electron from the core. The ratio of O_V to O_V+O_L was calculated to be 32% for LAN-15 catalysts. The percentage of O_V is increased for Ba-doped catalysts and found to be 33%, 44%, and 54% for LB2AN-15,

LB4AN-15, and LB6AN-15 catalysts, respectively, due to the charge balance created by the Ba cation in the perovskite structure and this increase is typically expected to neutralize the charge balance in the catalyst [165,304]. Verma et al. [64] reported a similar increase in oxygen vacancies for $La_{0.9-x}Ba_xSr_{0.1}Al_{0.9}Mg_{0.1}O_{3-\delta}$ perovskite oxide.

Due to the overlapping of the La 3d profile with the Ni 2p profile, we have considered the Ni 3p profile to examine the oxidation states of Ni on the catalyst surface. Wei et al. [14] observed a similar overlapping for $La_{0.8-x}Sr_xCr_{0.85}Ni_{0.15}O_3$ perovskite catalysts in DRM. In the case of LAN-15 catalysts, Ni 3p spectra show four peaks at 66.8, 69.4, 73, and 74.7 eV. The peaks at 66.8 and 69.4 are related to $3p_{1/2}$ metallic nickel (Ni^0) and the +2 oxidation state of nickel (Ni^{+2}). The peaks observed at 73 and 74.7 eV are related to the +3 oxidation of the aluminum (Al^{+3}) [305].

The Ni and Ba co-doped catalysts exhibit peaks at 66.3, 69.7, 70.5, and 73.2 eV are attributed to the presence of Ni^0, Ni^{2+}, $Ni^{3+,}$ and Al^{3+} on the catalyst surface [283]. The surface concentration of $Ni^0/Ni^{2+}+Ni^{3+}$ is calculated to be 34%, 28%, 30%, and 32% for LAN-15, LB2AN-15, LB4AN-15, and LB6AN-15 catalysts, respectively. Based on this, it was observed that the incorporation of Ba slightly decreased the reducibility of Ni on the catalyst surface. The XRD patterns of reduced catalysts showed the exsolution of Ni-phase along with $LaAlO_3$ perovskite oxide. Based on XPS and XRD results of reduced catalysts, it is conclusive that Ni nanoparticle exsolution occurred during the reduction process.

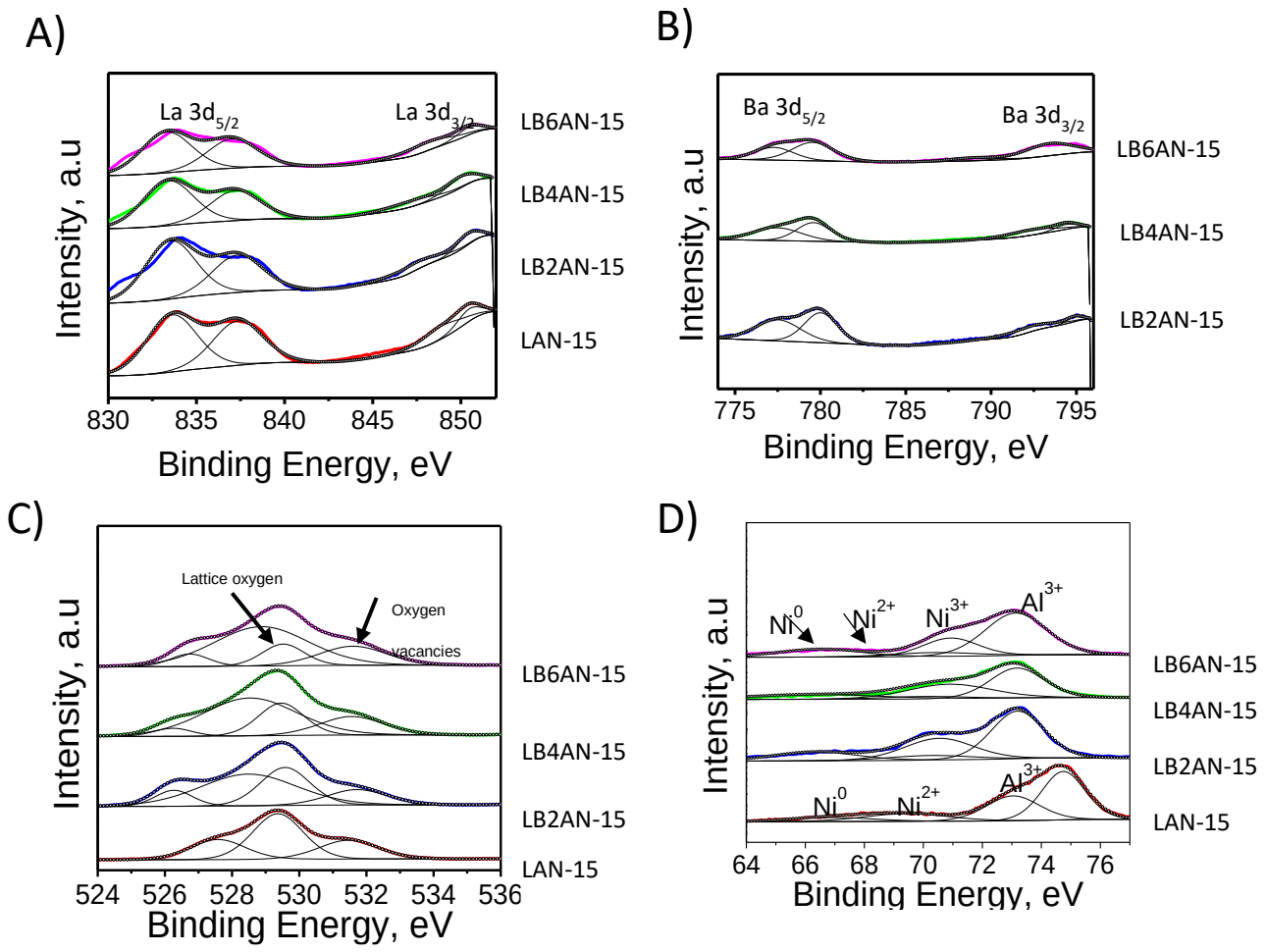

Fig.6. 6 High-resolution XPS of a A) La 3d, B) Ba 3d, C) O 1s, and D) Ni 3p profiles of catalysts reduced at 800 ℃ for 6 h in H_2

6.2.6 FESEM Analysis

The surface morphology of reduced catalysts is shown in Fig. 6.7 For all the catalysts, homogenous Ni nanoparticles are exsolved from the bulk to the surface during reduction. In the LAN-15, catalyst particles were highly agglomerated after reduction due to the poor metal support interaction between NiO and the perovskite support, as revealed from TPR analysis. Wei et

al.[185] observed particle agglomeration of Ni/$LaMnO_3$ reduced catalysts resulting from the weak metal-support interaction of NiO with $LaMnO_3$ perovskite support in DRM.

The inclusion of Ba improved the metal support interaction and the catalyst's thermal stability, which avoided particle sintering. As shown in the microscope images, the particle sintering reduced with an increase in the Ba amount. The average particle size was 38 nm, 30 nm, 27 nm, and 24 nm for LAN-15, LB2AN-15, LB4AN-15, and LB6AN-15 catalysts. A similar decrease in particle size was observed for $La_{1-x}Ba_xMnO_3$ perovskite oxide catalysts for an increase in Ba loading from 0 to 0.3 mol% [55].

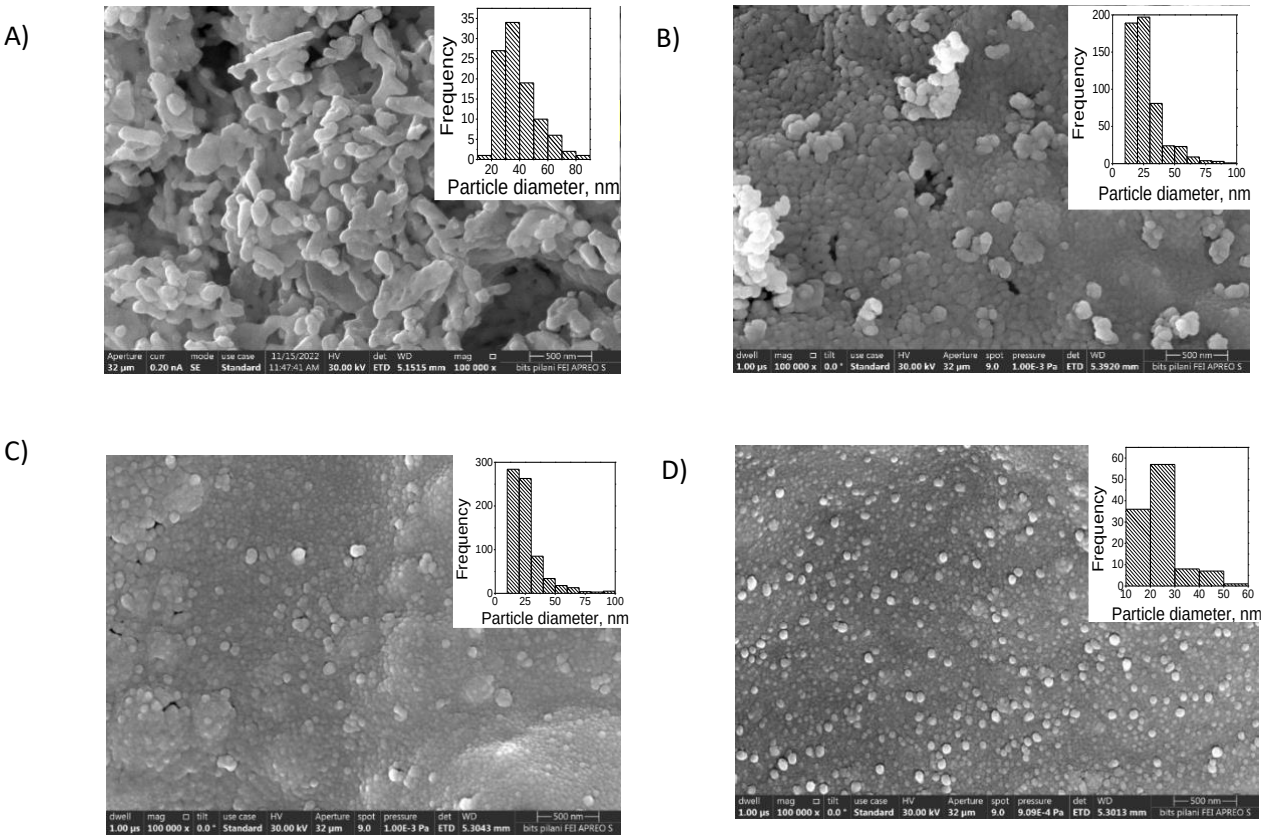

Fig.6. 7 FESEM analysis of reduced perovskite catalysts A) LAN-15, B) LB2AN-15, C) LB4AN-15, and D) LB6AN-15 at 800°C for 6 h in H_2

The morphology of the spent catalysts is studied using FESEM with EDS, as shown in Fig. 6.8. Among all the catalysts, LAN-15 showed high carbon deposition and particle agglomeration on the surface, and LB6AN-15 catalyst showed the least. The average particle size was found to be 45 nm, 40 nm, 35 nm, and 30 nm for LAN-15, LB2AN-15, LB4AN-15, and LB6AN-15 catalysts after DRBG for 12 h at 800°C. The EDX analysis (on selected areas) of the LAN-15 spent catalyst shows less La on the surface than the rest of the catalysts, maybe due to the deposition of the carbon present on the catalyst's surface. For Ba-doped catalysts, the carbon deposition was reduced due to the presence of high oxygen vacancies that provides oxygen species to the Ni sites, which enhances carbon gasification. Numerous studies in DRM signified the role of oxygen vacancies in promoting carbon gasification [282,306–309]. Furthermore, the sintering of the LAN-15 catalyst increased significantly, and particle size was found to be 77 nm after 40 h DRBG, as shown in Fig.6.9. A. Whereas less sintering was observed in LB6AN-15 catalysts, the average Ni particle size of the spent catalyst was 40 nm. The sintering resistance of the LB6AN-15 catalyst is owing to the oxygen vacancies and strong metal support interaction between exsolved Ni and the perovskite support revealed by XPS and TPR analysis.

6.2.7 TEM analysis

The HR-TEM images of LAN-15 catalysts show the presence of Ni nanoparticles on the perovskite oxide, as illustrated in Fig.6.10.A. Similarly, LB6AN-15 catalysts displayed exsolved Ni nano-particles from the perovskite support. The exsolution of Ni nanoparticles is confirmed with the elemental mapping of Ni (red colour) as shown in Fig 6.10.A, and 10.B. Similar Ni nanoparticle exsolution is observed by Wei et al. [283] for Ni-doped in $LaCrO_3$ perovskite oxide. Even though exsolution was there in both cases, the metal support interaction of the LAN-15 catalysts is weaker, which is confirmed by the low-temperature reduction peaks observed in the TPR analysis. On the

other hand, introducing Ba doping improved the metal-support interaction of the LB6AN-15 catalysts.

A)

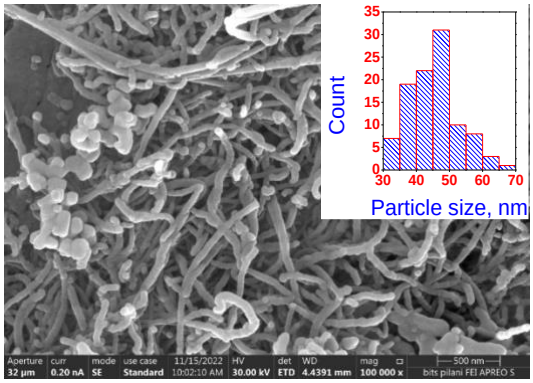

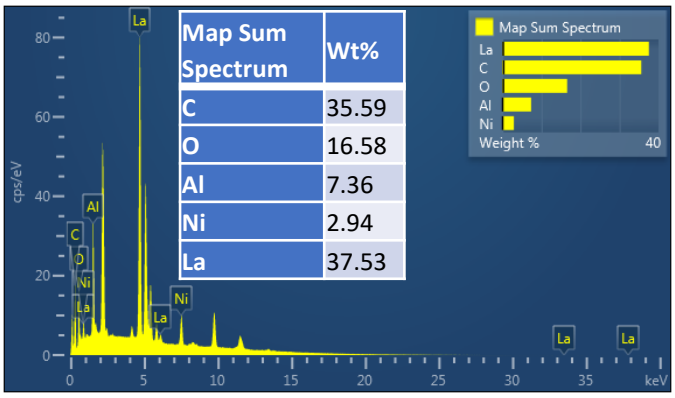

B)

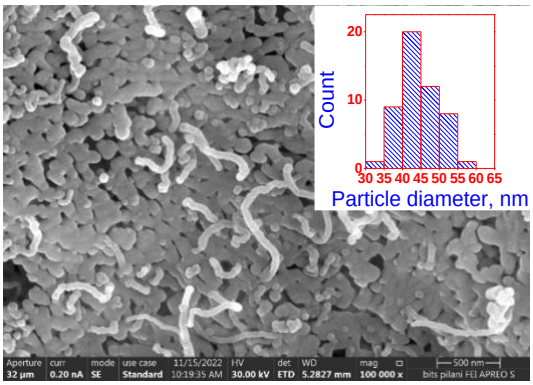

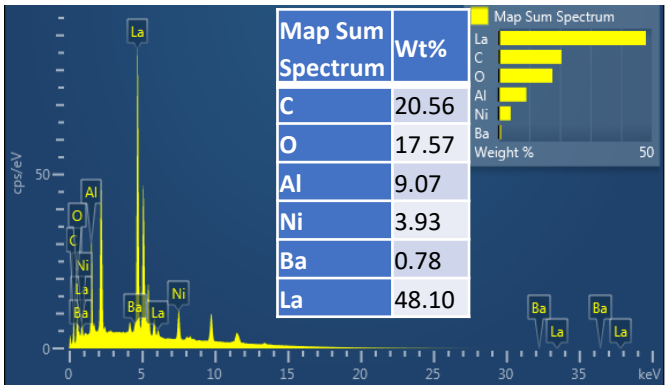

C)

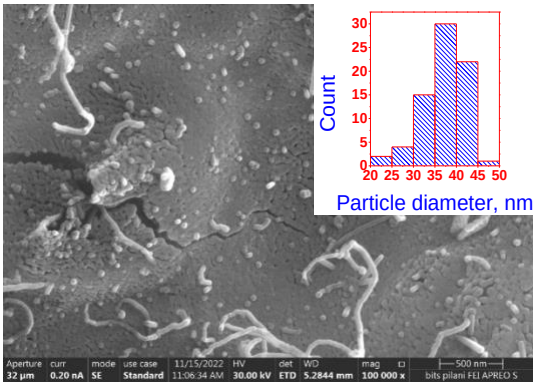

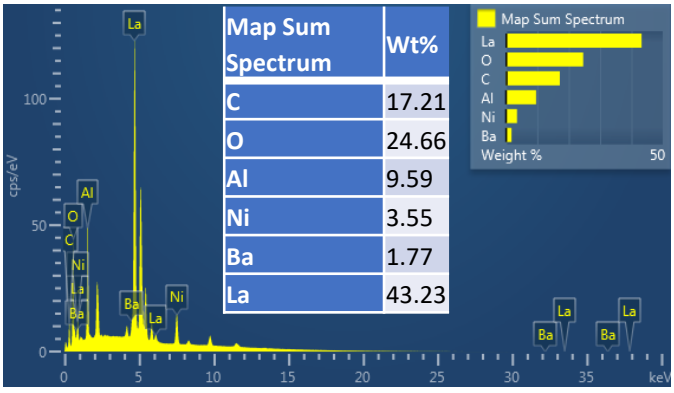

D)

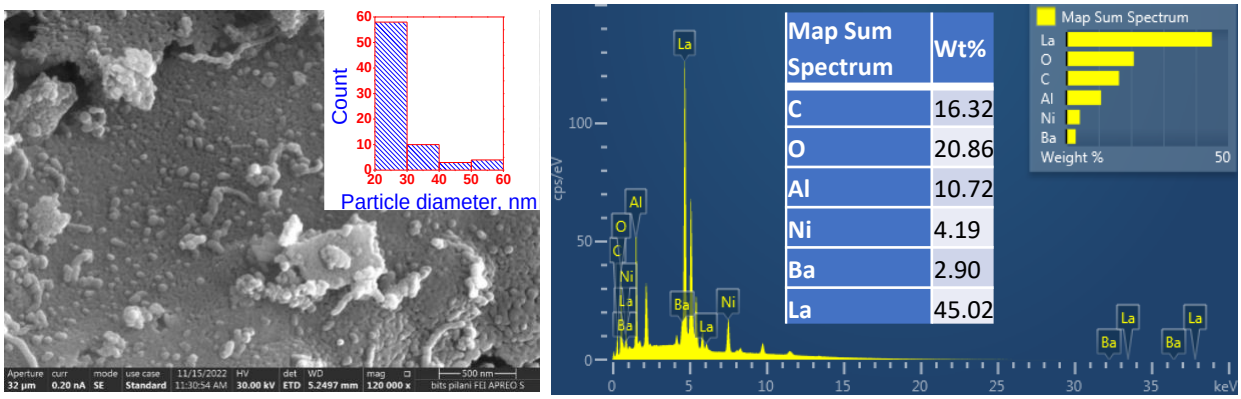

Fig.6. 8 FESEM and EDX analysis of spent catalysts A) LAN-15, B) LB2AN-15, C) LB4AN-15, and D) LB6AN-15 after 12 h DRBG for CH_4/CO_2=1.5 at 800°C

A)

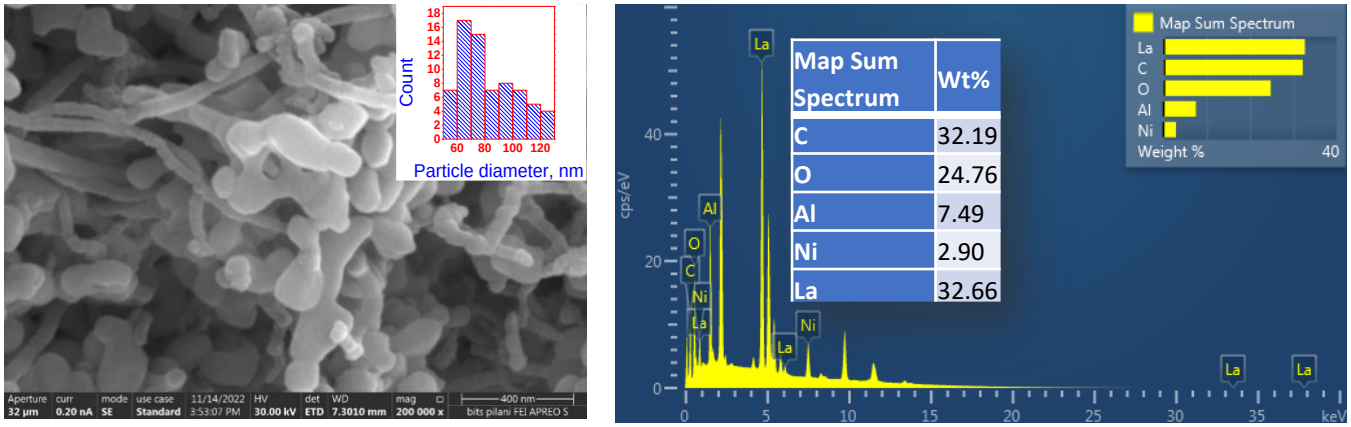

B)

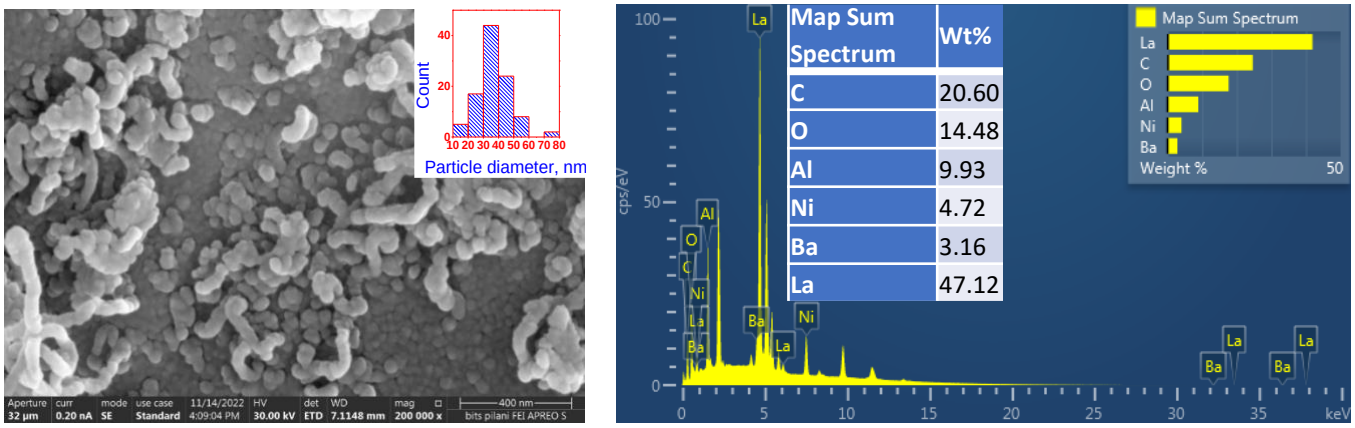

Fig.6. 9 FESEM and EDX analysis of spent catalysts A) LAN-15 and B)LB6AN-15 after 40 h DRBG for CH_4/CO_2=1.5 at 800°C

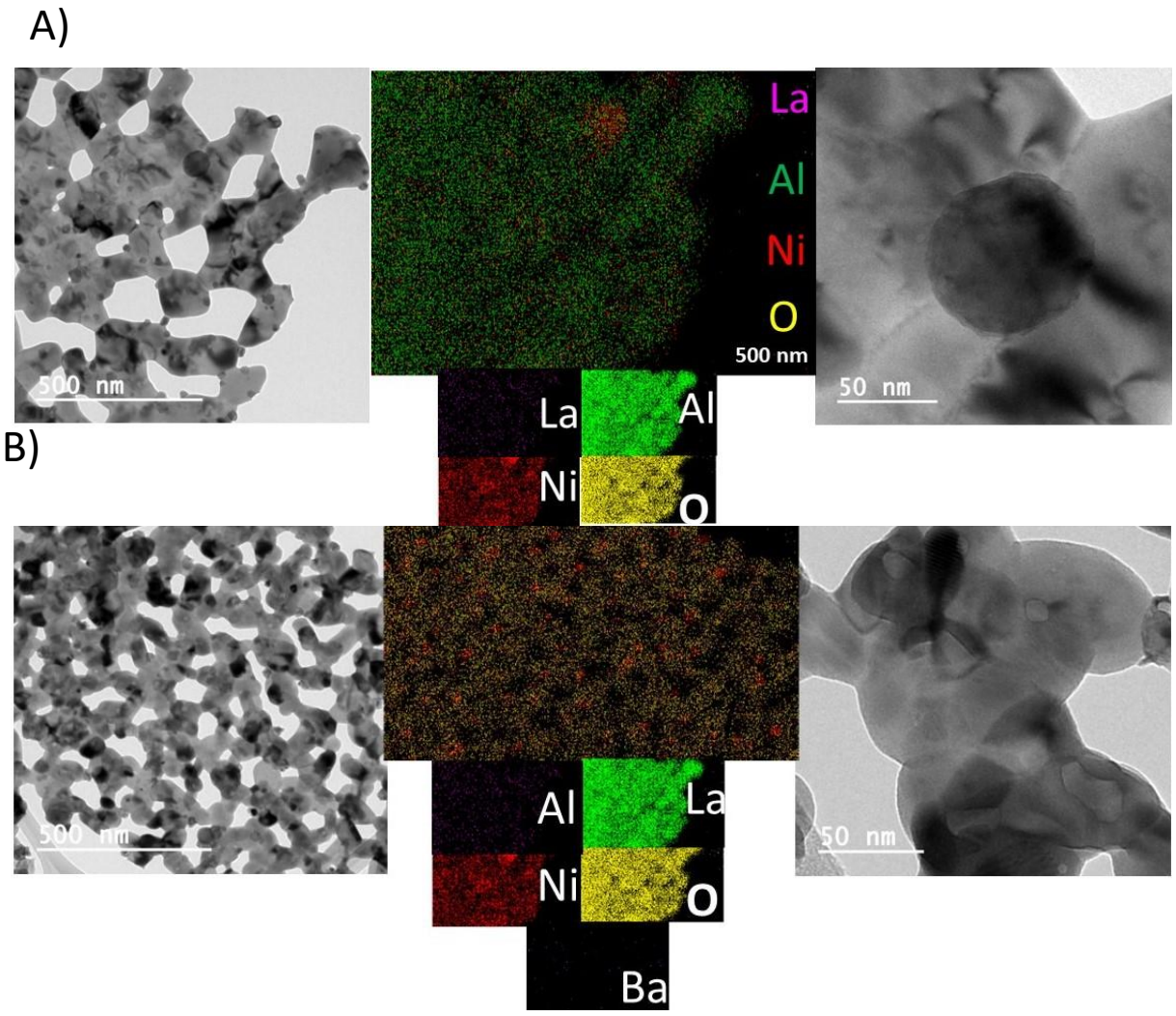

Fig.6. 10 HRTEM images and elemental mapping analysis of reduced catalysts A) LAN-15 and B) LB6AN-15

6.2.8 TGA-DTA

Carbon deposition on spent catalysts is determined using thermogravimetric analysis, as displayed in Fig.6.11 The amount of carbon formed on spent catalysts after 12 h TOS is calculated to be 18%, 13.4%, 9.5%, and 8.4% for LAN-15, LB2AN-15, LB4AN-15, and LB6AN-15 catalysts, respectively. Moreover, DTA analysis shows a broad shoulder exothermic peak between 400 – 600℃ for all spent catalysts, which can be attributed to filamentous carbon on the catalyst surface

[310,311]. The partial doping of Ba in La has facilitated the oxygen vacancies and helped to gasify the deposited carbon on the catalyst surface. A similar decrease in carbon deposition was observed for 5 wt% Ba promoted on 5 wt% Ni/YZr catalysts [312].

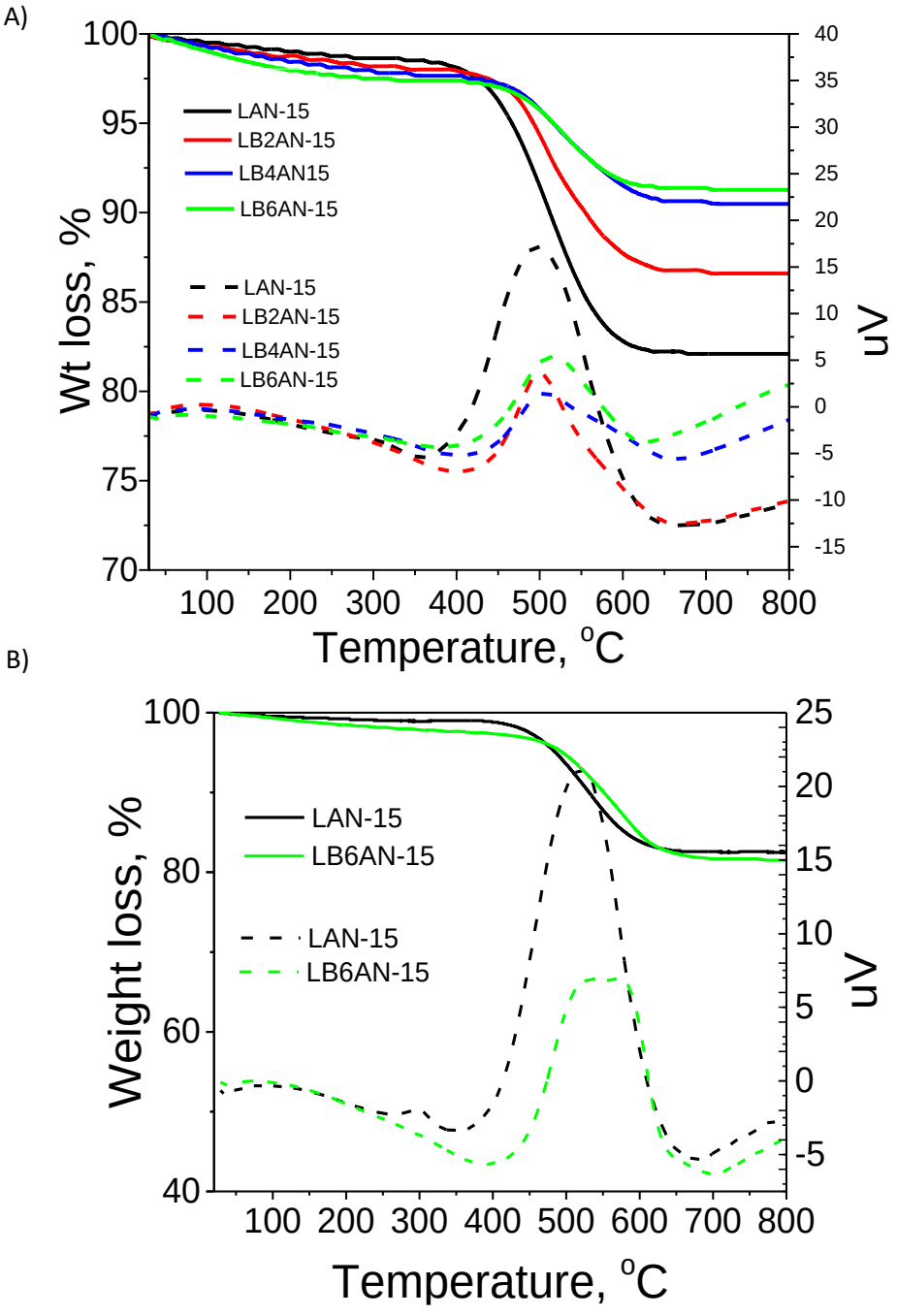

Fig.6. 11TGA-DTA analysis of spent catalysts A) after 12 h, B) 40 h time on stream for DRBG at 800°C for CH_4/CO_2=1.5.

The carbon deposition was reduced from 16 wt% to 4 wt% due to adding Ba. The carbon tolerance of Ba-promoted catalysts was attributed to the oxygen storage capacity, which helps to minimize the catalyst deactivation via the carbon gasification [312]. The size of the Ni nanoparticles in catalysts can significantly affect the coking performance in dry reforming of methane. Generally, smaller Ni particle size leads to a higher activity and selectivity towards the desired reaction, while larger particle sizes may result in higher carbon deposition and catalyst deactivation [39,313,314]. For instance, Aramouni et al. [39] studied the thermodynamic analysis of DRM on the effect of particle size on carbon formation. It was reported that carbon deposition could be avoided for a particle size of 5 – 6 nm. During DRM, CH_4 decomposes on metallic Ni^0 into reactive CH_x species near Ni crystallite for small Ni particles and away from bigger Ni particles. The CH_x species placed near Ni crystallites readily react with activated CO_2 and form CO and whereas, as CH_x species located far from the Ni crystallites, due to low reactivity with CO_2 will be deposited as carbon on the Ni particle surface and eventually block the active sites of Ni and leads to catalyst deactivation [308].

Further, the TGA-DTA (Fig.6.11.B) and FESEM (Fig.6.9.A) analysis of 40 h catalytic studies showed interesting results on coke deposition and Ni particle size for LAN-15 and LB6AN-15 catalysts. The Ni particle size was obtained at 77 nm and 40 nm, and carbon deposition was observed to be 18% and 19% for LAN-15 and LB6AN-15 catalysts, respectively. Even though significant particle sintering is observed in LAN-15 catalysts, the carbon deposition does not increase further after 12 h DRBG in the case of LAN-15 catalysts may be due to the reduced dissociation of CH_4 on the agglomerated Ni surface compared to the carbon gasification during DRBG [315].

A similar observation was reported in a recent study by Fonseca et al.[315], over 10 wt% Ni/CeO_2 catalysts in DRM. Authors observed that carbon deposition increases considerably (1.6 to 21 mg/gcat.h) for a Ni crystallite size of 10 to 30 nm and found to be decreased (5.9 mg/gcat.h) further increase in Ni size 45 nm after 24 TOS, due to the decrease in CH_4 conversions caused by the slow CH_4 decomposition. Similar observation was reported by Damaskinos et al. [316] for x Ni/$Ce_{0.8}Ti_{0.2}O_{2-\delta}$ (x = 3, 7.5 and 10 wt%) catalysts in DRM. Authors observed that carbon formation rate considerably increased from 20 nm to 40 nm for DRM at 750 C and thereafter it became constant. Even though both the catalysts had the same carbon deposition after 40 h, the activity of LAN-15 continuously decreased after 12 h with a deactivation rate of 1.14%/h and 0.93%/h of CH_4 and CO_2 conversions. In contrast, as discussed in the activity analysis, a less deactivation rate was observed at 0.37%/h and 0.26%/h of CH_4 and CO_2 conversions for LB6AN-15 catalysts. The decrease in catalytic activity is attributed to the sintering of Ni nanoparticles in the case of LAN-15 catalysts.

6.2.9 Raman Analysis

The nature of carbon on the spent catalyst is further studied using Raman analysis, as shown in Fig 6.12. Raman analysis reveals two prominent peaks at 1325 and 1580 cm^{-1} pertained to carbonaceous species' D and G bands. The D – band refers to the defective/disordered sp^2 carbon materials, whereas the G – band is related to graphitic carbon; between these two, graphitic carbon is mainly responsible for catalytic degradation. Additionally, the peak intensity ratio of the G to D – band (I_G/I_D) determines the graphitic nature of the carbon deposited on the catalyst surface [65]. The I_G/I_D values are calculated to be 1.32, 1.26, 1.0, and 0.85 for LAN-15, LB2AN-15, LB4AN-15, and LB6AN-15 catalysts, respectively, after 12 h TOS. The doping of Ba decreased the

graphitic nature of carbon on the catalyst surface, which is in agreement with the SEM analysis of the spent catalyst.

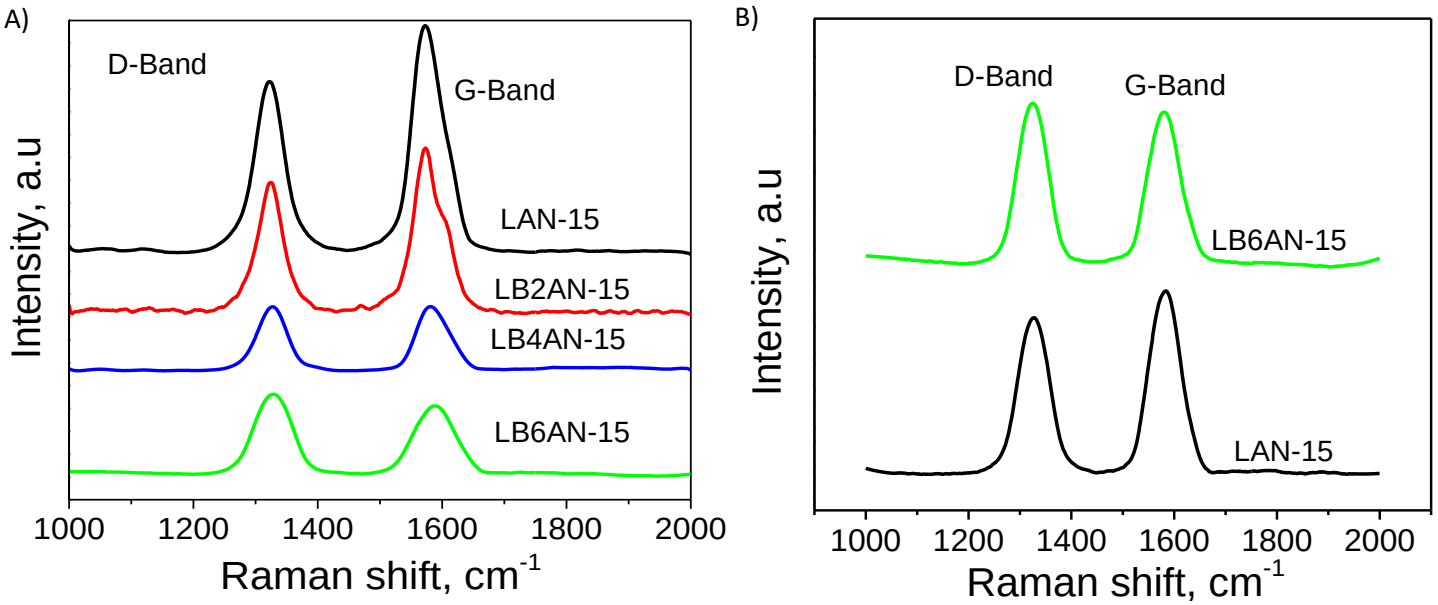

Fig.6. 12 Raman analysis of spent catalysts A) after 12 h, B) 40 h time on stream for DRBG at 800℃ for CH_4/CO_2=1.5.

Du et al. [317] reported similar D and G bands for $La_{0.9}Ce_{0.1}NiO_3$ and $LaNiO_3$ perovskite oxide catalysts in DRM. The Ce doping decreased the carbon's graphitic nature on the catalyst surface and improved the catalyst activity. Similar bands were observed for 40 h spent catalysts, as shown in Fig. 8. b. The I_G/I_D ratio of the catalysts was calculated to be 1.1 and 0.7 for LAN-15 and LB6AN-15 catalysts, respectively. Based on the Raman analysis, LAN15 shows higher graphitic carbon than LB6AN-15 catalysts.

6.3 Activity studies

The stability of the catalysts in DRBG was studied using short (12 h) and long-term (40 h) experiments. Figures 6 13 and 6 14 show the short-term stability of catalysts for two distinct feed ratios (CH_4 to CO_2), 1.5 and 2.0, of DRBG at 800 ^oC. The initial conversions of CH_4 and CO_2 for LAN-15, LB2AN-15, LB4AN-15, and LB6AN-15 were obtained to be 75% and 97%, respectively. The conversions of CH_4 and CO_2 were decreased after 2 h, and the final conversions after 12 h were found to be 70% and 94% for all the catalysts. It is obvious that CO_2 conversions are higher than CH_4 conversions because CO_2 is the limiting reactant in the feed mixture. The mole fractions of H_2 and CO follow similar trends of CH_4 and CO_2 conversions as depicted in Fig. 5.10. The steady-state H_2 and CO mole fractions are obtained to be 0.32 and 0.27 for all catalysts, respectively, and corresponding H_2/CO is greater than 1.0 for all tested catalysts, which denotes the absence of reverse water gas shift reaction (RWGS) [156]. Despite the carbon formation and particle agglomeration observed in TGA-DTA, the catalysts were highly active in the 12 h reaction, which may be due to the presence of the Ni on the carbon nanotube, as observed in the SEM of the spent catalyst.

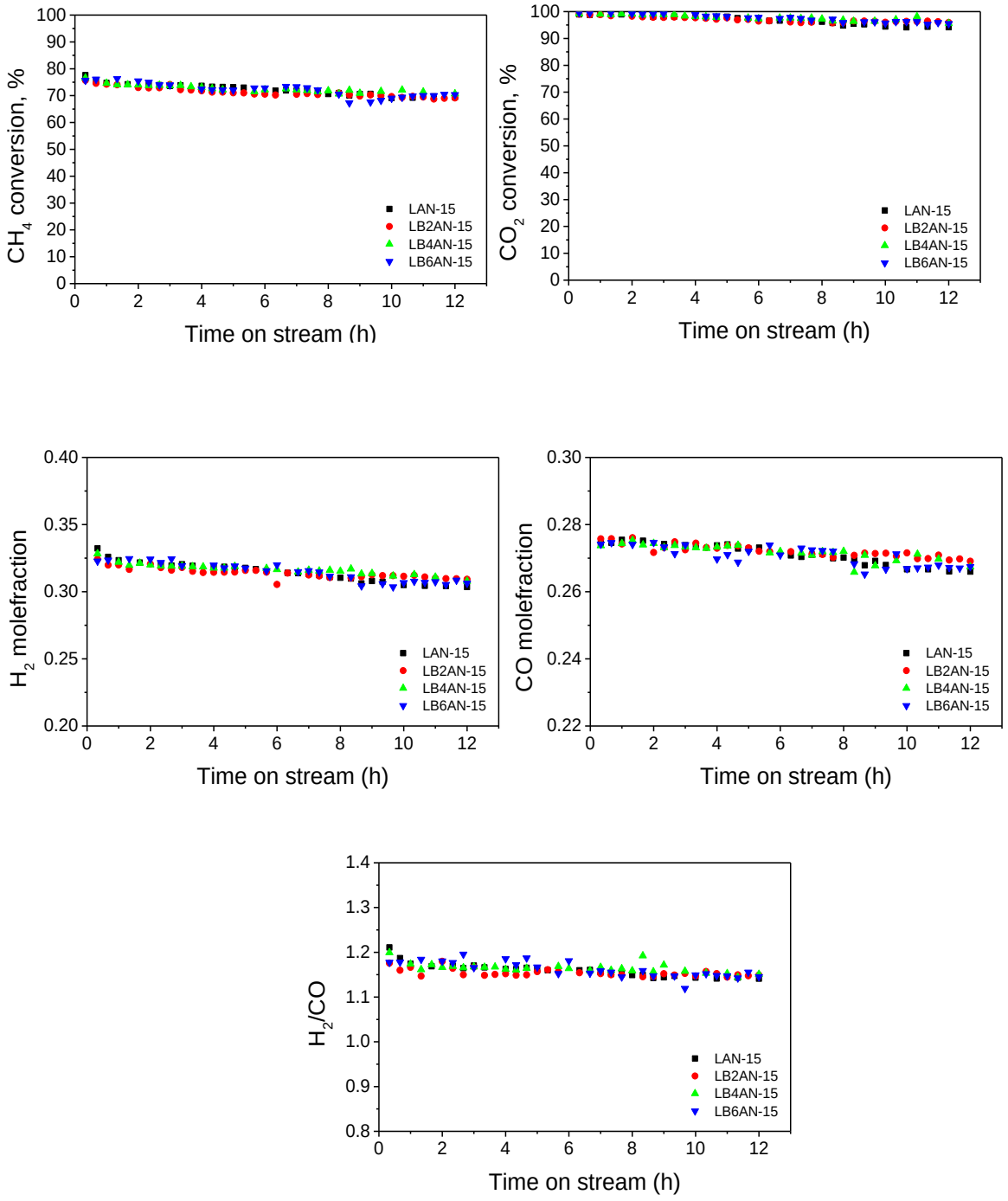

Fig.6. 13 CH_4, CO_2 conversions, H_2, CO mole fractions and H_2/CO values of LAN-15, LB2AN-15, LB4AN-15, and LB6AN-15 for CH_4/CO_2 = 1.5 at 800°C

Fig. 6.14. Shows the CH_4, CO_2 conversions, mole fractions of CO and H_2, and H_2/CO ratio of LAN-15, L2BAN-15, L4BAN-15, and L6BAN-15 catalysts for DRBG at 800℃ having a feed ratio of 2.0. The initial conversions of CH_4 and CO_2 were 61% and 99% for LAN-15 and LB2AN-15, LB4AN-15, and LB6AN-15 perovskite oxide catalysts. The conversions of CH_4 and CO_2 were decreased during the reforming, and the steady state conversions of LAN-15 obtained 52% and 90%. Similar deactivation behavior was observed for Ba-doped catalysts, but steady-state conversions were slightly improved, found to be 52%, 55%, and 55% of CH_4; final CO_2 conversions were obtained as 92%, 94%, and 94% for LB2AN-15, LB4AN-15, and LB6AN-15 catalysts respectively. The conversions of CH_4 are decreased with an increase in the feed ratio from 1.5 to 2.0, and no significant change was observed for CO_2 conversions. The obtained conversions are higher than in existing studies [222,318]. For instance, Sache et al. [318] reported a 50% CH_4 conversion for DRBG on Ni-doped pyrochlore ($Ni/La_2Zr_2O_7$) catalysts. The conversions of CH_4 decreased from 90% to 50%, with an increase in the CH_4/CO_2 ratio from 1.0 to 1.85 at 800℃. Similarly, Evans et al. [222] obtained a 44% conversion of CH_4 for $SrZr_{0.96}Ni_{0.04}O_3$ perovskite oxide catalysts for biogas reforming at 800℃ and CH_4/CO_2=2.0.

However, no significant change was observed for CO_2 conversions for feed ratios 1.5 and 2.0. Figure 11. c,d shows H_2 and CO mole fractions, which are in line with the CH_4 and CO_2 conversions. The H_2/CO ratio was calculated to be 1.02 and 1.07 for Ni and Ni – Ba co-doped catalysts. Based on the activity studies mentioned above, all the catalysts displayed high activity and stability in short-term activity tests 12 TOS. However, the spent catalyst characterizations such as TGA-DTA and FESEM reveal that the deposition of carbon and catalyst sintering was highest for LAN-15 catalysts and least for LB6AN-15 catalysts. Based on the carbon deposition and

particle sintering, LAN-15 and LB6AN-15 catalysts were selected for 40 h long-term activity studies to understand the effect of Ba in catalytic activity.

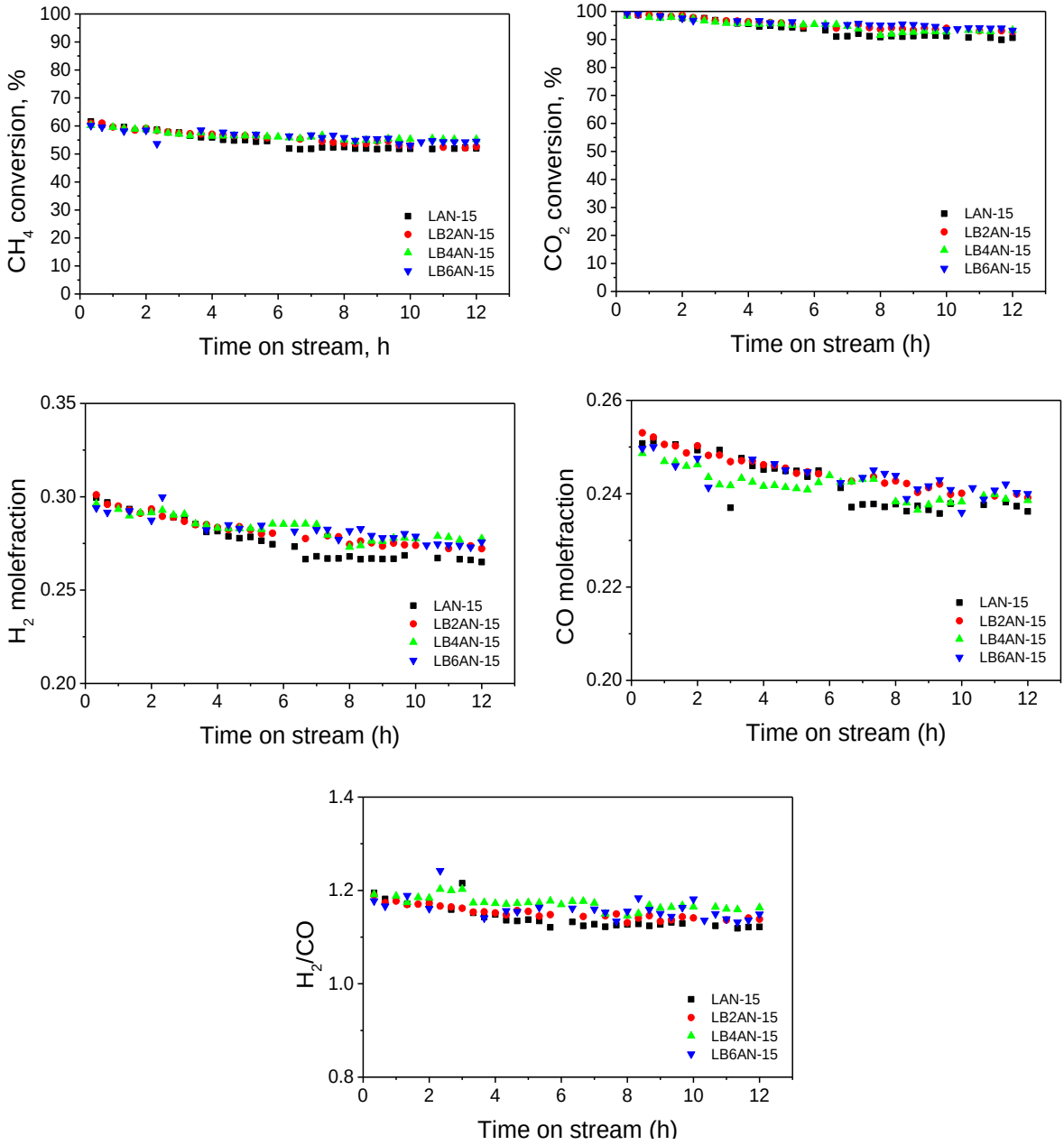

Fig.6. 14 CH_4, CO_2 conversions, H_2, CO mole fractions and H_2/CO values of LAN-15, LB2AN-15, LB4AN-15, and LB6AN-15 for CH_4/CO_2 = 2.0 at 800°C

Fig.6.15 compares 40 h activity analysis for LAN-15 and LB6AN-15 catalysts. The LB6AN-15 catalyst showed more stable catalytic activity than the LAN-15 catalyst at 800°C for CH_4/CO_2=1.5. Both the catalysts displayed a stable performance for an initial 12 h on DRBG operation, having a conversion of CH_4 = 71% and CO_2 = 94%, 90% for LB6AN-15 and LAN-15 catalysts, respectively. Afterward, the conversions of LAN-15 catalysts start to decrease at a deactivation rate of 1.2%/h and 1.1%/h of CH_4 and CO_2. The final conversions of CH_4 and CO_2 were found to be 35% and 60% for the LAN-15 catalyst. In contrast, the LB6AN-15 catalyst showed a stable activity of having a CH_4 conversion of 60% with less deactivation rate (0.45%) and CO_2 conversions of 91% after 40 h TOS. As a result of a decrease in CH_4 and CO_2 conversions of LAN-15, the corresponding H_2 and CO mole fractions are also decreased. The H_2/CO values are found to be 0.85 and 1.1 for LAN-15 and L6BAN-15 catalysts, respectively, after 40 h TOS. The conversions in this study are higher than in the existing DRBG experiments [65,318–320]. For instance, Latsiou et al. [320] studied DRBG over Ni – Al wet impregnated and eggshell catalysts and reported a 50% CH_4 conversion and 80% CO_2 conversion at 800 C for a feed ratio (CH_4/CO_2) of 1.5. Similarly, Sache et al. [318] reported 58% CH_4 and 76% CO_2 conversions over 10 wt% Ni doped in $La_2Zr_2O_7$ pyrochlore structure catalysts.

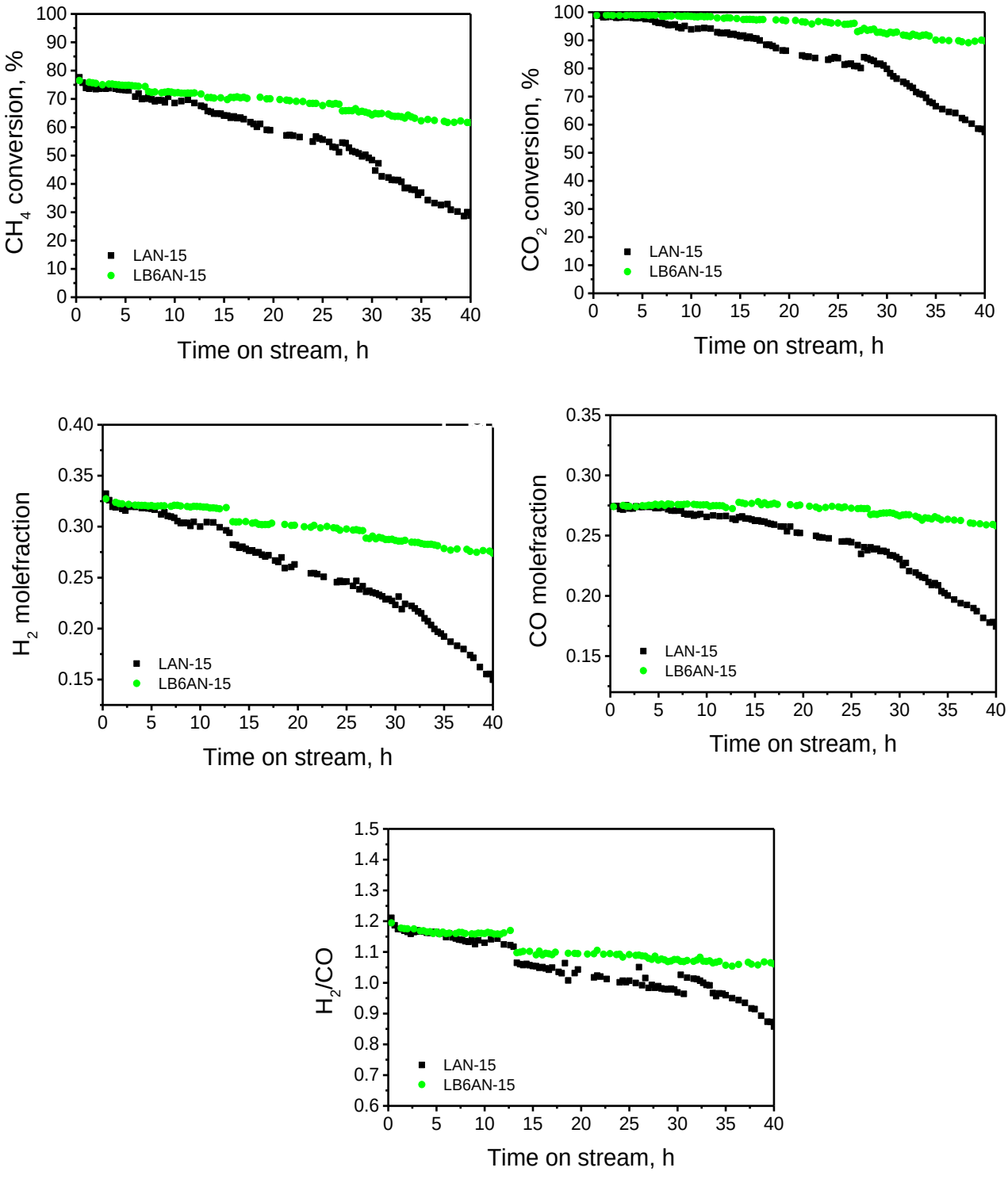

Fig.6. 15 CH_4, CO_2 conversions, H_2, CO mole fractions and H_2/CO values of LAN-15 and LB6AN-15 catalysts, at 800°C for CH_4/CO_2=1.5

The 40 h DRBG studies of LAN-15 and LB6AN-15 catalysts show the effect of Ba doping in catalytic activity. TGA-DTA analysis of 40 h LAN-15 spent catalysts showed 19% carbon deposition, the same as observed in 12 h LAN-15 spent catalysts. The type of carbon deposited on the catalyst surface filamentous was revealed from DTA analysis, which does not deactivate the catalysts in DRM due to the presence of active Ni on the tip of the carbon filament [51,321]. The Ni particle sintering was observed in the spent catalyst surface, and the particle size increased from 44 nm to 76 nm after 40 h DRBG. Based on the spent catalyst characterization, the loss of catalytic activity or deactivation of LAN-15 catalysts is attributed to the sintering of the catalyst more than carbon deposition. The sintering of the LAN-15 results from the weak metal-support interaction between the NiO particles and the perovskite structure, as evidenced by the TPR analysis. Similar catalytic deactivation was observed by Chai et al. [184] over $La_{0.46}Sr_{0.34}Ti_{0.9}Ni_{0.1}$ perovskite catalysts for DRM at 700℃ having a feed ratio of 1.0. The sintering of the Ni particles resulted from the weak metal-support interaction. Furthermore, loss in catalytic activity due to sintering is a significant challenge for developing Ni-based catalysts in DRM [211,322,323].

In this study, the sintering of the Ni nanoparticles was overcome by improved metal-support interaction between perovskite and Ni particles. This phenomenon was achieved by doping alkaline earth metals such as Ba in the La site. The partial doping of Ba in the La site improved the metal support interaction and tolerance to particle sintering, as revealed by TPR and FESEM analysis. It also enhanced oxygen vacancies within the LB6AN-15 perovskite oxide (as shown in the XPS analysis) system, improving oxygen mobility, and the presence of oxygen avoided the possible sintering of Ni particles during DRBG in LB6AN-15 catalysts [324]. The oxygen vacancies indirectly enhance the metal support interaction by bonding with the Ni particles, thus making it hard to reduce, as revealed in the TPR high-temperature peaks for the LB6AN-15

catalyst. A similar effect of oxygen vacancies was reported in the literature [324,325]. For instance, Du et al. [325] observed that the solid metal support interaction of Ni and CeO_2 resulted from the oxygen vacancies created within the CeO_2 nanoplates support. Furthermore, oxygen vacancies promote the activation of CO_2, which is highly beneficial for the gasification of carbon deposited on the catalyst [326]. Overall, the partial doping of Ba improved the catalysts' sintering resistance, thus eliminating catalyst deactivation. The LB6AN-15 catalyst showed superior catalytic activity than the LAN-15 catalyst due to the high oxygen vacancies and strong-metal support interaction between exsolved Ni and perovskite oxide.

6.4 Conclusions

In this study, Ni and Ba co-doped $La_{0.9}AlO_3$ perovskite oxide catalysts were prepared by citrate sol-gel synthesis, and activity experiments were performed at 800℃ for a feed ratio (CH_4/CO_2) of 1.5 and 2. All the prepared catalysts retained the perovskite structure after DRBG studies, which was confirmed with the XRD analysis of spent catalysts. Doping of Ba improved the thermal stability of the perovskite oxide catalyst, resulting from the strong metal support interaction as revealed in TPR analysis. Also, Ba-doped catalysts increased the oxygen vacancies in the perovskite oxide catalyst, and their amount was increased with Ba doping. The surface morphology of the reduced catalyst shows the sintering of Ni particles for LAN-15 catalysts, and particle sintering was found to be decreased with the substitution of Ba. TGA-DTA analysis of the spent catalysts (12 h) shows high carbon deposition for LAN-15 catalysts and less for LB6AN-15 catalysts. Irrespective of the different amounts of carbon deposition, the activity of the catalysts remains unchanged or unaffected during 12 h DRBG studies. However, long-term activity (40 h) experiments reveal the deactivation of the LAN-15 catalyst due to the sintering of the Ni particles. The LB6AN-15 catalyst showed high catalytic activity and stability for 40 h TOS due to strong metal support interaction and highly exsolved Ni nanoparticles on the catalyst surface, making it a desirable catalyst for DRBG.

7 Summary and Outlook

7.1 Conclusions

Dry reforming of biogas (DRBG) has recently gained prominence due to its environmentally friendly credentials. The technology involves using biogas without additional purification methods for CO_2 removal, making it highly attractive for commercialization. DRBG occurs at higher temperatures (> 700℃) over a metal catalyst, with nickel being the most preferred option due to its high activity and low cost. The syngas produced in this process has an H_2/CO ratio of 1.0, which is ideal for the FT synthesis to produce liquid fuels such as dimethyl ether and methanol. However, the main drawback of DRBG is the deactivation of the nickel catalyst. The nickel catalyst used in this process is susceptible to sintering and carbon deposition, which can cause deactivation within hours. This deactivation necessitates frequent replacement of the catalyst, making the commercialization of the process less attractive. While the deactivation of nickel, or any transitional metal catalyst, is inevitable, altering the chemical composition and physical properties of the catalyst can delay the deactivation time.

One way to delay deactivation of nickel catalyst is by changing the particle size of the catalyst. The smaller the particle size, the higher the surface area, which leads to higher activity. Additionally, finding the right balance between particle size and support interaction is crucial to optimize the performance of Ni-based catalysts. Optimizing the metal-support interaction can improve the catalyst's performance and delay deactivation. Moreover, dispersion is another crucial aspect that impacts the performance and stability of the catalyst. The low metal dispersion can lead to the sintering of particles, resulting in low catalytic activity. Furthermore, it is recommended that

the surface basicity of catalysts plays a critical role in CO_2 activation and the elimination of carbon deposition during the DRBG.

The Ni/γ-Al_2O_3 cordierite catalysts explored in this study demonstrated high stability in DRBG at 800℃ for 40 hours with CH_4/CO_2 ratios of 1.0, 1.5, and 2.0. The results indicate that increasing the calcination time of the catalysts from 4 h to 20 h improves their catalytic activity. This improvement is due to the increased diffusion of Mg and Si in the cordierite to the active alumina layer, forming a strong metal-support interaction. High-temperature annealing of the 20-hour calcined catalysts leads to the formation of highly stable Ni-Al and Ni-Mg spinels formed by the reaction between NiO, Al_2O_3, and MgO. The reduction of these spinels results in the formation of highly dispersed Ni nanoparticles (7 nm) on the catalyst surface, which have a strong metal support interaction as revealed from TEM and TPR analysis. In terms of activity, all catalysts (C-4, C-10, and C-20) showed similar activity at CH_4/CO_2 = 1.0, with CH_4 and CO_2 conversions are 95% and 86%, respectively, for 40 h TOS.

However, for CH_4/CO_2 from 1.0 to 1.5 and 2.0, the catalytic activity decreased due to increased carbon deposition on the catalyst surface. The activity order was C-20 > C-10> C-4 catalysts for 40 hours. Analysis of spent catalysts showed that the decrease in carbon deposition on the C-20 catalyst was due to smaller Ni nanoparticles on the catalyst surface. Additionally, high calcination time enhanced metal-support interaction, indirectly improving the dispersion of Ni catalysts. Surface morphology and Raman analysis of spent catalysts revealed different types of carbon deposition on the surface. Graphitic-natured tip-grown carbon was observed on the catalyst surface for C-4 and C-10. This type of carbon is active due to the presence of Ni on the tip of the carbon nanotubes but detrimental in the long term as it leads to continuous carbon buildup on the

catalyst surface, causing the Ni to be far away from the catalyst support and hindering carbon gasification.

In contrast, base-grown carbon was observed on the C-20 catalyst surface. This type of carbon is easily gasified due to the availability of surface oxygen species to the Ni. Additionally, the presence of Mg on the active layer of the C-20 catalyst improves CO_2 adsorption, thereby increasing CO_2 conversions and carbon gasification.

The experiments on Ni-based monoliths by varying calcination time, resulted in enhanced catalytic activity due to the strong metal support interaction and high Ni dispersion. Furthermore, the type of carbon deposition on the catalyst surface significantly affects its stability and reactivity. Base-grown carbon is found to be more easily gasified due to its accessibility to surface oxygen species and the presence of Mg on the active layer, which enhances CO_2 adsorption and activation. These findings provide valuable insight into the utilization of Ni/γ-Al_2O_3 cordierite catalysts for DRBG, which could have important implications for producing hydrogen and other value-added chemicals from renewable resources.

The inclusion of CeO_2 on Ni-loaded cordierite decreased the conversions of both CH_4 and CO_2 because the Ni-active sites were blocked by CeO_2. However, the addition of CeO_2 was found to reduce the graphitic nature of the carbon on the catalyst surface. The use of monolith catalysts has the potential to replace the pellets in scaling-up processes. However, before it can be widely adopted, extensive research is required on depositing the active layer on monolith substrates. One of the major challenges in this regard is finding ways to evenly distribute the catalytic layer on substrates with complex shapes. This is because some active layers are limited to a specific monolith area, making it difficult to achieve a uniform layer distribution through the wash coating

process. Further research and optimization of the deposition process are required to overcome this challenge.

Furthermore, Ni-based catalysts in perovskite structures can minimize carbon deposition, resulting in enhanced catalytic activity. The Ni exsolution from perovskite catalysts enhances anti-sintering and anti-coking properties. The catalysts $La_{0.9-x}Ba_xAl_{0.85}Ni_{0.15}O_3$ (x = 0, 0.02, 0.04, and 0.06; LAN-15, LB2AN-15, LB4AN-15, and LB6AN-15) were prepared using the citrate sol-gel synthesis method and calcined at 850 ℃ for 7 h. Activity experiments at 800 ℃ for a feed ratio of 1.5 and 2.0 showed high activity and stability for all catalysts for 12 h on stream. However, in the 40 h experiments, Ba-doped catalysts (LB6AN-15) displayed enhanced catalyst stability and stable conversions than LAN-15 catalysts (Ba = 0). Due to the poor metal interaction, the Ni particles are highly sintered with the particle size rising from 34 nm to 72 nm during DRBG for LAN-15 catalysts, but the presence of Ba decreased the particle sintering from 24 to 44 nm during the 40 h DRBG. XRD analysis of reduced and spent catalysts shows the host perovskite structure along with the active Ni phase. Ba doping increased oxygen vacancies within the lattice and improved carbon gasification, which was confirmed by the TGA-DTA of spent catalysts. Additionally, the nature of graphitic carbon was reduced for the Ba-doped catalysts. Furthermore, adding Ba improved the metal support interactions, which in turn helped Ni particle dispersion and tolerant to sintering.

In conclusion, DRBG is a promising technology for producing syngas, but the deactivation of the Ni-based catalyst used in the process is a significant hurdle for commercialization. However, catalyst deactivation can be minimized by controlling various factors that need to be considered, including particle size, metal-support interaction, dispersion, and basicity. In this study, Ni particle size is controlled by increasing the calcination time, resulting in the enhanced catalytic activity

and stability of Ni-based monoliths. Further, Ba doped Ni-exsolved perovskite with a controlled reduction in H_2 resulted in steady catalytic activity due to the improved dispersion and anti-sintering of active Ni nanoparticles. Moreover, the metal support interaction improved with the doping of Ba in the perovskite structure. Overall, the studied catalysts displayed high activity in DRBG for 40 h. Among all the catalysts studied, LB6AN-15 catalyst and C-20 monolith catalyst displayed enhanced catalytic activity in terms of CH_4 and CO_2 conversions, due to reduced carbon deposition and Ni particle sintering.

7.2 Future scope

The goal for DRBG is to achieve carbon-free operation with high catalytic activity and stability. Additionally, the catalyst should be tolerant to small concentrations of H_2S in biogas during the DRBG. Nickle-based catalysts are the best choice due to their enhanced C-H bond succession and availability. However, Ni-based catalysts must be developed to withstand harsh operating conditions to avoid catalyst deactivation and poisoning during the DRBG.

The present experiments were conducted at three different CH_4/CO_2 ratios of 1, 1.5, and 2.0. The primary issue was found to be catalyst sintering, and carbon formation, resulting in catalyst deactivation. Further studies could be conducted to control the Ni particle size using other preparation techniques such as spray pyrolysis and electrodeposition method. Spray pyrolysis involves spraying a solution containing the nickel precursor onto a high-temperature surface, resulting in rapid evaporation of the solvent and the formation of nickel particles of controlled size. While, in electrodeposition, depositing nickel onto a substrate, results in a catalyst with a controlled particle size.

Another way to minimize the catalyst deactivation is by intermittently adding an optimum amount of steam along with the biogas to gasify the deposited carbon on the catalyst surface. However, the rate of steam addition and duration to be studied thoroughly because excessive steam may lead to methane steam reforming and enhanced CO_2 formation from the water gas shift reaction. Additionally, the research can be carried out by periodic regeneration of the Ni catalyst by oxidation or reduction can remove deposited carbon and restore its activity and selectivity. Oxygen-containing gas such as air or carbon dioxide at high temperatures burn off the deposited carbon. The resulting Ni oxide can then be reduced back to metallic Ni by exposure to a reducing gas such as hydrogen. It's important to note that repeated regeneration cycles can lead to loss of catalyst activity and selectivity due to sintering or other deactivation mechanisms. Therefore, careful monitoring and optimization of the regeneration conditions and frequency may be necessary to ensure optimal catalyst performance and longevity.

The detrimental impact of impurities, such as NH_3 and O_2, on the performance and stability of catalysts is a noteworthy concern. It is imperative to conduct research aimed at developing a resilient catalyst that can effectively endure the presence of these impurities. Moreover, it is recommended to carry out in-situ investigations on the interaction between impurities such as H_2O, H_2S, NH_3, and O_2 and well-defined metal and oxide surfaces to gain insights into the modifications in their structural, morphological, and electronic characteristics during the DRBG process. The studies are expected to contribute towards the development of catalysts that exhibit resistance to carbon and other impurities during the DRBG.

Additionally, perovskite oxides are promising catalysts for biogas reforming due to their carbon-free operation and sulfur tolerance. Perovskite structures with A site deficiency have shown high Ni exsolution, making them an area of interest in DRBG research. Optimizing the doping

levels of A and B site metals is critical, as it impacts the catalyst's structural stability and catalytic activity. Moreover, the effect of the reduction temperature on A-site deficiency catalysts needs to be explored for high topotactic exsolution. Additionally, wash coating of perovskite oxides on the monolith surface is another approach to minimize internal diffusion resistances and pressure drop than in powdered catalysts. The commercial viability of developing carbon and sulfur-tolerant catalysts using perovskite structures must also be considered.

Moreover, the present study demonstrates that, with Ba doping in Ni-exsolved catalysts delays the catalyst deactivation for more than 24 h compared to non-Ba-doped perovskite catalysts. Further studies could investigate the addition of Ca or Mg along with Ba-doped Ni-exsolved catalysts for biogas containing trace amounts of H_2S. Additionally, studies could be extended to introducing a small amount of steam or oxygen along with biogas containing H_2S (in ppm level) to gasify adsorbed sulfur as SO_2 for the simultaneous regeneration of poisoned catalysts during the reforming.

Finally, it is essential to consider the economic feasibility of DRBG in comparison to other methods for producing syngas. Factors such as capital and operating costs, efficiency, and sustainability need to be considered when evaluating the potential of DRBG as a technology for producing fuels from renewable sources. In conclusion, the development of efficient and stable Ni-based catalysts for DRBG is crucial for the commercialization of this technology.

References

[1] Pomeranz K. The Great Divergence: China, Europe, and the making of the modern world economy. 2000.

[2] Acheampong AO, Boateng E, Amponsah M, Dzator J. Revisiting the economic growth–energy consumption nexus: Does globalization matter? Energy Econ 2021;102. doi:10.1016/j.eneco.2021.105472.

[3] Melsted O, Pallua I. The Historical Transition from Coal to Hydrocarbons: Previous Explanations and the Need for an Integrative Perspective. Can J Hist 2018;53:395–422. doi:10.3138/cjh.ach.53.3.03.

[4] Petrol B. BP Statistical Review of World Energy Statistical Review of World. Ed BP Stat Rev World Energy 2019:1–69.

[5] Chava R, D BAV, Roy B, Appari S. Recent advances and perspectives of perovskite-derived Ni-based catalysts for CO2 reforming of biogas. J CO2 Util 2022;65:102206. doi:10.1016/j.jcou.2022.102206.

[6] Shahriar Shafiee ET. When will fossil fuel reserves be diminished ? Energy Policy 2009;37:181–9. doi:10.1016/j.enpol.2008.08.016.

[7] Ullah Khan I, Hafiz Dzarfan Othman M, Hashim H, Matsuura T, Ismail AF, Rezaei-DashtArzhandi M, et al. Biogas as a renewable energy fuel – A review of biogas upgrading, utilisation and storage. Energy Convers Manag 2017;150:277–94. doi:10.1016/j.enconman.2017.08.035.

[8] Zamri MFMA, Hasmady S, Akhiar A, Ideris F, Shamsuddin AH, Mofijur M, et al. A comprehensive review on anaerobic digestion of organic fraction of municipal solid waste. Renew Sustain Energy Rev 2021;137:110637. doi:10.1016/j.rser.2020.110637.

[9] Leung DYC, Wang J. An overview on biogas generation from anaerobic digestion of food waste. Int J Green Energy 2016;13:119–31. doi:10.1080/15435075.2014.909355.

[10] Zhao X, Joseph B, Kuhn J, Ozcan S. Biogas Reforming to Syngas: A Review. IScience 2020;23:101082. doi:10.1016/j.isci.2020.101082.

[11] Baena-Moreno FM, le Saché E, Pastor-Pérez L, Reina TR. Membrane-based technologies for biogas upgrading: a review. Environ Chem Lett 2020;18:1649–58. doi:10.1007/s10311-020-01036-3.

[12] Zhang C, Su H, Baeyens J, Tan T. Reviewing the anaerobic digestion of food waste for biogas production. Renew Sustain Energy Rev 2014;38:383–92. doi:10.1016/j.rser.2014.05.038.

[13] Hartmann H, Ahring BK. Anaerobic digestion of the organic fraction of municipal solid waste: Influence of co-digestion with manure. Water Res 2005;39:1543–52. doi:10.1016/j.watres.2005.02.001.

[14] IEA (2020), Outlook for biogas and biomethane: Prospects for organic growth, IEA, Paris 2020:2020.

[15] Mittal S, Ahlgren EO, Shukla PR. Barriers to biogas dissemination in India: A review. Energy Policy 2018;112:361–70. doi:10.1016/j.enpol.2017.10.027.

[16] Kadam R, Panwar NL. Recent advancement in biogas enrichment and its applications. Renew Sustain Energy Rev 2017;73:892–903. doi:10.1016/j.rser.2017.01.167.

[17] Golmakani A, Ali Nabavi S, Wadi B, Manovic V. Advances, challenges, and perspectives of biogas cleaning, upgrading, and utilisation. Fuel 2022;317:123085. doi:10.1016/j.fuel.2021.123085.

[18] Abanades S, Abbaspour H, Ahmadi A, Das B, Ehyaei MA, Esmaeilion F, et al. A critical review of biogas production and usage with legislations framework across the globe. Int J Environ Sci Technol 2022;19:3377–400. doi:10.1007/s13762-021-03301-6.

[19] Abanades S, Abbaspour H, Ahmadi A, Das B, Ehyaei MA, Esmaeilion F, et al. A conceptual review of sustainable electrical power generation from biogas. Energy Sci Eng 2022;10:630–55. doi:10.1002/ese3.1030.

[20] Kabeyi MJB, Olanrewaju OA. Biogas Production and Applications in the Sustainable Energy Transition. J Energy 2022;2022:1–43. doi:10.1155/2022/8750221.

[21] Gao Y, Jiang J, Meng Y, Yan F, Aihemaiti A. A review of recent developments in hydrogen production via biogas dry reforming. Energy Convers Manag 2018;171:133–55. doi:10.1016/j.enconman.2018.05.083.

[22] Awe OW, Zhao Y, Nzihou A, Minh DP, Lyczko N. A Review of Biogas Utilisation, Purification and Upgrading Technologies. Waste and Biomass Valorization 2017;8:267–83. doi:10.1007/s12649-016-9826-4.

[23] Tanvidkar P, Appari S, Kuncharam BVR. A review of techniques to improve performance of metal organic framework (MOF) based mixed matrix membranes for CO2/CH4 separation. vol. 21. Springer Netherlands; 2022. doi:10.1007/s11157-022-09612-5.

[24] Maurya R, Tirkey SR, Rajapitamahuni S, Ghosh A, Mishra S. Recent advances and future prospective of biogas production. Elsevier Inc.; 2019. doi:10.1016/B978-0-12-817937-6.00009-6.

[25] Schiaroli N, Volanti M, Crimaldi A, Passarini F, Vaccari A, Fornasari G, et al. Biogas to Syngas through the Combined Steam/Dry Reforming Process: An Environmental Impact

Assessment. Energy & Fuels 2021;35:4224–36. doi:10.1021/acs.energyfuels.0c04066.

[26] Ashrafi M, Pfeifer C, Pröll T, Hofbauer H, Pro T, Hofbauer H. Experimental Study of Model Biogas Catalytic Steam Reforming : 2 . Impact of Sulfur on the Deactivation and Regeneration of Ni-Based Catalysts. Energy and Fuels 2008;22:4190–5. doi:10.1021/ef8000828.

[27] Savost'yanov AP, Yakovenko RE, Narochnyi GB, Bakun VG, Sulima SI, Yakuba ES, et al. Industrial catalyst for the selective Fischer–Tropsch synthesis of long-chain hydrocarbons. Kinet Catal 2017;58:81–91. doi:10.1134/S0023158417010062.

[28] da Silva Pinto RL, Vieira AC, Scarpetta A, Marques FS, Jorge RMM, Bail A, et al. An overview on the production of synthetic fuels from biogas. Bioresour Technol Reports 2022;18:101104. doi:10.1016/j.biteb.2022.101104.

[29] Van Der Laan GP, Beenackers AACM. Kinetics and Selectivity of the Fischer-Tropsch Synthesis: A Literature Review. Catal Rev - Sci Eng 1999;41:255–318. doi:10.1081/CR-100101170.

[30] Liu R, Ma Z, Sears JD, Juneau M, Neidig ML, Porosoff MD. Identifying correlations in Fischer-Tropsch synthesis and CO2 hydrogenation over Fe-based ZSM-5 catalysts. J CO2 Util 2020;41:101290. doi:10.1016/j.jcou.2020.101290.

[31] Shahabuddin M, Alam MT, Krishna BB, Bhaskar T, Perkins G. A review on the production of renewable aviation fuels from the gasification of biomass and residual wastes. Bioresour Technol 2020;312:123596. doi:10.1016/j.biortech.2020.123596.

[32] Balasubramanian P, Bajaj I, Hasan MMFF. Simulation and optimization of reforming reactors for carbon dioxide utilization using both rigorous and reduced models. J CO2 Util 2018;23:80–104. doi:10.1016/j.jcou.2017.10.014.

[33] Olah GA, Goeppert A, Czaun M, Prakash GKS. Bi-reforming of methane from any source with steam and carbon dioxide exclusively to metgas (CO-2H2) for methanol and hydrocarbon synthesis. J Am Chem Soc 2013;135:648–50. doi:10.1021/ja311796n.

[34] Jung S, Lee J, Moon DH, Kim KH, Kwon EE. Upgrading biogas into syngas through dry reforming. Renew Sustain Energy Rev 2021;143:110949. doi:10.1016/j.rser.2021.110949.

[35] Wang S, Lu GQ, Millar GJ. Carbon dioxide reforming of methane to produce synthesis gas over metal-supported catalysts: State of the art. Energy and Fuels 1996;10:896–904. doi:10.1021/ef950227t.

[36] Chein R, Yang ZW. H2S effect on dry reforming of biogas for syngas production. Int J Energy Res 2019;43:3330–45. doi:10.1002/er.4470.

[37] Han D, Kim Y, Cho W, Baek Y. Effect of Oxidants on Syngas Synthesis from Biogas

over 3 wt % Ni-Ce-MgO-ZrO2/Al2O3 Catalyst. Energies 2020;13:297. doi:10.3390/en13020297.

[38] Cao P, Adegbite S, Zhao H, Lester E, Wu T. Tuning dry reforming of methane for F-T syntheses: A thermodynamic approach. Appl Energy 2018;227:190–7. doi:10.1016/j.apenergy.2017.08.007.

[39] Abdel N, Aramouni K, Zeaiter J, Kwapinski W, Ahmad MN. Thermodynamic analysis of methane dry reforming : E ff ect of the catalyst particle size on carbon formation 2017;150:614–22. doi:10.1016/j.enconman.2017.08.056.

[40] Chein RY, Chen YC, Yu CT, Chung JN. Thermodynamic analysis of dry reforming of CH4 with CO2 at high pressures. J Nat Gas Sci Eng 2015;26:617–29. doi:10.1016/j.jngse.2015.07.001.

[41] Nikoo MK, Amin N a. S. Thermodynamic analysis of carbon dioxide reforming of methane in view of solid carbon formation. Fuel Process Technol 2010. doi:10.1016/j.fuproc.2010.11.027.

[42] Reference: GASEQ.co.uk. 2021. GASEQ Chemical Equilibrium Program. [online] Available at: http://www.GASEQ.co.uk/ 2021:2021.

[43] Li Y, Wang Y, Zhang X, Ding X, Liu Z, Zhu R, et al. Ni supported on natural clay of palygorskite as catalyst for dry reforming of methane: Thermodynamic analysis and impacts of preparation methods. Int J Hydrogen Energy 2022;47:20851–66. doi:10.1016/j.ijhydene.2022.04.195.

[44] Luk HT, Mondelli C, Ferré DC, Stewart JA, Pérez-Ramírez J. Status and prospects in higher alcohols synthesis from syngas. Chem Soc Rev 2017;46:1358–426. doi:10.1039/c6cs00324a.

[45] Penney TK, Nahil MA, Williams PT. Pyrolysis-catalytic steam/dry reforming of processed municipal solid waste for control of syngas H2:CO ratio. J Energy Inst 2022;102:128–42. doi:10.1016/j.joei.2022.03.001.

[46] Bartholomew C. Mechanisms of catalyst deactivation. Appl Catal A Gen 2001;212:17–60. doi:10.1016/S0926-860X(00)00843-7.

[47] Ochoa A, Bilbao J, Gayubo AG, Castaño P. Coke formation and deactivation during catalytic reforming of biomass and waste pyrolysis products: A review. Renew Sustain Energy Rev 2020;119. doi:10.1016/j.rser.2019.109600.

[48] Grams J, Ruppert AM. Catalyst stability—bottleneck of efficient catalytic pyrolysis. Catalysts 2021;11:1–24. doi:10.3390/catal11020265.

[49] Shah S, Sayono S, Ynzunza J, Pan R, Xu M, Pan X, et al. The effects of stoichiometry on

the properties of exsolved Ni-Fe alloy nanoparticles for dry methane reforming. AIChE J 2020;66:1–12. doi:10.1002/aic.17078.

[50] Gao X, Lin W, Ge Z, Ge H, Kawi S. Modification Strategies of Ni-Based Catalysts with Metal Oxides for Dry Reforming of Methane 2022:139–57.

[51] Baharudin L, Rahmat N, Othman NH, Shah N, Syed-Hassan SSA. Formation, control, and elimination of carbon on Ni-based catalyst during CO2 and CH4 conversion via dry reforming process: A review. J CO2 Util 2022;61:102050. doi:10.1016/j.jcou.2022.102050.

[52] Kawi S, Kathiraser Y, Ni J, Oemar U, Li Z, Saw ET. Progress in Synthesis of Highly Active and Stable Nickel-Based Catalysts for Carbon Dioxide Reforming of Methane. ChemSusChem 2015;8:3556–75. doi:10.1002/cssc.201500390.

[53] Appari S, Janardhanan VM, Bauri R, Jayanti S. Deactivation and regeneration of Ni catalyst during steam reforming of model biogas: An experimental investigation. Int J Hydrogen Energy 2014;39:297–304. doi:10.1016/j.ijhydene.2013.10.056.

[54] Guharoy U, Reina TR, Liu J, Sun Q, Gu S, Cai Q. A theoretical overview on the prevention of coking in dry reforming of methane using non-precious transition metal catalysts. J CO2 Util 2021;53:101728. doi:10.1016/j.jcou.2021.101728.

[55] Zhang YS, Zhu HL, Yao D, Williams PT, Wu C, Xu D, et al. Thermo-chemical conversion of carbonaceous wastes for CNT and hydrogen production: A review. Sustain Energy Fuels 2021;5:4173–208. doi:10.1039/d1se00619c.

[56] Chein RY, Chen YC, Chen WH. Experimental study on sulfur deactivation and regeneration of ni-based catalyst in dry reforming of biogas. Catalysts 2021;11. doi:10.3390/catal11070777.

[57] Frontera P, Antonucci PL, Macario A. Focus on materials for sulfur-resistant catalysts in the reforming of biofuels. Catalysts 2021;11:1–16. doi:10.3390/catal11091029.

[58] Li Y, Dai Z, Dong Y, Xu J, Guo Q, Wang F. Equilibrium prediction of acid gas partial oxidation with presence of CH4 and CO2 for hydrogen production. Appl Therm Eng 2016;107:125–34. doi:10.1016/j.applthermaleng.2016.05.076.

[59] Wachter P, Gaber C, Raic J, Demuth M, Hochenauer C. Experimental investigation on H2S and SO2 sulphur poisoning and regeneration of a commercially available Ni-catalyst during methane tri-reforming. Int J Hydrogen Energy 2021;46:3437–52. doi:10.1016/j.ijhydene.2020.10.214.

[60] Lo Faro M, Modafferi V, Frontera P, Antonucci P, Aricò AS. Catalytic behavior of Ni-modified perovskite and doped ceria composite catalyst for the conversion of odorized propane to syngas. Fuel Process Technol 2013;113:28–33.

doi:10.1016/j.fuproc.2013.03.010.

[61] Gaillard M, Virginie M, Khodakov AY. New molybdenum-based catalysts for dry reforming of methane in presence of sulfur: A promising way for biogas valorization. Catal Today 2017;289:143–50. doi:10.1016/j.cattod.2016.10.005.

[62] Yeo TY, Ashok J, Kawi S. Recent developments in sulphur-resilient catalytic systems for syngas production. Renew Sustain Energy Rev 2019;100:52–70. doi:10.1016/j.rser.2018.10.016.

[63] Yang E, Nam E, Lee J, Lee H, Park ED, Lim H, et al. Al 2 O 3 -Coated Ni/CeO 2 nanoparticles as coke-resistant catalyst for dry reforming of methane . Catal Sci Technol 2020:8283–94. doi:10.1039/d0cy01615b.

[64] Praserthdam S, Somdee S, Rittiruam M, Balbuena PB. Computational Study of the Evolution of Ni-Based Catalysts during the Dry Reforming of Methane. Energy and Fuels 2020;34:4855–64. doi:10.1021/acs.energyfuels.9b04350.

[65] Chava R, Purbia D, Roy B, Janardhanan VM, Bahurudeen A, Appari S. Effect of Calcination Time on the Catalytic Activity of Ni/γ-Al2O3 Cordierite Monolith for Dry Reforming of Biogas. Int J Hydrogen Energy 2021;46:6341–57. doi:10.1016/j.ijhydene.2020.11.125.

[66] He L, Ren Y, Fu Y, Yue B, Tsang S, He H, et al. Morphology-dependent catalytic activity of Ru/CeO2 in dry reforming of methane. Molecules 2019;24:526. doi:10.3390/molecules24030526.

[67] Egelske BT, Keels JM, Monnier JR, Regalbuto JR. An analysis of electroless deposition derived Ni-Pt catalysts for the dry reforming of methane. J Catal 2020;381:374–84. doi:10.1016/j.jcat.2019.10.035.

[68] da Fonseca RO, Rabelo-Neto RC, Simões RCC, Mattos L V., Noronha FB. Pt supported on doped CeO2/Al2O3 as catalyst for dry reforming of methane. Int J Hydrogen Energy 2020;45:5182–91. doi:10.1016/j.ijhydene.2019.09.207.

[69] Ballesteros-Plata D, Infantes-Molina A, Rodríguez-Castellón E, Cauqui MA, Yeste MP. Improving noble metal catalytic activity in the dry reforming of methane by adding niobium. Fuel 2022;308. doi:10.1016/j.fuel.2021.121996.

[70] de Araújo Moreira TG, de Carvalho Filho JFS, Carvalho Y, de Almeida JMAR, Nothaft Romano P, Falabella Sousa-Aguiar E. Highly stable low noble metal content rhodium-based catalyst for the dry reforming of methane. Fuel 2021;287. doi:10.1016/j.fuel.2020.119536.

[71] Maina SCP, Ballarini AD, Vilella JI, de Miguel SR. Study of the performance and stability in the dry reforming of methane of doped alumina supported iridium catalysts.

Catal Today 2020;344:129–42. doi:10.1016/j.cattod.2018.11.023.

[72] Ali S, Khader MM, Almarri MJ, Abdelmoneim AG. Ni-based nano-catalysts for the dry reforming of methane. Catal Today 2020;343:26–37. doi:10.1016/j.cattod.2019.04.066.

[73] Xu L, Wang F, Chen M, Yang H, Nie D, Qi L, et al. Alkaline-promoted Ni based ordered mesoporous catalysts with enhanced low-temperature catalytic activity toward CO2 methanation. RSC Adv 2017;7:18199–210. doi:10.1039/c7ra01673e.

[74] Kim BJ, Seo JC, Kim DH, Lee YL, Lee K, Roh HS. Oxygen defective bimodal porous Ni-CeO2−x-MgO-Al2O3 catalyst with multi-void spherical structure for CO2 reforming of CH4. J CO2 Util 2022;58:101917. doi:10.1016/j.jcou.2022.101917.

[75] Lee YL, Kim BJ, Park HR, Ahn SY, Kim KJ, Roh HS. Improving the catalytic activity in dry reforming reaction by enhancing the oxygen storage capacity of Ce0.8Zr0.2O2 support through hydrogen heat-treatment. J CO2 Util 2022;57:101903. doi:10.1016/j.jcou.2022.101903.

[76] Wang S, Lu GQ. Reforming of methane with carbon dioxide over Ni/Al2O3 catalysts: Effect of nickel precursor. Appl Catal A Gen 1998;169:271–80. doi:10.1016/S0926-860X(98)00017-9.

[77] Xu L, Liu W, Zhang X, Tao L, Xia L, Xu X, et al. Ni/La2O3 Catalysts for Dry Reforming of Methane: Insights into the Factors Improving the Catalytic Performance. ChemCatChem 2019;11:2887–99. doi:10.1002/cctc.201900331.

[78] Shahnazi A, Firoozi S. Improving the catalytic performance of LaNiO3perovskite by manganese substitution via ultrasonic spray pyrolysis for dry reforming of methane. J CO2 Util 2021;45:101455. doi:10.1016/j.jcou.2021.101455.

[79] Laosiripojana N, Sutthisripok W, Assabumrungrat S. Synthesis gas production from dry reforming of methane over CeO 2 doped Ni / Al 2 O 3 : Influence of the doping ceria on the resistance toward carbon formation 2005;112:13–22. doi:10.1016/j.cej.2005.06.003.

[80] Bereketidou OA, Goula MA. Biogas reforming for syngas production over nickel supported on ceria – alumina catalysts. Catal Today 2012;195:93–100. doi:10.1016/j.cattod.2012.07.006.

[81] Lustemberg PG, Mao Z, Salcedo A, Irigoyen B, Ganduglia-Pirovano MV, Campbell CT. Nature of the Active Sites on Ni/CeO 2 Catalysts for Methane Conversions . ACS Catal 2021;11:10604–13. doi:10.1021/acscatal.1c02154.

[82] Teh LP, Setiabudi HD, Timmiati SN, Aziz MAA, Annuar NHR, Ruslan NN. Recent progress in ceria-based catalysts for the dry reforming of methane: A review. Chem Eng Sci 2021;242:116606. doi:10.1016/j.ces.2021.116606.

[83] Roy S, Bauer T, Al-Dahhan M, Lehner P, Turek T. Monoliths as multiphase reactors: A review. AIChE J 2004;50:2918–38. doi:10.1002/aic.10268.

[84] Heck RM, Gulati S, Farrauto RJ. The application of monoliths for gas phase catalytic reactions. Chem Eng J 2001;82:149–56. doi:10.1016/S1385-8947(00)00365-X.

[85] Wang T, Li Y, Wang C, Zhang X, Ma L, Wu C. Synthesis gas production with NiO-MgO/γ-Al2O 3/cordierite monolithic catalysts in a pilot-scale biomass-gasification-reforming system. Energy and Fuels 2011;25:1221–8. doi:10.1021/ef1015268.

[86] Labhasetwar N, Saravanan G, Kumar Megarajan S, Manwar N, Khobragade R, Doggali P, et al. Perovskite-type catalytic materials for environmental applications. Sci Technol Adv Mater 2015;16:1–13. doi:10.1088/1468-6996/16/3/036002.

[87] Bai X, Xie G, Guo Y, Tian L, El-Hosainy HM, Awadallah AE, et al. A highly active Ni catalyst supported on Mg-substituted LaAlO3 for carbon dioxide reforming of methane. Catal Today 2021;368:78–85. doi:10.1016/j.cattod.2019.12.033.

[88] Marin CM, Popczun EJ, Nguyen-Phan T-D, Tafen DN, Alfonso D, Waluyo I, et al. Designing Perovskite Catalysts for Controlled Active-Site Exsolution in the Microwave Dry Reforming of Methane. Appl Catal B Environ 2020;284:119711. doi:10.1016/j.apcatb.2020.119711.

[89] Richards N, Carter JH, Parker LA, Pattisson S, Hewes DG, Morgan DJ, et al. Lowering the Operating Temperature of Perovskite Catalysts for N2O Decomposition through Control of Preparation Methods. ACS Catal 2020;10:5430–42. doi:10.1021/acscatal.0c00698.

[90] Kumar A, Kumar A, Krishnan V. Perovskite Oxide Based Materials for Energy and Environment-Oriented Photocatalysis. ACS Catal 2020;10:10253–315. doi:10.1021/acscatal.0c02947.

[91] Das S, Bhattar S, Liu L, Wang Z, Xi S, Spivey JJ, et al. Effect of Partial Fe Substitution in La0.9Sr0.1NiO3Perovskite-Derived Catalysts on the Reaction Mechanism of Methane Dry Reforming. ACS Catal 2020;10:12466–86. doi:10.1021/acscatal.0c01229.

[92] Kim HS, Jeon Y, Kim JH, Jang GY, Yoon SP, Yun JW. Characteristics of Sr1−xYxTi1−yRuyO3+/−δ and Ru-impregnated Sr1−xYxTiO3+/−δ perovskite catalysts as SOFC anode for methane dry reforming. Appl Surf Sci 2020;510:145450. doi:10.1016/j.apsusc.2020.145450.

[93] Zhu X, Huo P, Zhang Y ping, Cheng D guo, Liu C jun. Structure and reactivity of plasma treated Ni/Al2O3 catalyst for CO2 reforming of methane. Appl Catal B Environ 2008;81:132–40. doi:10.1016/j.apcatb.2007.11.042.

[94] Pham CQ, Nguyen VP, Van TT, Phuong PTT, Pham PTH, Trinh TH, et al. Syngas

Production from Biogas Reforming: Role of the Support in Nickel-based Catalyst Performance. Top Catal 2022. doi:10.1007/s11244-022-01750-y.

[95] He L, Ren Y, Yue B, Tsang SCE, He H. Tuning metal–support interactions on ni/al2 o3 catalysts to improve catalytic activity and stability for dry reforming of methane. Processes 2021;9. doi:10.3390/pr9040706.

[96] Chein R, Yang Z. Experimental Study on Dry Reforming of Biogas for Syngas Production over Ni-Based Catalysts. ACS Omega 2019;4:20911–22. doi:10.1021/acsomega.9b01784.

[97] Schwengber CA, Da Silva FA, Schaffner RA, Fernandes-Machado NRC, Ferracin RJ, Bach VR, et al. Methane dry reforming using Ni/Al2O3 catalysts: Evaluation of the effects of temperature, space velocity and reaction time. J Environ Chem Eng 2016;4:3688–95. doi:10.1016/j.jece.2016.07.001.

[98] Xu Y, Du X, Shi L, Chen T, Wan H, Wang P, et al. Improved performance of Ni/Al2O3 catalyst deriving from the hydrotalcite precursor synthesized on Al2O3 support for dry reforming of methane. Int J Hydrogen Energy 2021;46:14301–10. doi:10.1016/j.ijhydene.2021.01.189.

[99] E.Sommer AMG and M. Carbon dioxide reforming of methane on nickel catalysts. Chem Eng Sci 1989;44.

[100] Zhou L, Li L, Wei N, Li J, Basset J, Takanabe K, et al. Effect of NiAl 2 O 4 formation on Ni / Al 2 O 3 Stability during Dry Reforming of Methane. ChemCatChem 2015;7:2508–16. doi:10.1002/cctc.201500379.

[101] H.St.C.O"Neill, W.A. Dollase CRRI. Temperature Dependence of the Cation Distribution in Nickel Aluminate (NiAl204) Spinel: a Powder XRD Study. Phys Chem Miner 1991:302–19.

[102] Anil S, Indraja S, Singh R, Appari S, Roy B. ScienceDirect A review on ethanol steam reforming for hydrogen production over Ni / Al 2 O 3 and Ni / CeO 2 based catalyst powders. Int J Hydrogen Energy 2021;47:8177–213. doi:10.1016/j.ijhydene.2021.12.183.

[103] Pawar V, Ray D, Subrahmanyam C, Janardhanan VM. Study of Short-Term Catalyst Deactivation Due to Carbon Deposition during Biogas Dry Reforming on Supported Ni Catalyst. Energy and Fuels 2015;29:8047–52. doi:10.1021/acs.energyfuels.5b01862.

[104] Rahbar Shamskar F, Rezaei M, Meshkani F. The influence of Ni loading on the activity and coke formation of ultrasound-assisted co-precipitated Ni–Al2O3 nanocatalyst in dry reforming of methane. Int J Hydrogen Energy 2017;42:4155–64. doi:10.1016/j.ijhydene.2016.11.067.

[105] Kim SB, Eissa AAS, Kim MJ, Goda ES, Youn JR, Lee K. Sustainable Synthesis of a Highly Stable and Coke-Free Ni@CeO2 Catalyst for the Efficient Carbon Dioxide

Reforming of Methane. Catalysts 2022;12. doi:10.3390/catal12040423.

[106] Pizzolato M, Pian G Da, Ghedini E, Michele A Di, Menegazzo F, Cruciani G, et al. Study of the Synthetic Approach Influence in Ni / CeO 2 -Based Catalysts for Methane Dry Reforming 2022:634–47.

[107] Ou Z, Ran J, Qiu H, Huang X, Qin C. Uncovering the effect of surface basicity on the carbon deposition of Ni/CeO2 catalyst modified by oxides in DRM. Fuel 2023;335:126994. doi:10.1016/j.fuel.2022.126994.

[108] Pham CQ, Cao ANT, Pham LKH, Phuong PT, Tran TTV, Vo C-M, et al. Influence of synthesis routes on the performance of Ni nano-sized catalyst supported on CeO 2 -Al 2 O 3 in the dry reforming of methane . Adv Nat Sci Nanosci Nanotechnol 2022;13:035011. doi:10.1088/2043-6262/ac8de7.

[109] Ni Z, Djitcheu X, Gao X, Wang J, Liu H, Zhang Q. Effect of preparation methods of CeO2 on the properties and performance of Ni/CeO2 in CO2 reforming of CH4. Sci Rep 2022;12:1–10. doi:10.1038/s41598-022-09291-w.

[110] Rashid MU, Wan Daud WMA, Mohidem NA, Mohamad MB, Akhtar J, Azam M, et al. Methane dry reforming with CO2 over ceria supported Ni catalyst prepared by reverse microemulsion synthesis. Fuel 2022;317:123433. doi:10.1016/j.fuel.2022.123433.

[111] Gao S, Li Y, Guo W, Ding X, Zheng L, Wu L, et al. Morphology effect of ceria support with hierarchical structure on the catalytic performance for nickel-based catalysts in dry reforming of methane. Mol Catal 2022;533. doi:10.1016/j.mcat.2022.112766.

[112] Luisetto I, Tuti S, Battocchio C, Lo Mastro S, Sodo A. Ni/CeO2–Al2O3 catalysts for the dry reforming of methane: The effect of CeAlO3 content and nickel crystallite size on catalytic activity and coke resistance. Appl Catal A Gen 2015;500:12–22. doi:10.1016/j.apcata.2015.05.004.

[113] Kambolis A, Matralis H, Trovarelli A, Papadopoulou C. Ni/CeO2-ZrO2 catalysts for the dry reforming of methane. Appl Catal A Gen 2010;377:16–26. doi:10.1016/j.apcata.2010.01.013.

[114] Taufiq-Yap YH, Sudarno, Rashid U, Zainal Z. CeO2-SiO2 supported nickel catalysts for dry reforming of methane toward syngas production. Appl Catal A Gen 2013;468:359–69. doi:10.1016/j.apcata.2013.09.020.

[115] Grabchenko M, Pantaleo G, Puleo F, Kharlamova TS, Zaikovskii VI, Vodyankina O, et al. Design of Ni-based catalysts supported over binary La-Ce oxides: Influence of La/Ce ratio on the catalytic performances in DRM. Catal Today 2021;382:71–81. doi:10.1016/j.cattod.2021.07.012.

[116] Pawar V, Ponugoti P V., Janardhanan VM, Appari S. Experimental studies of catalyst

deactivation due to carbon and sulphur during <scp>CO</scp> 2 reforming of <scp>CH</scp> 4 over Ni washcoated monolith in the presence of H 2 S. Can J Chem Eng 2022;100:1858–67. doi:10.1002/cjce.24266.

[117] Leba A, Yıldırım R. Determining most effective structural form of nickel-cobalt catalysts for dry reforming of methane. Int J Hydrogen Energy 2020. doi:10.1016/j.ijhydene.2019.12.020.

[118] Agueniou F, Vidal H, Yeste MP, Hernández-garrido JC, Cauqui MA, Rodríguez-izquierdo JM, et al. Honeycomb monolithic design to enhance the performance of Ni-based catalysts for dry reforming of methane. Catal Today 2020:1–10. doi:10.1016/j.cattod.2020.07.030.

[119] Soloviev SO, Kapran AY, Orlyk SN, Gubareni E V. Carbon dioxide reforming of methane on monolithic Ni / Al 2 O 3 -based catalysts. J Nat Gas Chem 2011;20:184–90. doi:10.1016/S1003-9953(10)60149-1.

[120] Sollier BM, Gómez LE, Boix A V, Miró EE. Applied Catalysis A , General Oxidative coupling of methane on cordierite monoliths coated with Sr / La 2 O 3 catalysts . In fl uence of honeycomb structure and catalyst-cordierite chemical interactions on the catalytic behavior. Appl Catal A, Gen 2018;550:113–21. doi:10.1016/j.apcata.2017.10.023.

[121] Li S, Wang X, Cao M, Lu J, Qiu L, Yan X. Engineering the Interface and Interaction Structure on Highly Coke- Resistant Ni/CeO 2 -Al 2 O 3 Catalyst for Dry Reforming of Methane 2022:2212007–14. doi:10.14102/j.cnki.0254-5861.2022-0113.

[122] Rajput AS, Das T. Production of syngas by methane dry reforming over the catalyst ZNi 1-x Ce x : The effect of catalyst calcination and reduction temperature . J Chem Technol Biotechnol 2022. doi:10.1002/jctb.7276.

[123] Le Saché E, Santos JL, Smith TJ, Centeno MA, Arellano-Garcia H, Odriozola JA, et al. Multicomponent Ni-CeO2 nanocatalysts for syngas production from CO2/CH4 mixtures. J CO2 Util 2018;25:68–78. doi:10.1016/j.jcou.2018.03.012.

[124] Liang TY, Chen HH, Tsai DH. Nickel hybrid nanoparticle decorating on alumina nanoparticle cluster for synergistic catalysis of methane dry reforming. Fuel Process Technol 2020;201:106335. doi:10.1016/j.fuproc.2020.106335.

[125] Yang E, Nam E, Lee J, Lee H, Park ED, Lim H, et al. Al2O3-Coated Ni/CeO2nanoparticles as coke-resistant catalyst for dry reforming of methane. Catal Sci Technol 2020;10:8283–94. doi:10.1039/d0cy01615b.

[126] Zhang F, Liu Z, Chen X, Rui N, Betancourt LE, Lin L, et al. Effects of Zr Doping into Ceria for the Dry Reforming of Methane over Ni/CeZrO2 Catalysts: In Situ Studies with XRD, XAFS, and AP-XPS. ACS Catal 2020;10:3274–84. doi:10.1021/acscatal.9b04451.

[127] Agrafiotis C, Tsetsekou A. The effect of processing parameters on the properties of γ - alumina washcoats 2000;5:951–60.

[128] Pawar V, Appari S, Monder DS, Janardhanan VM. Study of the Combined Deactivation Due to Sulfur Poisoning and Carbon Deposition during Biogas Dry Reforming on Supported Ni Catalyst. Ind Eng Chem Res 2017;56:8448–55. doi:10.1021/acs.iecr.7b01662.

[129] Aybuke Leba RY. ScienceDirect Determining most effective structural form of nickel-cobalt catalysts for dry reforming of methane. Int J Hydrogen Energy 2019;45:4268–83. doi:10.1016/j.ijhydene.2019.12.020.

[130] Luisetto I, Sarno C, Felicis D De, Basoli F, Battocchio C, Tuti S, et al. Ni supported on $γ$ -Al 2 O 3 promoted by Ru for the dry reforming of methane in packed and monolithic reactors. Fuel Process Technol 2017;158:130–40. doi:10.1016/j.fuproc.2016.12.015.

[131] Ishihara T. Perovskite Oxide for Solid Oxide Fuel Cells 2009. doi:10.1007/978-0-387-77708-5.

[132] Travis W, Glover ENK, Bronstein H, Scanlon DO, Palgrave RG. On the application of the tolerance factor to inorganic and hybrid halide perovskites: A revised system. Chem Sci 2016;7:4548–56. doi:10.1039/c5sc04845a.

[133] Su YJ, Pan KL, Chang MB. Modifying perovskite-type oxide catalyst LaNiO3 with Ce for carbon dioxide reforming of methane. Int J Hydrogen Energy 2014;39:4917–25. doi:10.1016/j.ijhydene.2014.01.077.

[134] Yang E, Su Y, Hoon G, Ju D. Combined steam and CO 2 reforming of methane over La 1-x Sr x NiO 3 perovskite oxides. Catal Today 2017:0–1. doi:10.1016/j.cattod.2017.03.050.

[135] Moradi GR, Rahmanzadeh M, Khosravian F. The effects of partial substitution of Ni by Zn in LaNiO3 perovskite catalyst for methane dry reforming. J CO2 Util 2014;6:7–11. doi:10.1016/j.jcou.2014.02.001.

[136] De Lima SM, Peña MA, Fierro JLG, Assaf JM. La1-x Ca x NiO3 perovskite oxides: Characterization and catalytic reactivity in dry reforming of methane. Catal Letters 2008;124:195–203. doi:10.1007/s10562-008-9484-7.

[137] Gomes R, Costa D, Junior R, Santos M, Rodella C, Fréty R, et al. Dry Reforming of Methane over NiLa-Based Catalysts: Influence of Synthesis Method and Ba Addition on Catalytic Properties and Stability. Catalysts 2019;9:313. doi:10.3390/catal9040313.

[138] Jahangiri A, Pahlavanzadeh H, Aghabozorg H. Synthesis, characterization and catalytic study of Sm doped LaNiO 3 nanoparticles in reforming of methane with CO 2 and O 2. Int J Hydrogen Energy 2012;37:9977–84. doi:10.1016/j.ijhydene.2012.03.128.

[139] Nam JW, Chae H, Lee SH, Jung H, Lee KY. Methane dry reforming over well-dispersed Ni catalyst prepared from perovskite-type mixed oxides. vol. 119. Elsevier Masson SAS; 1998. doi:10.1016/s0167-2991(98)80537-5.

[140] Gallego GS, Batiot-Dupeyrat C, Barrault J, Florez E, Mondragón F. Dry reforming of methane over LaNi1-yByO3±δ (B = Mg, Co) perovskites used as catalyst precursor. Appl Catal A Gen 2008;334:251–8. doi:10.1016/j.apcata.2007.10.010.

[141] Valderrama G, Kiennemann A, Goldwasser MR. Dry reforming of CH4 over solid solutions of LaNi1-xCoxO3. Catal Today 2008;133–135:142–8. doi:10.1016/j.cattod.2007.12.069.

[142] Jahangiri A, Aghabozorg H, Pahlavanzadeh H. Effects of Fe substitutions by Ni in La–Ni–O perovskite-type oxides in reforming of methane with CO2 and O2. Int J Hydrogen Energy 2013;38:10407–16. doi:10.1016/j.ijhydene.2013.05.080.

[143] Kim J, Kim T, Yoo JW, Lee KB, Hong S. Carbon dioxide reforming of methane to synthesis gas over LaNi1−x Cr x O3 perovskite catalysts. Korean J Chem Eng 2012;29:1329–35. doi:10.1007/s11814-012-0057-5.

[144] Batiot-Dupeyrat C, Valderrama G, Meneses A, Martinez F, Barrault J, Tatibouët J. Pulse study of CO2 reforming of methane over LaNiO3. Appl Catal A Gen 2003;248:143–51. doi:10.1016/S0926-860X(03)00155-8.

[145] Maneerung T, Hidajat K, Kawi S. LaNiO 3 perovskite catalyst precursor for rapid decomposition of methane : Influence of temperature and presence of H 2 in feed stream. Catal Today 2011;171:24–35. doi:10.1016/j.cattod.2011.03.080.

[146] Wang M, Zhao T, Dong X, Li M, Wang H. Effects of Ce substitution at the A-site of LaNi0.5Fe0.5O3 perovskite on the enhanced catalytic activity for dry reforming of methane. vol. 224. Elsevier B.V.; 2018. doi:10.1016/j.apcatb.2017.10.022.

[147] Kwon BW, Oh JH, Kim GS, Yoon SP, Han J, Nam SW, et al. The novel perovskite-type Ni-doped Sr0.92Y0.08TiO3 as a reforming biogas (CH4 + CO2) for H2 production. Appl Energy 2018;227:213–9. doi:10.1016/j.apenergy.2017.07.105.

[148] Wei T, Jia L, Luo JL, Chi B, Pu J, Li J. CO2 dry reforming of CH4 with Sr and Ni co-doped LaCrO3 perovskite catalysts. Appl Surf Sci 2020;506:144699. doi:10.1016/j.apsusc.2019.144699.

[149] Oh JH, Kwon BW, Cho J, Lee CH, Kim MK, Choi SH, et al. Importance of Exsolution in Transition-Metal (Co, Rh, and Ir)-Doped LaCrO3 Perovskite Catalysts for Boosting Dry Reforming of CH4 Using CO2 for Hydrogen Production. Ind Eng Chem Res 2019;58:6385–93. doi:10.1021/acs.iecr.8b05337.

[150] Anil C, Modak JM, Madras G. Syngas production via CO2 reforming of methane over

noble metal (Ru, Pt, and Pd) doped LaAlO3 perovskite catalyst. Mol Catal 2020;484:110805. doi:10.1016/j.mcat.2020.110805.

[151] Pereñiguez R, Gonzalez-delaCruz VM, Caballero A, Holgado JP. LaNiO3 as a precursor of Ni/La2O3 for CO2 reforming of CH4: Effect of the presence of an amorphous NiO phase. Appl Catal B Environ 2012;123–124:324–32. doi:10.1016/j.apcatb.2012.04.044.

[152] Oliveira ÂAS, Medeiros RLBA, Figueredo GP, Macedo HP, Braga RM, Maziviero F V., et al. One-step synthesis of LaNiO3 with chitosan for dry reforming of methane. Int J Hydrogen Energy 2018;43:9696–704. doi:10.1016/j.ijhydene.2018.03.212.

[153] Singh S, Zubenko D, Rosen BA. Influence of LaNiO3 Shape on Its Solid-Phase Crystallization into Coke-Free Reforming Catalysts. ACS Catal 2016;6:4199–205. doi:10.1021/acscatal.6b00673.

[154] Moogi S, Hyun Ko C, Hoon Rhee G, Jeon B-HH, Ali Khan M, Park Y-KK. Influence of catalyst synthesis methods on anti-coking strength of perovskites derived catalysts in biogas dry reforming for syngas production. Chem Eng J 2022;437:135348. doi:10.1016/j.cej.2022.135348.

[155] Batiot-Dupeyrat C, Gallego GAS, Mondragon F, Barrault J, Tatibouët JM. CO2 reforming of methane over LaNiO3 as precursor material. Catal Today 2005;107–108:474–80. doi:10.1016/j.cattod.2005.07.014.

[156] Nair MM, Kaliaguine S, Kleitz F. Nanocast LaNiO 3 Perovskites as Precursors for the Preparation of Coke-Resistant Dry Reforming Catalysts. ACS Catal 2014;4:3837–46. doi:10.1021/cs500918c.

[157] Wang N, Yu X, Wang Y, Chu W, Liu M. A comparison study on methane dry reforming with carbon dioxide over LaNiO3 perovskite catalysts supported on mesoporous SBA-15, MCM-41 and silica carrier. Catal Today 2013;212:98–107. doi:10.1016/j.cattod.2012.07.022.

[158] Gallego J, Batiot-dupeyrat C, Mondrag F. Severe Deactivation of a LaNiO 3 Perovskite-Type Catalyst Precursor with H 2 S during Methane Dry Reforming 2009:4883–6. doi:10.1021/ef900409x.

[159] Gallego GS, Batiot-Dupeyrat C, Barrault J, Mondragón F. Dual active-site mechanism for dry methane reforming over Ni/La 2O3 produced from LaNiO3 perovskite. Ind Eng Chem Res 2008;47:9272–8. doi:10.1021/ie800281t.

[160] Su Y, Pan K, Chang M. Modifying perovskite-type oxide catalyst LaNiO3 with Ce for carbon dioxide reforming of methane. Int J Hydrogen Energy 2014;39:4917–25. doi:10.1016/j.ijhydene.2014.01.077.

[161] Lima SM, Assaf JM, Peña MA, Fierro JLG. Structural features of La1-xCexNiO3 mixed

oxides and performance for the dry reforming of methane. Appl Catal A Gen 2006;311:94–104. doi:10.1016/j.apcata.2006.06.010.

[162] Gallego GS, Marín JG, Batiot-Dupeyrat C, Barrault J, Mondragón F. Influence of Pr and Ce in dry methane reforming catalysts produced from La1−xAxNiO3−δ perovskites. Appl Catal A Gen 2009;369:97–103. doi:10.1016/j.apcata.2009.09.004.

[163] Ibrahim AA, Fakeeha AH, Al-fatesh AS. Enhancing hydrogen production by dry reforming process with strontium promoter. Int J Hydrogen Energy 2014;39:1680–7. doi:10.1016/j.ijhydene.2013.11.050.

[164] Sutthiumporn K, Kawi S. Promotional effect of alkaline earth over Ni-La2O3 catalyst for CO2 reforming of CH4: Role of surface oxygen species on H2 production and carbon suppression. Int J Hydrogen Energy 2011;36:14435–46. doi:10.1016/j.ijhydene.2011.08.022.

[165] Valderrama G, Goldwasser MR, Navarro CU De, Tatibouët JM, Barrault J, Batiot-Dupeyrat C, et al. Dry reforming of methane over Ni perovskite type oxides. Catal Today 2005;107–108:785–91. doi:10.1016/j.cattod.2005.07.010.

[166] Sun Y, Zhang G, Cheng H, Liu J, Li G. Kinetics and mechanistic studies of methane dry reforming over Ca promoted 1Co–1Ce/AC-N catalyst. Int J Hydrogen Energy 2021;46:531–42. doi:10.1016/j.ijhydene.2020.09.192.

[167] Ghods B, Meshkani F, Rezaei M. Effects of alkaline earth promoters on the catalytic performance of the nickel catalysts supported on high surface area mesoporous magnesium silicate in dry reforming reaction. Int J Hydrogen Energy 2016;41:22913–21. doi:10.1016/j.ijhydene.2016.10.020.

[168] Yang EH, Noh YS, Ramesh S, Lim SS, Moon DJ. The effect of promoters in La0.9M0.1Ni0.5Fe0.5O3 (M = Sr, Ca) perovskite catalysts on dry reforming of methane. Fuel Process Technol 2015;134:404–13. doi:10.1016/j.fuproc.2015.02.023.

[169] Komarala EP, Komissarov I, Rosen BA. Effect of Fe and Mn Substitution in LaNiO3 on Exsolution, Activity, and Stability for Methane Dry Reforming. Catalysts 2019;10:27. doi:10.3390/catal10010027.

[170] Odedairo T, Ma J, Chen J, Zhu Z. Cr-Doped La-Ni-O Catalysts Derived from Perovskite Precursors for CH4-CO2 Reforming under Microwave Irradiation. Chem Eng Technol 2016;39:1551–60. doi:10.1002/ceat.201500702.

[171] Alipour Z, Rezaei M, Meshkani F. Effects of support modifiers on the catalytic performance of Ni/Al 2O3 catalyst in CO2 reforming of methane. Fuel 2014;129:197–203. doi:10.1016/j.fuel.2014.03.045.

[172] Zhang Q, Feng X, Liu J, Zhao L, Song X, Zhang P, et al. Hollow hierarchical Ni/MgO-

SiO2 catalyst with high activity, thermal stability and coking resistance for catalytic dry reforming of methane. Int J Hydrogen Energy 2018;43:11056–68. doi:10.1016/j.ijhydene.2018.05.010.

[173] Titus J, Goepel M, Schunk SA, Wilde N, Gläser R. The role of acid/base properties in Ni/MgO-ZrO2–based catalysts for dry reforming of methane. Catal Commun 2017;100:76–80. doi:10.1016/j.catcom.2017.06.027.

[174] Kim WY, Jang JS, Ra EC, Kim KY, Kim EH, Lee JS. Reduced perovskite LaNiO3 catalysts modified with Co and Mn for low coke formation in dry reforming of methane. Appl Catal A Gen 2019;575:198–203. doi:10.1016/j.apcata.2019.02.029.

[175] Mousavi M, Nakhaei Pour A, Gholizadeh M, Mohammadi A, Kamali Shahri SM. Dry reforming of methane by La 0. 5 Sr 0 . 5 NiO 3 perovskite oxides: influence of preparation method on performance and structural features of the catalysts. J Chem Technol Biotechnol 2020;95:2911–20. doi:10.1002/jctb.6451.

[176] Kim SM, Abdala PM, Margossian T, Hosseini D, Foppa L, Armutlulu A, et al. Cooperativity and dynamics increase the performance of NiFe dry reforming catalysts. J Am Chem Soc 2017;139:1937–49. doi:10.1021/jacs.6b11487.

[177] Margossian T, Larmier K, Kim SM, Krumeich F, Müller C, Copéret C. Supported bimetallic NiFe nanoparticles through colloid synthesis for improved dry reforming performance. ACS Catal 2017;7:6942–8. doi:10.1021/acscatal.7b02091.

[178] Theofanidis SA, Galvita V V, Poelman H, Marin GB. Enhanced carbon-resistant dry reforming Fe-Ni catalyst: Role of Fe. ACS Catal 2015;5:3028–39. doi:10.1021/acscatal.5b00357.

[179] Arandiyan H, Li J, Ma L, Hashemnejad SM, Mirzaei MZ, Chen J, et al. Methane reforming to syngas over LaNi xFe 1-xO 3 (0≤x≤1) mixed-oxide perovskites in the presence of CO 2 and O 2. J Ind Eng Chem 2012;18:2103–14. doi:10.1016/j.jiec.2012.06.004.

[180] Song X, Dong X, Yin S, Wang M, Li M, Wang H. Effects of Fe partial substitution of La 2 NiO 4 /LaNiO 3 catalyst precursors prepared by wet impregnation method for the dry reforming of methane. Appl Catal A Gen 2016;526:132–8. doi:10.1016/j.apcata.2016.07.024.

[181] Nakamura T, Petzow G, Gauckler LJ. Stability of the perovskite phase LaBO3 (B = V, Cr, Mn, Fe, Co, Ni) in reducing atmosphere I. Experimental results. Mater Res Bull 1979;14:649–59. doi:10.1016/0025-5408(79)90048-5.

[182] Araujo GC de, Lima SM de, Assaf JM, Peña MA, Fierro JLG, do Carmo Rangel M. Catalytic evaluation of perovskite-type oxide LaNi1-xRuxO3 in methane dry reforming.

Catal Today 2008;133–135:129–35. doi:10.1016/j.cattod.2007.12.049.

[183] Nuvula S, Sagar TV, Valluri DK, Sai Prasad PS. Selective substitution of Ni by Ti in LaNiO 3 perovskites: A parameter governing the oxy-carbon dioxide reforming of methane. Int J Hydrogen Energy 2018;43:4136–42. doi:10.1016/j.ijhydene.2017.08.180.

[184] Chai Y, Fu Y, Feng H, Kong W, Yuan C, Pan B, et al. A Nickel-Based Perovskite Catalyst with a Bimodal Size Distribution of Nickel Particles for Dry Reforming of Methane. ChemCatChem 2018;10:2078–86. doi:10.1002/cctc.201701483.

[185] Wei T, Jia L, Zheng H, Chi B, Pu J, Li J. LaMnO3-based perovskite with in-situ exsolved Ni nanoparticles: a highly active, performance stable and coking resistant catalyst for CO2 dry reforming of CH4. Appl Catal A Gen 2018;564:199–207. doi:10.1016/j.apcata.2018.07.031.

[186] Gao Y, Chen D, Saccoccio M, Lu Z, Ciucci F. From material design to mechanism study: Nanoscale Ni exsolution on a highly active A-site deficient anode material for solid oxide fuel cells. Nano Energy 2016;27:499–508. doi:10.1016/j.nanoen.2016.07.013.

[187] Kwon O, Joo S, Choi S, Sengodan S, Kim G. Review on exsolution and its driving forces in perovskites. J Phys Energy 2020;2:032001. doi:10.1088/2515-7655/ab8c1f.

[188] Kousi K, Tang C, Metcalfe IS, Neagu D. Emergence and Future of Exsolved Materials. Small 2021;2006479. doi:10.1002/smll.202006479.

[189] Tang C, Kousi K, Neagu D, Metcalfe IS. Trends and Prospects of Bimetallic Exsolution. Chem - A Eur J 2021;27:6666–75. doi:10.1002/chem.202004950.

[190] Mousavi M, Nakhaei Pour A. Performance and structural features of LaNi 0.5 Co 0.5 O 3 perovskite oxides for the dry reforming of methane: influence of the preparation method. New J Chem 2019;43:10763–73. doi:10.1039/C9NJ01805K.

[191] De Lima SM, Assaf JM. Ni-Fe catalysts based on perovskite-type oxides for dry reforming of methane to syngas. Catal Letters 2006;108:63–70. doi:10.1007/s10562-006-0026-x.

[192] Yadav PK, Das T. Production of syngas from carbon dioxide reforming of methane by using LaNixFe1−xO3 perovskite type catalysts. Int J Hydrogen Energy 2019;44:1659–70. doi:10.1016/j.ijhydene.2018.11.108.

[193] Carrillo AJ, Serra JM. Exploring the stability of fe–ni alloy nanoparticles exsolved from double-layered perovskites for dry reforming of methane. Catalysts 2021;11:4–6. doi:10.3390/catal11060741.

[194] Neagu D, Oh TS, Miller DN, Ménard H, Bukhari SM, Gamble SR, et al. Nano-socketed nickel particles with enhanced coking resistance grown in situ by redox exsolution. Nat

Commun 2015;6. doi:10.1038/ncomms9120.

[195] Neagu D, Tsekouras G, Miller DN, Ménard H, Irvine JTS. In situ growth of nanoparticles through control of non-stoichiometry. Nat Chem 2013;5:916–23. doi:10.1038/nchem.1773.

[196] Wei T, Qiu P, Jia L, Tan Y, Yang X, Sun S, et al. Power and carbon monoxide co-production by a proton-conducting solid oxide fuel cell with La0.6Sr0.2Cr0.85Ni0.15O3-dfor on-cell dry reforming of CH4by CO2. J Mater Chem A 2020;8:9806–12. doi:10.1039/d0ta03458d.

[197] Shah S, Xu M, Pan X, Gilliard-Abdulaziz KL. Exsolution of Embedded Ni-Fe-Co Nanoparticles: Implications for Dry Reforming of Methane. ACS Appl Nano Mater 2021;4:8626–36. doi:10.1021/acsanm.1c02268.

[198] Zubenko D, Singh S, Rosen BA. Exsolution of Re-alloy catalysts with enhanced stability for methane dry reforming. Appl Catal B Environ 2017;209:711–9. doi:10.1016/j.apcatb.2017.03.047.

[199] Audasso E, Kim YY, Cha J, Cigolotti V, Jeong H, Jo YS, et al. In situ exsolution of Rh nanoparticles on a perovskite oxide surface: Efficient Rh catalysts for Dry reforming. Korean J Chem Eng 2020;37:1401–10. doi:10.1007/s11814-020-0592-4.

[200] Ligthart DAJM, Van Santen RA, Hensen EJM. Influence of particle size on the activity and stability in steam methane reforming of supported Rh nanoparticles. J Catal 2011;280:206–20. doi:10.1016/j.jcat.2011.03.015.

[201] Kim GS, Lee BY, Ham HC, Han J, Nam SW, Moon J, et al. Highly active and stable Sr0.92Y0.08Ti1−xRuxO3−d in dry reforming for hydrogen production. Int J Hydrogen Energy 2019;44:202–12. doi:10.1016/j.ijhydene.2018.03.116.

[202] Papargyriou D, Miller DN, Irvine JTS. Exsolution of Fe-Ni alloy nanoparticles from (La,Sr)(Cr,Fe,Ni)O3 perovskites as potential oxygen transport membrane catalysts for methane reforming. J Mater Chem A 2019;7:15812–22. doi:10.1039/c9ta03711j.

[203] Joo S, Kwon O, Kim S, Jeong HY, Kim G. Ni-Fe Bimetallic Nanocatalysts Produced by Topotactic Exsolution in Fe deposited PrBaMn 1.7 Ni 0.3 O 5+ δ for Dry Reforming of Methane . J Electrochem Soc 2020;167:064518. doi:10.1149/1945-7111/ab8390.

[204] Padi SP, Shelly L, Komarala EP, Schweke D, Hayun S, Rosen BA. Coke-free methane dry reforming over nano-sized NiO-CeO2 solid solution after exsolution. Catal Commun 2020;138:105951. doi:10.1016/j.catcom.2020.105951.

[205] Joo S, Lim C, Kwon O, Zhang L, Zhou J, Wang J-Q, et al. The first observation of Ni nanoparticle exsolution from YSZ and its application for dry reforming of methane. Mater Reports Energy 2021;1:100021. doi:10.1016/j.matre.2021.100021.

[206] Bhattar S, Krishnakumar A, Kanitkar S, Abedin A, Shekhawat D, Haynes DJ, et al. 110th Anniversary: Dry Reforming of Methane over Ni-and Sr-Substituted Lanthanum Zirconate Pyrochlore Catalysts: Effect of Ni Loading. Ind Eng Chem Res 2019;58:19386–96. doi:10.1021/acs.iecr.9b02434.

[207] le Saché E, Pastor-Pérez L, Garcilaso V, Watson DJ, Centeno MA, Odriozola JA, et al. Flexible syngas production using a La2Zr2-xNixO7-δ pyrochlore-double perovskite catalyst: Towards a direct route for gas phase CO2 recycling. Catal Today 2020;357:583–9. doi:10.1016/j.cattod.2019.05.039.

[208] Naeem MA, Abdala PM, Armutlulu A, Kim SM, Fedorov A, Müller CR. Exsolution of Metallic Ru Nanoparticles from Defective, Fluorite-Type Solid Solutions Sm2Ru xCe2-xO7 to Impart Stability on Dry Reforming Catalysts. ACS Catal 2020;10:1923–37. doi:10.1021/acscatal.9b04555.

[209] Haynes DJ, Shekhawat D, Berry D, Roy A, Spivey JJ. Effect of calcination temperature on steam reforming activity of Ni-based pyrochlore catalysts. J Rare Earths 2020;38:711–8. doi:10.1016/j.jre.2019.07.015.

[210] Cho E, Lee YH, Kim H, Jang EJ, Kwak JH, Lee K, et al. Ni catalysts for dry methane reforming prepared by A-site exsolution on mesoporous defect spinel magnesium aluminate. Appl Catal A Gen 2020;602:117694. doi:10.1016/j.apcata.2020.117694.

[211] Littlewood P, Xie X, Bernicke M, Thomas A, Schomäcker R. Ni0.05Mn0.95O catalysts for the dry reforming of methane. Catal Today 2015;242:111–8. doi:10.1016/j.cattod.2014.07.054.

[212] Park YS, Kang M, Byeon P, Chung SY, Nakayama T, Ko T, et al. Fabrication of a regenerable Ni supported NiO-MgO catalyst for methane steam reforming by exsolution. J Power Sources 2018;397:318–24. doi:10.1016/j.jpowsour.2018.07.025.

[213] Kumar N, Kanitkar S, Wang Z, Haynes D, Shekhawat D, Spivey JJ. Dry reforming of methane with isotopic gas mixture over Ni-based pyrochlore catalyst. Int J Hydrogen Energy 2019;44:4167–76. doi:10.1016/j.ijhydene.2018.12.145.

[214] Lin C, Jang JB, Zhang L, Stach EA, Gorte RJ. Improved Coking Resistance of "intelligent" Ni Catalysts Prepared by Atomic Layer Deposition. ACS Catal 2018;8:7679–87. doi:10.1021/acscatal.8b01598.

[215] Joo S, Kwon O, Kim K, Kim S, Kim H, Shin J, et al. Cation-swapped homogeneous nanoparticles in perovskite oxides for high power density. Nat Commun 2019;10:1–9. doi:10.1038/s41467-019-08624-0.

[216] Joo S, Seong A, Kwon O, Kim K, Lee JH, Gorte RJ, et al. Highly active dry methane reforming catalysts with boosted in situ grown Ni-Fe nanoparticles on perovskite via

atomic layer deposition. Sci Adv 2020;6:1–9. doi:10.1126/sciadv.abb1573.

[217] Joo S, Kim K, Kwon O, Oh J, Kim HJ, Zhang L, et al. Enhancing Thermocatalytic Activities by Upshifting the d-Band Center of Exsolved Co-Ni-Fe Ternary Alloy Nanoparticles for the Dry Reforming of Methane. Angew Chemie - Int Ed 2021;60:15912–9. doi:10.1002/anie.202101335.

[218] Dama S, Ghodke SR, Bobade R, Gurav HR, Chilukuri S. Active and durable alkaline earth metal substituted perovskite catalysts for dry reforming of methane. Appl Catal B Environ 2018;224:146–58. doi:10.1016/j.apcatb.2017.10.048.

[219] De Caprariis B, De Filippis P, Palma V, Petrullo A, Ricca A, Ruocco C, et al. Rh, Ru and Pt ternary perovskites type oxides BaZr(1-x)MexO3 for methane dry reforming. Appl Catal A Gen 2016;517:47–55. doi:10.1016/j.apcata.2016.02.029.

[220] Ruocco C, De Caprariis B, Palma V, Petrullo A, Ricca A, Scarsella M, et al. Methane dry reforming on Ru perovskites, AZrRuO 3 : Influence of preparation method and substitution of A cation with alkaline earth metals. J CO2 Util 2019;30:222–31. doi:10.1016/j.jcou.2019.02.009.

[221] Alenazey F, AlOtaibi B, Otaibi RAL, Alyousef Y, Alqahtania S, Qazaq A, et al. A Novel Carbon-Resistant Perovskite Catalyst for Hydrogen Production Using Methane Dry Reforming. Top Catal 2021;64:348–56. doi:10.1007/s11244-020-01406-9.

[222] Evans SE, Staniforth JZ, Darton RJ, Ormerod RM. A nickel doped perovskite catalyst for reforming methane rich biogas with minimal carbon deposition. Green Chem 2014;16:4587–94. doi:10.1039/C4GC00782D.

[223] Khazaal MH, Staniforth JZ, Alfatlawi ZA, Ormerod RM, Darton RJ. Enhanced Methane Reforming Activity of a Hydrothermally Synthesized Codoped Perovskite Catalyst. Energy and Fuels 2018;32:12826–32. doi:10.1021/acs.energyfuels.8b02848.

[224] Yafarova L V., Chislova I V., Zvereva IA, Kryuchkova TA, Kost V V., Sheshko TF. Sol–gel synthesis and investigation of catalysts on the basis of perovskite-type oxides GdMO3 (M = Fe, Co). J Sol-Gel Sci Technol 2019;92:264–72. doi:10.1007/s10971-019-05013-3.

[225] Choudhary VR, Mondal KC, Mamman AS, Joshi UA. Carbon-free dry reforming of methane to syngas over NdCoO 3 perovskite-type mixed metal oxide catalyst. Catal Letters 2005;100:271–6. doi:10.1007/s10562-004-3467-0.

[226] Nijhuis TA, Beers AEWW, Vergunst T, Hoek I, Kapteijn F, Moulijn J a., et al. Preparation of monolithic catalysts. Catal Rev 2001;43:345–80. doi:10.1081/CR-120001807.

[227] Esposito S. “Traditional” sol-gel chemistry as a powerful tool for the preparation of supported metal and metal oxide catalysts. Materials (Basel) 2019;12:1–25.

doi:10.3390/ma12040668.

[228] MODAN EM, PLĂIAȘU AG. Advantages and Disadvantages of Chemical Methods in the Elaboration of Nanomaterials. Ann “Dunarea Jos” Univ Galati Fascicle IX, Metall Mater Sci 2020;43:53–60. doi:10.35219/mms.2020.1.08.

[229] Subramani K. Fabrication of hydrogel micropatterns by soft photolithography. Emerg Nanotechnologies Manuf 2014:279–93. doi:10.1016/B978-0-323-28990-0.00011-7.

[230] Bajpai N, Tiwari A, Khan SA, Kher RS, Bramhe N, Dhoble SJ. Effects of rare earth ions (Tb, Ce, Eu, Dy) on the thermoluminescence characteristics of sol-gel derived and γ-irradiated SiO2 nanoparticles. Luminescence 2014;29:669–73. doi:10.1002/bio.2604.

[231] Wang B, Lin H, Xu J, Chen H, Wang Y. CaMg2Al16O27:Mn4+-based red phosphor: A potential color converter for high-powered warm W-led. ACS Appl Mater Interfaces 2014;6:22905–13. doi:10.1021/am507316b.

[232] Peng T, Huajun L, Yang H, Yan C. Synthesis of SrAl2O4:Eu, Dy phosphor nanometer powders by sol-gel processes and its optical properties. Mater Chem Phys 2004;85:68–72. doi:10.1016/j.matchemphys.2003.12.001.

[233] Niederberger M, Pinna N. Metal oxide nanoparticles in organic solvents : synthesis, formation, assembly and applications (Engineering Materials and Processes). Berlin, Germany: Springer; 2009.

[234] Bokov D, Jalil AT, Chupradit S, Suksatan W, Ansari MJ, Shewael IH, et al. Nanomaterial by Sol-Gel Method : Synthesis and Application 2021;2021.

[235] Pham CQ, Nguyen V-P, Van TT, Phuong PTT, Pham PTH, Trinh TH, et al. Syngas Production from Biogas Reforming: Role of the Support in Nickel-based Catalyst Performance. Top Catal 2023;66:262–74. doi:10.1007/s11244-022-01750-y.

[236] Kurdi AN, Ibrahim AA, Al-Fatesh AS, Alquraini AA, Abasaeed AE, Fakeeha AH. Hydrogen production from CO2 reforming of methane using zirconia supported nickel catalyst. RSC Adv 2022;12:10846–54. doi:10.1039/d2ra00789d.

[237] Lanre MS, Abasaeed AE, Fakeeha AH, Ibrahim AA, Al-awadi AS, Jumah A, et al. Lanthanum – Cerium-Modified Nickel Catalysts for Dry Reforming of Methane 2022.

[238] Taylor P, Nijhuis TA, Beers AEW, Vergunst T, Hoek I, Moulijn JA. Catalysis Reviews : Science and Engineering Preparation of monolithic catalysts n.d.:37–41. doi:10.1081/CR-120001807.

[239] Özdemir H, Öksüzömer MAFF, Gürkaynak MA. Effect of the calcination temperature on Ni/MgAl2O4 catalyst structure and catalytic properties for partial oxidation of methane. Fuel 2014;116:63–70. doi:10.1016/j.fuel.2013.07.095.

[240] Ciambelli P, Palma V, Palo E. Comparison of ceramic honeycomb monolith and foam as Ni catalyst carrier for methane autothermal reforming. Catal Today 2010;155:92–100. doi:10.1016/j.cattod.2009.01.021.

[241] Usman M, Wan Daud WMA. An investigation on the influence of catalyst composition, calcination and reduction temperatures on Ni/MgO catalyst for dry reforming of methane. RSC Adv 2016;6:91603–16. doi:10.1039/C6RA15256B.

[242] Katheria S, Gupta A, Deo G, Kunzru D. Effect of calcination temperature on stability and activity of Ni/MgAl2O4 catalyst for steam reforming of methane at high pressure condition. Int J Hydrogen Energy 2016;41:14123–32. doi:10.1016/j.ijhydene.2016.05.109.

[243] Goyal N, Pant KK, Gupta R. Hydrogen production by steam reforming of model bio-oil using structured Ni/Al2O3 catalysts. Int J Hydrogen Energy 2013;38:921–33. doi:10.1016/j.ijhydene.2012.10.080.

[244] Wu P, Li X, Ji S, Lang B, Habimana F, Li C. Steam reforming of methane to hydrogen over Ni-based metal monolith catalysts. Catal Today 2009;146:82–6. doi:10.1016/j.cattod.2009.01.031.

[245] Habibi N, Wang Y, Arandiyan H, Rezaei M. Effect of substitution by Ni in MgAl2O4spinel for biogas dry reforming. Int J Hydrogen Energy 2017;42:24159–68. doi:10.1016/j.ijhydene.2017.07.222.

[246] Brussino P, Bortolozzi JP, Dalla Costa BO, Banús ED, Ulla MA. Double effect of La as a promoter for Ni/Al2O3 cordierite monoliths in the oxydehydrogenation of ethane (ODE). Appl Catal A Gen 2019;575:1–10. doi:10.1016/j.apcata.2019.02.010.

[247] Azam MA, Syafira N, Manaf A. Aligned carbon nanotube from catalytic chemical vapor deposition technique for energy storage device : a review 2013:1455–76. doi:10.1007/s11581-013-0979-x.

[248] Villegas L, Masset F, Guilhaume N. Wet impregnation of alumina-washcoated monoliths: Effect of the drying procedure on Ni distribution and on autothermal reforming activity. Appl Catal A Gen 2007;320:43–55. doi:10.1016/j.apcata.2006.12.011.

[249] Han JW, Kim C, Park JS, Lee H. Highly coke-resistant Ni nanoparticle catalysts with minimal sintering in dry reforming of methane. ChemSusChem 2014;7:451–6. doi:10.1002/cssc.201301134.

[250] Pinheiro ANAL, Pinheiro ANAL, Valentini A, Filho JM, Sousa FF d. De, Sousa JR d. De, et al. Analysis of coke deposition and study of the structural features of MAl 2 O 4 catalysts for the dry reforming of methane. Catal Commun 2009;11:11–4. doi:10.1016/j.catcom.2009.08.003.

[251] Li X, Li D, Tian H, Zeng L, Zhao Z, Gong J. Applied Catalysis B : Environmental Dry

reforming of methane over Ni / La 2 O 3 nanorod catalysts with stabilized Ni nanoparticles 2017;202:683–94. doi:10.1016/j.apcatb.2016.09.071.

[252] Rodrigues CP, Schmal M. Nickel-alumina washcoating on monoliths for the partial oxidation of ethanol to hydrogen production. Int J Hydrogen Energy 2011;36:10709–18. doi:10.1016/j.ijhydene.2011.05.175.

[253] Arbag H. Effect of impregnation sequence of Mg on performance of mesoporous alumina supported Ni catalyst in dry reforming of methane. Int J Hydrogen Energy 2018;43:6561–74. doi:10.1016/j.ijhydene.2018.02.063.

[254] Mustu H, Yasyerli S, Yasyerli N, Dogu G, Dogu T, Djinović P, et al. Effect of synthesis route of mesoporous zirconia based Ni catalysts on coke minimization in conversion of biogas to synthesis gas. Int J Hydrogen Energy 2015;40:3217–28. doi:10.1016/j.ijhydene.2015.01.023.

[255] Cakiryilmaz N, Arbag H, Oktar N, Dogu G, Dogu T. Effect of W incorporation on the product distribution in steam reforming of bio-oil derived acetic acid over Ni based Zr-SBA-15 catalyst. Int J Hydrogen Energy 2018;43:3629–42. doi:10.1016/j.ijhydene.2018.01.034.

[256] Arbag H, Yasyerli S, Yasyerli N, Dogu G, Dogu T, Osojnik ɤrnivec IG, et al. Coke minimization during conversion of biogas to syngas by bimetallic tungsten-nickel incorporated mesoporous alumina synthesized by the one-pot route. Ind Eng Chem Res 2015;54:2290–301. doi:10.1021/ie504477t.

[257] Charisiou ND, Tzounis L, Sebastian V, Hinder SJ, Baker MA, Polychronopoulou K, et al. Investigating the correlation between deactivation and the carbon deposited on the surface of Ni/Al 2 O 3 and Ni/La 2 O 3 -Al 2 O 3 catalysts during the biogas reforming reaction. Appl Surf Sci 2019;474:42–56. doi:10.1016/j.apsusc.2018.05.177.

[258] Goula MA, Charisiou ND, Papageridis KN, Delimitis A, Pachatouridou E, Iliopoulou EF. Nickel on alumina catalysts for the production of hydrogen rich mixtures via the biogas dry reforming reaction: Influence of the synthesis method. Int J Hydrogen Energy 2015;40:9183–200. doi:10.1016/j.ijhydene.2015.05.129.

[259] Goula MA, Charisiou ND, Siakavelas G, Tzounis L, Tsiaoussis I, Panagiotopoulou P, et al. Syngas production via the biogas dry reforming reaction over Ni supported on zirconia modified with CeO2 or La2O3 catalysts. Int J Hydrogen Energy 2017;42:13724–40. doi:10.1016/j.ijhydene.2016.11.196.

[260] Zhang P, Debroy T, Seetharaman S. Interdiffusion in the MgO-Al2O3 spinel with or without some dopants. Metall Mater Trans A Phys Metall Mater Sci 1996;27:2105–14. doi:10.1007/BF02651865.

[261] DAVIS RF, PASK JA. Diffusion and Reaction Studies in the System Al2O3-SiO2. J Am Ceram Soc 1972;55:525–31. doi:10.1111/j.1151-2916.1972.tb13421.x.

[262] Salaev MA, Liotta LF, Vodyankina OV. Lanthanoid-containing Ni-based catalysts for dry reforming of methane: A review. Int J Hydrogen Energy 2022;47:4489–535. doi:10.1016/j.ijhydene.2021.11.086.

[263] Chang ACCC, Lee KY. Biogas reforming by the honeycomb reactor for hydrogen production. Int J Hydrogen Energy 2016;41:4358–65. doi:10.1016/j.ijhydene.2015.09.018.

[264] Charisiou ND, Iordanidis A, Polychronopoulou K, Yentekakis I V., Goula MA. Studying the stability of Ni supported on modified with CeO 2 alumina catalysts for the biogas dry reforming reaction. Mater Today Proc 2018;5:27607–16. doi:10.1016/j.matpr.2018.09.081.

[265] Pawar V, Ponugoti P V., Janardhanan VM, Appari S. Experimental studies of catalyst deactivation due to carbon and sulphur during CO2 reforming of CH4 over Ni washcoated monolith in the presence of H2S. Can J Chem Eng 2021:1–10. doi:10.1002/cjce.24266.

[266] Luisetto I, Sarno C, De Felicis D, Basoli F, Battocchio C, Tuti S, et al. Ni supported on $γ$-Al2O3promoted by Ru for the dry reforming of methane in packed and monolithic reactors. Fuel Process Technol 2017;158:130–40. doi:10.1016/j.fuproc.2016.12.015.

[267] Tsiotsias AI, Charisiou ND, Sebastian V, Gaber S, Hinder SJ, Baker MA, et al. A comparative study of Ni catalysts supported on Al2O3, MgO–CaO–Al2O3 and La2O3–Al2O3 for the dry reforming of ethane. Int J Hydrogen Energy 2021;47:5337–53. doi:10.1016/j.ijhydene.2021.11.194.

[268] Düdder H, Kähler K, Krause B, Mette K, Kühl S, Behrens M, et al. The role of carbonaceous deposits in the activity and stability of Ni-based catalysts applied in the dry reforming of methane. Catal Sci Technol 2014;4:3317–28. doi:10.1039/c4cy00409d.

[269] Schuepfer DB, Badaczewski F, Guerra-Castro JM, Hofmann DM, Heiliger C, Smarsly B, et al. Assessing the structural properties of graphitic and non-graphitic carbons by Raman spectroscopy. Carbon N Y 2020;161:359–72. doi:10.1016/j.carbon.2019.12.094.

[270] Bokobza L, Bruneel JL, Couzi M. Raman spectroscopy as a tool for the analysis of carbon-based materials (highly oriented pyrolitic graphite, multilayer graphene and multiwall carbon nanotubes) and of some of their elastomeric composites. Vib Spectrosc 2014;74:57–63. doi:10.1016/j.vibspec.2014.07.009.

[271] Malard LM, Pimenta MA, Dresselhaus G, Dresselhaus MS. Raman spectroscopy in graphene. Phys Rep 2009;473:51–87. doi:10.1016/j.physrep.2009.02.003.

[272] Ferrandon MS, Byron C, Celik G, Zhang Y, Ni C, Sloppy J, et al. Grafted nickel-promoter catalysts for dry reforming of methane identified through high-throughput

experimentation. Appl Catal A Gen 2022;629:118379. doi:10.1016/j.apcata.2021.118379.

[273] González JJJ, Da Costa-Serra JFF, Chica A. Biogas dry reforming over Ni–Ce catalyst supported on nanofibered alumina. Int J Hydrogen Energy 2020;45:20568–81. doi:10.1016/j.ijhydene.2020.02.042.

[274] Chen J, Wang R, Zhang J, He F, Han S. Effects of preparation methods on properties of Ni/CeO2–Al2O3 catalysts for methane reforming with carbon dioxide. J Mol Catal A Chem 2005;235:302–10. doi:10.1016/j.molcata.2005.04.023.

[275] Qin Z, Chen L, Chen J, Su T, Ji H. Ni/CeO2 prepared by improved polyol method for DRM with highly dispersed Ni. Greenh Gases Sci Technol 2021;20:1–20. doi:10.1002/ghg.2129.

[276] Chava R, D BAV, Roy B, Appari S. Recent advances and perspectives of perovskite-derived Ni-based catalysts for CO2 reforming of biogas. J CO2 Util 2022;65:102206. doi:10.1016/j.jcou.2022.102206.

[277] Chen TY, Pan RY, Fung KZ. Effect of divalent dopants on crystal structure and electrical properties of LaAlO3 perovskite. J Phys Chem Solids 2008;69:540–6. doi:10.1016/j.jpcs.2007.07.039.

[278] Agüero FN, Beltrán AM, Fernández MA, Cadús LE. Surface nickel particles generated by exsolution from a perovskite structure. J Solid State Chem 2019;273:75–80. doi:10.1016/j.jssc.2019.02.036.

[279] Kostogloudis G. Chemical reactivity of perovskite oxide SOFC cathodes and yttria stabilized zirconia. Solid State Ionics 2000;135:529–35. doi:10.1016/S0167-2738(00)00433-1.

[280] Yadav D, Kumar U, Nirala G, Mall AK, Upadhyay S. Effect of acceptor Na1+ doping on the properties of perovskite SrCeO3. J Mater Sci Mater Electron 2019;30:15772–85. doi:10.1007/s10854-019-01963-0.

[281] Ramantani T, Bampos G, Vavatsikos A, Vatskalis G, Kondarides DI. Propane Steam Reforming over Catalysts Derived from Noble Metal (Ru, Rh)-Substituted LaNiO3 and La0.8Sr0.2NiO3 Perovskite Precursors. Nanomaterials 2021;11:1931. doi:10.3390/nano11081931.

[282] Bhavani AG, Kim WY, Lee JS. Barium Substituted Lanthanum Manganite Perovskite for CO 2 Reforming of Methane. ACS Catal 2013;3:1537–44. doi:10.1021/cs400245m.

[283] Wei T, Jia L, Luo JL, Chi B, Pu J, Li J. CO2 dry reforming of CH4 with Sr and Ni co-doped LaCrO3 perovskite catalysts. Appl Surf Sci 2020;506:144699. doi:10.1016/j.apsusc.2019.144699.

[284] Chen W, Zhao G, Xue Q, Chen L, Lu Y. High carbon-resistance Ni/CeAlO3-Al2O3 catalyst for CH4/CO2 reforming. Appl Catal B Environ 2013;136–137:260–8. doi:10.1016/j.apcatb.2013.01.044.

[285] Chandradass J, Kim KH. Size-controlled synthesis of LaAlO3 by reverse micelle method: Investigation of the effect of water-to-surfactant ratio on the particle size. J Cryst Growth 2009;311:3631–5. doi:10.1016/j.jcrysgro.2009.06.012.

[286] da Silva CA, de Miranda PE V. Synthesis of LaAlO3 based materials for potential use as methane-fueled solid oxide fuel cell anodes. Int J Hydrogen Energy 2015;40:10002–15. doi:10.1016/j.ijhydene.2015.06.019.

[287] Naz F, Saeed K. Synthesis of barium oxide nanoparticles and its novel application as a catalyst for the photodegradation of malachite green dye. Appl Water Sci 2022;12:1–11. doi:10.1007/s13201-022-01649-9.

[288] Guru S, Bajpai AK, Amritphale SS. Influence of nature of surfactant and precursor salt anion on the microwave assisted synthesis of barium carbonate nanoparticles. Mater Chem Phys 2020;241:122377. doi:10.1016/j.matchemphys.2019.122377.

[289] Bazeera AZ, Amrin MI. Synthesis and Characterization of Barium Oxide Nanoparticles. IOSR J Appl Phys 2017;01:76–80. doi:10.9790/4861-17002017680.

[290] Ma Y, Su P, Ge Y, Wang F, Xue R, Wang Z, et al. A Novel LaAlO3 Perovskite with Large Surface Area Supported Ni-Based Catalyst for Methane Dry Reforming. Catal Letters 2022. doi:10.1007/s10562-021-03910-3.

[291] Figueredo GP, Medeiros RLBA, Macedo HP, de Oliveira ÂAS, Braga RM, Mercury JMR, et al. A comparative study of dry reforming of methane over nickel catalysts supported on perovskite-type LaAlO3 and commercial A-Al2O3. Int J Hydrogen Energy 2018;43:11022–37. doi:10.1016/j.ijhydene.2018.04.224.

[292] Park YH, Kim JY, Moon DJ, Park NC, Kim YC. Effect of LaAlO3-supported modified Ni-based catalysts on aqueous phase reforming of glycerol. Res Chem Intermed 2015;41:9603–14. doi:10.1007/s11164-015-2020-7.

[293] Wei T, Jia L, Luo J-L, Chi B, Pu J, Li J. CO2 dry reforming of CH4 with Sr and Ni co-doped LaCrO3 perovskite catalysts. Appl Surf Sci 2020;506:144699. doi:10.1016/j.apsusc.2019.144699.

[294] Al-Fatesh AS, Ibrahim AA, Osman AI, Albaqi F, Arasheed R, Francesco F, et al. Optimizing Barium Oxide Promoter for Nickel Catalyst Supported on Yttria–Stabilized Zirconia in Dry Reforming of Methane. SSRN Electron J 2022. doi:10.2139/ssrn.4133231.

[295] Ning X, Wang Z, Zhang Z. Fermi Level shifting, Charge Transfer and Induced Magnetic

Coupling at La0.7Ca0.3MnO3/LaNiO3 Interface. Sci Rep 2015;5:8460. doi:10.1038/srep08460.

[296] Fabián M, Arias-Serrano BI, Yaremchenko AA, Kolev H, Kaňuchová M, Briančin J. Ionic and electronic transport in calcium-substituted LaAlO3 perovskites prepared via mechanochemical route. J Eur Ceram Soc 2019;39:5298–308. doi:10.1016/j.jeurceramsoc.2019.07.038.

[297] Yabe T, Kamite Y, Sugiura K, Ogo S, Sekine Y. Low-temperature oxidative coupling of methane in an electric field using carbon dioxide over Ca-doped LaAlO3 perovskite oxide catalysts. J CO2 Util 2017;20:156–62. doi:10.1016/j.jcou.2017.05.001.

[298] Ahmad N, Wahab R, Manoharadas S, Alrayes BF, Alharthi F. Utilization of greenhouse gases for syngas production by dry reforming process using reduced banio3 perovskite as a catalyst. Sustain 2021;13. doi:10.3390/su132413855.

[299] Spasojevic I, Sauthier G, Caicedo JM, Verdaguer A, Domingo N. Oxidation processes at the surface of BaTiO3 thin films under environmental conditions. Appl Surf Sci 2021;565. doi:10.1016/j.apsusc.2021.150288.

[300] Gan R, Nishida Y, Haneda M. Effect of B Site Substitution on the Catalytic Activity of La-Based Perovskite for Oxidative Coupling of Methane. Phys Status Solidi Basic Res 2022;3:1–7. doi:10.1002/pssb.202100544.

[301] Gopi UV, Bhojane P, Smaran KS. Engineering oxygen-deficient nanocomposite comprising LaNiO3-δ and reduced graphene oxide for high-performance pseudocapacitors. J Energy Storage 2022;54:105301. doi:10.1016/j.est.2022.105301.

[302] Cheng CR, Tsai MH, Hsu TH, Li MJ, Huang CL. Resistive switching characteristics and mechanism of lanthanum yttrium oxide (LaYO3) films deposited by RF sputtering for RRAM applications. J Alloys Compd 2023;930:167487. doi:10.1016/j.jallcom.2022.167487.

[303] Che W, Wei M, Sang Z, Ou Y, Liu Y, Liu J. School of Chemistry , Chemical Engineering and Life Science and State Key Laboratory of. J Alloys Compd 2017. doi:10.1016/j.jallcom.2017.10.027.

[304] Valderrama G, Kiennemann A, Goldwasser MR. La-Sr-Ni-Co-O based perovskite-type solid solutions as catalyst precursors in the CO2 reforming of methane. J Power Sources 2010;195:1765–71. doi:10.1016/j.jpowsour.2009.10.004.

[305] Garbarino G, Wang C, Cavattoni T, Finocchio E, Riani P, Flytzani-Stephanopoulos M, et al. A study of Ni/La-Al2O3 catalysts: A competitive system for CO2 methanation. Appl Catal B Environ 2019;248:286–97. doi:10.1016/j.apcatb.2018.12.063.

[306] Bhattar S, Abedin MA, Kanitkar S, Spivey JJ. A review on dry reforming of methane over

perovskite derived catalysts. Catal Today 2020. doi:10.1016/j.cattod.2020.10.041.

[307] Wei T, Pan X, Wang S, Qiu P, Du X, Liu B, et al. Ce-enhanced LaMnO 3 perovskite catalyst with exsolved Ni particles for H 2 production from CH 4 dry reforming . Sustain Energy Fuels 2021:5481–9. doi:10.1039/d1se01111a.

[308] da Fonseca RO, Ponseggi AR, Rabelo-Neto RC, Simões RCC, Mattos L V., Noronha FB. Controlling carbon formation over Ni/CeO2 catalyst for dry reforming of CH4 by tuning Ni crystallite size and oxygen vacancies of the support. J CO2 Util 2022;57:101880. doi:10.1016/j.jcou.2021.101880.

[309] Wu L, Xie X, Ren H, Gao X. A short review on nickel-based catalysts in dry reforming of methane: Influences of oxygen defects on anti-coking property. Mater Today Proc 2019;42:153–60. doi:10.1016/j.matpr.2020.10.697.

[310] Park J-H, Yeo S, Chang T-S. Effect of supports on the performance of Co-based catalysts in methane dry reforming. J CO2 Util 2018;26:465–75. doi:10.1016/j.jcou.2018.06.002.

[311] Chava Ramakrishna, Purbia Devendra, Roy Banasri, Janardhanan Vinod M, Bahurudeen A AS, Chava R, Purbia D, Roy B, Janardhanan VM, Bahurudeen A, et al. Effect of Calcination Time on the Catalytic Activity of Ni/γ-Al2O3 Cordierite Monolith for Dry Reforming of Biogas. Int J Hydrogen Energy 2021;46:6341–57. doi:10.1016/j.ijhydene.2020.11.125.

[312] Al-Fatesh AS, Patel R, Srivastava VK, Ibrahim AA, Naeem MA, Fakeeha AH, et al. Barium-Promoted Yttria-Zirconia-Supported Ni Catalyst for Hydrogen Production via the Dry Reforming of Methane: Role of Barium in the Phase Stabilization of Cubic ZrO2. ACS Omega 2022. doi:10.1021/acsomega.2c00471.

[313] Hussien AGS, Polychronopoulou K. A Review on the Different Aspects and Challenges of the Dry Reforming of Methane (DRM) Reaction. Nanomaterials 2022;12. doi:10.3390/nano12193400.

[314] Hussien AGS, Damaskinos CM, Dabbawala A, Anjun DH, Vasiliades MA, Khaleel MTA, et al. Elucidating the role of La3+/Sm3+ in the carbon paths of dry reforming of methane over Ni/Ce-La(Sm)-Cu-O using transient kinetics and isotopic techniques. Appl Catal B Environ 2022;304:121015. doi:10.1016/j.apcatb.2021.121015.

[315] da Fonseca RO, Ponseggi AR, Rabelo-Neto RC, Simões RCC, Mattos L V, Noronha FB. Controlling carbon formation over Ni/CeO2 catalyst for dry reforming of CH4 by tuning Ni crystallite size and oxygen vacancies of the support. J CO2 Util 2022;57:101880. doi:10.1016/j.jcou.2021.101880.

[316] Damaskinos CM, Zavašnik J, Djinović P, Efstathiou AM. Dry reforming of methane over Ni/Ce0.8Ti0.2O2-δ: The effect of Ni particle size on the carbon pathways studied by

transient and isotopic techniques. Appl Catal B Environ 2021;296. doi:10.1016/j.apcatb.2021.120321.

[317] Du Z, Petru C, Yang X, Chen F, Fang S, Pan F, et al. Development of stable La0.9Ce0.1NiO3 perovskite catalyst for enhanced photothermochemical dry reforming of methane. J CO2 Util 2023;67:102317. doi:10.1016/j.jcou.2022.102317.

[318] le Saché E, Alvarez Moreno A, Reina TR. Biogas Conversion to Syngas Using Advanced Ni-Promoted Pyrochlore Catalysts: Effect of the CH4/CO2 Ratio. Front Chem 2021;9:1–10. doi:10.3389/fchem.2021.672419.

[319] Chava R, Bhaskar AVD, Roy B, Appari S. Reforming of model biogas using Ni/CeO2/γ-Al2O3 monolith catalyst. Mater Today Proc 2022:2–7. doi:10.1016/j.matpr.2022.06.234.

[320] Latsiou AI, Bereketidou OA, Charisiou ND, Georgiadis AG, Avraam DG, Goula MA. Synthesis and Mathematical Modelling of the Preparation Process of Nickel-Alumina Catalysts with Egg-Shell Structures for Syngas Production via Reforming of Clean Model Biogas. Catalysts 2022;12. doi:10.3390/catal12030274.

[321] Luisetto I, Tuti S, Romano C, Boaro M, Di Bartolomeo E, Kesavan JK, et al. Dry reforming of methane over Ni supported on doped CeO2: New insight on the role of dopants for CO2 activation. J CO2 Util 2019;30:63–78. doi:10.1016/j.jcou.2019.01.006.

[322] Yao Z, Jiang J, Zhao Y, Luan F, Zhu J, Shi Y, et al. Insights into the deactivation mechanism of metal carbide catalysts for dry reforming of methane via comparison of nickel-modified molybdenum and tungsten carbides. RSC Adv 2016;6:19944–51. doi:10.1039/C5RA24815A.

[323] Franz R, Pinto D, Uslamin EA, Urakawa A, Pidko EA. Impact of Promoter Addition on the Regeneration of Ni/Al2O3 Dry Reforming Catalysts. ChemCatChem 2021;13:5034–46. doi:10.1002/cctc.202101080.

[324] Deng J, Cai M, Sun W, Liao X, Chu W, Zhao XS. Oxidative methane reforming with an intelligent catalyst: Sintering-tolerant supported nickel nanoparticles. ChemSusChem 2013;6:2061–5. doi:10.1002/cssc.201300452.

[325] Du Y, Qin C, Xu Y, Xu D, Bai J, Ma G, et al. Ni nanoparticles dispersed on oxygen vacancies-rich CeO2 nanoplates for enhanced low-temperature CO2 methanation performance. Chem Eng J 2021;418. doi:10.1016/j.cej.2021.129402.

[326] Sharifianjazi F, Esmaeilkhanian A, Bazli L, Eskandarinezhad S, Khaksar S, Shafiee P, et al. A review on recent advances in dry reforming of methane over Ni- and Co-based nanocatalysts. Int J Hydrogen Energy 2021. doi:10.1016/j.ijhydene.2021.11.172.

List of Publications

Journals

1. **R.Chava**, D.Purbia, B.roy, Vinod.M, A. Bahurudeen, and S. Appari, Effect of calcination time on the catalytic activity of Ni/Al_2O_3 cordierite monolith for dry reforming of biogas, Int J Hydrogen Energy 2020; 46 (9), 6341-6357, DOI:10.1016/j.ijhydene.2020.11.125
2. **R. Chava**, B.A Verma D, S. Appari and B. Roy, Recent advances and perspectives of perovskite-derived Ni-based catalysts for CO_2 reforming of biogas, J CO_2 Util 2022; 65,102206, DOI:10.1016/j.jcou.2022.102206
3. **R.Chava,** A.K Seriyala, B.A Verma D, K.Yeluvu, B.Roy, and S.Appari, Investigation of Ba-doping in A-site deficient Perovskite Ni-exsolved catalysts for Biogas Dry Reforming, Int J Hydrogen Energy 2023, DOI: 10.1016/j.ijhydene.2023.03.464

Peer-reviewed Conference Journals

4. **R. Chava**, B.A Verma D, S. Appari and B. Roy, Reforming of model biogas using $Ni/CeO_2/\gamma\text{-}Al_2O_3$ monolith catalyst, Mater Today Proc 2022; 72, 134-139, DOI:10.1016/j.matpr.2022.06.234
5. **R.Chava,** H.Mehta, B.Roy, and S.Appari, Dual reforming of model biogas for syngas production on $Ni/C\text{-}Al_2O_3$ and Ni-C/ZSM-5 cordierite monolith catalysts, Mater Today Proc, 2022; 76, 393-397, DOI: 10.1016/j.matpr.2022.11.468

Publications in Other research area

6. SS Shukla, **R. Chava**, S Appari, A Bahurudeen, Sustainable use of rice husk for the cleaner production of value-added products, J Envi Chem Eng 2021;10 (1), 106899, DOI:10.1016/j.jece.2021.106899

7. A. K Seriyala, **R. Chava,** S. Appari, B.Roy, Study of the Sn and La addition on Ni/CeO_2 catalyst for hydrogen production by low temperature steam reforming of ethanol, Int J Hydrogen Energy (under review)

Conferences Attended

1. **R. Chava,** B Verma, B. Roy, S. Appari, " Reforming of model biogas using $Ni/CeO_2\text{-}Al_2O_3$ monolith catalyst", $NMTE^2A$ 2022, Novel Materials and Technologies for Energy Applications, BITS PILANI, Hyderabad Campus, Feb 18-19, 2022

2. **R. Chava**, B. Roy, S.Appari, " Dry reforming of biogas over $Ni\text{-}Mg/Al_2O_3$ and $Ni\text{-}Ce/Al_2O_3$ monolith catalysts", CHEMCON 2021, Sustainable Utilization of Resources for Chemicals and Mineral Sectors, CSIR Bhubaneswar, Dec 26-30, 2021

Biography of the candidate

Ramakrishna Chava completed his Bachelor of Technology in Chemical Engineering from R.V.R & J. C College of Engineering in Guntur, Andhra Pradesh. He then pursued a Master of Engineering in Chemical Engineering from BITS PILANI, Pilani in 2017, where he was awarded the prestigious DAAD fellowship. During his Master's, he worked as a Visiting Research Scholar at TU Braunschweig from November 2016 to March 2017. In 2018, Ramakrishna joined BITS PILANI as a Ph.D student under the guidance of Prof. Srinivas Appari and Prof. Banasri Roy. His research interests lie in the areas of catalysis, biogas reforming, waste to energy, and Fischer-Tropsch process.

Biography of the Supervisor

Dr. Srinivas Appari has expertise in heterogeneous catalysis and detailed surface kinetic modeling. He completed Ph.D. from IIT Hyderabad, M.Tech from JNTU Hyderabad, and B.Tech from Osmania University. Aftter his Ph.D, he worked as Postdoctoral Research Fellow in Institute for Materials Chemistry and Engineering, Kyushu University, Japan. Currently, he is working on the hydrogen production and value-added chemicals from alternative feedstocks like biomass and biogas via catalytic routes. He also explores the methanol and dimethyl ether from CO_2 hydrogenation on various catalysts. His reserach interest also includes machine learning approaches for catalyst design, and Process modeling and simulation. His work has received two prestigious awards from the Japan Institute of Energy consecutively in 2015 and 2016. Presently, he is supervising three PhD students and two ME students, and 10 ME students completed their thesis successfully. He and his group published more than 30 peer reviewed journals that significantly contribute to heterogeneous catalysis and biomass conversion. His group research

work cited more than 774 citations with h-index 15 and i-10 index 18. Currently he is working as an Associate professor in the chemical engineering department at BITS- Pilani, Pilani campus.

- Institute Website: https://www.bits-pilani.ac.in/pilani/srinivasappari/Profile
- Google Scholar: https://scholar.google.com/citations?user=ceTKjfoAAAAJ&hl=en
- ORCID ID: 0000-0001-5253-1266
- Web of Science Researcher ID: C-3389-2018

Biography of the Co-Supervisor

Dr. Banasri Roy by training is a materials scientist. She completed her Ph.D. in materials engineering from Colorado School of Mines & National Renewable Energy Laboratory (NREL), USA, M. Tech in materials engineering from IIT-Kanpur, M.Sc. in applied physics from University of Puerto Rico, USA, B. Tech in chemical technology & B. Sc. (with honor) in chemistry from Calcutta University. The exercise in multidisciplinary research fields helps her to understand the advanced theory of characterization and data analysis. Dr. Roy has vast expertise in materials synthesis, analytical characterization (regarding SEM/TEM, XRD, TGA, RAMAN, XPS, DTA-TGA, UV-Vis spectroscopy, etc.), and data analysis.

She has extensively worked on the development of Nanocatalyst systems for renewable energy production from ethanol and biomasses. Her current focus is on the utilization of waste (agricultural and others) to convert to energy sources and other value-added chemicals. She also works on the development of nanoparticles for environmental pollution control and other applications. Her research interest includes surface modification of different biomaterials to improve biocompatibility.

She is one of the SERB-POWER fellowship recipients of 2021 and was awarded the ULAM-NAWA fellowship by the Polish National Agency for Academic Exchange. Two Ph.D and 14 ME students completed their thesis successfully under her guidance and currently she is supervising two Ph.D and two ME students. She authored and co-authored 45 peer-reviewed papers in different international journals, achieving around 1322 citations, 28 i-index, and 19 h-index. Currently, she is affiliated with the chemical engineering department of BITS- Pilani, Pilani campus.

- Institute Website: https://universe.bits-pilani.ac.in/pilani/broy/profile
- Google Scholar: https://scholar.google.com/citations?user=HF4Inh8AAAAJ&hl=en
- ORCID ID: 0000-0001-6365-2282
- Web of Science Researcher ID: AAQ-6273-2021